**DE GRUYTER**

J. Paulo Davim (Ed.)

# DRILLING TECHNOLOGY

## FUNDAMENTALS AND RECENT ADVANCES

J. Paulo Davim (Ed.)
**Drilling Technology**

# De Gruyter Series in Advanced Mechanical Engineering

Series Editor
J. Paulo Davim

## Volume 3

# Drilling Technology

Fundamentals and Recent Advances

Edited by
J. Paulo Davim

**DE GRUYTER**
OLDENBOURG

**Editor**
Prof. Dr. J. Paulo Davim
University of Aveiro
Dept. of Mechanical Engineering
Campus Santiago
3810-193 Aveiro
Portugal
pdavim@ua.pt

# Preface

Drilling is a repeatedly practiced machining process in industry due to its need for component assembly in mechanical parts and structures in several materials. It is expected that an important part of machining time is consumed performing drilling operations. Therefore, the use of advanced machines, appropriate strategies and special drilling tools can significantly reduce the machining time required for drilling operations, and consequently the production costs. In addition, the quality of holes produced is also very important. For these reasons and other, an improvement in the drilling technology is very important for modern manufacturing industries.

The current volume aims to provide recent information on advances in drilling technology in six chapters. Chapter 1 of the book provides information on "Efficient drilling of high-silicon aluminum alloys," Chapter 2 is dedicated to "Deep hole gun drilling of nickel-based superalloys," Chapter 3 described "On a new model pertaining to the high-speed drilling of titanium alloy Ti-6Al-4V," Chapter 4 contains information on "Drilling of composite materials: methods and tools," Chapter 5 describes "Challenges when machining of natural fiber-reinforced composites: A review" and finally, Chapter 6 is dedicated to "Analysis and optimization of hole quality parameters in cenosphere-multiwall carbon nanotube hybrid composites drilling using artificial neural network and gravitational search technique."

The current volume can be used as a research book for final undergraduate engineering course or as a topic on drilling technology at the postgraduate level. In addition, this book can serve as a useful reference for academics, researchers, mechanical, industrial, production, manufacturing and materials engineers, professionals in drilling technology and related fields. The scientific importance of this book is obvious for many important centers of research, laboratories and universities as well as industries. Consequently, it is expected this book will inspire and stimulate others to launch research in this field of drilling technology.

The Editor acknowledges De Gruyter for this opportunity and professional support. Finally, I would like to thank all the chapter authors for their availability for this editorial project.

<div align="right">

J. Paulo Davim
Aveiro, Portugal
September 2018

</div>

# About the Editor

**J. Paulo Davim** received his Ph.D. degree in Mechanical Engineering in 1997, M.Sc. degree in Mechanical Engineering (materials and manufacturing processes) in 1991, Mechanical Engineering degree (5 years) in 1986, from the University of Porto (FEUP), the Aggregate title (Full Habilitation) from the University of Coimbra in 2005 and the D.Sc. from London Metropolitan University in 2013. He is Eur Ing by FEANI-Brussels and Senior Chartered Engineer by the Portuguese Institution of Engineers with an MBA and Specialist title in Engineering and Industrial Management. Currently, he is Professor at the Department of Mechanical Engineering of the University of Aveiro, Portugal. He has more than 30 years of teaching and research experience in Manufacturing, Materials, Mechanical and Industrial Engineering, with special emphasis in Machining & Tribology. He has also interest in Management, Engineering Education and Higher Education for Sustainability. He has guided large numbers of postdoc, Ph.D. and master's students as well as has coordinated and participated in several financed research projects. He has received several scientific awards. He has worked as evaluator of projects for international research agencies as well as examiner of Ph.D. thesis for many universities in different countries. He is the Editor in Chief of several international journals, Guest Editor of journals, books Editor, book Series Editor and Scientific Advisory for many international journals and conferences. Presently, he is an Editorial Board member of 25 international journals and acts as reviewer for more than 80 prestigious Web of Science journals. In addition, he has also published as editor (and co-editor) more than 100 books and as author (and co-author) more than 10 books, 80 book chapters and 400 articles in journals and conferences (more than 200 articles in journals indexed in Web of Science core collection/h-index 47+/6500+ citations and SCOPUS/h-index 53+/9000+ citations).

# Contents

Krishnaraj Vijayan, Simin Nasseri, Vitale Kyle Castellano, Herve Sobtaguim,
Joshua Hilderbrand and Hari Chealvan

J. Babu, Lijo Paul and J. Paulo Davim

Akshay Hejjaji, Redouane Zitoune, Ameur Mohamed Fayçal,
Bougherara Habiba

V. N. Gaitonde, Shashikant, Anand Lakkundi, S. R. Karnik,
A. S. Deshpande, J. Paulo Davim

# List of contributing authors

**Viktor P. Astakhov**
General Motors Business Unit of PSMi, 1792
Elk Ln, Okemos, MI 48864 USA

**J. Babu**
Department of Mechanical Engineering, St.
Joseph's College of Engineering & Technology,
Choondacherry,686579, Kerala, India

**Vitale Kyle Castellano**
Kennesaw State University, Southern
Polytechnic College of Engineering and
Engineering Technology, Mechanical
Engineering Department

**Hari Chealvan**
PSG College of Technology, Coimbatore, India

**J. Paulo Davim**
Department of Mechanical Engineering,
University of Aveiro, Campus Santiago,
3810-193 Aveiro, Portugal

**A. S. Deshpande**
Department of Mechanical Engineering, Gogte
Institute of Technology, Belagavi – 590 008,
Karnataka, India

**V. N. Gaitonde**
Department of Industrial and Production
Engineering, B. V. B. College of Engineering
and Technology, Hubli-580 031, Karnataka,
India

**Bougherara Habiba**
Department of Mechanical & Industrial
Engineering, Ryerson University, Toronto,
Canada

**Akshay Hejjaji**
Institut Clément Ader, CNRS UMR 5312,
Université de Toulouse, Toulouse,
France

**Joshua Hilderbrand**
Kennesaw State University, Southern
Polytechnic College of Engineering and
Engineering Technology, Mechanical
Engineering Department

**S. R. Karnik**
Department of Electrical and Electronics
Engineering, B. V. B. College of Engineering
and Technology, Hubli-580 031, Karnataka,
India

**Anand Lakkundi**
Department of Industrial and Production
Engineering, B. V. B. College of Engineering
and Technology, Hubli-580 031, Karnataka,
India

**Ameur Mohamed Fayçal**
Ecole Nationale Supérieure de Technologie
Algiers, Algeria

**Simin Nasseri**
Kennesaw State University, Southern
Polytechnic College of Engineering and
Engineering Technology, Mechanical
Engineering Department
SiminNasseri (0000-0002-6036-053X), 1100
South Marietta Pkwy, Marietta, GA, 30060

**Swapnil Patel**
General Motors Business Unit of PSMi, 1255
Beach Ct., Saline MI 48176, USA

**Lijo Paul**
Department of Mechanical Engineering, St.
Joseph's College of Engineering & Technology,
Choondacherry,686579, Kerala, India

**Shashikant**
Department of Industrial and Production
Engineering, B. V. B. College of Engineering and
Technology, Hubli-580 031, Karnataka, India

**Herve Sobtaguim**
Kennesaw State University, Southern
Polytechnic College of Engineering and
Engineering Technology, Mechanical
Engineering Department

**Guan Leong TNAY**
Machining Technology Group, Singapore
Institute of Manufacturing Technology, 71,
Nanyang Drive, Singapore 638075

**Krishnaraj Vijayan**
PSG College of Technology, Coimbatore,
India

**Keng Soon WOON**
Department of Mechanical Engineering,
National University of Singapore, 10, Kent
Ridge Crescent, Singapore 119260

**Swee Hock YEO**
School of Mechanical & Aerospace
Engineering, Nanyang Technological
University, 50, Nanyang Avenue, Singapore
639798

**Redouane Zitoune**
Institut Clément Ader, CNRS UMR 5312,
Université de Toulouse, Toulouse, France

Viktor P. Astakhov and Swapnil Patel

# 1 Efficient drilling of high-silicon aluminum alloys

**Abstract:** This chapter presents the most important features of high-penetration rate (HPR) drilling of high-silicon aluminum alloys (HSAA). It explains a necessity of implementation of HPR tools and well-designed machining operations that has become possible due to development of a number of new tool materials and coatings, new cutting inserts and tool designs, new tool holders, powerful precision machines, part fixtures, advanced controllers and so on. As the penetration rate is the product of the tool's (workpiece) rotational speed and cutting feed, the major constraints of these two parameters are considered and a number of practical recommendation for increasing the penetration rate are made as the first level of the analysis. At the second level of the analysis, the correlations between the chemical composition and physical properties of HSAA and drilling tool/process parameters are explained. As HSAA are die casting alloys, the casting defect and their influence on tool performance are analyzed. It is pointed out that polycrystalline diamond (PCD) is a material of choice for HPR drilling tools for HSAA. The common problems with the existing PCD drilling tool are analyzed and the basic design of a cross-PCD drill is suggested.

## 1.1 Introduction

In the context of a global competition, manufacturing companies are compelled to improve their productivities through the optimizations of their production operations including machining. Aluminum die casting alloys are lightweight, offer good corrosion resistance, ease of casting, good mechanical properties and dimensional stability. They are widely used as foundry alloys for a variety of different applications. For example, engine blocks and pistons for air compressors employed in the automotive industry are cast from Al–Si-based alloys. Casting alloys are distinguished from wrought alloys that contain 95% or more aluminum and are not used for castings but are used for applications such as can stock, gutters, siding, airplane skins and so on. In the automotive industry, transmission and engine components are made of high-silicon aluminum alloys (hereafter, HSAA), which have a high strength-to-weight ratio. Aluminum is cast at a temperature of 650°C (1200°F). It is alloyed with silicon (9%) and copper (3.5%) to form the Aluminum Association 380 alloy (UNS A03800). Silicon increases the melt fluidity and reduces machinability. Copper increases hardness and reduces ductility. By greatly reducing the amount of copper (less than 0.6%), the chemical resistance is improved by making AA 360 (UNS A03600) well suited for use in marine environments and in automotive transmissions (valve bodies, case and torque converter housings). HSAA with

more than 13% Si are used in automotive transmissions (pump cover) and engines (for cylinder castings).

## 1.2 Short analysis of the known studies

There have been various literatures for tool performance in metal-matrix composites (MMCs) and all literature show agreement with difficulty in machining MMCs – tool-like hardness of reinforcement particles in MMCs results in excessive tool wear and poor surface properties of the workpiece [1]. An oblique cutting force model constructed by Dabade et al. [2] showed 40% to 60% of the reinforced particles contribute to the abrasion at chip-tool interface. El-Gallab et at. [3] studied tool performance of PCD, TiN-coated carbide tools and $Al_2O_3$/TiC tools and concluded that PCD tools show superior wear resistance over other tool materials. Furthermore, PCD tool wear can be minimized by increasing feed and cutting speed (as high as 0.45 mm/rev and 894 m/min were tested). Umer et al. [1] developed a finite element model to study tool performance for machining Al-based MMCs and showed that tool stresses increase with increase in feed and cutting tool temperature increase with increase in cutting speed. El-Gallab et al. [3] recommend 25 μm grain size. PCD was used by Muthukrishnan et al. [4] (Grade 1500) to machine A356/SiC/10p and results confirmed that higher cutting speeds result in relatively easier removal of the hard SiC particles. However, at higher speed, tool wear was much higher due to abrasive properties of SiC. Caroline et al. [5] conducted a tool wear study for machining A380 reinforced with 20 vol.% SiC with PCD and chemical vapor deposition (CVD)-coated carbide; higher wear was observed on CVD insert compared to PCD insert. PCD insert outlasted three times the CVD insert. Tool wear is believed to be caused by a combination of the abrasive wear and the adhesive wear mechanisms [5, 6] that explains faster rate of flank wear on the CVD insert than PCD insert. Caroline et al. [5] also concludes that aluminum film adhered to diamond tool surface, very often plugs some tool material with it as the layer gets scratched by SiC, which was also implied by El-Gallab et al. [3]. In author's opinion, however, tool wear is not of prime concern in HPR drilling (e.g., 12 mm drill diameter, 24,000 rpm and feed not less than 0.3 mm/rev) in modern manufacturing plant setting. The prime concerns are the quality of drilled holes (taken as the criterion of tool life) and tool reliability assured by the proper selection of most suitable drill geometry, tool material and precise manufacturing of the drill as per the tool drawing. Unbiased tool manufacturer's evaluation is necessary to achieve best precision in manufacturing quality of the HPR drills.

For carbide turning inserts, formation of built-up edge (BUE) at lower speeds defines the tool wear, and thermal softening defines tool wear at higher speeds and feeds concluded by Seeman et al. [6]. Majority of researchers agree on the actual surface roughness achieved by cutting tool being better than theoretical surface roughness [4, 7]. There have been various studies conducted to learn tool

performance, tool wear and workpiece surface integrity while machining MMCs. However, none or very few studies show actual production-based scenario. Die cast MMCs are not just difficult to machine because of abrasive-reinforced particles [8] but also due to presence of various inclusions, porosity and impurities. In addition, condition of machining surface also plays very important role in tool wear. For example, drilling of cored holes where die casting supplier has 1.8 mm positional tolerance on core location requires very different approach than a blind hole where presence of porosity is very common. In our experience, studying tool wear in an assumed homogeneous mixture is faraway to resolve actual production issues. Innovative tool designs and root cause analysis techniques are must to keep the production cost low and quality at the best.

## 1.3  Urgent need for high-efficiency drilling and constraints

### 1.3.1  The rising need for innovation

Drilling of HSAA always presented a great challenge even in the recent past with relatively low cutting speeds and carbide cutting tools due to their unique properties, such as combination of a soft easy-to-adhere Al matrix and highly abrasive particles including silicon and sludge. This challenge, however, was never properly addressed due to two reasons:

1.  The machining time in a cycle time of manufacturing part was so insignificant that the reduction of machining time did not affect the machining efficiency. This is because manual part loading–unloading, part and tool setting on the machine, part gaging in the machine and so on took most of this time. As a result, a reduction of the machining time due to the use of advanced (and thus more expensive) cutting tools and optimization of machining processes was not requested and, therefore, discouraged as manufacturing professionals did not see any benefits of such activities.

2.  In the not-too-distant past, the components of a machining system were far from perfection, and thus it was not possible to utilize the advantages of advanced drilling tools. Tool specialists were frustrated with old machines having insufficient power and no rigid spindles, part fixtures that clamped parts differently every time, part materials with inconsistent essential properties, tool holders that could not hold tools without excessive run outs assuring their proper position and starting bushing plates that had been used for years without replacement; low concentration often contaminated metal working fluids (hereafter MWFs) also known as coolants that were more damaging than beneficial to the cutting tool, manual sharpening and presetting of cutting tools and limited range of cutting speeds and feeds. Under these conditions, the most advanced (and thus expensive) drilling tools, therefore, performed

practically the same (or even worse) as basic tools made in local tool shops. As a result, any further development in tool improvement was discouraged as leading tool manufacturers did not see any return on investment in such developments.

This has been rapidly changing since the beginning of the twenty-first century as global competition forced many manufacturing companies; first of all car manufacturers, to increase efficiency and quality of machining operations. To address these issues, leading tool and machine manufacturers have developed a number of new products – new tool materials and coatings, new cutting inserts and tool designs, new tool holders, powerful precision machines, part fixtures, advanced controllers that provide a wide spectrum of information on cutting operations and so on. All this led to increased efficiency of machining operations in industry by increasing working speeds, feed rates, tool life and reliability. These changes can be called the "silent" machining revolution as they happened in rather short period of time. Implementation of the listed developments led to a stunning result: *for the first time in the manufacturing history, the machining operating time became a bottleneck in the part machining cycle time*. Therefore, the implementation of high-penetration rate (hereafter HPR) tools and well-designed machining operations became a necessity.

### 1.3.2 Major constraints on high-penetration rate

As known [9], the productivity of a drilling operation is determined by the drill penetration rate commonly known as the feed rate. It is calculated as follows:

$$\text{Penetration rate} = f_m = f \cdot n \tag{1.1}$$

where $f_m$ is the feed rate (mm/min), $f$ is the cutting feed (mm/rev) and $n$ is the drilling tool rotational speed (rpm). The drilling tool rotation speed is calculated as follows:

$$n = \frac{1000v}{\pi d_{dr}} \tag{1.2}$$

where $v$ is the cutting speed in drilling (m/min), $d_{dr}$ is the drill diameter (mm) and $\pi = 3.141$.

It directly follows from eqs. (1.1) and (1.2) that the penetration rate/productivity rate can be increased either by increasing the cutting speed or by increasing the cutting feed or both simultaneously. According to the authors' experience, a common mistake made in the industry is multiple attempts to increase these parameters for ordinary drilling tools with ungrounded hopes for success. Specialists and practitioners in the field should realize that there are some constraints on each of the listed ways to

increase drilling productivity. These constraints should be clearly understood for successful implementation of HPR drilling tools, and thus drilling operations.

A graphical representation of constraints are shown in Fig. 1.1. As can be seen, there are two groups of constraints: force factor constraints and contact constraints. As a new approach, the authors propose that these two groups should be analyzed at two levels. The first level is an analysis of these constraints for HPR drilling, as a whole, and the second level is their analysis accounting on the specifics of drilling of HSAA. The results of the first level of such an analysis are applicable to HPR drilling/ drill particularities for drilling of vast variety of work materials, whereas the analysis of the second level can only be carried out through analyzing mechanical, metallurgical and physical properties of HSAA.
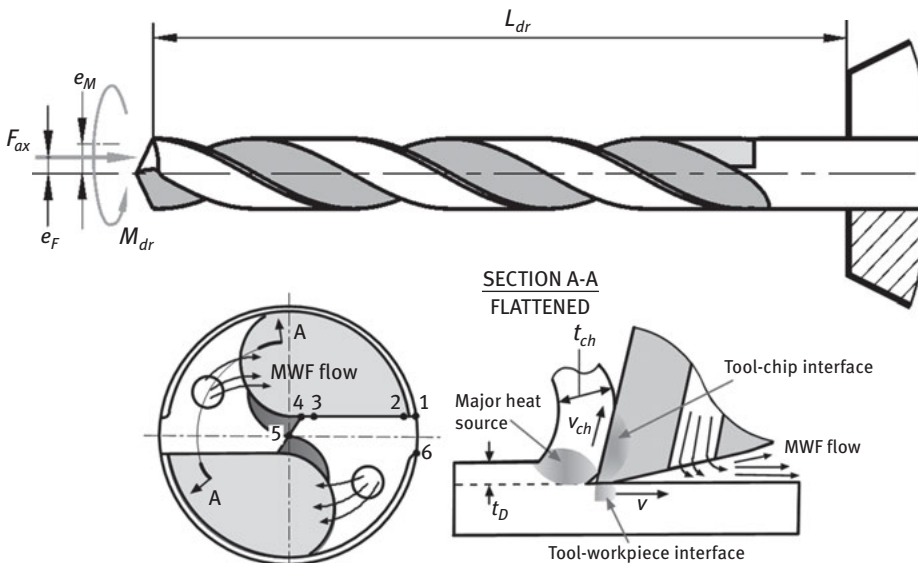


**Figure 1.1:** Graphical representation of constraints in high productivity drilling.

## 1.4 First level of the constraints analysis

The first level of our analysis show the following results:

1. The power requirement for drilling is entirely defined by the drilling torque, $M_{dr}$, whereas axial force, $F_{ax}$, provides no contribution to this power. However, these force factors are not independent as they are determined from the projection of the same cutting force [9]. It is to say that the greater the drilling torque the greater the axial force for a given drilling tool design/geometry.
2. Assuming to the first approximation that the energy needed to drill a certain volume of the work material is constant, one can conclude that the power

required for HPR drilling increases proportionally to this rate. For example, if the penetration rate is increased twice, the power needed for drilling should also increase twice. As a result, the force factors ($M_{dr}$ and $F_{ax}$) increase proportionally. Therefore, much stronger drills capable of withstanding greater drilling torque and axial force are needed for the same length of the drill, $L_{dr}$ (Fig. 1.1).

3. As shown earlier [9], there are two feasible ways (for a given drill material and length) to increase drill resistance for the discussed force factors. On one hand, we can increase the drill's web diameter and decrease the flute cross-sectional areas. On the other hand, an increase in the drill penetration rate leads to the directly proportional increase in the volume of the drilled work material, that is, the volume of the chip to be removed over the chip flutes. This unavoidably leads to the first contradiction in the drill design: both listed ways to increase drill resistance to the force factors lead to decrease in the flute cross-sectional area; the increased volume of the chip to be removed requires greater cross-sectional area of the flute.

4. The axial force, $F_{ax}$, and drilling torque, $M_{dr}$, shown in Fig. 1.1 is actually the resultant of the theoretical (made for an ideal drill) balance of multiple force factors acting on the drill. As a result, $F_{ax}$ is normally shown as along the drill rotational axis, whereas the axis of action of $M_{dr}$ is shown as coincident with this axis [9]. Although in reality it is not quite so as the drill design and geometry parameters made with certain tolerances can be tolerated when penetration rate is "normal." Moreover, the tolerances on many geometry and design parameters were not even listed in tool manufacturing drawings. A "small" price to pay for such an ignorance is the quality of the drilled holes (dimensional, shape and surface roughness) so that when improved quality of the machined hole is required, two- or even three-pass operation (rough drilling, semi-finishing and reaming) is used. Moreover, to prevent excessive drill wandering caused by radial vibrations due to its asymmetry, the width of the cylindrical margins (the distance between points 1 and 6 in Fig. 1.1) was significantly increased that caused substantial rubbing of these margins against the wall of the hole being drilled. When the machining time in the total cycle time was insignificant, it was tolerated.

Obviously, such an approach cannot be tolerated in HPR drilling where the machining time is accounted for a fraction of a second. Moreover, in modern machine shops, for example, in the automotive industry, the quality requirements for drilled holes today are the same as they used to be for reamed holes just a decade ago. The cutting speed over the same time period has tripled and the penetration rate has doubled. Under such conditions, a more realistic force model should be considered as shown in Fig. 1.1, for example, the resultant axial force should be considered as shifted by certain distance $e_F$ from the rotational axis, whereas the drilling torque should be considered as acting over the axis shifted by distance $e_M$ from the drill rotational axis. The greater the $e_F$ and $e_M$, the lower will be the quality of the machined surface and lower tool life.

Among the process parameters having the greatest influence on these shifts is the system run out (included run out of the tool, tool holder and spindle), tool lip height variation and flute spacing [9]. Therefore, the proper drill design/ manufacturing tolerances on the HPR drill's geometry and design parameters must be utilized to the extent of $e_F$ and $e_M$.

5. As mentioned above, the drill penetrations rate can be increased either by increasing the cutting speed or by increasing the cutting feed or both simultaneously. The limit of the cutting feed depends on both the properties of the work and the tool materials. In other words, it is set by the allowable normal stress over the tool-chip interface (see Fig. 1.1). When the cutting feed and thus the normal stress over the tool-chip interface exceeds this limit, the whole rake face cracks in the manner shown in Fig. 1.2. Therefore, the tool material of maximum possible compressive and transverse rupture strength should be used.
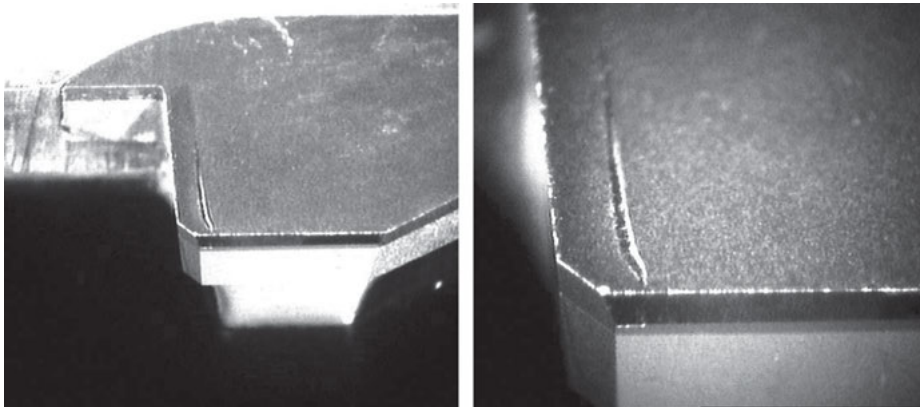


**Figure 1.2:** A crack developed on the tool rake face behind the tool-chip contact area due to high contact stresses on the rake face.

6. The limit of the cutting speed also depends on both work and tool materials (their mechanical, metallurgical and physical properties), tool design, geometry and MWF parameters and other parameters that define the conditions over the tool-chip and tool-workpiece interfaces (see Fig. 1.1). Although the analysis of these conditions should be carried out for a given work material (it is presented later for the case of drilling of HSAA), an important conclusion can be made, and the rule can be formulated at this stage of considerations. This conclusion includes the following:

- Because the rotation is the prime motion in drilling (no matter what actually rotates – drilling tool, workpiece, or both), the maximum cutting speed is at drilling tool (drill, reamer, etc.) corner (point 1 in Fig. 1.1).
- The amount of the work material removed by a small segment 1-2 adjacent to the drill corner of the major cutting edge 1-4 is much greater than that by its

inner segment 3-4. Therefore, the chip velocity ($v_{ch}$ in Fig. 1.1) over the tool-chip interface on the rake face of segment 1-2 is much higher than that for segment 3-4. As a result, much greater temperature over the tool-chip interface and rake face wear occur on the rake face of segment 1-2 compared to segment 3-4.

–   The distance travel by segment 1-2, and thus by the tool-workpiece interface (forms always even for a sharp tool due to spring back of the work material) over the time of one tool revolution is much greater that that by segment 3-4. As a result, As a result, much greater temperature over the tool-workpiece interface and rake face wear occur on the flank face of segment 1-2 compared to segment 3-4.

–   Rubbing or even burnishing of the portion of the drill cylindrical margin adjacent to the drill corner 1 (1-6 in Fig. 1.1) adds additional heat, and thus contributes to high temperature of the tool material around the drill corner.

As a result of the discussed above, the maximum wear of drilling tools occurs in the vicinity of the corner as shown in Fig. 1.3. Surprisingly, not much attention to the conditions of the drill corner is paid in the design of conventional drills. For example, the outlets of the MWF (coolant) hole on the tool flank faces are located close to chip flutes and connected to these flutes by additional gashes (grooves) leaving no chance to MWF to reach the drill corner where it is mostly needed. Obviously, this should be changed in the design of HPR tools.



**Figure 1.3:** Showing that the maximum wear occurs in the vicinity of the drill corner.

The foregoing analysis clearly indicates that prime attention in the tool/process design should be paid to the improved conditions (increased wear resistance, reduced temperature) at the region of the drill corner. Figure 1.4 shows one of many possible modification of the drill design for HPR drilling. SECTION A-A(a) shows a design with a central MWF (coolant) channel 1, which is connected by two side channels 2 with an opening 3 made in the drill body and flank faces. SECTION A-A(b) shows a design with two helical MWF (coolant) channels 4 connected through side channels 5
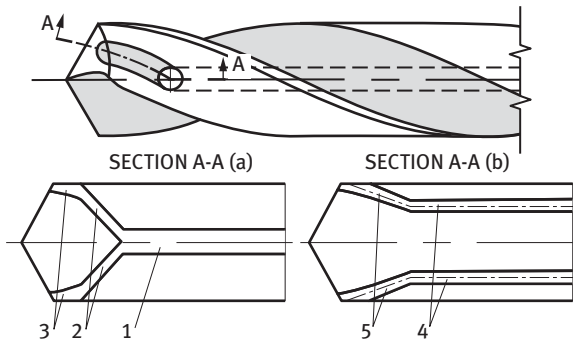
**Figure 1.4:** Modified drill design for HPR drilling.

with the drill flank faces. As a result, much better cooling and lubrication conditions in the vicinity of the drill corners are achieved. Obviously, special preforms are needed for the described designs – this is a part of the price paid for the increased penetration rate.

## 1.5 Second level of the analysis of constraints: work-material specific level

As mentioned above, the second work-material specific level of the analysis of constraints is needed to design application-specific HPR drilling tools. In this chapter as its title implies, such an analysis is carried out for HSAA.

It is true that the chemical composition and some properties of the work material are often included into the body of various research papers, books, industrial reports and other materials that present results of studies related to metal cutting and tool design. What is commonly lacking is the analysis of quantitative correlations of the listed composition and properties with the preprocess decisions, including particularities of the cutting tool design and selected machining regime as well as with the results obtained. Moreover, in the authors' opinion, the most relevant properties of the work material are often left out of considerations. This significantly lowers the obtained results in terms of their usefulness in the design work-material specific machining processes and cutting tools. This section aims to present an example of the proper analysis of the chemical composition, mechanical and physical properties of the work material, namely HSAA, as related to the HPR drilling process and cutting tool design.

### 1.5.1 General information about HSAA

Although a variety of aluminum alloys can be die cast from primary or recycled metal, designers select a standard alloy listed below:

- Alloy A360 (ANSI/AA A360.0) offers higher corrosion resistance, superior strength at elevated temperatures and somewhat better ductility, but is more difficult to cast.
- Alloy A380 (ANSI/AA A380.0) is by far the most widely cast of the aluminum die casting alloys, offering the best combination of material properties and ease of production. It is specified for most product applications. Some of the uses of this alloy include electronic and communications equipment, automotive components, engine brackets, transmission and gear cases, appliances, lawn mower housings, furniture components and hand and power tools.
- Alloy 383 (ANSI/AA 383.0) and alloy 384 (ANSI/AA 384.0) are alternatives to A380 for intricate components requiring improved die filling characteristics. Alloy 383 offers improved resistance to hot cracking (strength at elevated temperatures).
- Alloy 390 (ANSI/AA B390.0) was developed for automotive engine blocks. Its resistance to wear is excellent; its ductility is low. It is used for die cast valve bodies and compressor housings and pistons.
- Alloy A13 (ANSI/AA A413.0) offers excellent pressure tightness, making it a good choice for hydraulic cylinders and pressure vessels. Its casting characteristics make it useful for intricate components.

To understand the challenges in machinability of these HSAA, one needs to analyze their chemical composition and mechanical and physical properties relevant to their machinability, not only in qualitative sense of this term (as it is usually carried out [10–13]), but also in quantitative meaning of this concept as revealed by Astakhov [14]. As tool wear is the major obstacle in any attempt to increase productivity of machining and in improving quality of machined parts, prime attention should be paid to reveal the prevailing mechanism of this wear and a place (places) on the tool where this wear takes place [15].

For further comparison, two materials most widely used in the automotive industry HSAAs are selected, namely A380 and 390.

### 1.5.2 Analysis of the chemical composition

Table 1.1 presents chemical composition of common die casting alloys. An analysis of the chemical composition of HSAA should be carried out together with their phase diagram shown in Fig. 1.5. If one pays a close attention to this diagram then he or she can conclude that HSAA termed as alloys in all technical documents, standards and research paper are not actually alloys but rather MMCs. This is because aluminum has zero solid solubility in silicon at room temperature so that Al–Si phase diagram differs from the "standard" phase diagrams [16]. As follows from Fig. 1.5, there is no beta phase and so this phase is "replaced" by pure silicon (one can think of it as a beta phase that consists only of silicon) [17, 18]. HSAA include two distinctive

**Table 1.1:** Chemical composition of common die casting alloys.

| Aluminum Die Casting Alloys | | | | | | |
|---|---|---|---|---|---|---|
| ANSI/AA | A360 | A380 | 383 | 384 | 390 | A13 |
| Nominal Comp. | Mg 0.5 | Cu 3.5 | Cu 2.5 | Cu 3.8 | Cu 4.5 | Si 12.0 |
| | Si 9.5 | Si 8.5 | Si 10.5 | Si 11.0 | Si 17.0 | |
| **Detailed Composition** | | | | | | |
| Silicon Si | 9.0–10.0 | 7.5–9.5 | 9.5–11.5 | 10.5–12.0 | 16.0–18.0 | 11.0–13.0 |
| Iron Fe | 1.3 | 1.3 | 1.3 | 1.3 | 1.3 | 1.3 |
| Copper Cu | 0.6 | 3.0–4.0 | 2.0–3.0 | 3.0–4.5 | 4.0–5.0 | 1.0 |
| Manganese Mn | 0.35 | 0.50 | 0.50 | 0.50 | 0.50 | 0.35 |
| Magnesium Mg | 0.4–0.6 | 0.10 | 0.10 | 0.10 | 0.45–0.65 | 0.10 |
| Nickel Ni | 0.50 | 0.50 | 0.30 | 0.50 | 0.10 | 0.50 |
| Zinc Zn | 0.50 | 3.0 | 3.0 | 3.0 | 1.5 | 0.50 |
| Tin Sn | 0.15 | 0.35 | 0.15 | 0.35 | – | 0.15 |
| Titanium Ti | – | – | – | – | 0.10 | – |
| Others Each | – | – | – | – | 0.10 | – |
| Total Others | 0.25 | 0.50 | 0.50 | 0.50 | 0.20 | 0.25 |
| Aluminum Al | Balance | Balance | Balance | Balance | Balance | Balance |
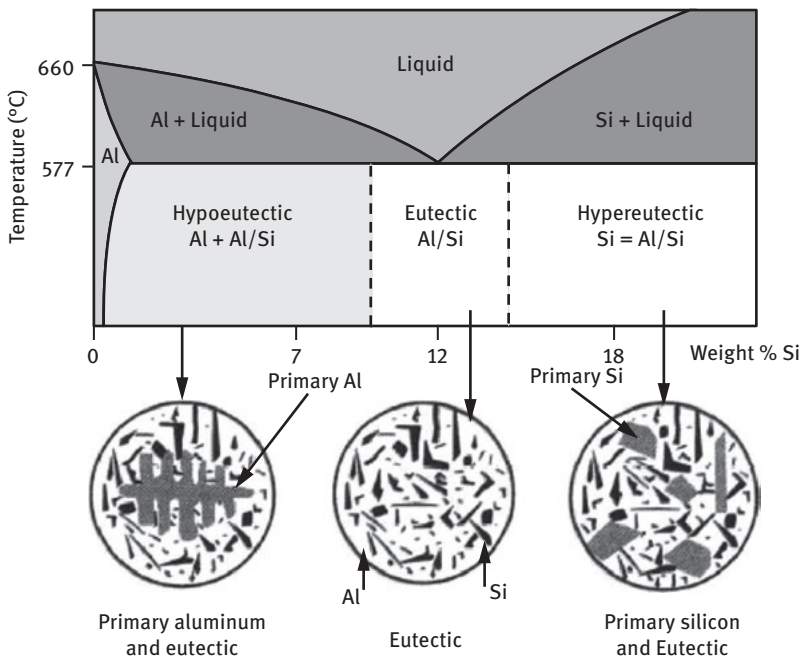


**Figure 1.5:** Aluminum − silicon phase diagram and microstructures.

components: (1) aluminum as the matrix metal and (2) silicon as reinforcement, each of which has its own microstructure and interfaces between them. In near-eutectic mixtures (between the dashed lines in Fig. 1.5), Si is non-lamellar in form and appears, in section, as separate flakes (Fig. 1.6(a)), although studies have shown that the flakes are, in fact, interconnected three dimensionally. The A380 near-eutectic composition is often used, as this gives a lower melting point and makes them cheaper to cast. In hypereutectic A390 with >16wt.% Si, primary Si forms first. The primary Si produces a large diamond phase that can be seen in the micrograph of A390 (Fig. 1.6(b)).



(a)                                    (b)
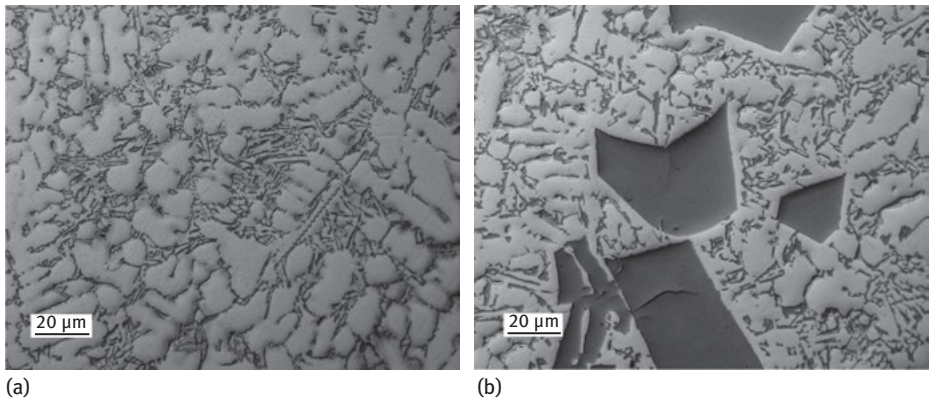
**Figure 1.6:** Microstructures of: (a) Alloy 380 and (b) alloy 390.

The considered structures are directly related to the machining properties of these alloys [8]. The summary of the chemical composition and metallographic analyses is as follows. Because HSAA are composite materials, one needs to deal with machinability of two solid distinctive phases: soft aluminum matrix and hard Si reinforcement particles. As a result, two different types of wears are observed in machining of HSAA: adhesion and abrasion.

In case of A380 alloy, Si is non-lamellar in form and appears, in section, as separate flakes (Fig. 1.5(a)), adhesion wear prevails over abrasion one when a drilling process (machining regime, MWF supply parameters, etc.) and cutting tool (primarily the adequate selection of the cutting tool material) are set/designed properly [19]. A typical wear pattern of adhesion wear of a carbide drill is shown in Fig. 1.7(a).

A simplified mechanism of adhesion wear can be represented as follows. Strong adhesion takes place between surfaces free of oxides under high contact pressure. The harder the contact pressure the rougher the tool contact surface, the stronger the adhesion bonding. Due to high plastic deformation of the chip and high contact pressures at the tool-chip and tool-workpiece interface (Fig. 1.1), extreme pressure and antiwear additives in MWF cannot penetrate into these interfaces [20]. As a result

(a)                                             (b)
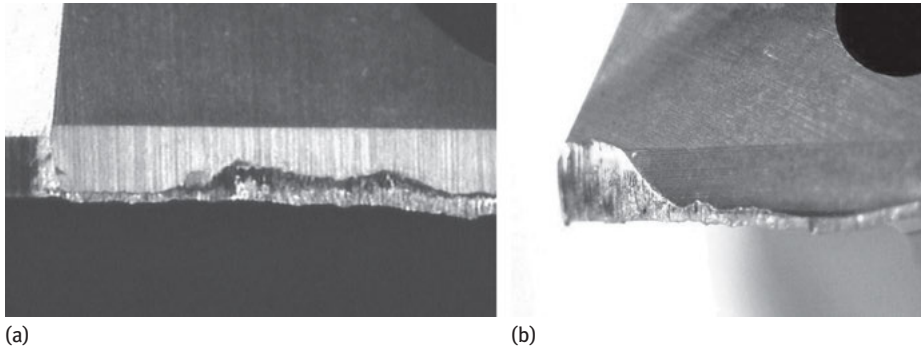
**Figure 1.7:** Wear patterns: (a) adhesion wear and (b) abrasion wear.

of adhesion of the work material (converted into the chip) and the tool rake face, the so-called built-up edge (commonly referred to as BUE in the literature on metal machining) is formed. BUE is not stable in metal cutting so it changes within each cycle of chip formation [20]. As BUE adheres to the rake face, the adhesion causes mechanical bonding (as glue with a piece of paper). When BUE is periodically removed by the moving chip (as its height becomes sufficient), it brings a small piece of the tool material with it (as the glue removed from the paper). The process repeats itself over period of time with normal tool usage so the tool becomes worn by this process. As adhesion wear progresses, the rake face becomes more rough and the cutting edge more round so the extent and height of BUE grows as the strength of adhesion bonds increases. This may cause local chipping or even bulk breakage of the tool.

Because adhesion of the work material to the tool rake face is caused by mechanical bonding, any measure to reduce the strength of these bonds is beneficial in machining of HSAA. To suggest the most effective measures, one needs to understand the essence of BUE, and thus the proper means to reduce its harming influence of high-efficient/high-speed machining of HSAA. Some most relevant findings can be listed as follows.

In engineering sense, adhesion can be thought of as consisting of two mechanisms. The first one is adhesion between contact materials (Type 1 adhesion) and the second one is adhesion due to roughness of the contact surfaces (Type 2 adhesion), disregard to what materials they are made of.

Type 1 adhesion occurs in the contact of two metals when some additional energy is supplied in this contact. Thermal energy is often used in soldering and brazing to create adhesion bonds with soldering/brazing filler material (BFM). These bonds form, however, if oxides are removed from the surface by thorough cleaning and application of the flux to prevent oxidation during the heating process. Mechanical energy applied to create high contact pressure can also facilitate adhesion. To form strong adhesion bonds, the contact pressure should be very high and contact

surfaces should be free of oxides. In metal cutting, these two conditions are met. First, the pressure at the tool-chip interface is high as the highest contact pressure at the tool-chip contact is the case [20]. Second, the chip contact surface is the juvenile freshly formed surfaces free of oxides. Due to high contact pressure, the moving chip "cleans" the tool rake face from oxides.

Although not all metals form the adhesion bonds and Type 1 does not occur between metals and ceramics, aluminum (as the matrix material in HSAA) forms adhesion bonds with cobalt commonly found in tool materials as high-speed steels and sintered carbides. As high-speed steel is not the tool material of choice in high-speed machining of HSAA due to lack of wear resistance, Type 1 adhesion is considered for sintered carbides (hard metals according to ISO classification).

Sintered carbides are MMC materials having the structure as shown in Fig. 1.8. The binder in carbides is cobalt, which holds tungsten carbide (WC) ceramic particles. Note that there are no bonds between WC gains. Because aluminum does not form adhesion bonds with ceramic WC grains, it adheres only to the cobalt matrix. The greater the cobalt content in sintered carbide, the stronger Al–Co adhesion bonds, the greater the adhesion wear.
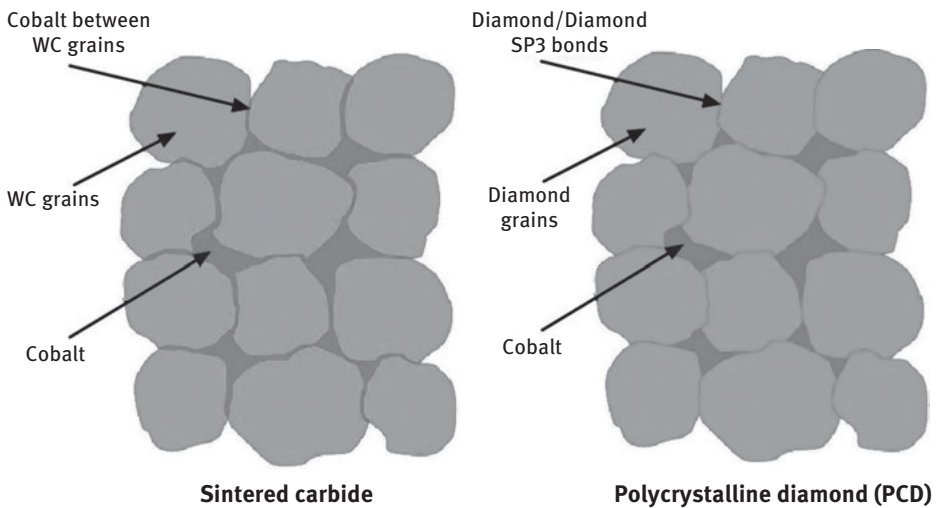


**Figure 1.8:** Schematic structures of sintered carbide and PCD tool materials.

Most of modern grades of sintered carbide contain a great amount of cobalt (10%–12%) because this amount of cobalt helps to keep the grain size small on sintering. As a result, such grades possess both high hardness and toughness needed in machining. It works well in machining of carbon and low alloy steels as BUE (adhesion of the work and tool materials) disappears when the cutting speed exceeds approximately 70 m/min, which is well below those commonly used in machining of such work

materials. It does not work well in machining of HSAA due to high adhesion wear (great BUEs). Figure 1.9 shows an example of an excessive BUE on the rake face of a drill made of 10% Co carbide. Unfortunately, sintered carbide grades with 10%–12% Co are normally used for HSAA drilling tools.
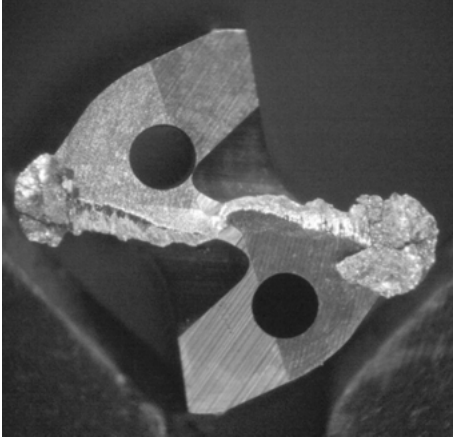


**Figure 1.9:** Excessive BUE on the rake face of a drill made of 10% Co carbide.

The most feasible way to reduce Type 1 adhesion in drilling HSAAs is to use low-cobalt carbide grades. According to the authors' experience, even when 6% Co carbide grades are used, tool life of various drilling tools increases by 30%–50%. Further reduction of cobalt content to 3%–4% should be beneficial. Two aspects of such grades should be kept in mind. First, low-cobalt grades are not on-shelf products (e.g., carbide rods for manufacturing drills and reamers) as many carbide manufacturers almost entirely switched their production to high-cobalt grades. Second, the lower the cobalt content the more brittle the carbide grade. As a result, chipping may present some problems in grinding drilling tools when older machines and coarse grinding wheels combined with excessive grinding feeds are used.

Polycrystalline diamond (PCD) tool material is the material of choice in machining of HSAA [21]. When it is used in drilling tools, BUE, and thus adhesion wear is not normally the case. As a result, tool life in HSAA machining is 20–30 times greater compared to carbide tools. The reason for this is the different role of cobalt in PCD compared to carbide. A PCD tool material is normally made in the form of discs. As the diamond powder is packed against a WC-Co substrate, cobalt is the source for the catalyst metal that promotes the sintering process. When the cobalt reaches its melting temperature of 1435°C at 5.8 GPa, it is instantaneously squeezed into the open porosity left in the layer of compacted diamond powder.

The result of the process is a disc consisting of the WC-Co substrate and diamond layer of certain thickness strongly bonded with this substrate. In this disc, PCD composite is a fully dense mass of randomly oriented, intergrown micron-size diamond particles that are sintered together in the presence of a metallic catalyst phase.

Small pockets of the catalyst phase, which promotes the necessary intergrowth between the diamond particles, are left behind within the composite material. Deformation in the presence of catalyst is induced in the particles and the strongest diamond-to-diamond bonding (known as SP3 bonds) occurs during sintering. After sintering and formation of SP3 bonds, cobalt does not play any structural role in PCD so that it can be removed (leached). The essence of cobalt leaching is as follows (U.S. Pat. Nos. 4,224,380 and 4,288,248). After finishing the PCD conventionally, the metallic phase can is removed from the compact by acid treatment, liquid zinc extraction and electrolytic depleting or similar processes, leaving a compact of substantially 100% abrasive particles. For advanced drilling applications, cobalt is removed up to 200 µm deep into the PCD layer.

It is clearly seen in a schematic structure of PCD shown in Fig. 1.8 that there is no cobalt between diamond-to-diamond SP3 bonds even if it is not leached. Therefore, Type 1 adhesion does not occur as there is no continuous cobalt "network" on PCD surface as in the surface of sintered carbide.

Figure 1.10(a) shows the structure as a typical PCD disk (blank). Fine diamond powder sintered together into a dense uniform mass, approximately 0.5 or 2.0 mm thick, supported on a substrate of cemented carbide. Nowadays, PCD blanks are made as disks of up to 74 mm in diameter $D_{dd}$. As can be seen in the structure of the PCD layer (Fig. 1.10(a), only very small islands of cobalt can be observed on the surface (the white spots) so Type 1 adhesion does not occur.
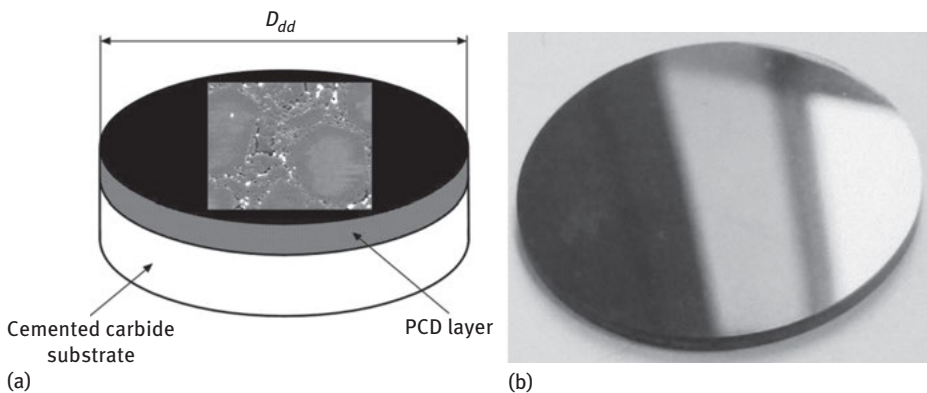


**Figure 1.10:** A typical PCD blank: (a) structure and (b) polished surface.

As mentioned above, Type 2 adhesion occurs due to roughness of the contact surfaces disregard to what materials they are made of. Adhesion, and thus BUE are most common due to rough grinding of the rake and flank faces of carbide tools. The worst scenario in machining of HSAA takes place when a high-cobalt grade is used and the rake and flank faces excessive surface roughness and is coarse as shown in
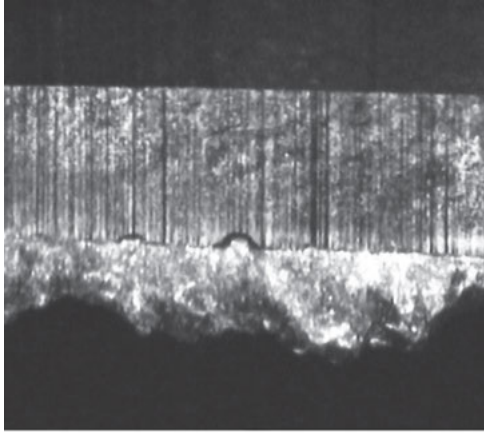
(a)
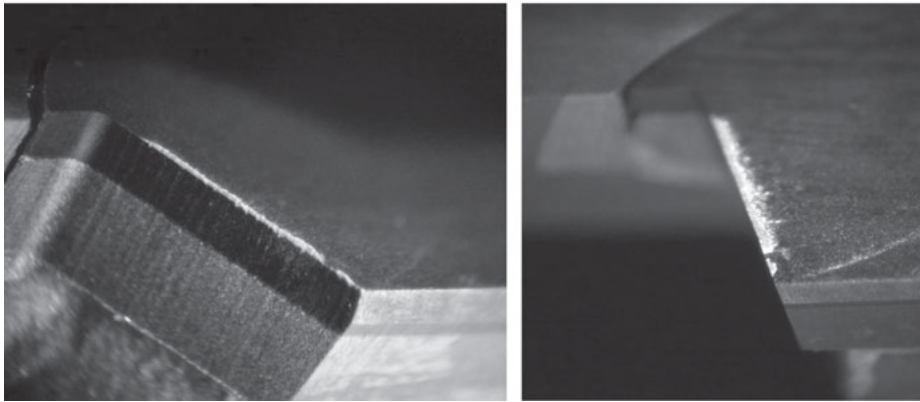


(b)

**Figure 1.11:** Type 2 adhesion: (a) carbide tool and (b) PCD tool.

Fig. 1.11(a). In the design and manufacturing of many PCD tools, the rake face of PCD normally remains untouched as the PCD disk surface is highly polished as shown in Fig. 1.10(b) for preventing the occurrence of Type 2 adhesion. However, when the flank face is made rough (i.e., by improper selection of the electrical discharge machining (EDM) regime or electrical discharge grinding (EDG)), the resultant cutting edge is serrated, so Type 2 adhesion takes place as shown in Fig. 1.11(b). Although the strength and extent of Type 2 adhesion are much smaller compared with carbide tools, it is often sufficient to damage the quality of the machined surface and significantly lower tool life. Type 2 adhesion tools takes place when the polished rake face of PCD is modified by applying the so-called T-land with negative rake face. Rough cutting edges combined with high contact pressure due to negative rake angles create a visible BUE. The strength of adhesion bonds, however, is not high, so BUE can be easily removed even by a fingernail.

Type 2 adhesion takes place on the rake face of PCD drilling tools when this surface needs to be ground to achieve the final tool configuration. The problem is twofold: (1) the grain size of PCD tool material used for drilling tool is in the range of 5–15 μm, (2) grinding of PCD by diamond grinding wheels of the same hardness is not the case of classical grinding but rather a process of crashing of SP3 bonds and plowing of PCD crystals out of the surface. The relatively rough ground surface is a result of such a grinding that Type 2 adhesion takes places. Figure 1.12 shows that the rake face of drills is covered by a thin layer of aluminum due to Type 2 adhesion. This layer significantly increases friction over the tool-chip interface, and thus the cutting force should be kept in mind in the design of tools and in the setting of operational parameters. The former means that the "slim" point grinds of drilling tools used for HSAA with carbide drilling tools should not be used, whereas the latter means that the allowable drilling torque/ axial force on the computer numerical control (CNC) machine (known as the digital way) should be increased at least by 30% compared to that used for carbide drills.
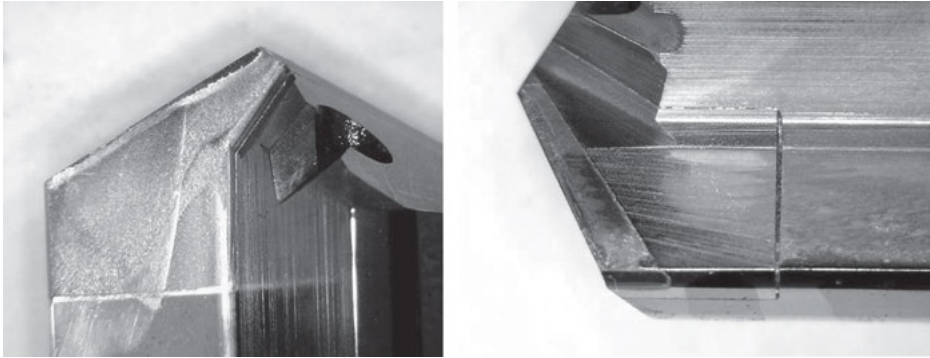


**Figure 1.12:** Appearance of Type 2 adhesion on the rake face of PCD drills.

As mentioned above, the maximum abrasive wear of drilling tools occurs in the vicinity of the corner due to a number of reasons discussed in Section 1.3. Figure 1.3 and 1.7(b)) show the typical appearance of abrasive wear. As can be seen, the worn surface contains deep scratches in the direction of sliding left by silicon abrasive particles found in the work material. The best way to reduce abrasion in HSAA machining is to increase the hardness of the work material. In case of carbide drilling tools, low-cobalt grades not just reduce adhesion wear but also abrasive wear as the harness of the carbide tool materials increases. PCD is the material of choice in machining of HSAA because it has high hardness.

The foregoing analysis allows formulating design/application suggestions for carbide and PCD drilling tools in machining of HSAA as follows:

1. For carbide drilling tools: (a) Low-cobalt carbide grade should be used to reduce both adhesion and abrasion wear; (b) the surface roughness of the rake and flank

faces adjacent to the cutting edge should be no worse than Ra 0.32 μm; (c) the outlets of the MWF holes on the flank faces should be positioned as close as possible to the tool corners.

2. For PCD tools: (a) The flank faces of PCD inserts should be ground with surface roughness not worse than Ra 0.6 μm; (b) no T-lands with negative rake angles on the rake face should be used; (c) when the rake face of the tool is to be ground to achieve the final shape of the drilling tool, the design of the drill point should be reinforced in the region of chisel edge, and <5 μm grain size of PCD grades or multimodal grades that combine several grain sizes to achieve smoother surface on grinding should be used.

In the authors' opinion based on experience in the field, the lack of information on PCD drilling tool geometry and wear mechanisms can be explained by difficulties of conducting experimental studies at universities and R&D facilities. Tool life of carbide tools used in steel machining is measured in minutes. To carry out tool life tests and thus to obtain information on the wear pattern to reveal the wear mechanism, conventional machines, fixtures and inexpensive standard tools are used. A dozen workpieces (normally standard bars) are typically sufficient to complete the study. This is not nearly the case in machining of HSAA with PCD tools where tool life is measured by tens of thousands of parts. A special, expensive high-speed machine with precision bearings (having spindle run out no more than 0.5 μm at full radial and axial loads with active control and vibration suspensions), special coolants (concentration, filtration, pH, anti-foam and anti-rust additives, etc.), and special non-regroundable cutting tools (cost of a common PCD tool varies from $1,000 to $10,000 depending on tool diameters and number of stages are needed). Each test point requires a new tool. The listed particularities make PCD testing difficult, expensive, time-consuming, and thus not feasible in university labs and small R&D facilities.

### 1.5.3 Analysis of the mechanical and physical properties

Table 1.2 presents the relevant mechanical and physical properties of common die casting alloys. As before, further analysis is going to concentrate on two materials most widely used in the automotive industry HSAAs are selected, namely A380 and A390. This analysis reveals the following.

For A380 alloy, the ultimate tensile strength is twice greater than the yield strength for only 3.5% elongation. It means that severe strain hardening takes place over each cycle of chip formation. Figure 1.13 shows the heavily serrated appearance of the chip-free surface. Two important conclusions can be drawn from this property of A380 alloy. First, great variations of the drilling torque and axial force take place within each cycle of chip formation, so the drilling system should be rigid

**Table 1.2:** Relevant mechanical and physical properties of common die casting alloys.

**Aluminum Die Casting Alloys**

| ANSI | A360 | A380 | 383 | 384 | 390 | A13 |
|---|---|---|---|---|---|---|
| **Mechanical Properties** | | | | | | |
| Ultimate Tensile Strength (MPa) | 320 | 320 | 310 | 330 | 320 | 290 |
| Yield Strength (MPa) | 170 | 160 | 150 | 170 | 250 | 130 |
| Elongation (%) | 3.5 | 3.5 | 3.5 | 2.5 | <1 | 3.5 |
| Hardness (BHN) | 75 | 80 | 75 | 85 | 120 | 80 |
| Shear Strength (MPa) | 180 | 190 | – | 200 | – | 170 |
| Young's Modulus (GPa) | 71 | 71 | 71 | 71 | 71 | 71 |
| Poisson's Ratio | 0.33 | 0.33 | 0.33 | 0.33 | 0.33 | 0.33 |
| **Physical Properties** | | | | | | |
| Melting Range (°C) | 557–596 | 540–595 | 516–582 | 516–582 | 510–650 | 574–582 |
| Density (g/cm$^3$) | 2.63 | 2.71 | 2.74 | 2.82 | 2.73 | 2.66 |
| Specific Heat (J/kg°C) | 963 | 963 | 963 | – | – | 963 |
| Thermal Conductivity (W/m°K) | 113 | 96.2 | 96.2 | 96.2 | 134 | 121 |
| Coefficient of Thermal Expansion (μm/m°K) | 21.0 | 21.8 | 21.1 | 21.0 | 18.0 | 21.6 |
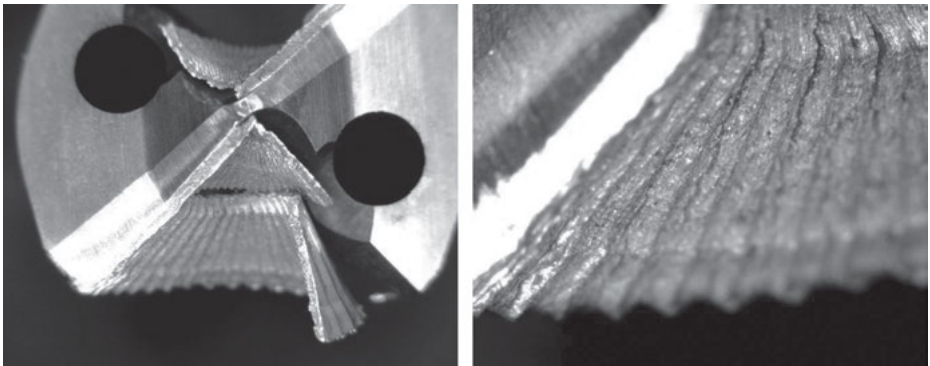


**Figure 1.13:** Heavily serrated appearance of the chip-free surface due to cycles in chip formation.

to prevent vibration of HPR drilling. Second, the so-called peck drilling – a drilling operation that periodically retracts the tool to clear chips or flood the hole with MWF – should not be used to deal with the problem of chip removal from long holes, though it is recommended by many literature sources on drilling, and the peck drilling cycle is a standard part of many drilling machine CNC controllers.

The elasticity module *E* (Young's module) is a measure of the slope of the tensile test curve in the elastic portion of the strength curve (tensile strength increase per length unit). In other words, it is a measure of a material's elastic recovery known as spring back [9]. The *E*-module for die casting HSAA is 71 GPa (see Table 1.2), which is about one-third of that for steel. This means that the elastic change of form in response to a given stress is three times greater than that of steel. This fact directly affects the design and geometry parameters of the round tools as follows:

–   Back taper of the drills and reamers should be increased proportionally compared to that used for tools meant for steel and cast iron drilling.
–   The clearance angle on the cutting portion of the tool should be increased proportionally to prevent rubbing of the work material (spring back of the bottom of the hole being machined).

Density – Lightness is the outstanding and best known characteristic of HSAA. According to Table 1.2, the range of density for die casting HSAA is 2.63–2.82 g/cm$^3$, which is around one-third of that of steel. The low density of aluminum accounts for it being lightweight but this does not affect its strength. Although density is not normally considered as a property affecting machinability of materials, it does play a significant role in combination with other physical properties as discussed further.

Specific heat (heat capacity) – HSAAs have a relatively high specific heat when compared with other metals on a weight basis, that is, 963 J/kg, which is higher than that of any common metal except magnesium (e.g., specific heat of steels is 490–500 J/kg). On a volume basis, however, *the heat capacity of aluminum is less than any of the heavier metals*. In other words, specific heat should be considered together with density to understand the thermal properties of HSAA.

Thermal conductivity – The thermal conductivity of die cast HSAA is in the range of 96.2–134 W/m°K so that it is 63.8% of the International Annealed Copper Standard (IACS). However, because of its low specific gravity, its *mass thermal conductivity* is twice that of copper.

Thermal expansion – In case of aluminum, the coefficient of thermal expansion is nonlinear over the range from –200°C to +600°C but for practical purposes it is assumed to be constant in the temperature range of 20°C–100°C. The coefficient of thermal expansion of alloys is affected by the nature of their constituents. The presence of silicon and copper reduces expansion while magnesium increases it. The coefficient of thermal expansion is 21.0 µm/m°K for A380 alloy and 18.0 µm/m°K for 390 alloy that is approximately twice than of steels.

The foregoing analysis shows that spring back, density-adjusted specific heat, thermal conductivity and thermal expansion of die cast HSAA are much greater than those found in commonly machined work materials. The proper accounting for these properties in the drill/process design should be as follows:

–   The clearance angle of HPR drills should be significantly increased to the values shown in Table 1.3. According to the authors' experience, optimization (making

**Table 1.3:** Recommended clearance angles for drills.

| Drill diameter range (mm) | Suggested clearance angle (°) |
| --- | --- |
| 0.35–1.00 | 26 |
| 1.05–2.50 | 24 |
| 2.55–3.00 | 22 |
| 3.05–6.50 | 20 |
| 6.55–8.95 | 18 |
| 9.00–13.00 | 16 |
| 13.10–20 | 14 |
| >20 | 12 |

them close to the values shown in Table 1.3) of the normal clearance angles of HPR drills, that is meant for HPR drilling of HSAA in the setting of the largest transmission plant resulted in a two-time increase in tool life, three-time reduction of the drill breakage and their premature failures and a 30% increase in the allowable penetration rate.

- The back taper of HPR drills should be significantly increased. This measure is needed to prevent severe rubbing on tool margins that can ruin the quality of machined surface, scoring on the margins' edges, excessive margin wear and oversize condition of machined holes (rapid expansion of the machined hole due to excessive heating and then its contraction on cooling). The authors' experience shows that 2–3 μm per millimeter of tool length for drills and 1–2 μm per millimeter of tool length for reamers are good starting points.
- Clean MWFs of high concentration (no less than 9%), sufficient flow rate, with filtration preferable 10 μm should be used.

Unfortunately, there is no understanding of the listed issues in industry so that the drills with the back taper and clearance angles meant for steel and cast iron drilling are used for HPR machining of HSAA. The same problem can be pointed put in the research community, where in books, papers and other research document the clearance angle, back taper, particular carbide/PCD grade used in the tool/process under investigation are not even mentioned.

## 1.6 Casting defects affecting drilling

### 1.6.1 Porosity

The formation of pores is one of the biggest problems of die casting. Shrinkage and gas pores are the principal types of internal porosity in die castings. It is crucial to

determine which type of porosity is involved, because the measures required are nearly exact opposites. It is usually possible to determine the type of porosity by magnifying the material by 25–150 times.

### 1.6.1.1 Gas pores

Gas pores nearly always take the form of trapped bubbles, which usually look like a series of round holes in the casting. The inner surfaces of the pores are often smooth, with either a shiny or dull finish. Gas pores are formed primarily by trapped gas, water vapor or burnt lubricant.

Hydrogen gas dissolves in the liquid molten aluminum alloy from the atmosphere. Its solubility varies directly with temperature and the square root of pressure. During the cooling and solidification of molten aluminum, dissolved hydrogen in excess of the extremely low solid solubility may precipitate in molecular form, resulting in the formation of primary and/or secondary voids. There are two types of hydrogen porosity occurring in the die cast:

- The inter-dendritic porosity, which is encountered when hydrogen contents are sufficiently high that the hydrogen gets rejected at solidification due to high pressures above atmospheric.
- Secondary (micron-size) porosity occurs when dissolved hydrogen contents are low, and void formation is characteristically critical.

Porosity and porosity-size inclusions present a serious challenge in HPR drilling of HSAA as a myriad of pores should be thought of as a countless number of small sharp razor-type edges enhanced by hard SiC microinclusions. These literally shave the tool when their amount is excessive. Figure 1.14(a) shows an example of an excessively worn carbide drill and Fig. 1.14(b) shows the result of an autopsy of the machined
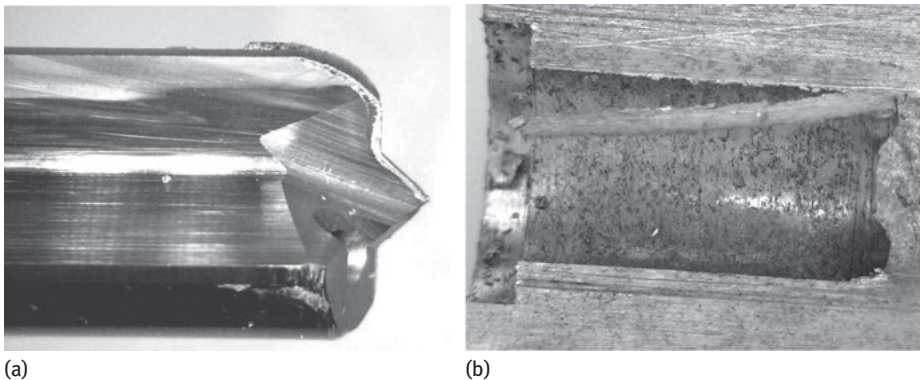


(a)                                          (b)

**Figure 1.14:** Excessive abrasive wear due to casting porosity: (a) appearance of a worn drill and (b) result of the autopsy of the machined hole.

hole where porosity and microinclusions can clearly be seen. Unfortunately, there is no standard procedure for microporosity and microinclusion assessment in terms of their influence on tool wear. As a result, the problem should be dealt with on a case-by-case basis with detailed autopsy of parts and collecting the relevant information.

### 1.6.1.2 Shrinkage/suction pores

Shrinkage pores (called cavities when it comes to tool failures) are the result of increases in density that occur when the metal changes from molten to solid form. The metal shrinks both during solidification and cooling. For aluminum, the volume reduction is roughly 4%–5%. Shrinkage pores occur in the hottest part of the casting, that is, the last part to solidify. With die casting, the greater portion of the shrinkage is compensated by the high post-filling pressure that is applied during solidification. It is important that the gating system is properly formed, so that the part near the mouth does not solidify before the rest of the casting; if that happens, the post-filling pressure does not have the intended effect.

A relatively small shrinkage pores/cavities are shown in Fig. 1.15(a). They are caused by the shrinkage of liquid during solidification. Casting cavities are large shrinkage pores as shown in Fig. 1.15(b). Normally, a drill breaks when it attempts to cut through such a cavity because its force balance is violated as one side of the drill cuts the air. As discussed by Astakhov [22], the proper drill performance completely relies on the drill force balance so the resultant axial force and drilling torque do not cause drill bending. If this balance is disturbed, however, the drill would bend. The greater violation of the force balance the greater the bending, the higher the chance of drill breakage. However, this is only a part of the problem. When a twist drill is compressed by the axial force, drill becomes a bit shorter. If the axial force is suddenly removed from one of the cutting edge as this edge collapses into a cavity, this drill partially unwinds so one of its edges jumps ahead causing drill bending and this edge tries to cut a way too much of the work material. This destroys the tool 100% of the time.

### 1.6.2 Sludge

The high-pressure die-casting sludge is referred to various compounds made up of oxides, such as alumina ($Al_2O_3$) and magnesia ($MgO$), and primary crystals that contain Al, Si, Fe, Mn, Mg and/or Cr [23, 24]. These oxides and crystals have high melting points and high specific gravities. The formation of sludge phases is a temperature-dependent process in combination with concentrations of iron and manganese independent of the silicon content. One of the common sludge phase is hard complex intermetallic multicomponent sludge, $Al_{15}(FeMn)_3Si_2$ – phase [25]. The Fe-rich particles can be twice as large as the Si particles, and the cooling rate has a
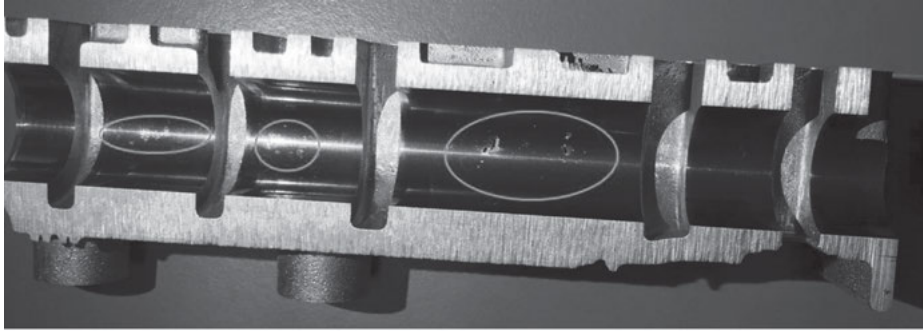
(a)
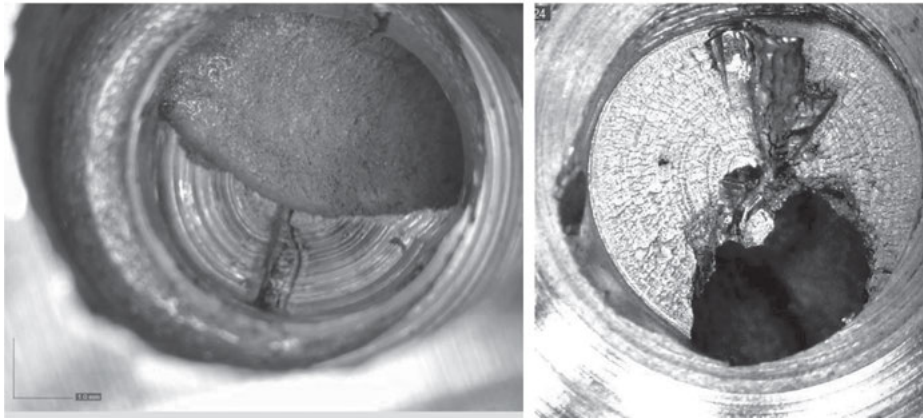


(b)

**Figure 1.15:** Casting defects: (a) small shrinkage pores and (b) large cavities.

direct impact on the kinetics and quantities and size of Fe-rich intermetallic components present in the microstructure.

The oxides form during alloy melting and treatment. Generally, aluminum die casting alloys contain higher levels of Fe than the other foundry aluminum alloys to eliminate or alleviate the die soldering. Fe in aluminum alloys forms compounds of different morphologies, such as needles, Chinese scripts and polygons. The needle-shape of Fe-rich compounds is detrimental to the alloy's mechanical properties. So, in aluminum die casting alloys, Mn or Cr, or some other elements are added to alter the morphology of the Fe-rich compounds to those less detrimental ones. The higher Fe content and its correcting elements, such as Mn and Cr, can result in the formation of different complex intermetallic compounds, some of which may be categorized as sludge.

Oxide films are formed in connection with various kinds of turbulence, for example, when a melt is tapped from a smelting furnace. Oxides can also be added to a melt via ingots and other charging materials that are not clean and dry. Iron-rich

particles can form in a melt and give rise to pores and shrinkage effects. The particles can be shaped like discs and contribute to a drastic reduction of the ductility. Normally, in order to reduce the harmful effects of Fe, alloys should contain as little of it as possible. For die casting reasons, however, the amount of Fe is 1.3wt%, which is very high that causes problems in machining.

Magnesium in aluminum alloys oxidizes and with time and temperature reacts with oxygen and aluminum oxide to form spinel. Many oxide forms display densities similar to that of molten aluminum and sizes that reduce the effectiveness of gravimetric separation. In addition, most oxides are wet by molten aluminum, reducing the effectiveness of mechanical separation methods. Inclusions occur as varying types with differing sizes and shapes. Aluminum oxides are of different crystallographic or amorphous forms as films, flakes and agglomerated particles. Magnesium oxide is typically present as fine particulate. Spinels can be small hard nodules or large complex shapes. Aluminum carbide and aluminum nitride can be found in smelted aluminum, but are usually of size and concentration of no significance in aluminum castings. Refractory and other exogenous inclusions may be identified by their appearance and composition.

Because such inclusions are hard, they can also have negative effects on cut ability, with wear or breakdown of cutting tools as a result. Figure 1.16(a) shows appearance of small inclusions. Conditionally, inclusions are small when their size does not exceed 1/10 of the tool/drill diameter. As these inclusions are very hard, they cause drilling tool chipping in the manner shown in Fig. 1.16(b). If not detected timely by the machine controller, this chipping then results in drill breakage. When amount of sludge is excessive as shown in Fig. 1.17, the tool breaks unconditionally.

### 1.6.3 Other casting defects

#### Surface defects

Most surface defects are visible and result in rejection of the casting. Cold flows comprise the most common type of surface defect. They are caused when the metal begins to solidify as two metal fronts approach each other. In order to avoid such defects, it is important for the gating system be properly formed, and for the metal and the molding tools to be kept at the correct temperature.

#### Laminations

Laminations are formed when two layers of molten metal do not combine to form a homogeneous solid. This happens when a layer of partly solidified metal with an oxidized surface flows over the upper surface of a similar layer. The layers remain separate from each other, though they may be joined at some places where no oxide film was formed when the two flows came together. The layers may adhere to each other to
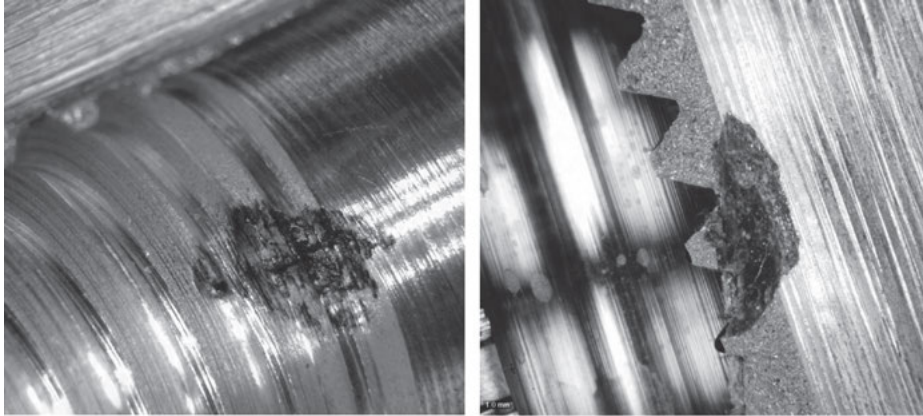
(a)
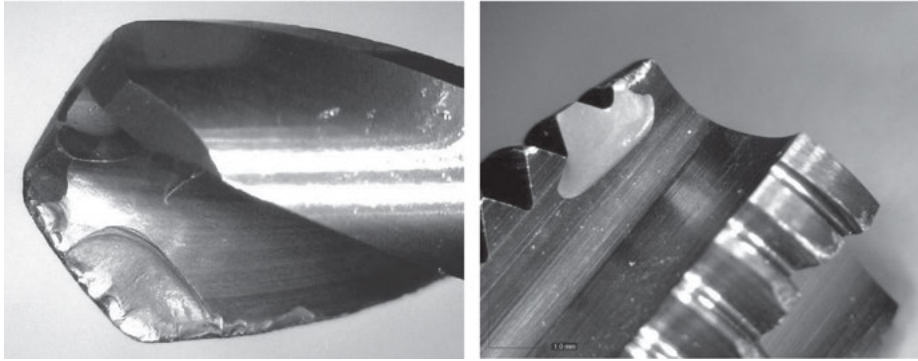
(b)

**Figure 1.16:** Showing (a) appearance of a hard inclusion in a part section and (b) chipping of the tool rake face due to collision of the tool with an inclusion.
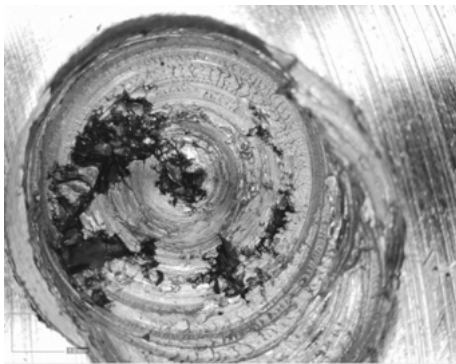


**Figure 1.17:** Excessive sludge found at the bottom of the hole where the drill was broken.

some extent, but a slight external pressure can cause them to separate. For example, tumbling prior to surface treatment can produce openings in the laminate so that fluid can work its way in and cause bubbles to form between the opposing surfaces. Another problem is that the layers may partially separate and cause measuring errors.

**Flushing**

Flushing in the molding tool can be the result of several factors. Among them is the high speed that is required at the mouth, the condition of the molding tool and the temperature where the melt contacts the tool. The extent of inclusions is also important, and the chemical reaction of the aluminums with the molding tool may be, as well. The erosion-like effects that can be seen on the molding tool during the casting process are often combinations of erosion and corrosion, both of which occur at high temperatures.

## 1.7 Advanced design of PCD drills for HPR drilling of HSAA

### 1.7.1 Problems with the existing designs

Since PCD blanks (Fig. 1.10) became commercially available, multiple drilling tools for machining nonferrous materials were designed and implemented. Because the cost of earlier PCD blanks was high, initial applications of PCD were mainly for expensive finishing tools, for example, reamers where both surface finish and diametric accuracy were of prime concern. Those years, specialists learned how to braze PCD tips and how to trim and finish grinded PCD-tipped tools through the painful trial-and-error method. Low-speed structurally nonrigid machines, inadequate tool holders (primarily with excessive run out) and nonavailability of high-pressure MWF internal (through spindles) supply limited applicability of PCD tools. As discussed above, this has been changing rapidly since the beginning of the twenty-first century. Leading tool and machine manufacturers have developed new powerful precision machines having a wide range of speeds and feeds, tool materials and coatings, new tool holders, automated workholding fixtures, advanced machine controllers and so on. As a result, the use of PCD tools in drilling of HSAA has significantly widened for various drilling applications as reaming, drilling, spotfacing, countersinking and so on.

PCD-tipped tools are widely used in modern HSAA machining. A typical PCD-tipped straight flute drill with internal high-pressure MWF supply is shown in Fig. 1.18(a). It has a cemented carbide body and the two PCD tips brazed in the pockets made (normally EDMed) on the periphery of its terminal end. As can be seen, such a drill has two combined major cutting edges, each consisting of the PCD and carbide portions. The idea behind this design was crystal clear. As discussed above, the maximum wear of drilling tools occurs in the vicinity of the corner (Fig. 1.3), the placement of a PCD tip in this region of the major cutting edge should solve the

(a)

(b)

(c)
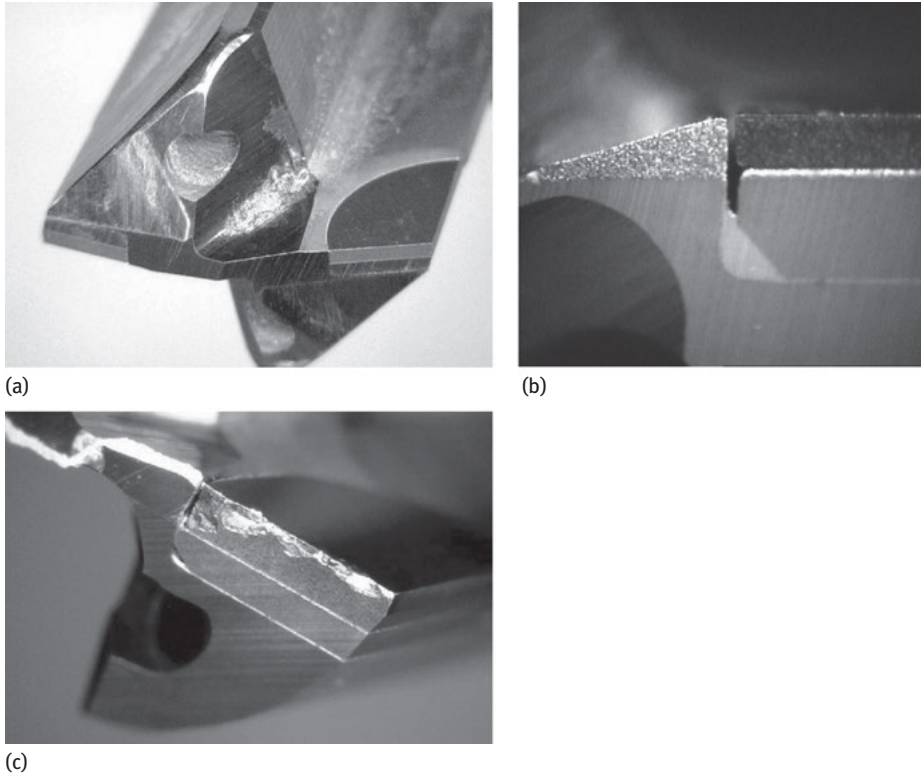
**Figure 1.18:** Showing (a) typical PCD-tipped drill and (b) major problem in high-speed applications.

problem, that is, it should help to increase tool life while enjoying the high quality of PCD machining.

When PCD-tipped drills were used at relatively low (for the PCD tool material) cutting speeds and moderate penetration rates, their performance was satisfactory. With wider implementation of HPR (due to increased spindle speeds), it was found that PCD-tipped drills have two inherent problems that cannot be resolved even in principle. The first problem is that the tool life of the carbide portion of the drill is much lower compared to PCD inserts, and thus this portion often defines tool life. Moreover, on tool re-sharpening, a great amount of the carbide portion should be ground off to restore the normal working condition of this portion, whereas it is not feasible for PCD inserts. Multiple attempts to used EDM or EDG to ablate both the carbide and PCD portions of the tool led to even further decrease in the life of the carbide portion as the performance of such tools is inferior to that finished with the grinding wheel.

Leading point grinding machine builders (for PCD/carbide tools) have been trying to address this problem for last few years. For example, ANCA Co. now offers

the new EDGe erosion machine with the adaptive eSpark erosion power generator for control over the energy level of the spark, surface finish, material removal and cycle time. It is to say that the carbide and PCD portions of a tool are ED ground with different energy/number of impulses that improve their qualities.

The second problem with PCD-tipped drills is the gaps between the PCD inserts and the carbide body as shown in Fig. 1.18(b). These gaps are caused by the following:

– When a PCD insert is brazed into a tool body using a common brazing technology (e.g., the induction brazing), the BFM does not adhere to the PCD layer, that is, the only carbide substrate is actually brazed to the drill body.
– When a tool is re-tipped, it is difficult to remove the remaining BFM from the pocket of the carbide body so that when new PCD inserts are brazed, their position may not be as intended. One may wonder, however, why not to apply more heat and thus to melt the remaining of BFM. The problem is that the amount of heat in PCD brazing is always limited to avoid overheating of the PCD tool material.

No matter how small is the gap, the temperature in HPR drilling is high enough to cause the work material plastic flow into this gap with harmful consequences. First, it causes the formation of an aluminum deposit on the rake face that, in turn, causes radial drill vibrations, and thus chipping (on the flank faces) of PCD inserts. Second, the material that flows into the gap creates a splitting wedge often causing chipping of the PCD layer (Fig. 1.18(c)). According to the authors' experience, this happens at high-speed drilling, no matter how small is the gap.

### 1.7.2 Cross-PCD drill design and implementation practice

#### 1.7.2.1 Traditional approaches
The discussed disadvantages of PCD-tipped drills were known for long time, practically since the beginning of their practical applications. As a result, a number of attempts were made in the development of the so-called full-face (cross-PCD) drills, that is, the drills having major cutting edge, chisel edge and margins made of PCD. Depending upon the technology used for manufacturing such drills, cross-PSD drills can be broadly divided as follows: (1) PSD is sintered in a part of the drill body, and (2) a fully sintered PCD segment(s) is brazed into the drill body.

The essence of multiple design variations of the first PCD drill type is in sintering a PCD layer inside a slot made in a carbide blank to form the nib. The nib is then brazed to the drill body, EDMed and finished to the final shape of the drill. The essence of the second PCD drill type is the use of a sintered PCD wafer having a PCD layer sintered together with two carbide substrates. Such blanks are readily available

in the market nowadays. As the wafer has two cemented carbide substrates, it can be assembled (using brazing) with the drill body having an axial slot and brazed to this body. After the brazing, the drill is trimmed and ground.

The major problem with the discussed cross-PCD drills is that a significant amount of cobalt should be placed in the mix (grade powder) to assure sintering as the carbide nib or two carbide substrate acts as shields preventing the pressure and temperature that are needed to fully sinter a "standard" (low cobalt) grade powder. The resultant product (PCD) is not as strong as that "normally" sintered as the process temperature and pressure are insufficient for the development of strong SP3 bonds.

Although the discussed design found wide use in machining of fiber-reinforced plastics and other composite materials at low cutting speeds and feeds, the application practice of such drills in HPR drilling of HSAA revealed the following problems:

1. Because of significant amount of cobalt used, BUE still persists on this drill type, though in different forms. When such drills are used, the ground rake face is covered by a thin layer of aluminum that eventually develops the BUE with all above-listed consequences. The test results show that the development of the BUE does not correlate with tool wear. Rather, it begins to develop since the first drilled holes.

2. Because different parts of PCD did not have the same exposition to sintering temperature and pressure, the properties of the PCD insert vary along its length deteriorating to the drill's center. As a result, when used for HSAA, the following happens:
   – Aluminum forms the BUE as a thin layer on the rake face that significantly increases contact stresses.
   – The sharp cutting edge collapses due to high contact stresses becoming round that increase the cutting force even further.

3. The relatively low strength of PCD sintered that way combined with high forces cause drill breakage in the drill center. All the attempts to improve manufacturing quality of these drill by better grinding of the rake face, improving the drill geometry and so on were of a little help.

### 1.7.2.2  Advanced cross-PCD drills for HSAA

This method of manufacture became possible due to the development of two important technologies: (1) manufacturing of PCD of substantial thickness that then can be EDMed out of the carbide substrate, (2) a brazing procedure of freestanding PCD insert (i.e., without an integral carbide backing) onto carbide bodies. Figure 1.19 shows schematically the sequence in manufacturing the cross-PCD drills. As can be seen, a fully sintered V-shaped PCD insert is first placed in a pocket made in a carbide body. The reason for machining the pocket in this form is twofold:
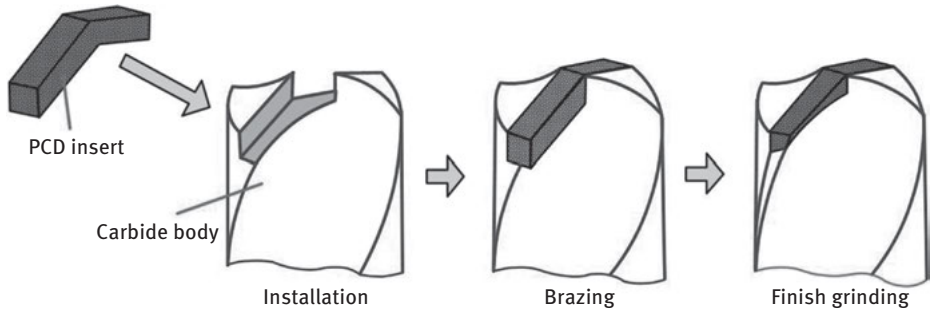
**Figure 1.19:** Schematic representation of the sequence in manufacturing the cross-PCD drills.

- To braze the PCD tip, the V-shaped segment is simply placed into the pocket that, by virtue of its matching geometry, causes the PCD tip to be automatically centered. Brazing is carried out by pressing the segment against the side of the pocket, while maintaining gentle pressure on the apex. Using this arrangement set in a vacuum brazing furnace while using a specially developed and now commercially available paste brazing filler, a perfect braze can be guaranteed each time.
- Apart from locating the segment, the V-shaped pocket has a dramatic effect on the amount of material that needs to be removed from the flute area. By eliminating the PCD from certain areas, standard grinding instead of sophisticated flute grinding can be used to produce the necessary angles in the flute area.

After brazing, the drill is finished using EDG or conventional grinding on specially developed point grinding machine for PCD tools. Note that such machines are commercially available (e.g., Walter Helitronic Power Diamond, ANCA EDGe erosion and tool grinding machine).

Figure 1.20 presents the most essential design/geometry features of the cross-PCD drill for HSAA. It is optimized for high-precision holes based on the general theory of drilling [9] and multiple tests run at high rotational speed (24,500 rpm) and penetration rate of 5,100 mm/min. The following particularities of the developed design/geometry can be pointed out:

- The true four-faces flank face design that assures its self-centering ability
- Partial split-point design (VIEW I in Fig. 1.20) to balance bending strength of PCD tool material and reliable removal of the chip formed by the two parts of the chisel edge
- High primary clearance angle of the major cutting edges (SECTIONS A-A and B-B in Fig. 1.20) that decreases the length of the tool-workpiece interfaces and improve the sharpness of the major cutting edges
- A special step design of the drill corner. As can be seen, the drill includes "the roughing stage" (7.415 mm dia.) and "the finishing stage" (7.915 mm dia.) to maintain very close diameter tolerance over entire tool life
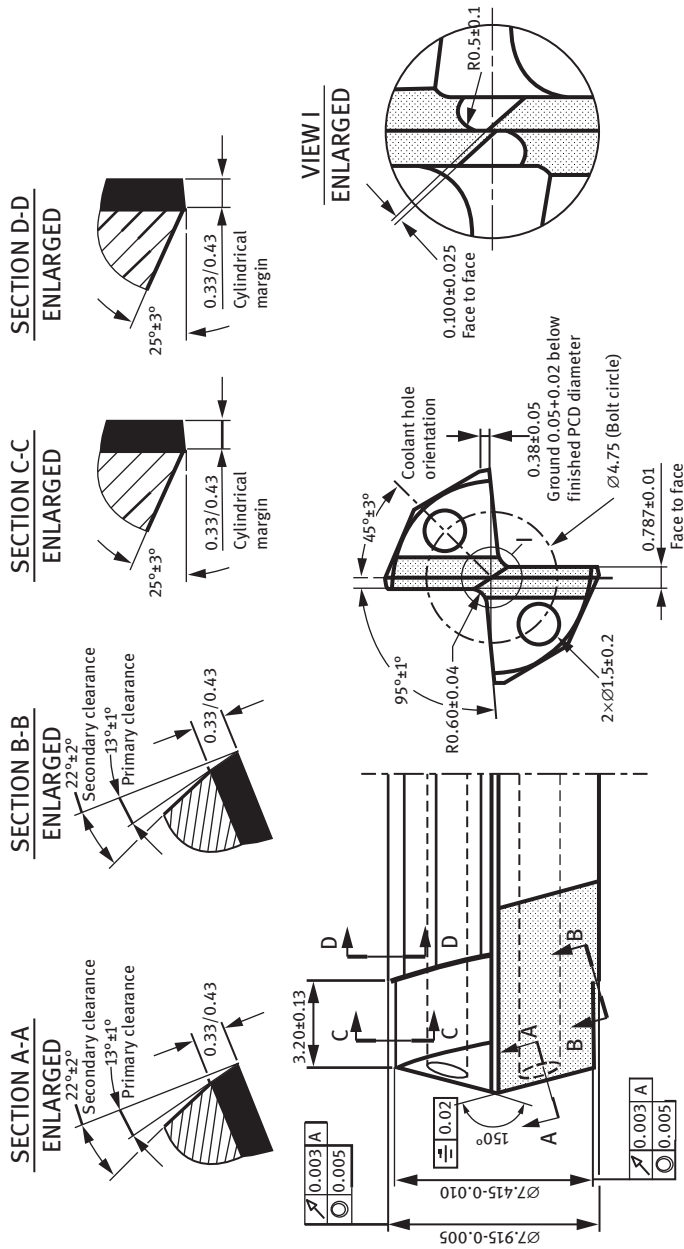
LIP HEIGHT VARIATION: 0.005 max
FLUTE SPACING: 0.08 max
WEB SYMMETRY: 0.08 max
CHISEL EDGE CENTRALITY: 0.01 max
Backtaper: 3 µm per mm.

**Figure 1.20:** Most essential design/geometry features of the cross-PCD drill for HSAA.

- The width of the primary margins is less than the thickness of the PCD layer (SECTIONS C-C and D-D in Fig. 1.20) that assures that only PCD is in contract with the hole being drilled properly fuming its roughness
- The auxiliary margins made on the drill carbide body (width 0.38 mm) are ground below the finished PCD diameter. This prevents their contact with the machined hole during normal operations while they provide some help to maintain drill stability when the drill enters the hole. Obviously, this requires a special CNC point grinding procedure where each margin is ground individually. Moreover, PCD margins are ground using a modified creep-feed grinding (gradual introduction of the grinding wheel with low feed) as grinding of PCD margins to the low surface roughness (Ra <0.2 μm) requires use of a rigid, high-horsepower multi-axis CNC machine designed to handle the high contact stresses.
- To assure close shape tolerances (true position, circularity and straightness) of drilled holes, special quality requirements as the lip height variation, flute spacing, web symmetry and chisel adage centrality are set as shown in Fig. 1.20. Obviously, to inspect these parameters, a CNC tool inspection mashie (e.g., Zoller Genius) is needed and special procedures are required.
- As a carbide custom-made preform is used for the drill body, the maximum (allowable by the strength of the tool) diameter of the MWF holes is used. The angular location of MWF holes to the drill flute face and the so-called bolt circle diameter (4.75 mm in Fig. 1.20) are optimized to deliver the maximum MWF flow rate to the region of the drill corners, that is to maximize tool life. In an ideal case, the listed parameters should be optimized using together finite element and fluid dynamic software packages.

Figure 1.21(a) shows a new drill designed and manufactured according to the listed specifications. Figure 1.21(b) shows drill appearance after tool life that was set at
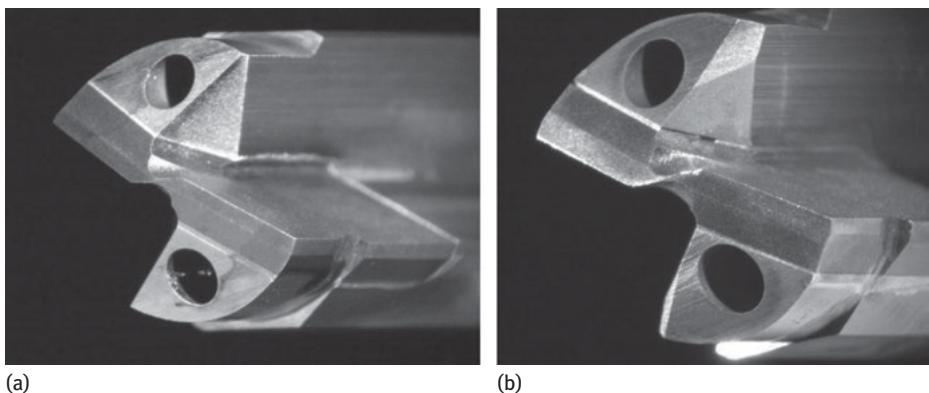


(a)                                          (b)

**Figure 1.21:** Showing the proposed drill for HPR drilling of HSAA: (a) new tool and (b) tool after tool life (25,000 holes).

25,000 holes (TCH – torque converter housing – A380) of a 6-speed automatic transmission. As can be seen, the tool wear is noticeable only over the chisel edge and the corners of the drill finishing stage.

# References

[1] Umer, U., Kishawy, H., Ghandeharium, A., Xie, L., Al-Ahmari, A., On modeling tool performance while machining aluminum-based metal matrix composites. The International Journal of Advanced Manufacturing Technology, 2017. London: Springer-Verlag. 92: pp. 19–30.

[2] Dabade, U., Dapkekar, D., Joshi, S., Modeling of chip–tool interface friction to predict cutting forces in machining of Al/SiCp composites. International Journal of Machine Tools and Manufacture, 2009. London: Elsevier. 49: pp. 690–700.

[3] El-Gallab, M., Sklad, M., Machining of Al/SiC particulate metal-matrix composites. Journal of Materials Processing Technology, 1998. New York: Elsevier. 83: pp. 1–8.

[4] Muthukrishnan, N., Murugan, M., Prahlada Rao, K., Machinability issues in turning of Al-SiC (10p) metal matrix composites. The International Journal of Advanced Manufacturing Technology, 2008. London: Springer. 39: pp. 1–8.

[5] Caroline, J.E., Feng, H., Lau, W. M., Machining of an aluminum/SiC composite using diamond inserts. Journal of Materials Processing Technology, 2000. New York: Elsevier. 102: pp. 25–29.

[6] Seeman, M., Ganesan, G., Karthikeyan, R., Study on tool wear and surface roughness in machining of particulate aluminum metal matrix composite-response surface methodology approach. The International Journal of Advanced Manufacturing Technology, 2010. London: Springer. 48: pp. 613–624.

[7] Quigley, O., Monaghan, J., O'Reilly, P., Factors affecting the machinability of an Al/SiC metal-matrix composite. Journal of Materials Processing Technology, 1994. New York: Elsevier. 43: pp. 21–36.

[8] Das, S., Mondal, D.P., Dixit, G., Correlation of abrasive wera with microstrucrure and mechanical properties of pressure die-cast aluminum hard-particle composite. Metallurgical and Materials Transactions, 2001. Springer US. 32A: pp. 633–642.

[9] Astakhov, V.P., *Drills: Science and Technology of Advanced Operations*. 2014, Boca Raton, FL: CRC Press.

[10] Ilio, A.D., Paoletti, A., Machinability aspects of metal matrix composites, in *Machining of Metal Matrix Composites*, J.P. Davim, Editor. 2012, Springer-Verlag: London. pp. 63–77.

[11] Santos, M.C., Machado, A.R., Sales, W.F., Barrozo, M.A.S., Ezugwu, E.O., Machining of aluminum alloys: A review. International Journal of Advanced Manufacturing Technology, 2016. 86: pp. 3067–308.

[12] Sornakumar, T., Kathiresan, M., Machining studies of die cast aluminum alloy-silicon carbide composites. International Journal of Minerals, Metallurgy and Materials, 2010. 17: pp. 648–653.

[13] Karthikeyan, R., Ganesan, G., Nagarazan, R.S., Pai, B.C., A critical study on machining of Al/SiC composites. Materials and Manufacturing Processes, 2001. 16: pp. 47–60.

[14] Astakhov, V.P., Machinability: Existing and advanced concepts, in *Machinability of Advanced Materials*, J.P. Davim, Editor. 2014, Wiley-ISTE. pp. 1–57.

[15] Zedan, Y., Alkahtani, S.A., Samuel, F.H., Effects of alloying elements on the machinability of near-eutectic Al-Si casting alloys, in *Machinability of Advanced Materials*, J.P. Davim, Editor. 2014, Waley: London. pp. 119–144.

[16] Davis, J.R., *Aluminum and Aluminum Alloys*. 1993, Metals Park, OH: ASM.

[17]  Nishida, Y., *Introduction to Metal Matrix Composites: Fabrication and Recycling*. 2013, Tokyo: Springer.

[18]  Davis, J.R., ed. *Alloying: Understanding the Basics*. 2001, ASM: Metal Park, OH.

[19]  Hakami, F., Pramanik, A., Basak, A.K., Tool wear and surface quality of metal matrix composites due to machining: A review. Proc IMechE Part B: Journal of Engineering Manufacture, 2017. 231: pp. 739–752.

[20]  Astakhov, V.P., *Tribology of Metal Cutting*. 2006, London: Elsevier.

[21]  Davim, P.D., Diamond tool performance in machining metal–matrix composites. Journal of Materials Processing Technology, 2002. 128: pp. 100–105.

[22]  Armarego, E.J.A., Cheng, C.Y., et al., Drilling with flat rake face and conventional twist drills—II. experimental investigation, International. Journal of Machine Tools and Manufacture, 1972. 12: pp. 37–54.

[23]  Liu, L., Samuel, F.H., Assessment of melt cleanliness in A356.2 aluminium casting alloy using the porous disc filtration apparatus technique: Part II Inclusion analysis. Journal of Materials Science, 1997. 32(33): pp. 27–44.

[24]  Ferraro, S., Fabrizi, A., Timelli, G., Evolution of sludge particles in secondary die-cast aluminum alloys as function of Fe, Mn and Cr contents. Materials Chemistry and Physics, 2015. 153: pp. 168–179.

[25]  Tillova, E., Chalupova, M., Hurtalova, L., Evolution of the Fe-rich phases in recycled Al-Si-Cu-Mg cast alloy during solution treatment. Communications – Scientific letters of the University of Zilina. 12(4): pp. 95–101.

Keng Soon Woon, Guan Leong Tnay and Swee Hock Yeo

# 2 Deep hole gun drilling of nickel-based superalloys

**Abstract:** Miniature deep holes with length to diameter ratios above 100 are commonly produced with mechanical gun drilling because of the efficiency of this process in meeting stringent straightness and finishing requirements. However, such superiority diminishes while drilling nickel-based superalloys such as Inconel 718. This chapter addresses the fundamental cause arising from a critical change in the generation of cutting force that induces adverse impacts on deflection of drills, burnishing along the hole and the eventual deterioration in straightness accuracy. The unique tool wear and failure modes are discussed in detail to provide insights into the underlying challenges, especially on the severe thermal-mechanical loading conditions. To improve tool life during the process, an effective methodology that increases coolant efficiency through strategic optimization of drill designs is presented. Besides this, a new approach in designing pilot holes for gun drilling based on pilot hole and gun drill design compatibility is described, as effective tool-work engagement enhances drilling stability that benefits tool life as well as straightness accuracy. Finally, exploratory solutions to the adverse impacts of re-sharpening gun drills with primitive manual grinding apparatus – a long-standing challenge in multiple-pass gun drilling are also duly addressed.

## 2.1 Introduction: background and definition

Gun drilling is a high aspect ratio drilling process to produce deep holes between 0.5 mm and 40 mm in diameter and typical depth range between 10 and 100 times of the hole diameter. Using special gun drilling equipment and know-how, extreme length to diameter ratios of up to 625 have been reported [1]. Early patents related to the process were mostly granted in between mid-eighteenth century and beginning of nineteenth century [2–6]. Although the process was first invented to produce solid gun barrels [7], it has been constantly improved and adapted to many different industrial applications, including complex tools and molds, medical, energy, hydraulic cylinders, military & defense, automotive, aerospace and oil & gas [8].

Gun drills rely on a set of asymmetrical cutting edges with off-centered drill point geometries to remove materials while penetrating a hole – a distinguishing feature from conventional twist drills with symmetrical cutting edges as shown in Figure 2.1. Removing materials via asymmetrical cutting, though uncommon in machining practices is managed through active balancing of the resultant cutting and radial forces on special ground-bearing surfaces – another unique provision on gun drills.
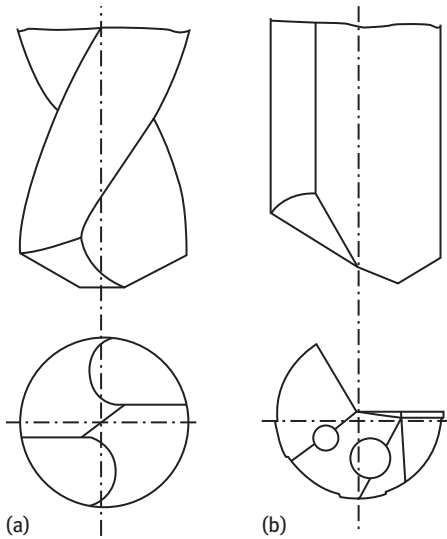
**Figure 2.1:** (a) Conventional twist drill; and (b) gun drill.

Combination of both key features bring about the self-piloting capabilities in gun drilling [9], which makes it technically feasible to achieve extremely high aspect ratio drilling.

In gun drilling of deep holes, most of the successful applications are performed in a single pass at high feed rates. On top of the obvious productivity gains through the time saved in changing of new tools and resetting of drilling configurations, single-pass drilling usually leads to higher accuracy by preventing accelerated straightness deviation arising from cumulative drill re-sharpening errors. This explains the superior performance in terms of both quality and productivity in drilling deep holes with gun drilling on conventional materials, such as aluminum, copper, brass, cast iron, steel, stainless steel and so on. However, the same level of consistent performance is hardly encountered on nickel-based superalloys that are often used in challenging engineering applications involving high pressure and high temperature. This is largely due to the much greater work hardenability and heat resistivity of this class of materials, as documented well in machining literatures [10, 11]. Therefore, while drilling deep holes, gun drills degrade rapidly with excessive frictional heating on cutting edges and bearing surfaces and large asymmetrical cutting forces on the drill tip [12]. As a result, catastrophic drill breakages during the process are frequently encountered – leading to unsalvageable hole misalignments and material scrap. To reduce the risk of such costly damages, industry practitioners often perform drilling on nickel-based superalloys with conservative speeds, feeds and depths. By doing so the frequency of re-sharpening, the time needed for drilling and the idle time of machine tool increases. Consequently, operating cost of the process becomes enormously high while the production efficiency is significantly

impacted. But such a trade-off does not always guarantee a satisfactory outcome. The issues pertaining to deep hole gun drilling of nickel-based superalloys are summarized in Figure 2.2.
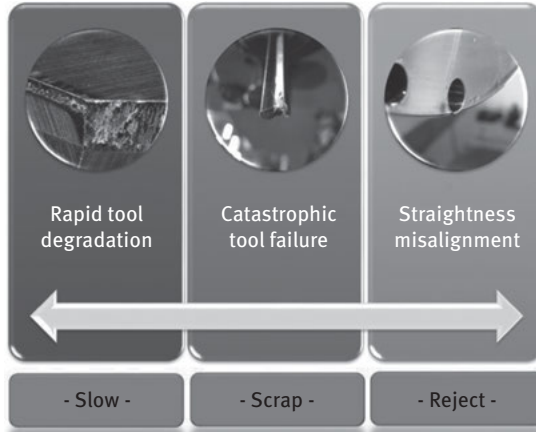


**Figure 2.2:** Challenges in drilling deep holes on nickel-based superalloys.

This chapter addresses the production issues described above with a practical approach, developed from the end user's perspective. For the sake of consistency, discussions throughout the chapter are based on the authors' findings on Inconel 718. It begins with a concise review of commercial gun drill designs and features, including nose grind contour, coolant hole and bearing pad. Next, the mechanics of the drilling process that originates from material removal through cutting and the influence of the cutting forces generated on drill deflection, wall deformation and process kinematics are analytically described. Following this, an in-depth study of various tool wear and failure modes of gun drills is presented as guidelines for failure analysis. Finally, a practical series of optimization methodologies through coolant application, pilot hole drilling, drill re-sharpening and cutting-edge preparation is provided. In a nutshell, this chapter aims to prepare one to understand fundamental constraints of the process and to discover future opportunities with the practical solutions presented.

## 2.2 Gun drill design

A gun drill consists of three major components: (1) carbide tip, (2) shank and (3) driver. Features and geometries of the drill are shown in Figure 2.3. The drill tip is asymmetrical with the inner and outer cutting edges located on the same side. The drill tip is also having a back taper with a step down of 1–2 μm diameter smaller for every 10 mm of the drill length. Multiple clearance angles are provided on the flank face to allow

(a) Top view
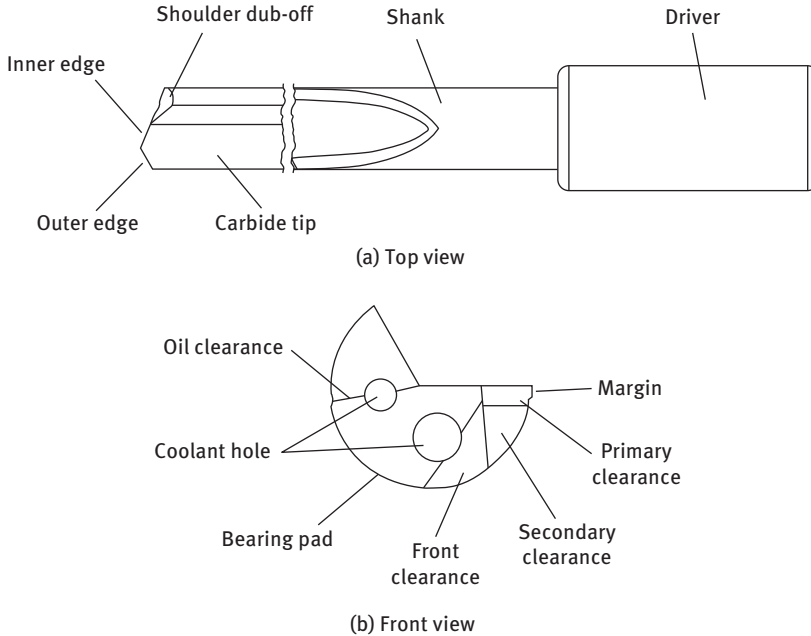


(b) Front view

**Figure 2.3:** Gun drill features and geometries: (a) Top view and (b) front view.

coolant to reach to the cutting edges. While the oil clearance angle is prepared on the shoulder dub-off to enable coolant to remove the chips from the cutting zone and to cool the cutting edges. Gun drill shank and driver are made of heat-treated alloy steel. The shank, driver and carbide tip alligned and brazed together. The shank is designed with a V-shaped channel to create more space for chip removal from the cutting zone. To prevent direct mechanical burnishing the shank diameter is designed with 0.2 mm smaller than the tip diameter.

## 2.2.1 Nose grind contour

Gun drills are most prominently defined with three drill geometries namely the outer cutting angle $\phi_o$, inner cutting angle $\phi_i$ and drill apex offset $A_p$ from drill diameter $D$. Refer to Figure 2.4. The unique combination of these critical geometries that forms the nose of a gun drill – known as nose grind. During the process, a chip is produced by the cutting edges as a whole. One part of it is produced by the outer cutting edge at $\phi_o$ and the other part by the inner cutting edge at $\phi_i$, with their respective widths defined by the location of the drill apex $A_p$. Both of these parts are merged along the interface as the chip grows and leads to a progressive formation of the so-called backbone [9] that will collide on the sidewalls and break.
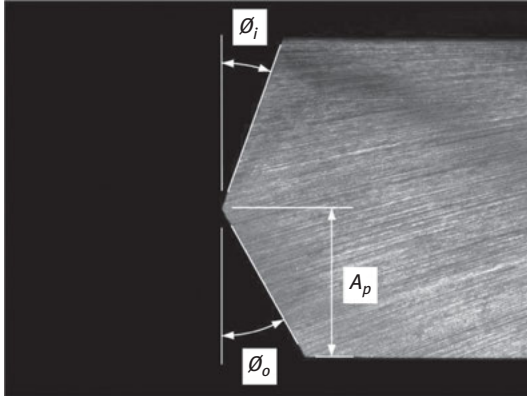
**Figure 2.4:** Nose grind contour consists of outer cutting angle $\phi_o$, inner cutting angle $\phi_i$ and drill apex offset $A_p$.

The most commonly encountered nose grind contours in the industry are N8, N4, N13 and N73, which are based on the Eldorado Tool Co. designs. They are chosen mainly based on work material while hole specification and acceptance criteria are also considered to uphold a balance between productivity and accuracy, as well as the overall cost-effectiveness. The generic description of the nose grinds and application rules of thumb [7] are given as follows:

- N8 with $\phi_o$ =30°, $\phi_i$ =20° and $A_p$=D/4 is the general purpose nose grind for most conventional materials, such as steel and stainless steel under normal operational conditions. It is also commonly used for any new drilling jobs.
- N4 with $\phi_o$ =15°, $\phi_i$ =20° and $A_p$=D/4 is used for special aluminum alloys and woods when N8 is unable to deliver satisfactory results.
- N13 with $\phi_o$ =40°, $\phi_i$ =5° and $A_p$=D/4 is suitable for harder and more brittle metals such as cast iron with the large outer cutting angle. The design also permits greater feed than N8 on softer and more ductile materials.
- N73 with $\phi_o$ =30°, $\phi_i$ =10° and $A_p$=D/3 has the strongest drill point among the commercial nose grinds. It is mostly used for angular drilling, interrupted drilling of stacked materials and crossed drilling.

## 2.2.2 Coolant hole

In gun drilling, coolant that is supplied under high pressure travels along the internal conduits of drill shafts and drill tips before being ejected through coolant hole(s) on the face of a gun drill to reach the drill point. Configuration of the coolant holes thus plays an important role in through-shaft coolant delivery of the process; chiefly, in regulating the coolant volume and pressure. Three types of configurations are commercially available namely one-hole, two-hole and kidney-shaped as shown in Figure 2.5. The one-hole configuration is widely used on drills smaller than 6 mm
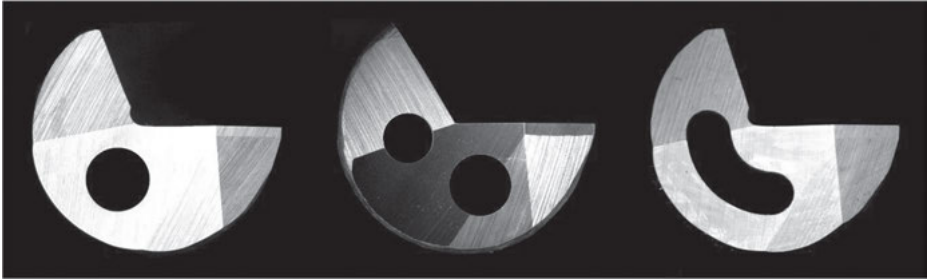
**Figure 2.5:** One-hole, two-hole and kidney-shaped coolant hole configuration.

in diameter, whereas the two-hole is suited for drills larger than 6 mm. Kidney-shape is mostly intended for miniature drilling of special materials.

In general, the performance involved in delivering high-pressure coolant to the drill point improves from 1-hole to 2-hole and with kidney-shaped being the best. Having the single largest orifice with an outlet of $0.2D^2$, the kidney-shaped configuration that spans between 89° and 178° is capable of "flooding" the entire rake faces at high pressure. For a 2-hole configuration with a top and bottom outlets of $0.05D^2$ and $0.1D^2$ respectively located at 75°and 164° from the drill center, reasonable amount of coolant can be found at the drill point, though pressure of the combined flow is reduced. As a comparison, the one-hole configuration with an effective outlet of $0.05D^2$ produces a stronger stream of coolant but most of the flow is deflected back into the V-channel and thus resulted in poorer access to the cutting edges.

### 2.2.3 Bearing pads

Gun drills are constantly deflected by cutting forces generated on the outer cutting edges due to the asymmetrical nose grind designs of the drills. Counterbalancing of such deflections is important to uphold straightness of the deep holes. This is carried out by incorporating bearing pads on gun drills as an auxiliary feature to support the drills. Essentially, bearing pads improve the support by increasing the fit of the rotating drills within the holes. By doing so the holes are constantly burnished by the bearing pad, which helps to improve hole finishing.

Four bearing pad designs as shown in Figure 2.6 are commonly used in the industry. The different designs are used to cater for the wide range of engineering materials. To promote stability of gun drills during the process, the bearing pads can either be a single continuous surface or they can also be a set of peripheral contours strategically distributed along the circumference of gun drills. For example, the G-type is suitable for most general materials as the design has adequate support in the hole due to large surface contact area. On the other hand, the C-type is designed
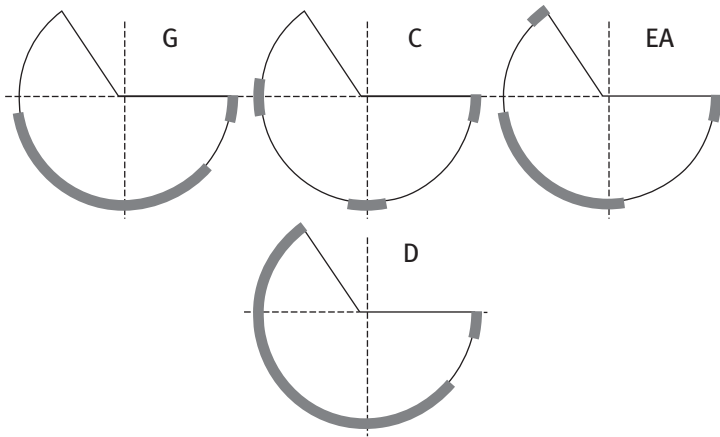
**Figure 2.6:** Various commercially available bearing pad designs.

for tight hole diameter control or when additional finishing is required on difficult machine materials like nickel-based alloys such as Inconel materials or stainless steel. The EA-type has an elaborated three-point support to cater for interrupted cutting conditions such as cross-drilling on soft materials like aluminium and brass. But it is not suitable for materials with high nickel contents due to the large burnishing force involved. Finally, the D-type with the largest surface contact area renders maximum support and thus the most ideal design to minimize drift on highly ductile materials such as graphite-rich cast iron.

## 2.3 Process mechanics

Like other machining processes, the mechanics of gun drilling is mainly governed by the operating conditions. To prevent tool failures while drilling deep holes on Inconel 718, conservative parameters are usually implemented. According to [13–15], feed rates for drilling Inconel 718 are suppressed between 8.95 and 23.3 mm/min. Combining with the low rotational speeds of 873–1,650 rpm to minimise work hardening, uncut chip thickness is reduced to a fine range between 8.9 and 14.1μm – transforming the drilling process to micron-scale cutting. Moreover, commercial gun drills are found to have cutting edge sharpness, defined as tool edge radius, $r_e$, of 4.84 to 6.14 μm (based on 60 drills from 4 brands). A sample measurement is shown in Figure 2.7. Thus, along with the downscaling of cutting magnitude that approaches $r_e$ in micron-scale, the tool edge radius effects on the process mechanics are activated. This section describes the elements of process mechanics from cutting force generation, drill deflection, wall deformation and the overall kinematics as governed by such effects.
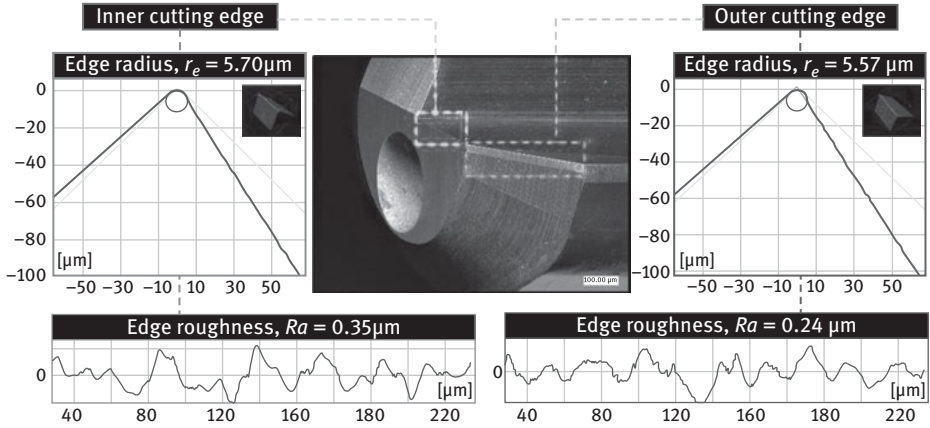
**Figure 2.7:** Cutting edge measurement of a gun drill according to ISO 25178-6 [1].

### 2.3.1 Cutting force

With the significance of tool edge radius effects, the new process model requires redefinition of force generations that considers both cutting and plowing. As shown in Figure 2.8, the inner *i* and outer *o* cutting edges of the gun drill are divided into a finite number of cutting elements with a width:

$$dw_{i,o} = \frac{dr}{cos\phi_{i,o}}$$



(a)  (b)
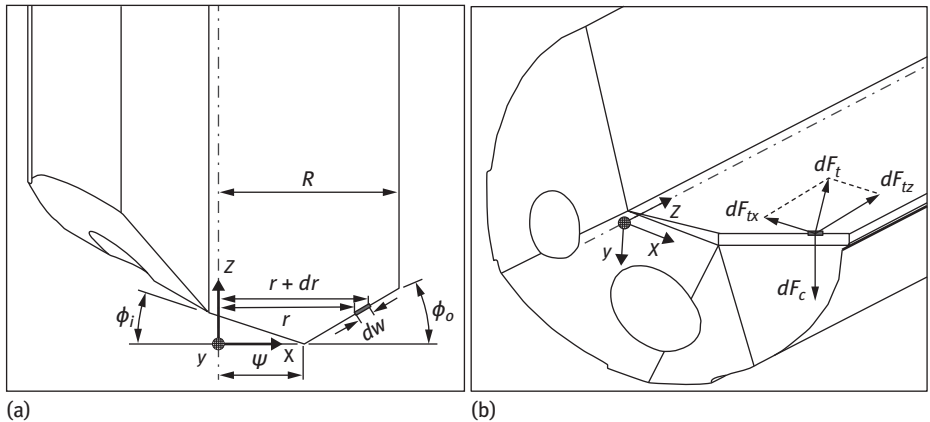
**Figure 2.8:** Cutting force generation on a gun drill. (a) Top view and (b) isometric view [1].

where $r$ is the drill radius, $\phi_i$ and $\phi_o$ are the inner and outer cutting angle angles. Uncut chip thickness on the cutting edges is as follows:

$$t_0 = f cos\phi_{i,o}$$

Instantaneous shear force over the cutting element is defined as follows:

$$dF_s = \frac{kt_0 dw}{sin\phi_n} = \frac{kfdr}{sin\phi_n}$$

where $k$ is material shear flow stress and $\phi_n$ is the instantaneous shear angle determined from the J-C constitutive model.

Thus, the instantaneous cutting and thrust components are as follows:

$$dF_c' = dF_s \frac{cos(\phi_n - \gamma_n)}{cos\chi_n} \text{ and } dF_t' = dF_s \frac{sin(\varnothing_n - \gamma_n)}{cos\chi_n}$$

where $\chi_n$ is the angle between $dF_s$ and resultant of $dF_c'$ and $dF_t'$.

Effective rake angle $Y_n$ is governed by $t_O$ and $r_e$ [4], in which

$$\gamma_n = sin^{-1}\left(\frac{t_0}{r_e} - 1\right) \text{ when } \frac{t_0}{r_e} < \left(\frac{t_0}{r_e}\right)_{lim}; \text{ or } \gamma_n = \gamma \text{ when } \frac{t_0}{r_e} > \left(\frac{t_0}{r_e}\right)_{lim}$$

$$\gamma_n = \gamma \text{ when } \frac{t_0}{r_e} > \left(\frac{t_0}{r_e}\right)_{lim}$$

Plowing components [5] in the directions of $dF_c'$ and $dF_t'$ are as follows:

$$dF_c'' = \sigma dw_{i,o} r_e tan\left(\frac{\pi}{4} + \frac{\gamma_n}{2}\right); \text{ and}$$

$$dF_t'' = \sigma dw_{i,o}\left(1 + \frac{\pi}{2}\right) r_e tan\left(\frac{\pi}{4} + \frac{\gamma_n}{2}\right)$$

Total cutting and thrust forces on inner and outer edges are as follows:

$$F_{ci} = \int_0^\psi \left(dF_{ci}' + dF_{ci}''\right) \text{ and } F_{ti} = \int_0^\psi \left(dF_{ti}' + dF_{ti}''\right)$$

$$F_{co} = \int_\psi^R \left(dF_{co}' + dF_{co}''\right) \text{ and } F_{to} = \int_\psi^R \left(dF_{to}' + dF_{to}''\right)$$

Transforming the localized forces to the main axes, they become

$$F_x = F_{ti} \times sin\phi_i - F_{to} \times cos\phi_o$$

$$F_y = F_{ci} + F_{co}$$

$$F_z = F_{ti} \times cos\phi_i + F_{to} \times cos\phi_o$$

### 2.3.2 Drill deflection

Drill deflection is primarily caused by $F_z$ where the long and slender structure is compressed and buckled. A modified version with Euler's column theory is hereby proposed. As shown in Figure 2.9, driver of the drill is fixed and the tip is pinned. Considering misalignments at the tip $\delta_t$ and whip guide $\delta_w$, the deflections are as follows:

$$y_1(x) = U_1 cos\varphi x + V_1 sin\varphi x + \delta_t + \frac{R_w}{F_z}(L - x) - \frac{R_t}{F_z}(l_1 - x)$$

for $0 < x < l_1$ and

$$y_2(x) = U_2 cos\varphi x + V_2 sin\varphi x + \delta_t + \frac{R_t}{F_z}(L - x) \text{ for } l_1 < x < L$$
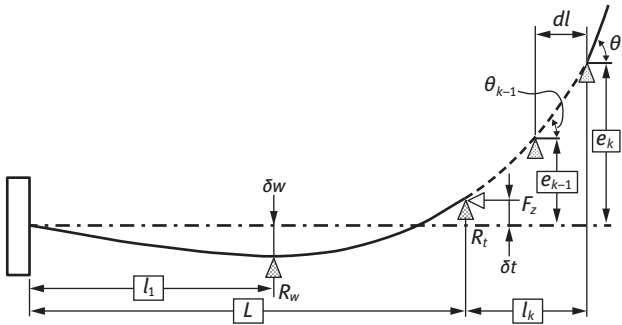


**Figure 2.9:** Gun drill deflection profile as deep hole drilling advances [1].

where $R_w$ and $R_t$ are reaction forces at the whip guide and drill tip, respectively, whereas $U_1$, $U_2$, $V_1$ and $V_2$ are deformation coefficients that vary with the depth of drilling. Here the thrust constant is $\varphi = \sqrt{F_z/E_s I_s}$ where $E_s$ is elastic modulus of drill stem and $I_s$ is area moment of inertia of its cross section.

After drill penetration is extended into the workpiece, drill deflection within the hole is governed by the drill tip inclination:

$$\theta_k = \frac{dy_2}{dx} = -U_2\varphi sin\varphi x + V_2\varphi cos\varphi x - \frac{R_t}{F_z}$$

$U_1$, $U_2$, $V_1$, $V_2$, $R_w$ and $R_t$ are determined by solving the coefficient matrix [6] with the boundary conditions as follows:

$$
\begin{bmatrix}
1 & 0 & 0 & 0 & L/F_z & -l_1/F_z \\
0 & \omega & 0 & 0 & -1/F_z & 1/F_z \\
cos\varphi l_1 & sin\varphi l_1 & 0 & 0 & (L-l_1)/F_z & 0 \\
0 & 0 & cos\varphi l_1 & sin\varphi l_1 & (L-l_1)/F_z & 0 \\
0 & 0 & cos\varphi L & sin\varphi L & 0 & 0 \\
-\varphi sin\varphi l_1 & \omega cos\varphi l_1 & \omega sin\varphi l_1 & -\varphi cos\varphi l_1 & 0 & 1/F_z
\end{bmatrix}
\begin{bmatrix}
U_1 \\
V_1 \\
U_2 \\
V_2 \\
R_w \\
R_t
\end{bmatrix}
=
\begin{bmatrix}
-\delta_t \\
0 \\
-\delta_w - \delta_t \\
-\delta_w - \delta_t \\
0 \\
0
\end{bmatrix}
$$

Hence, the new drill deflection from the drilling axis after drill tip advancement of $dl$ to drilling depth of $l_k$ is as follows:

$$e_k = e_{k-1} + \theta_{k-1}dl$$

where $e_{k-1}$ and $\theta_{k-1}$ are drill deflection and drill tip inclination of the previous cycle, respectively. Changes in $e_{k-1}$ is updated in each iteration to account for the total cumulative error in the current $e_k$.

### 2.3.3 Wall deformation

Thin walls along the deep hole are deformed by bearing pads. Generation of large process force brings about comparable reaction force on the bearing pads in magnitude. Associated with simultaneous drill rotation, rolling contact is established where deformation is induced through a combination of transverse shearing and orthogonal compression. As shown in Figure 2.10, when thin wall is deformed, the drill deviates at the same magnitude $U_i$ on the same plane. Total deformation consists of both elastic $E_i$ and plastic $P_i$ components, and thus

$$Ui = \delta Ei + \delta Pi$$

Elastic deformation can be approximated to orthogonal Hertzian contact [16] considering the spherical-shaped bearing pads:

$$\delta E = \frac{3}{8\sqrt{R}} \frac{F_r\left(1-\vartheta^2\right)}{E_{inc}}$$

where $\vartheta$ is the Poisson's ratio and $E_{inc}$ is the elastic modulus of the Inconel 718 workpiece.
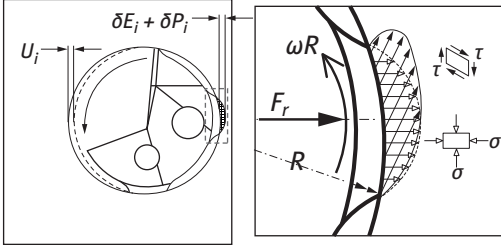
**Figure 2.10:** Elastic-plastic deformation via rolling contact on bearing pads [1].

On the other hand, materials in the vicinity the surface is plastically deformed [17] and in the direction of traversal of the bearing pad when the elastic limited is exceeded:

$$\delta P = \left[ \frac{1}{R} \left( \frac{F_r}{2k_c} \right)^2 \middle/ \left( 1 + \frac{\pi}{2} \right)^2 \right] + \frac{1}{R^2} \left( \frac{F_r}{2k_c} \right)^3$$

Reaction force on the bearing pads $F_r$ is a strong function of the main process forces where $F_r \equiv \sqrt{F_x^2 + F_y^2 + F_z^2}$.

### 2.3.4 Process kinematics

With the understanding of quantitative effects of tool edge radius on drill deflection and wall deformation, the trajectory function for deep hole gun drilling of Inconel 718 can now be defined in a parametric vector form as follows:

$$\mathbf{H}(t) = [R cost + e(t) + U(t)] \, \boldsymbol{i} + (R sint) \boldsymbol{j} + \frac{f_r}{2\pi} t \boldsymbol{k}$$

where $e(t)$ and $U(t)$ are the drill deflection and wall deformation functions as defined in Sections 2.2 and 2.3, respectively, whereas $t$ varies from 0 to $2\pi$ for a complete drill rotation.

As shown in Figure 2.11, the kinematic properties of each point on the curve are described with the tangent **T**, normal **N** and binormal **B** unit vectors [18]:

$$\mathbf{T} = \frac{d\mathbf{H}}{ds} \text{ and } \mathbf{N} = \frac{\frac{d\mathbf{T}}{ds}}{\left\| \frac{d\mathbf{T}}{ds} \right\|} \; ; \; \mathbf{B} = \mathbf{T} \times \mathbf{N}$$

where $d/ds$ is the derivative with respect to the arc length, $s$:

$$s(t) = \int_0^t \mathbf{H}'(t) dt$$

$\mathbf{H}'(t)$ is the velocity vector over non-zero curvature.
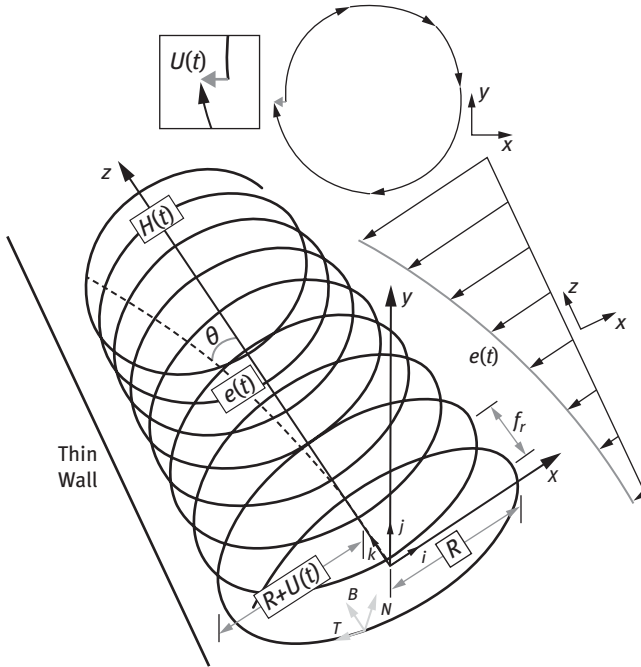
**Figure 2.11:** Kinematics of deep hole gun drilling under the combined effects of drill deflection and thin wall deformation [1].

### 2.3.5 A case study

To evaluate the validity and robustness of the model, two sets of mutually exclusive experiments were carried out separately at two test sites. Each experiment involved the drilling of two horizontal blind holes with 8 mm in diameter and 1,000 mm in length, giving a uniform aspect ratio of 125. The entrance wall thickness was 5 mm. Inconel 718 workpiece, in the form of a 2.0 m cylindrical bar with 53.3%–53.6% of Ni + Co and average yield strength between 1,034 and 1,165 MPa was shared between the test sites. Column-type gun drilling machines, Miroku MHG-2000 J-NC and Auerbach AX3 TLF were used for Test-1 and Test-2. Emulsion fluids with 10%–15% neat oil and extreme pressure (EP) additives were applied at 50–70 bar for cooling and lubrication.

The two sets of drills from different brands were single flute, slash-type nose design. Apex offset, $A_o$ was quarter of the drill diameter, D and inner $\phi_i$ and $\phi_o$ outer cutting angles of 20° and 30°. The bearing pad configurations for Test-1 and Test-2 were C and G, respectively. The average tool edge radius $r_e$ of the former was 5.33 μm (0.37 standard deviation) and 5.23 μm (0.33 standard deviation) for the latter. Coupled with a fixed feed rate $f$ of 5 mm/min and varying rotational speed $\omega$ of 1,400 rpm and 700 rpm for Test-1 and Test-2, the resultant uncut chip thicknesses $t_0$
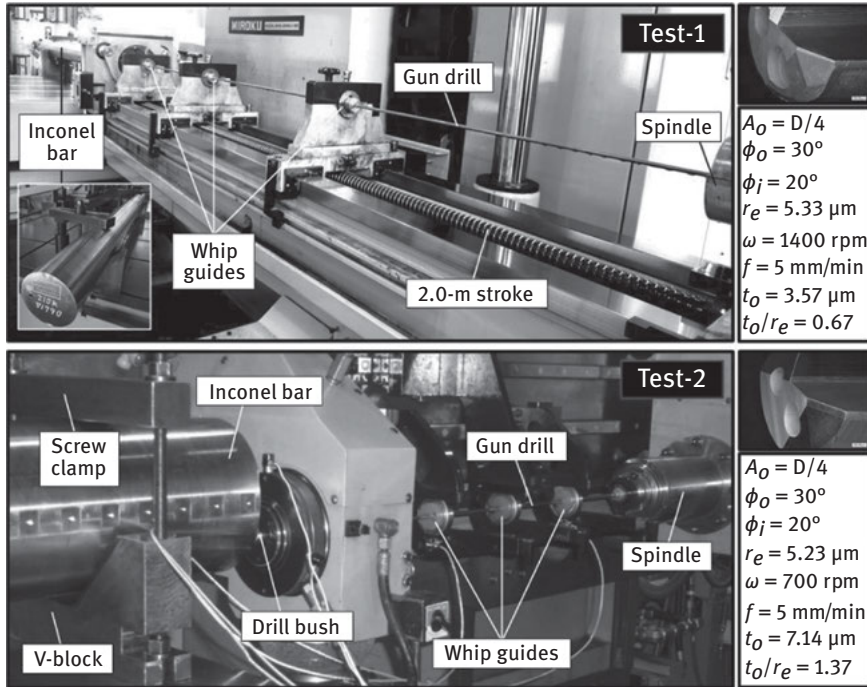
**Figure 2.12:** Experimental setup, drilling conditions and tool geometries [1].

were 3.57 µm and 7.14 µm. The averages $t_o/r_e$ of the two tests were 0.67 and 1.37. The setup and test conditions are summarized in Figure 2.12. Each drilling cycle was kept to 50 mm and thus 20 cycles were needed to complete a hole. A total of 80 drilling cycles was performed in this study.

The effects of tool edge radius on hole misalignment in deep hole gun drilling of Inconel-718 originate primarily from the mechanics of chip formation. At $t_0/r_e{<}1$, materials are removed through a thrust-dominated mechanism that significantly increases the main process thrust force $F_z$ along the drilling axis as a comparison to that of a cutting-dominated mechanism at $t_0/r_e{<}1$. With the increase in $F_z$, deflection and buckling of the long and slender gun drill is amplified as drilling advances, resulting in severe deviation in the final straightness through accumulation of straightness error in every drilling cycle. As shown in Figure 2.13, difference in straightness deviation produced through these two modes of chip formation mechanism was predicted and experimentally validated to reach up to three times.

In addition, the change in main process cutting forces, $F_x$ and $F_y$ have enormous effects on the loading conditions between the bearing pads and the thin walls. Although tight contact between the surfaces is deliberately promoted to enhance the drill's self-piloting capability, large reaction forces on the bearing pads induce elastic and plastic deformation on the thin walls through rolling contact, resulting in planar deviation of
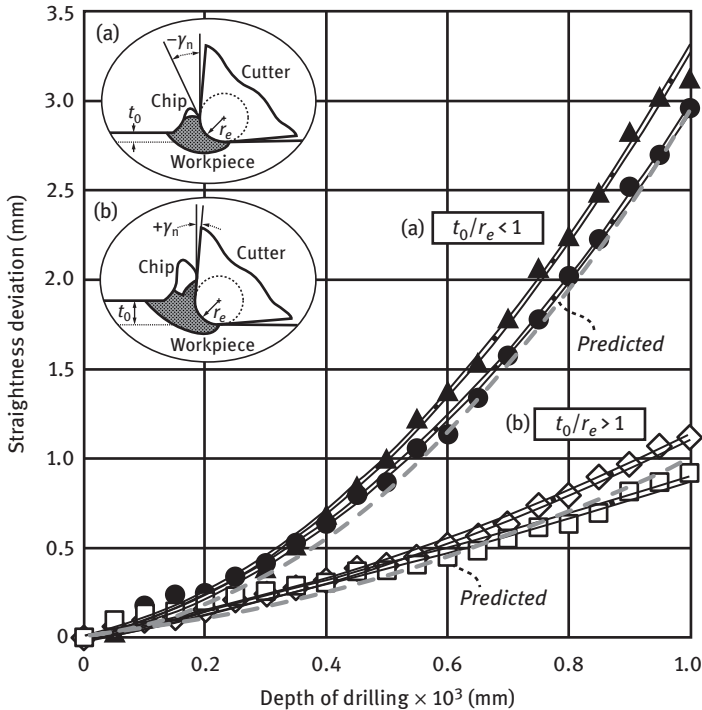
**Figure 2.13:** Comparisons between experimental and predicted hole straightness deviation results. (a) Thrust-dominated mechanism at $t_0/r_e < 1$ and (b) cutting-dominated mechanism at $t_0/r_e > 1$[1].

drill from the drilling axis toward the deformed wall. Such deformation is also thermally facilitated by the concentration of frictional heat on the thin wall as compared to the other half of the hole that has more uniform heat dissipation into the bulk materials.

## 2.4 Tool degradation

Drilling deep holes on Inconel 718 is challenging. Primarily, this class of materials is highly prone to work hardening [19]. When a layer of work material is cut from the surface, hardness of the subsequent layer is increased through subsurface deformation and thus higher cutting force is induced on the cutting edges for removing same amount of materials. Moreover, aggressive transfer of cutting heat to the gun drills is also evident [20] as the thermal conductivity of Ni-based materials is much lower than that of cemented carbide drill tips. Gun drills are thus subjected to intense cutting loads throughout the exhaustive process of drilling deep holes, both thermal and mechanical. As a result, cutting edges and bearing pads on gun drills degrade rapidly and often leads to catastrophic failures if such rapid tool degradation is not properly managed.

### 2.4.1 General wear

Under normal operating operations, tool wear is developed on seven parts of the drill as shown in Figure 2.14. Tool wear on the cutting edges is formed by erosion during cutting, whereas on the bearing pads it is mainly caused by the built-up edges. The built-up edges arise from the welding of the workpiece material onto the cutting edges due to extreme temperature generated from the rubbing and whipping actions of the drill. When chips grow bigger in size, they flow on the rake faces of both the inner and outer cutting edges continuously at different rates. The rate of chip flow changes according to the cutting speed reduction from the outer diameter to the centre of the drill. The flow of chip generates continuous mechanical abrasion to the rake faces due to highly abrasive particles in Inconel 718 and this leads to the increase in local temperature on the rake faces through frictional heating. Most of the heat is conducted into the carbide instead of being carried away by the chip. As a result, crater wear is developed on the rake faces.
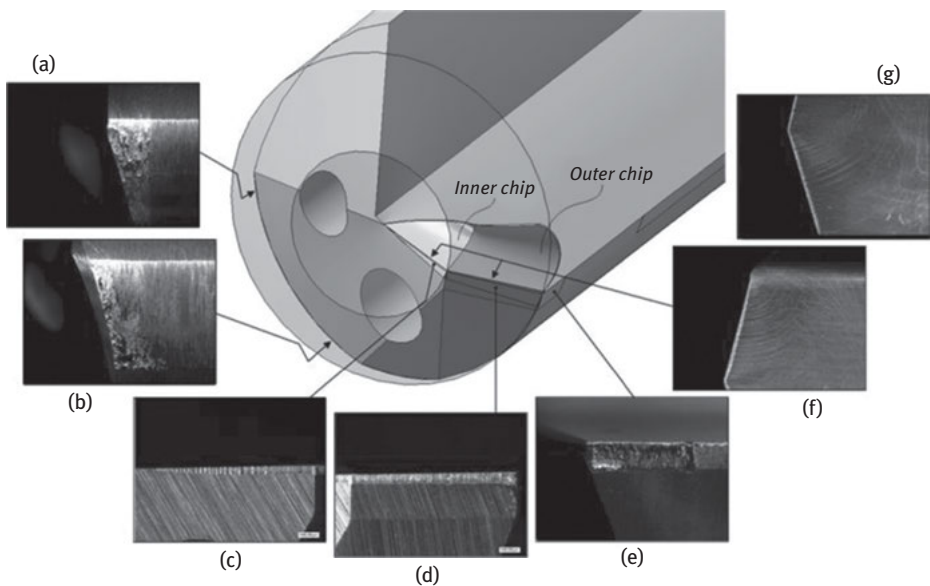


**Figure 2.14:** General wear on gun drills. (a) Upper bearing pad, (b) lower bearing pad, (c) inner flank face, (d) outer flank face, (e) side margin, (f) inner rake face and (g) outer rake face [21].

Moreover, tool wear on the flank faces of the cutting edges is developed simultaneously following constant adherence with the bottom of the hole. This is largely due to elastic recovery of the tough Inconel materials after a cut is made, despite the incorporation of relief angles. But further increase of the magnitude of relief angles may not be feasible to maintain the strength of the cutting edges. Thus,

wear development on the flank faces of both inner and outer cutting edges is inevitable.

As gun drilling cuts in an asymmetric configuration, the thrust and cutting force components deflect the drill tip toward the wall of the hole continuously in the radial direction. The deflecting mechanism is counterbalanced by the bearing pads and side margins. Thus, bearing pads are subjected to the resultant force in the opposite cutting direction when the drill tip is forced against the side wall of the hole and lead to severe frictional contact as the drill rotates continuously. As a consequence, significant adhesive and abrasive wear are developed on the bearing pads and side margin.

### 2.4.2 Thermal-mechanical damage

As chips are formed and flow continuously on the rake face, two types of damages are induced – thermal and mechanical. Initially, the rake face is abraded mechanically by flowing chips as Inconel materials contain hard particles that cause abrasive wear along the contact length. This is illustrated in Figure 2.15. Subsequently, significant amount of heat is generated through frictional sliding of continuous chip flow as well as plastic deformation during chip formation.

Most of the heat is transferred to the rake face as the thermal conductivity of cemented carbide is significantly higher than that of Inconel 718, often by at least four times. Due to this physical driving factor, temperatures on the rake face can exceed 1,000°C in some extreme cases depending on the speed of flowing chips. Moreover, high intensity of elastic recovery induces great localized compressive pressure on the rake face. Under such a high temperature and pressure condition, further thermal-mechanical damage due to adhesive wear is unavoidable.

### 2.4.3 Notching

Notching on flank faces as shown in Figure 2.16 is commonly encountered while drilling Inconel 718 due to excessive elastic recovery. This prevents cutting edges from shearing the chips cleanly, thereby leaving uncut material for the next cutting cycle while at the same time leading to the formation of such wear. The intensity of elastic recovery is governed by the yield strength of the nickel-based superalloy. When the yield strength $\sigma_y$ is high, the magnitude of elastic recovery $\alpha$ increases correspondingly:

$$\alpha = \frac{\sigma_y \cdot \varepsilon_p}{E}$$

where $\varepsilon_p$ is equivalent plastic strain and $E$ is the Young's modulus of the material.
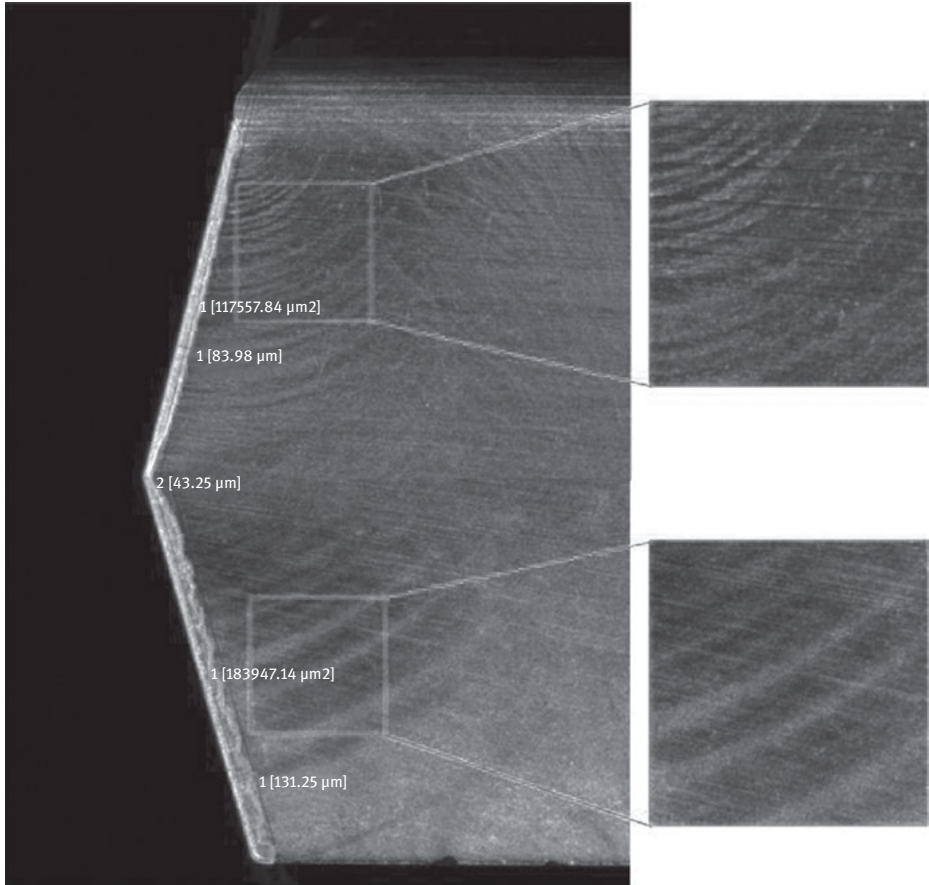
**Figure 2.15:** Crater wear on rake faces associated with abrasion and burnt marks [22].

Although the relative surface speed $V_f$ on the flank face is not as high as the rake face, the high compressive forces $F_n$ at the localized tool-work interface can lead to severe frictional sliding and thus frictional forces $F_f$. The frictional forces generate extreme heat flux $Q$ through rubbing and plowing actions on the flank face:

$$F_f = \mu . F_n$$

$$Q = \eta . F_f . V_f$$

where $\mu$ is the coefficient of friction and $\eta$ is the fraction of heat generation. With the heat resistivity of Inconel 718, significant heat is transferred on to the drill through conduction, and lead to random formation of built-up edges on the flank face. When
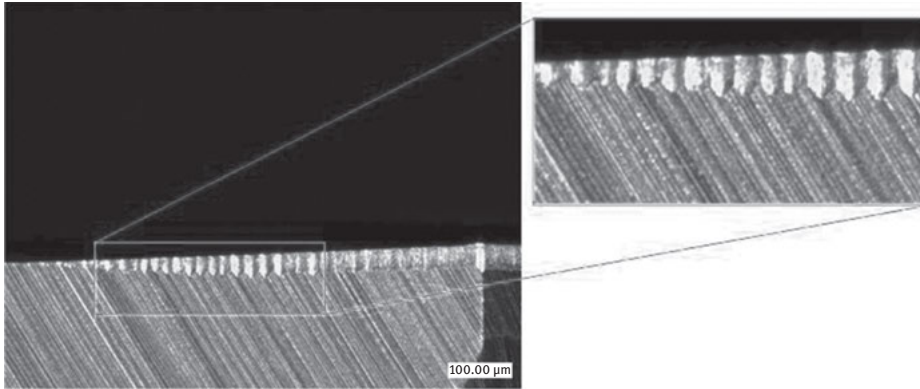
**Figure 2.16:** Notch damage on flank faces subsequent to cyclical abrasion and adhesive wear [21].

these built-up edges break down, notching on the flank face is formed. The volumetric loss of work material is given as follows [23]:

$$V = K_{adhesion}.e^{aT}.V_c.w.\sigma.\Delta t$$

where $K_{adhesion}$ is the adhesive wear constant for tool-workpiece combination, $a$ is the hardness constant, $T$ is the temperature, $V_c$ is the surface velocity over the flank face, $w$ is the width of cut, $\sigma$ is the average normal stress and $\Delta t$ is the time interval. The vicious wear mechanism is depicted in Figure 2.17.
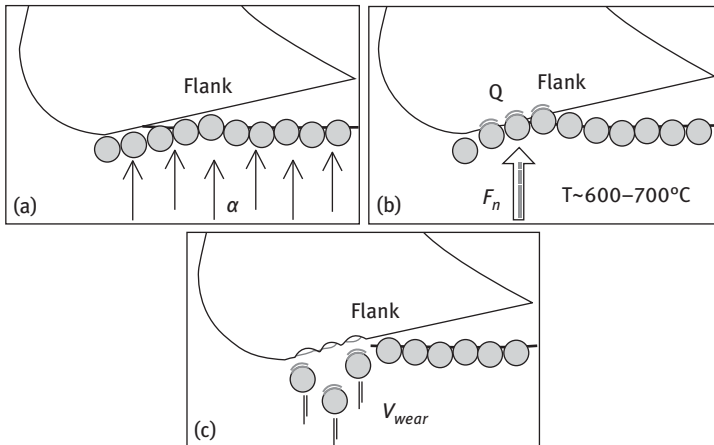


**Figure 2.17:** Formation of notch damage in the process. (a) Spring back of machined surface with an average magnitude $\alpha$, (b) localized temperature rise through frictional heating, leading to the formation of built-up edge and (c) collapse of built-up edge that forms notches [21].

### 2.4.4 Edge flaking

When chips are not broken effectively during the process, a unique mode of edge flaking on the rake face as shown in Figure 2.18, is constantly encountered. It concentrates at the intersection between the outer cutting edge and the side margin. The coverage of the flaking has the tendency to spread along the outer cutting edge in the direction toward the drill apex as well as expanding laterally across the outer rake face, being distant away from the outer cutting edge and deep into the V-channel.
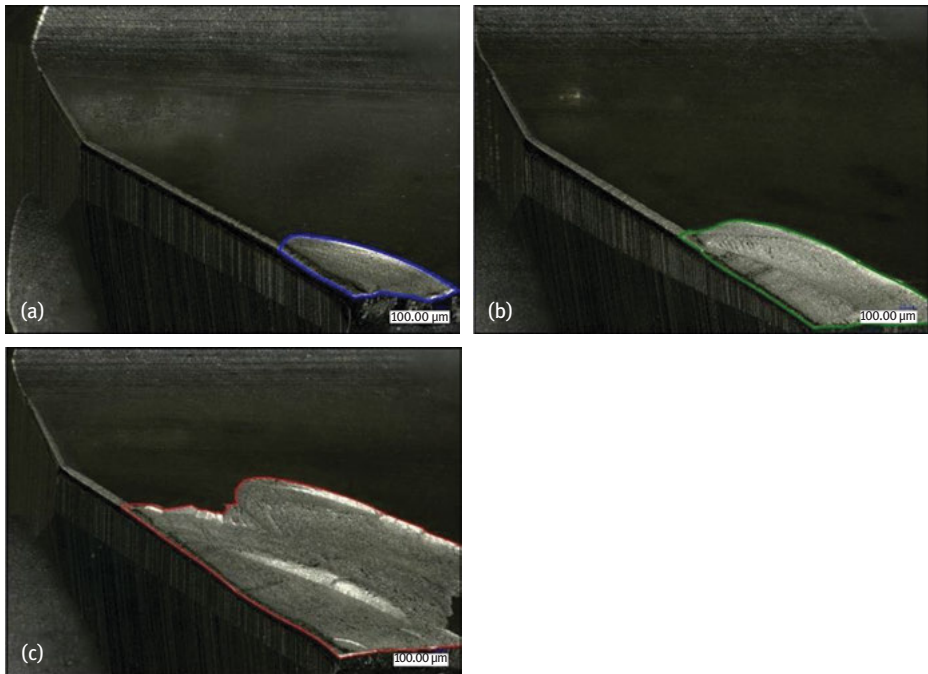


**Figure 2.18:** Concentration of flaking at the intersection between the outer cutting edge and the side margin in the initial stage (a) that expands across the rake face (b) through subsurface crack propagation till the cutting edge loses its entire cutting ability (c) [22].

During the process, the region of interest is subjected to much greater thermal and mechanical loading than other parts of the drill as frictional sliding of chip flow, strain rate during material shearing and cutting force increases correspondingly with cutting speed. Such a concentrated loading condition is validated via a finite element analysis as shown in Figure 2.19. The main driving factor is the high cutting speed at the outer diameter of the rotating drill. Along with dynamic whip and lateral shock of the drills, stress concentration sites such as minor defects on the cutting edges expand rapidly as long chips affect the coolant supply to the cutting edges and lead to rapid increase in
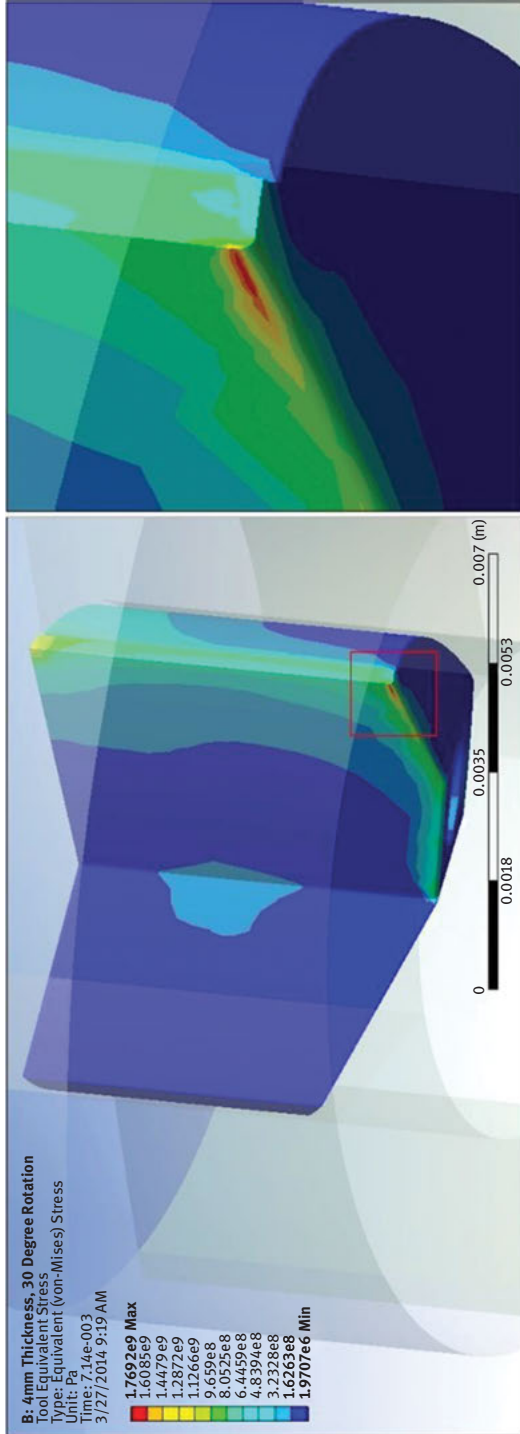
**Figure 2.19:** Concentration of stress between outer cutting edge and side margin.

temperature. Once the long chips are broken, coolant supply is resumed and the temperature drops immediately.

With such intense temperature change taking place continuously, cyclical thermal expansion and contraction on the stress concentration sites result, in the form of tensile and compressive stresses as shown in Figure 2.20(a). Through such a cyclical thermal loading, subsurface defects propagate from the outer cutting edge and side margin separately while spreading toward the vicinity regions on the rake face. As depicted in Figure 2.20(b), the advancing crack fronts from both directions would meet and merge with one another eventually, forming a network of subsurface crack that leads to massive flaking on the rake face. Continuous drilling with such a drill expands the damage across the rake face until the cutting edge loses its cutting ability entirely and the drill would then fail catastrophically.
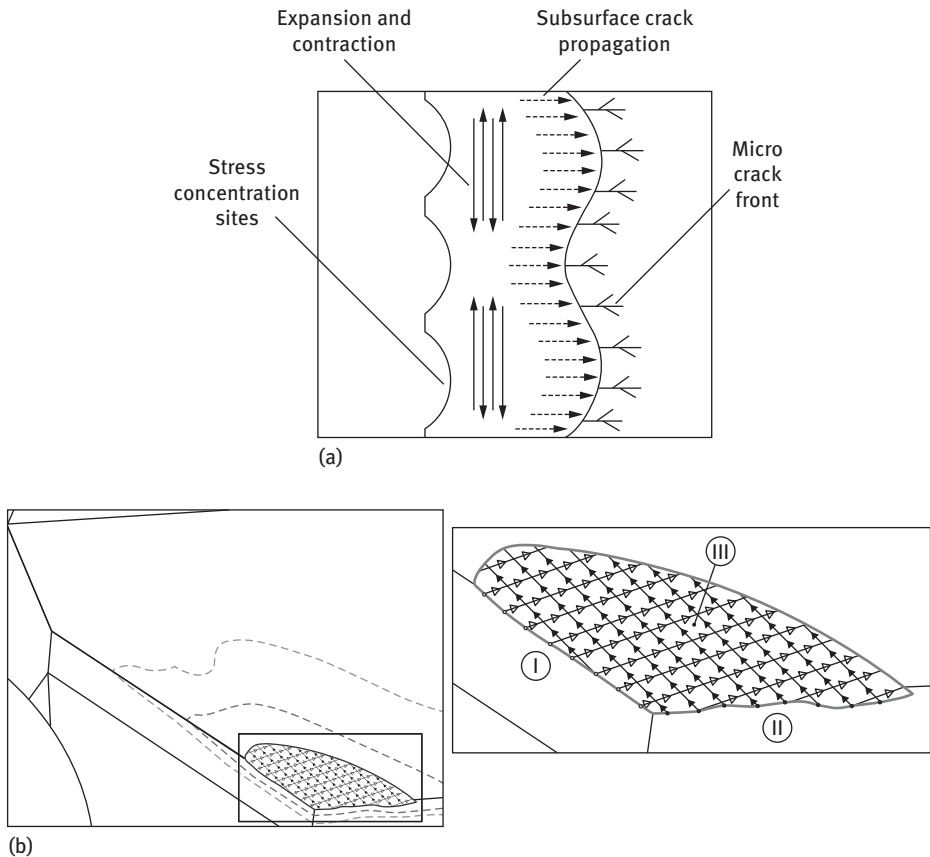


**Figure 2.20:** Mechanism of thermal fatigue failure. (a) Subsurface crack propagation from surface defects due to violent fluctuation in surface temperature and (b) formation of a large subsurface cracking network (III) that leads to catastrophic flaking through the merger of crack propagation from outer cutting edge (I) and side margin (II) [22].

## 2.5 Coolant application

It is obvious from the wear and failure of gun drills that successful implementation of the process relies on highly effective coolant application. Significant work on this regard has been previously reported [24–26]. Though coolant effectiveness is governed by its chemical and physical properties, the flow behaviour of coolant is determined by geometries of gun drill. This offers a convenient way to improve coolant effectiveness through strategic optimization of commercial drill designs. This section describes a case study based on computational fluid dynamics (CFD) where the effects of nose grind contour, coolant hole configuration and shoulder dub-off angle are studied. The scope is summarized in Figure 2.21.
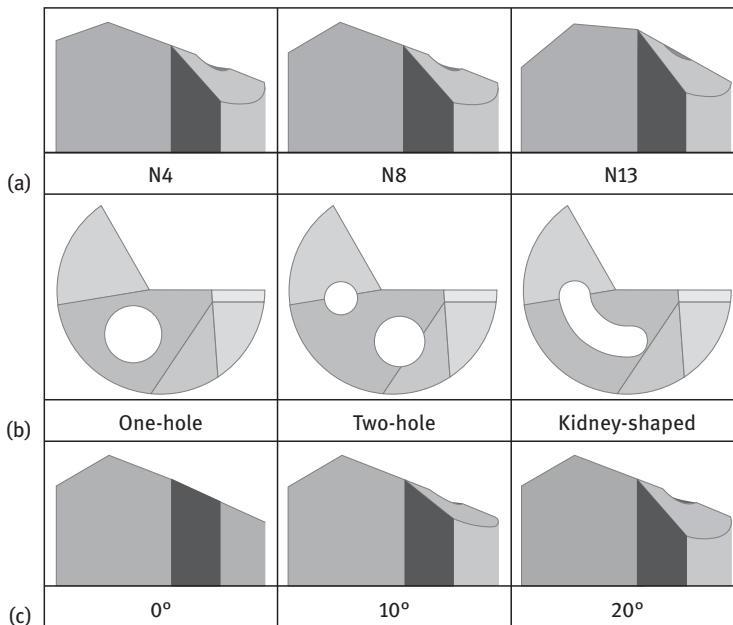


**Figure 2.21:** Scope of evaluation. (a) Nose grind contour, (b) coolant hole configuration and (c) shoulder dub-off angle [27].

### 2.5.1 Coolant transport passage

Coolant flow is a continuum. The change in drill geometries alters the fluid transport passage of the whole flow system and governs its conditions to flow. Every alteration made to the fluid transport passage changes the overall hydraulic resistance [28] of the system, a property that determines the efficiency in momentum and energy transfer of the flowing coolant as well as the amount of pressure loss in the process. This will determine the ultimate efficiency of coolant application at the

cutting zone in deep hole gun drilling. The coolant transport passage of gun drilling includes the bottom clearance, shoulder dub-off and V-channel as shown in Figure 2.22.
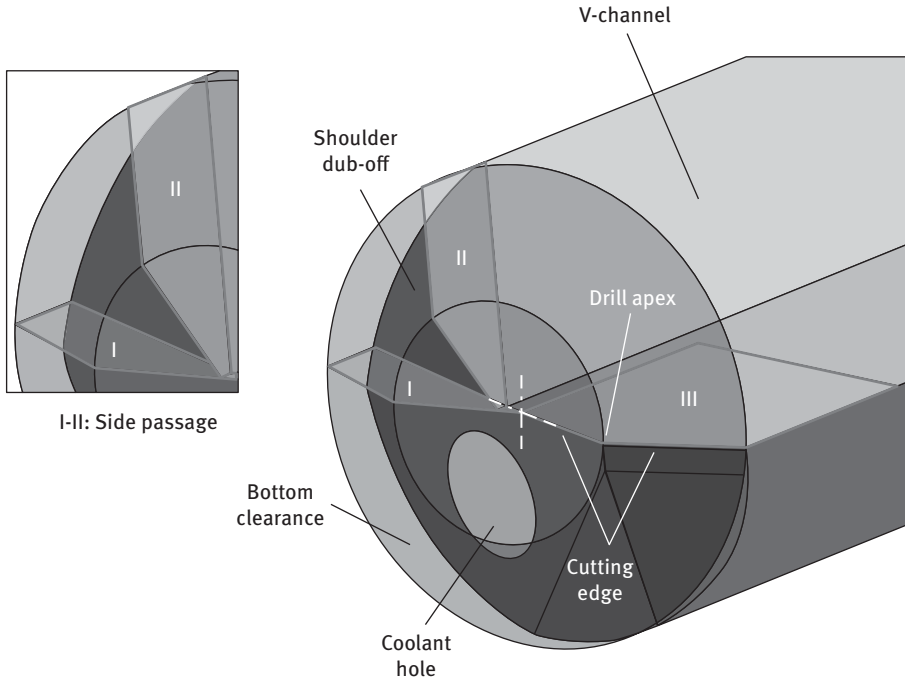


**Figure 2.22:** Coolant transport passage of a gun drilling process comprises bottom clearance, shoulder dub-off and V-channel for high-pressure coolant supply. I, II and III denote bottom clearance outlet, shoulder dub-off outlet and drill rake face, respectively. The side passage connects between the bottom clearance outlet I and shoulder dub-off outer II [27].

Deflection of coolant flow takes places within the conduit that connects between the bottom clearance outlet I and the shoulder dub-off outlet II, also known as the side passage. Its shape function is defined by the outer edge angle, inner edge angle, drill apex offset and shoulder dub-off angle. In other words, varying a single or combinations of these drill geometries will influence the directions of coolant flow. To some extreme extents, coolant flow can be completely deflected from the rake face of the gun drill – leading to the formation of stagnation zones over the cutting edges [29]. As a result, the affected drill degrades rapidly without sufficient cooling and lubrication and its ultimate tool life will be deeply impacted. The work done determined the flow efficiency in the side passage and the wetting quality on the rake face for different gun drill designs based on the distributions of hydraulic pressure over the bottom clearance outlet I, shoulder dub-off outlet II and drill rake face III.

### 2.5.2 Nose grind contour effects

Figure 2.23 shows the transitional pressure conditions on I, II and III for the three commercial nose grind contour designs investigated in this study. It is noticeable that N4 with the combinations of an outer edge angle $\phi_o$ of 20° and a slightly smaller inner edge angle $\phi_i$ of 15° is able to ensure minimum loss of hydraulic pressure on the rake face. On the contrary, N13 with a large $\phi_o$ of 40° and a relatively small $\phi_i$ of 5° deflects high-pressure coolant to the back of the cutting edges – resulting in great loss of hydraulic pressure in the vicinity of III. Such pressure loss is attributed to strong deflection of coolant streamline, due to the intense pressure build-up at I and sudden expansion of the transport passage leading to III. These observations indicate the importance of $\phi_i/\phi_o$ in regulating hydraulic pressure over the rake face. N4 has a $\phi_i/\phi_o$ of 0.75 to perform best, whereas N13 that suffers huge pressure loss has a $\phi_i/\phi_o$ of 0.13. Following this trend, the performance of N8 with a $\phi_i/\phi_o$ of 0.67 is found to be in between N4 and N13.
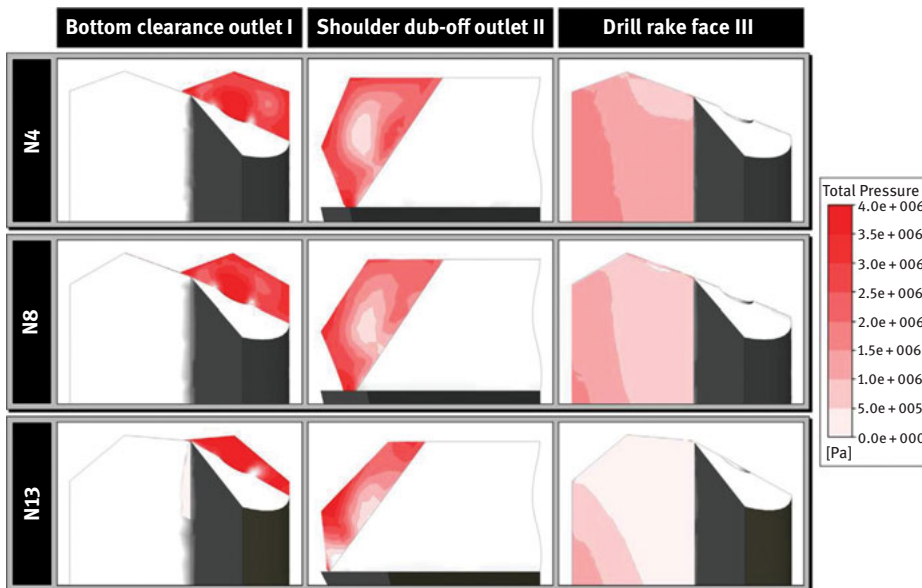


**Figure 2.23:** Hydraulic pressure analysis of commercial nose grind contour designs: N4 $\phi_o$=20°, $\phi_i$=15°, $A_p$=D/4; N8: $\phi_o$=30°, $\phi_i$=20°, $A_p$=D/4 and N13: $\phi_o$=40°, $\phi_i$=5°, $A_p$=D/4. Remarks: Outer edge angle $\phi_o$, inner edge angle $\phi_i$ and drill apex offset $A_p$ [27].

### 2.5.3 Coolant hole configuration effects

With efficient nose grind contour designs, gun drills have to be coupled with the correct coolant hole configurations to achieve better results. Of all commercial designs

available in the market, including the one-hole, two-hole and kidney-shaped configurations, the reason for using the latter is obvious. As shown in Figure 2.24, the kidney-shaped configuration that has the single largest orifice spanning across the face of the drill is capable in delivering high volume of coolant with good conservation of hydraulic pressure over the rake face. This is a good assurance to evacuate chips efficiently. Although the effective orifice area of the kidney-shaped and two-hole configurations is comparable, the difference in their performance is huge as the latter suffers significant pressure loss when the individual supply of coolant from the upper hole (smaller) and lower holes (bigger) is combined at the bottom clearance. The mixture of two streams of coolant with different flow properties such as pressure, volume and velocity would result in vortex formation at the bottom clearance that extends into the dub-off zone and then V-channel. Thus, the kidney-shaped configuration that delivers high volume of coolant supply with homogenous flow conditions, without the presence of vortexes in the transport passage has the best performance.
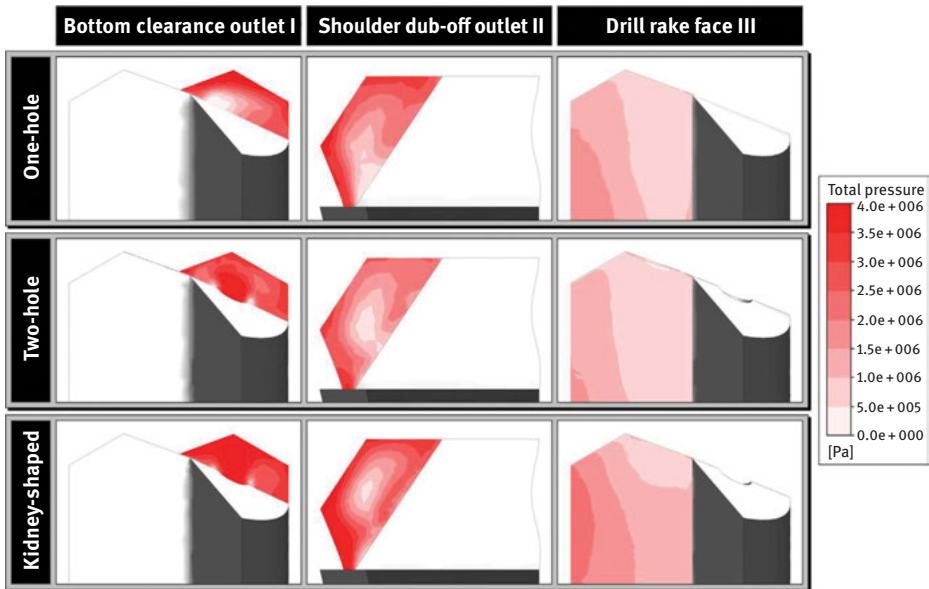


**Figure 2.24:** Hydraulic pressure analysis of coolant hole configurations: One-hole, two-hole and kidney-shaped [27].

### 2.5.4 Shoulder dub-off angle effects

The last critical geometry is the shoulder dub-off angle $\varphi_d$, one of the least understood gun drill geometries for effective coolant application, in which commercial gun drills are commonly shipped with a 20°, irrespective of the hole specifications, work

materials and finishing requirements. But such a large $\varphi_d$ can be a design error. As shown in Figure 2.25, the use of 20° deflects the highly pressurized coolant to the back of the cutting edges and causes the loss in hydraulic pressure on the rake face III. Such pressure loss can be traced back to the shoulder dub-off outlet II where a generous relief at 20° is unable to provide the required hydraulic resistance for the build-up of sufficient pressure. This is especially critical for deep penetration of coolant delivery into the cutting zone to evacuate chips and remove excessive heat from the rake faces. Such conditions can be immediately improved with smaller $\varphi_d$. At 0°–10°, the narrower transport passages can preserve more hydraulic pressure at II that affects the subsequent flushing on III at high pressure.
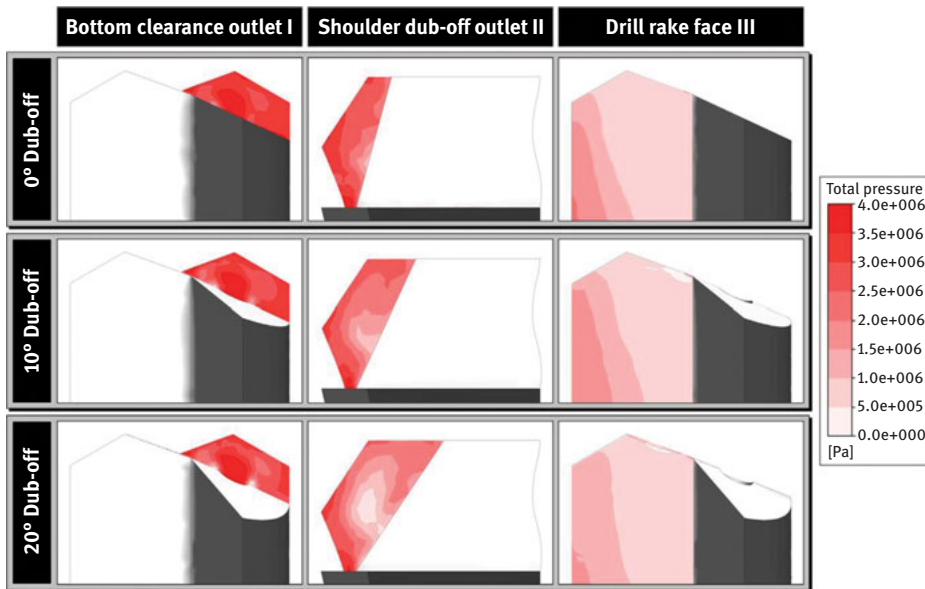


**Figure 2.25:** Hydraulic pressure analysis of shoulder dub-off angles: 0°, 10° and 20° [27].

### 2.5.5 Optimized design

An optimized drill design was proposed based on the CFD analyses in Sections 5.2–5.4. As shown in Figure 2.26, combining the N4/N8 nose grind contour, kidney-shaped coolant hole configuration and shoulder dub-off angle $\varphi_d$ of 0°–10°, one should achieve better results with the salient merits of each geometry. To compare its tool life performance with that of the commercial drill designs studied in this chapter, a drilling test on Inconel 718 was carried out. Every drill design was subjected to a total drilling of 50 mm in depth with each cycle of drilling fixed at 10 mm. After each drilling cycle, the flank wear *VB* induced by the process that defines tool life of the drills was measured. The results are summarized in Figure 2.27. It is noticeable that the ranking of
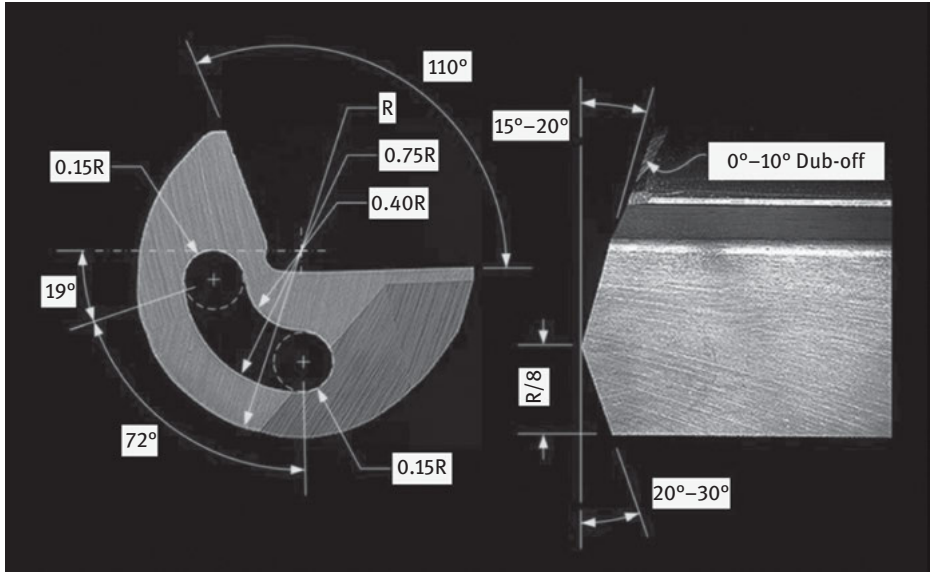
**Figure 2.26:** An optimized drill design for effective coolant application [27].
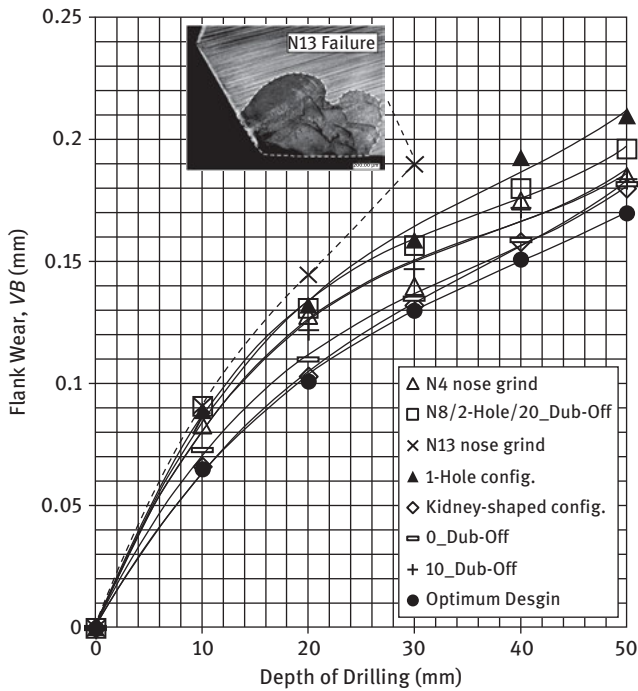


**Figure 2.27:** Tool life validation for different drill designs and features [27].

tool life performance shows apparent agreement with the present CFD analysis, with the N13 nose grind contour failed midway through the test.

## 2.6 Pilot hole drilling

To facilitate accurate drill penetration into workpieces, dedicated gun drilling machines are designed to house special bushes to prevent the "walking phenomenon" [30] and the subsequent "bell-mouth formation" [31] as the cutting edges are only in partial contact with the workpiece. But the guide-bush solution does not always warrant the drilling accuracy as expected, due to difficulty in controlling bush dimensions [31]. An alternative method involves the preparation of pilot holes [32] prior to the gun drilling process. With much larger cutting forces produced, the pilot-hole solution is more assuring while drilling Inconel materials. This section presents a systematic methodology to establish matching pilot holes that are compatible with varying gun drill designs. A process parameter known as "engagement ratio" is introduced to quantify the efficiency of tool-work engagement.

### 2.6.1 Engagement performance

Forces in gun drilling can be resolved into radial ($F_r$), cutting ($F_c$) and thrust ($F_t$) components. The process is stable when the resultant of cutting and radial force ($F_{rc}$) is balanced by the reaction forces ($F_{r1}$, $F_{r2}$ and $F_{r3}$) on the bearing pads. Refer to Figure 2.28(a). As the cutting edges are partially engaged in the early stages, sudden changes in $F_t$ deteriorate the engagement accuracy significantly and lead to cutting
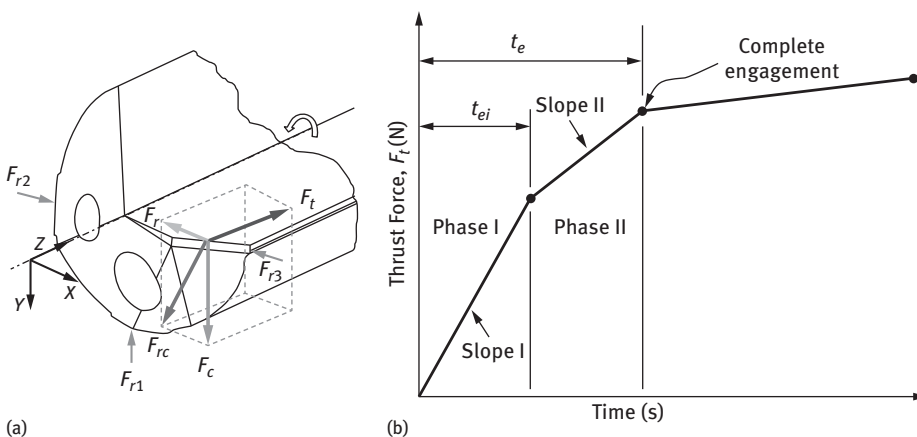


**Figure 2.28:** (a) Force system of gun drilling and (b) thrust force variation during engagement [33].

edge chipping. With this regard, the shape profile of pilot holes has a governing effect as well as the time required for complete engagement.

The engagement cycle is divided into two phases as shown in Figure 2.28(b). Phase I involves the start of drilling until one of the edges is engaged completely, whereas Phase II marks the completion of engagement where both cutting edges are completely engaged. The time required for different phases of engagement has significant influence on the rate of change in $F_t$, which is defined by Slope I and Slope II for Phase I and Phase II, respectively. Should one of the edges engage quickly with the workpiece, the sudden change in $F_t$ will damage the drills in the form of chipping.

To quantify engagement performance, the "engagement ratio" (ER) defined as the time required to complete Phase I, $t_{ei}$ over the total engagement time $t_e$ is used:

$$\text{Engagement ratio, } \text{ER} = \frac{t_{ei}}{t_{ei}}$$

The range of ER is between 0 and 1. This value describes the influence of thrust force $F_t$ on Slope I. When ER is almost 0, the cutting edge is engaged with the workpiece abruptly while the drill is delayed in completing the full engagement. Slope I is much more vertically inclined than Slope II. On the other hand, ER close to 1 indicates the time taken to complete Phase I and the total engagement time are almost equal. Both Slope I and Slope II are inclined at similar gradients, which indicates smooth and efficient engagement that is more preferred than otherwise.

### 2.6.2 Engagement time

ER is calculated based on the drill geometry and pilot hole profile combination. There is a total of four different possibilities, as shown in Figures 2.29–2.32 in Table 2.1. Gun drills are characterized with four geometries, including inner cutting edge angle $\varphi_i$, outer cutting edge angle $\varphi_o$, drill apex offset from center $\psi$ and drill radius $R$. While pilot holes are characterized with the angle of conical bottom $\theta$, the dotted lines indicate the final locations of the drills after traveling for $L_e$ to achieve complete engagement in Phase II. Phase I completes when drills travel from point "c" and reach point "r", Phase I is considered complete and the time required $t_{ei}$ is calculated using eqs. (2.1), (2.3), (2.5) and (2.7). For Case I, II and IV, the drills firstly engage with the workpiece on the drill apex; whereas for Case III, the outer most point makes the first contact.

### 2.6.3 A case study

A dedicated study was carried out on DMU 80P duoBLOCK® five axis machining center. A combination of four gun drill designs and three pilot hole profiles were

**Table 2.1:** Four cases of tool-work engagement [33].

| Graphical Representation of Case I to IV | Equations for engagement time |
|---|---|



**Figure 2.29:** Case I.
$l_i + l_c > l_o$ ; $L_e = l_i + l_c$

Case I: $l_i + l_c > l_o; L_e = l_i + l_c$
At the end of Phase I – Outer edge will be in complete contact

$$t_{ei} = \frac{l_o}{f} = \frac{\psi\left(tan\varphi_o - cot\frac{\theta}{2}\right)}{f} \qquad (2.1)$$

$$t_e = \frac{L_e}{f} = \frac{\psi\left(tan\varphi_i + cot\frac{\theta}{2}\right)}{f} \qquad (2.2)$$



**Figure 2.30:** Case II.
$l_i + l_c < l_o$ ; $L_e = l_o$

Case II: $l_i + l_c < l_o; L_e = l_o$
At the end of Phase I – Inner edge will be in complete contact

$$t_{ei} = \frac{l_i + l_c}{f} = \frac{\psi\left(tan\varphi_i + cot\frac{\theta}{2}\right)}{f} \qquad (2.3)$$

$$t_e = \frac{L_e}{f} = \frac{(R - \psi)\left(tan\varphi_o - cot\frac{\theta}{2}\right)}{f} \qquad (2.4)$$



**Figure 2.31:** Case III : $\frac{\theta}{2} > \varphi_o$; $L_e = l_i + l_c + l_o$

Case III: $\frac{\theta}{2} > \varphi_o$; $L_e = l_i + l_c + l_o$
At the end of Phase I – Outer edge will be in complete contact

$$t_{ei} = \frac{l_o}{f} = \frac{(R - \psi)\left(cot\frac{\theta}{2} - tan\varphi_o\right)}{f} \qquad (2.5)$$

$$t_e = \frac{\psi\left(tan\varphi_i + cot\frac{\theta}{2}\right) + (R - \psi)\left(cot\frac{\theta}{2} - tan\varphi_o\right)}{f}$$

$$(2.6)$$

*(continued)*

**Table 2.1:** (*continued*)

| Graphical Representation of Case I to IV | Equations for engagement time |
|---|---|
|  **Figure 2.32:** Case IV. $\theta = 180°$, $L_e = l_o$ | Case IV: $\theta = 180^o$ (Flat bottom pilot hole), $L_e = l_o$. At the end of Phase I – Inner edge will be in complete contact. $$t_{ei} = \frac{l_i}{f} = \frac{\psi tan\varphi_i}{f} \qquad (2.7)$$ $$t_e = \frac{L_e}{f} = \frac{(R - \psi)tan\varphi_o}{f} \qquad (2.8)$$ |



**Figure 2.33:** Combinations of various gun drill and pilot hole geometries [33].

tested. The feed rate (*f*) and the cutting speed were kept 8 m/min (0.010 mm/rev) and 20 mm/min respectively. A total of 12 distinct combinations were used during the experiments as shown in Figure 2.33.

Conical pilot holes C130 and C140 were drilled with self-centering twist drills with lip angles 130° and 140° respectively. The twist diameter *D* was 7.8 mm and pilot holes were drilled to the depth of 1.5D. The holes were then reamed to final diameter of 8 mm. End mills were used to machine four flat bottom pilot holes. The diameter and roundness values of the reamed holes were measured with coordinates-measuring machines (CMM) and found to be in the tolerance range of IT7 to eliminate the effects of pilot hole finishing on the engagement behavior. Cutting forces were acquired using Kistler Type 9257B multicomponent dynamometer, and vibrations were captured using accelerometer sensor Kistler Type 8762A50. Two repetitions were performed for each drilling condition. The mechanical properties of workpiece material are given in Table 2.2.

**Table 2.2:** Mechanical properties of Inconel 718 workpiece.

| Yield Point (MPa) | Tensile Strength (MPa) | Elongation (%) | Area Reduction (%) | Hardness (HRC) |
|---|---|---|---|---|
| 1,058 | 1,327.5 | 10 | 20 | 42 |

### 2.6.3.1 Slope I and Slope II

To calculate Slope I, the thrust force $F_t$ is plotted against time $t$. The time to complete Phase I $t_{ei}$ and II $t_e$ were calculated using eqs. (1)–(8). The magnitudes of thrust force at the completion of Phase I and Phase II are determined from the graph. The procedure is illustrated with the experimental condition C140-DB as shown in Figure 2.34. The same procedure is repeated for all of the remaining conditions. The results are summarized in Table 2.3.
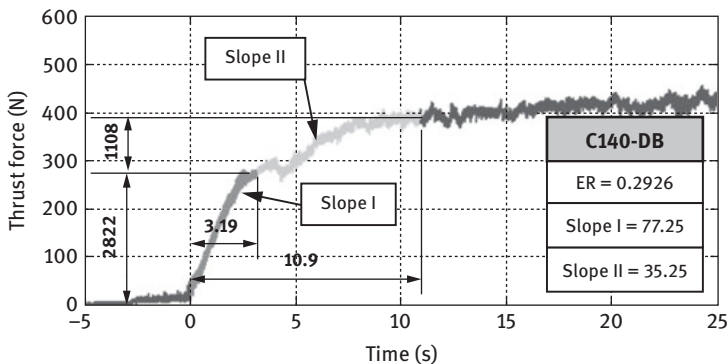


**Figure 2.34:** Calculation of Slope I and II based on thrust force characteristics [33].

**Table 2.3:** ER and Slope values for experimental conditions [33].

| Case No. | Experimental Condition | $t_{ei}$ | $t_e$ | ER | Slope I (°) | Slope II(°) |
|---|---|---|---|---|---|---|
| I | C140-DA | 0 | 9.5 | 0 | 90 | 52.05 |
| | C140-DB | 3.19 | 10.9 | 0.29 | 77.25 | 35.67 |
| | C140-DD | 2.13 | 5.40 | 0.39 | 80.60 | 69.42 |
| | C130-DB | 1.67 | 12.45 | 0.13 | 78.76 | 38.64 |
| | C130-DC | 5.6 | 8.3 | 0.67 | 68.78 | 37.12 |
| | C130-DD | 1.11 | 6.47 | 0.17 | 82 | 70.04 |
| II | C140-DC | 6.75 | 7.13 | 0.94 | 67.34 | 41.35 |
| III | C130-DA | 1.53 | 12.43 | 0.12 | 84.18 | 21.27 |
| IV | F-DA | 4.01 | 5.46 | 0.73 | 75.15 | 67.33 |
| | F-DB | 5.45 | 8.66 | 0.62 | 70.06 | 52.95 |
| | F-DC | 1.31 | 12.58 | 0.10 | 83.80 | 50 |
| | F-DD | 1.76 | 11.54 | 0.15 | 78.11 | 54.23 |

### 2.6.3.2 Engagement performance

The effects of pilot hole profile on Slope I and drill conditions are summarized in Figure 2.35. When drill DC is used with a flat pilot hole (F-DC), the inner edge engages with the workpiece rapidly (ER= 0.1) and leads to a sudden spike in thrust force on the inner edge. The inner edge is thus damaged under the high value Slope I of 83.8. Whereas, the same drill geometry when used with the conical pilot hole profile (C140-DC), both edges are engaged gradually (ER=0.94) with relatively less drastic changes in thrust force (Slope I= 67.34). Therefore, both cutting edges are preserved unlike the case of C140-DC.
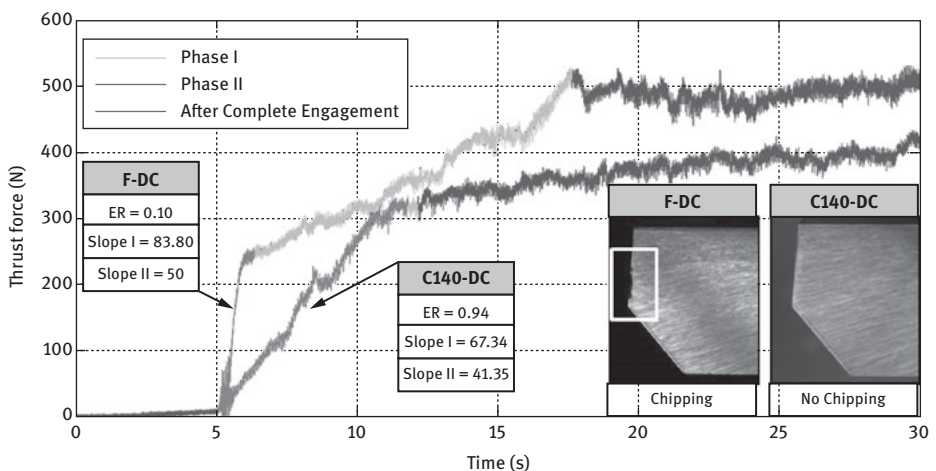


**Figure 2.35:** A sample effect of pilot hole geometry on engagement performance [33].

In general, when ER< 0.4, edge chipping is severe. However, when ER> 0.6, uniform wear is observed along both the cutting edges due to more gentle and stable engagement. The study shows that drills with inner angle less than 10° are susceptible to chipping when flat bottom pilot holes are used. Other drills with greater inner angles have stable engagement with flat pilot hole. The range for good engagement while drilling Inconel 718 is 0.6 < ER < 1. These findings are summarized in Figure 2.36. This shows that ER is a simple and effective indicator for tool-work engagement performance. In summary, conical bottom hole is recommended for gun drills with inner cutting edge angles less than 10°, whereas flat bottom is recommended for all other drill designs.
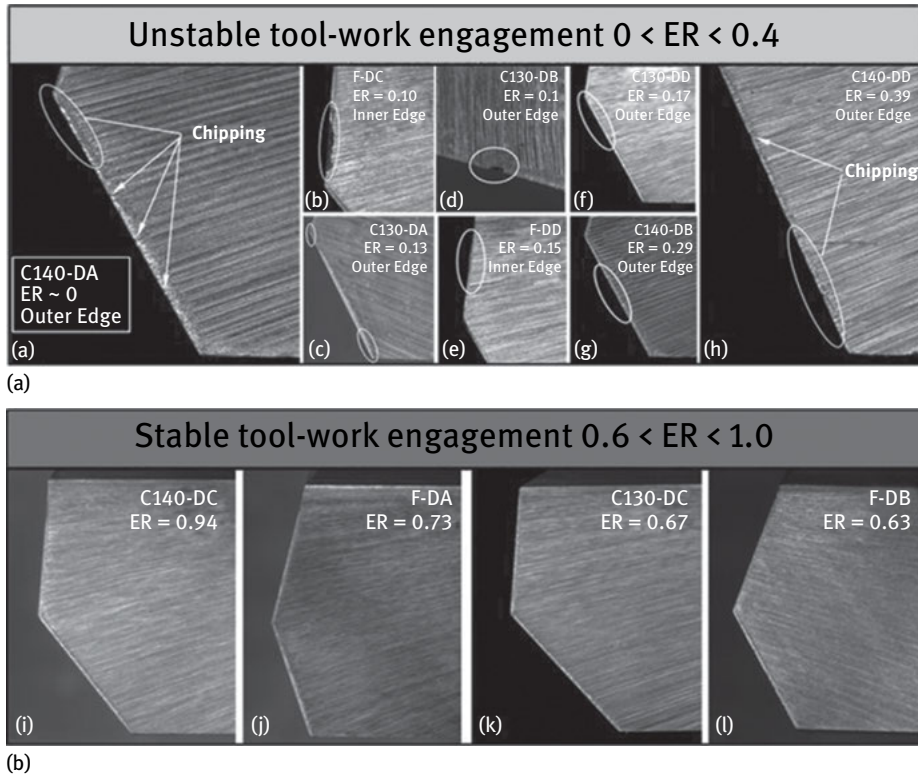


**Figure 2.36:** Effect of engagement ratio on tool edge chipping (a) Unstable Engagement and severe chipping on cutting edge for 0 < ER < 0.4 and (b) smooth engagement and uniform wear along cutting edge engagement for 0.6 < ER < 1 [33].

## 2.7  Gun drill re-sharpening

Despite the importance of tool geometry [34], workpiece geometry [35] and drill stem support [36], the capability to re-sharpen gun drills with high levels of accuracy and

consistency is a critical prerequisite to produce a straight hole. However, this is hardly achievable by industrial practitioners who are commonly equipped with primitive and highly skill-dependent grinding apparatus. Currently, a worn out gun drill is manually re-sharpened using a traditional manual grinder and the cutting angles are checked with glass magnifiers and vernier calipers. As such less competent operators in terms of skills and experience are unable to reproduce gun drill geometries accurately and repeatedly. This contributes to the deterioration in hole straightness accuracy.

### 2.7.1 Manual grinding

For the drilling of deep holes on Inconel 718, maximum drilling depths are typically fixed around 50 mm as the drilling efficiency reduces constantly with the development of wear on the cutting edges and bearing pads. By the end of every drilling cycle, the drills are retrieved from the partially drilled hole, dismounted from the machine and then re-sharpened manually by the operator with a manual grinding machine.

The drill re-sharpening process relies on a dedicated three-axis gun drill fixture. The fixture is integrated with a universal tool grinder with a single-speed work spindle and fixed grinding axis. Cup-type, vitrified diamond grinding wheel is used for material removal with the intention to maintain the uniformity of cutting edges. Gun drills are then mounted on fixture with the security of the carbide tip on a V-clamp and the drill stem is supported with an extended balancing rest.

Drill geometries to be reground in sequence are the primary relief, secondary relief, inner relief, oil clearance, front clearance and lead-in chamfer. Each geometry is generated through manual manipulation of the swing-, tilt- and twist-axis to yield the right combination of compound angles. After the main axes are set, gun drills are then fed into the rotating grinding wheel to remove damaged areas on different parts of the drills. By the end of the six-step re-sharpening cycle, fresh cutting edges and geometries are reproduced.

### 2.7.2 Re-sharpening accuracy

When multiple passes of drilling are performed on Inconel materials, the resultant hole straightness is governed by the re-sharpening consistency of the nose grind that defines the drill apex and cutting edges. To keep the holes straight along the drill path, the drilling process has to be steadily balanced between chip formation on the cutting edges and burnishing on the bearing pads. Therefore, the control of accurate drill geometries with high level of repeatability in each cycle of the exhaustive deep hole drilling operation is of practical significance. But conventional gun drill re-sharpening is incapable to realize the stringent requirements through manual grinding.

Deviation of nose grind geometries for re-sharpened drills and new drills alongside with the cumulative deviation of each geometry from the idealistic design values are shown in Figure 2.37. In general, manufacturing of new drills with high-precision computer numerical control (CNC) tool grinder is able to ensure high levels of accuracy as compare to the re-sharpened drills. The standard deviation of outer cutting angle, inner approach angle and drill apex offset are 0.36°, 0.09° and 23.9 μm for the new drills compared to 0.54°, 0.37° and 45.6 μm for the re-sharpened drills. Combining the geometric errors of new drills and re-sharpened drills yield cumulative standard deviation of 0.57°, 0.42° and 39.9 μm for the three critical geometries as tabulated in Table 2.2. The maximum difference in drill apex offset is 169.2 μm, approximately 8.8% of the mean value of 1,932.9 μm. Such re-sharpening inaccuracy causes premature tool failure and result in undesirable drilling results.
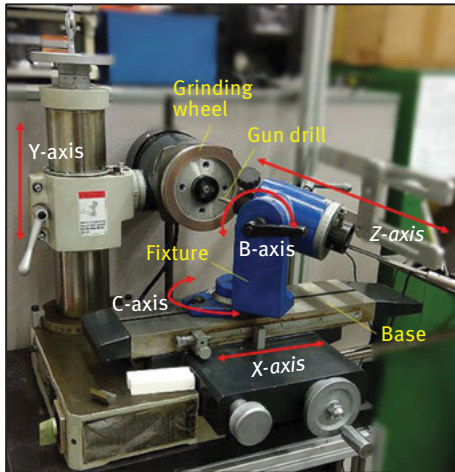


**Figure 2.37:** Machine axes for clearance generation.

### 2.7.3 Tool failure

As gun drills are asymmetric, the thrust and cutting forces deflect the drill tips into the radial direction. Such deflection is supposedly counterbalanced by the bearing pads and side margin to enable the self-guiding action if the nose grinding is accurate. The self-guiding efficiency of gun drills deteriorate, leading to an unstable process where the intended drilling path could no longer be maintained in the successive drilling cycles. Under such undesirable conditions, two modes of tool failure are swiftly developed based on the re-sharpened profiles:

*Type-1:* larger inclusive angles, longer cutting lands and drill apex shifts
*Type-2:* smaller inclusive angles, shorter cutting lands and drill apex shifts.

As shown in Figure 2.38, the drill apex of Type-1 re-sharpened drill tip is sharper but weaker with a smaller apex inclusive angle, $\theta$. With the shift in drill apex, the tip is deflected from the original drilling direction as it is engaged with the preceding hole profile of different shapes. The apex point is damaged prematurely with a small $\theta$ as the tip deflects and results in whipping and chattering. Significant damage on the bearing pad results when the tip is subjected to extra vibratory loads in the radial direction.
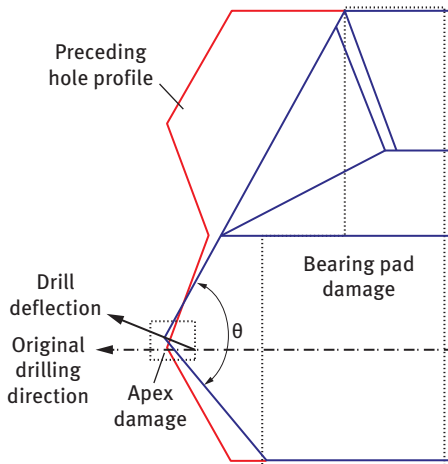


**Figure 2.38:** (a) Side view and (b) isometric view.

In contrast, Type-2 re-sharpened profile is blunter and stronger owing to the larger apex inclusive angle as shown in Figure 2.39. The tip is deflected from the original drilling direction when it is engaged with the preceding hole profile as the consequence of drill apex shift. The stability of the revolving drill tip is severely compromised largely due to imbalance cutting between the inner and outer edges. The inner cutting edge is more prone to chipping as its strength is lower than the outer cutting edge due to a larger relief angle. Once the inner edge is damaged, the process becomes even more unstable, leading to greater whipping and chattering that is detrimental to the side margin. Cracks are ultimately formed at the margin, propagate to the rake face of the outer cutting edge that is already subjected to intense imbalanced cutting load and resulted in catastrophic flaking.

### 2.7.4 Clearance regeneration

Five operational axes are used to re-sharpen gun drill on universal tool grinders. They include the Z-, C-, B-, X- and Y-axis as shown in Figure 2.37. The three main axes that govern gun drill geometries are the Z-, C- and B-axis where the depth of cut clearance

Preceding
hole profile

Edge
chipping

Original
drilling
direction

$\theta$

Drill
deflection

Margin wear
& flaking
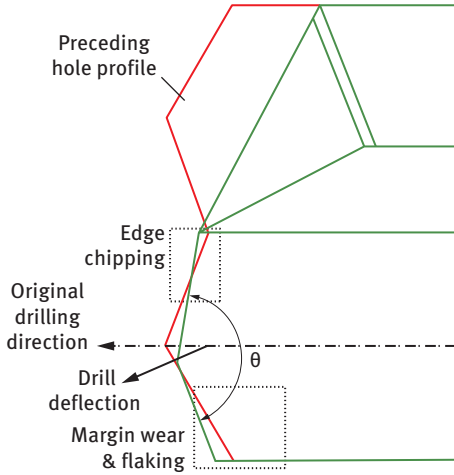
**Figure 2.39:** (a) Illustration of a 2.8-m gun drill for high aspect ratio drilling on Inconel 718 and (b) limited working space of a standard drag finishing machine.

$h_i$, the outer $\phi_o$ and inner $\phi_i$ cutting edge angle and the clearance angle $\alpha_{ni}$ are respectively controlled. The Y-axis is used to position and level the grinding wheel vertically with the tip of a gun drill, whereas the X-axis shifts the drill fixture to align the gun drill tips with the grinding wheel in the horizontal plane. During the grinding process, the X-axis is oscillated manually to prevent the drill from burnishing. The most critical task in drill re-sharpening is the regeneration of four clearances on gun drills that governs the tool life of gun drills. The process is described as follows:

Refer to Figure 2.40, it starts off with the regeneration of the secondary clearance. The drill fixture is brought to the height $Y_1$ expressed as follows:

$$Y_1 = \{(m_d \times tan\ \varphi_1) + L + H_C\} \times cos\ \varphi_1 \times sin\ \alpha_{n1-s}$$

where $H_C$ is the distance between the swing center and tilt center of Z-axis, which is manipulated according to the following equation:

$$h_1 = h_o x\ cos(\alpha_{n1-s})\ and\ h_o = a_{ri} or\ a_{mi} + 0.1$$

where $h_1$ is the secondary clearance ground off length, $\alpha_{n1-s}$ is the secondary clearance angle, $h_o$ is the total rake wear, $a_{ri}$ is the length of wear or flaking, $a_{mi}$ is the length of margin wear and 0.1 mm is the additional cutting depth to remove micro chipping.

Therefore, advancement of the gun drill fixture in the Z-axis is as follows:

$$h_{f1} = h_1 + [L - \{(m_d \times tan\varphi_1 + L) \times cos\varphi_1\}] + \{LL\ \times cos\varphi_1 \times (1 - cos\alpha_{n1-s})\}$$

where $h_{f1}$ is the Z-axis movement value for secondary clearance, $L$ is the distance from swing center to drill point, $m_d$ is the apex drill point and $\varphi_1$ is the outer angle
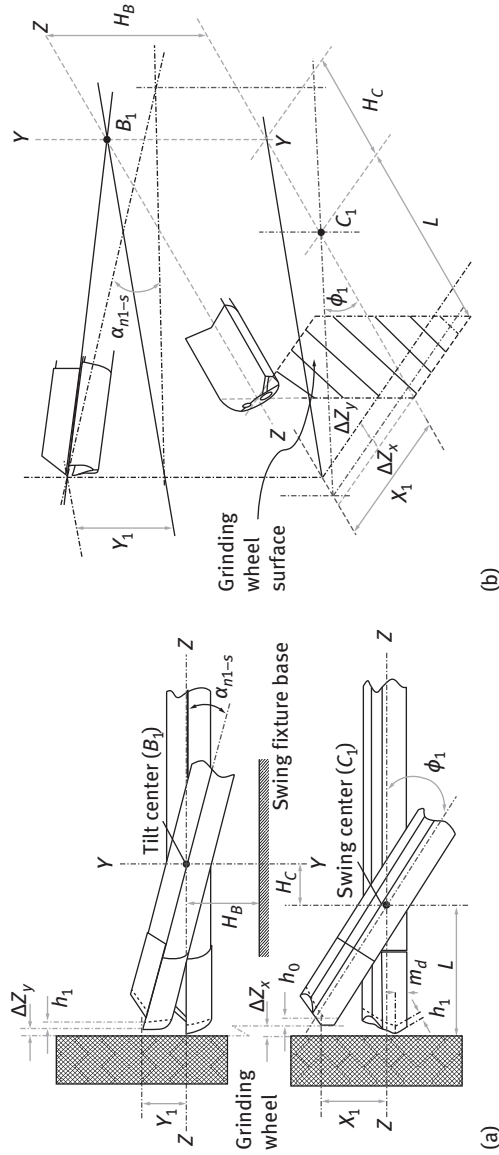
**Figure 2.40:** (a) Side view and (b) isometric view.

Following this, the *inner clearance* is approached with the Z-axis as follows:

$$h_3 = (h_1 + h_2) \times (cos\varphi_2/cos\varphi_1) \times cos\,\alpha_{n1-I} \text{ and } h_2 = 0.2 \times tan(\alpha_{n1-p})$$

where $h_3$ is the inner clearance ground off length, $\varphi_2$ is the inner angle, $\alpha_{n1-i}$ is the inner clearance angle, $h_2$ *is the primary clearance ground off length* and $\alpha_{n1-p}$ is the primary clearance angle.

Therefore, the total Z-axis movement of the drill fixture is as follows:

$$h_{f3} = h_3 + \Delta Z_{x3} + \Delta Z_{y3}$$

with $\Delta Z_{x3} = [\{(m_d \text{ x } tan\,\varphi_1 + L) \text{ x } cos\,\varphi_1\} - \{(a_{r1} + 0.1) \text{ x } cos\,\alpha_{n1-s}\}] - [\{L - (m_d \text{ x } tan\,\varphi_2)\} \text{ x } cos\,\varphi_2]$

and

$$\Delta Z_{y3} = [\{L - (m_d \times tan\,\varphi_1)\} \times cos\,\varphi_2] \times (1 - cos\,\alpha_{n1-i})$$

where $h_{f3}$ is the Z-axis movement value for inner clearance, $\Delta Z_{x3}$ is the distance between the cutting edge and the grinding wheel and $\Delta Z_{y3}$ is the distance between the clearance face and the grinding wheel

To regrind the *shoulder dub-off*, the Z-axis movement is as follows:

$$h_{f4} = \Delta Z_{x4} + \Delta Z_{y4}$$

with $\Delta Z_{x4} = \{(D/2)/cos\,\varphi_2\} \times sin(\varphi_3 - \varphi_2)$

and

$$\Delta Z_{y4} = [\{(D/2) \times cos30/cos\alpha_{n1-d}\} \times sin(\alpha_4 + \alpha_{n1-d})] \times cos\,\varphi_3$$

where $\alpha_{n1-d}$ is the shoulder dub-off angle

The last step realizes the *front clearance with the* Z-axis movement:

$$h_{f5} = \{L + H_C - (h_2/cos\varphi_1)\} \times (1 - cos\alpha_{n1-f})$$

where $h_{f5}$ is the Z-axis movement value for front clearance and $\alpha_{n1-f}$ is the front relief angle.

## 2.8 Cutting edge preparation

To deliver respectable gun drilling results and productivity on Inconel 718, the integrity of both cutting edges on a gun drill must be consistently restored to uphold the stability

of the drilling process. However, the control of cutting edge integrity via drill re-sharpening is challenging as the re-sharpening process is intended to reproduce drill geometries and cutting angles. Therefore, a dedicated process to prepare cutting edges of gun drills is needed and can be adapted from existing shop-floor activities such as deburring, surface finishing and precision shaping. Mechanical-based processes such as drag finishing, abrasive jet machining, abrasive flow machining and those using abrasive tools are among the most popular in the industry.

## 2.8.1 Problems with mechanical-based processes

Many constraints are preventing existing mechanical-based processes from being implemented on long gun drills. Primarily, limited working space. As majority of the processes were designed to carry out finishing on small parts and components, the effective working space on the machine tools is unable to accommodate the extreme lengths of gun drills that could reach beyond 2 m as shown in Figure 2.41. Typical working space of popular mechanical-based processes such as drag finishing is only between 300 and 400 mm and therefore it is unable to cater for the extreme lengths of gun drills.



(a)                                      (b)
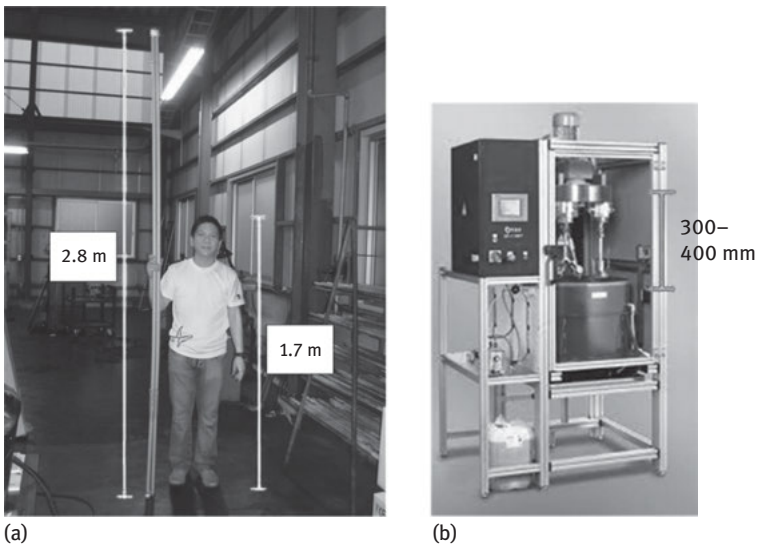
**Figure 2.41:** (a) Illustration of a 2.8-m gun drill for high aspect ratio drilling on Inconel 718 and (b) limited working space of a standard drag finishing machine.

Among the mechanical-based processes, water jet machining is a sound alternative. With controllable high-pressure water jet, precision material removal can be achieved through erosion without generation of heat. High temperature will lead to

the formation of thermally stressed layers on the cutting edges, which is highly detrimental to the sustainability of the drills during the process. However, the implementation of this process is not economical as a complimentary process. First, the footprint of standard water jet machines is large as it is primarily used for large parts made of temperature-sensitive materials, usually aerospace applications. Second, a multi-axis nozzle system is required to generate fine contours on the intricate surfaces of the cutting edges.

### 2.8.2 Common abrasive tools

As a complimentary process, ideal implementation of cutting edge preparation has to be direct, productive and without the need of further post-processing to maintain its cost-effectiveness. Techniques that involve the use of abrasive tools could fulfill such criteria with no special equipment required and the processing time is usually short, that is, within seconds. Only reasonable accuracy of the translational motion and rotational speeds should be provided.

All the abovementioned techniques using abrasive tools are more feasible than other processes to be deployed in the production floor to overcome the constraint of drill lengths during cutting edge preparation. A feasibility study performed using the most commonly available abrasive tools, namely diamond filament wheels (#400-finest) and silicon carbide flaps wheels (#320-finest). The former has diamond abrasives embedded to nylon filaments that forms a brush, whereas the latter is essentially sandpapers carved, arranged and bound into a wheel, as shown in Figure 2.42.



(a)                                      (b)
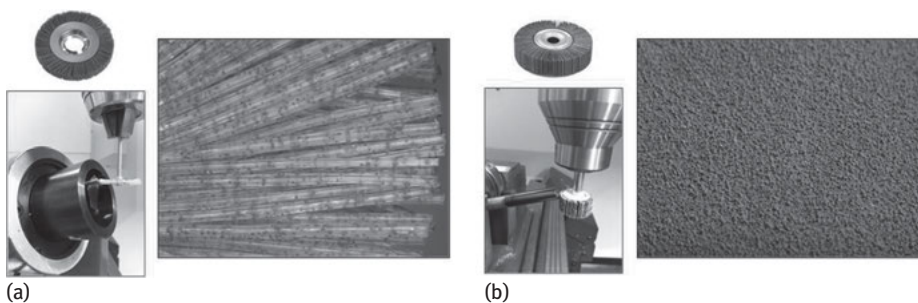
**Figure 2.42:** Feasibility study of cutting edge preparation on gun drills with common abrasive tools. (a) Diamond filament wheels and (b) silicon carbide slap wheels.

From our experimental study, it was found that deep chipping on the cutting edges are unable to be removed with the use of diamond filament wheels. As a result, the
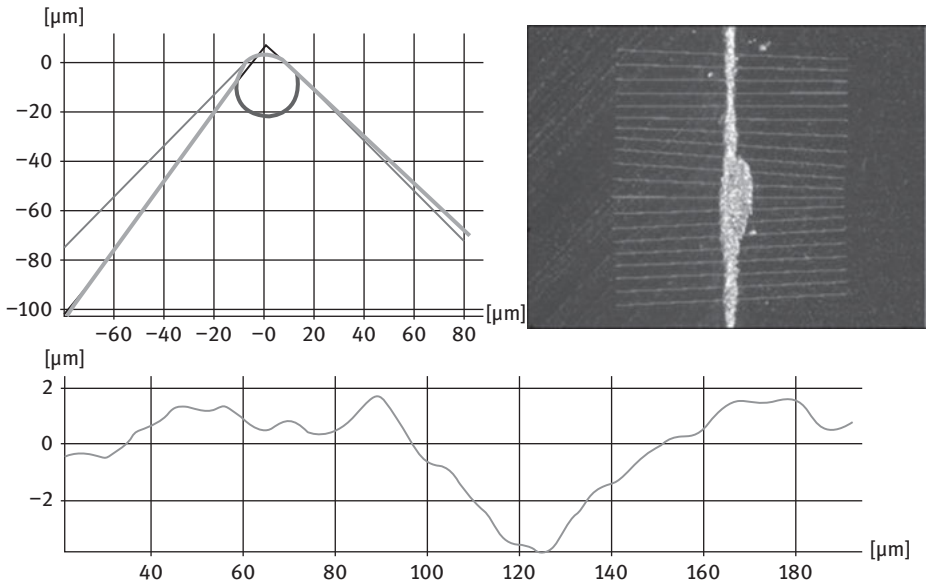
**Figure 2.43:** Inability to remove deep chipping using diamond filament wheel that leads to large $R_z$.

resultant $R_z$ is enomoursly large – up to 2.9 µm for the sample shown in Figure 2.43. This is the most serious drawback of diamond filament wheels, largely due to lack in abrasive density and rigidity of the nylon filaments. Moreover, performance of this tool in edge radii regeneration is also not stable, ranging between 7 and 12 µm among 6 cutting edges using the identical setup and conditions.

On the other hand, the edge roughness produced with the use of silicon carbide flap wheels was not consistent, ranging between 0.3 and 0.7 µm among six cutting edges. However, the inability to regenerate symmetrical cutting edges, between the rake and flank faces is the most critical weakness of this type of abrasive tools as shown in Figure 2.44. This is largely because of the one-sided abrasive surface of the flap
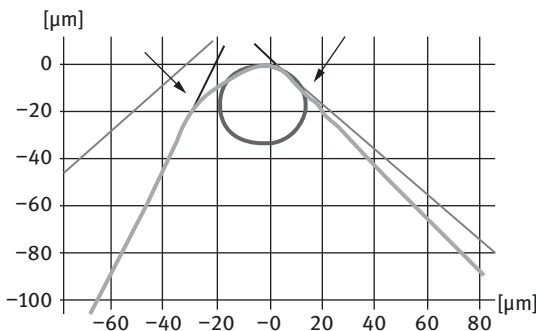


**Figure 2.44:** Generation of asymmetrical cutting edges with silicon carbide flap wheels.

wheels. To finish the edges symmetrically, the drills have to be dismounted and repositioned. Once the drills are released from the initial clamping, it will be impossible to relocate the reference points on the cutting edges.

### 2.8.3 Soft grinding wheel

To achieve desirable results, fine material removal is performed in a stable, controlled and defined manner to restore specified edge geometry, topography and finishing. One unique type of soft grinding wheels made of nonwoven nylon fabric coated with alumina oxide abrasives by polyurethane resin as shown in Figure 2.45 is found to be highly effective. These wheels are used mainly for light surface modification such as minor deburring and plastic modeling. A wide range of grit size is commercially available, from 240, 320, 400, 600, 800, 1,000 to 1,500. Coupled with suitable process parameters, the results are very encouraging.
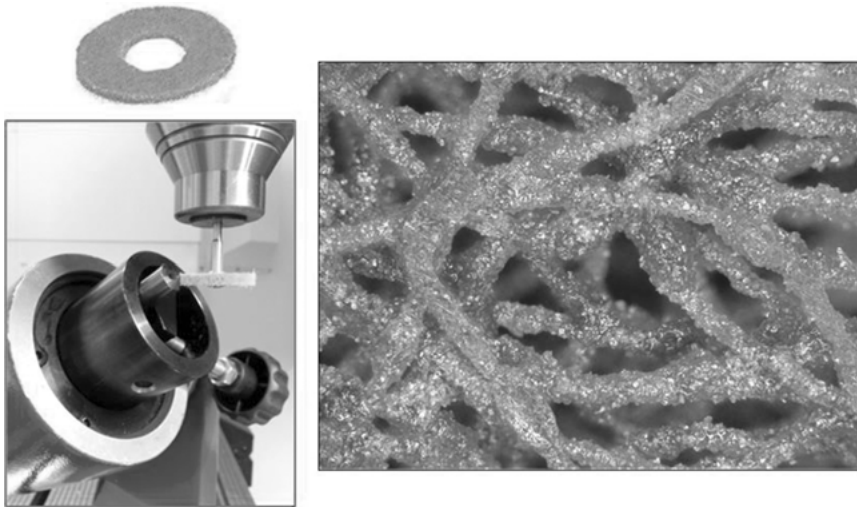


**Figure 2.45:** Experimental setup of cutting edge preparation using soft grinding wheel (left) and cross-sectional view of the soft grinding wheel at X200 magnification (right).

Refer to Figure 2.46, the procedure in using soft grinding wheels is described as follows:
1. Select grit size of the grinding wheels based on drill re-sharpening condition, depth of drilling and the work material being drilled.
2. To start off with the preparation of the outer cutting edge with an angle of $\phi_o$, mount and align the grinding wheel to form a three-dimensional orthogonal

configuration relative to the outer cutting edge. The distance between the wheel and the edge is kept at 100μm.

3. Program clockwise (*cw*) rotational speed, feed rate *f*, depth of cut *DOC* based on drill re-sharpening condition, depth of drilling and the work material being drilled.
4. Perform grinding on the rake face by feeding the wheel toward the outer cutting edge at *f*, with *cw* wheel rotation at $+\omega$.
5. After the wheel has traveled up till *DOC*, it is hold for *t* seconds.
6. The wheel is then retracted at $-f$ with continuous rotation at $+\omega$ to the starting position, following the opposite direction of the feeding path.
7. Program counter clockwise (*ccw*) rotational speed $-\omega$, feed rate *f*, cutting depth *DOC* based on drill re-sharpening condition, depth of drilling and the work material being drilled.
8. Perform grinding on the flank face by feeding the wheel toward the outer cutting edge at *f*, with *ccw* wheel rotation at $-\omega$.
9. After the wheel has traveled up till *DOC*, it is hold for *t* seconds.
10. The wheel is then retracted at $-f$ with continuous rotation at $-\omega$ to the starting position, following the opposite direction of the feeding path. Preparation of the outer cutting edge is thus completed.
11. Repeat steps 2–10 to prepare the inner cutting edge with an angle of $\phi_i$.
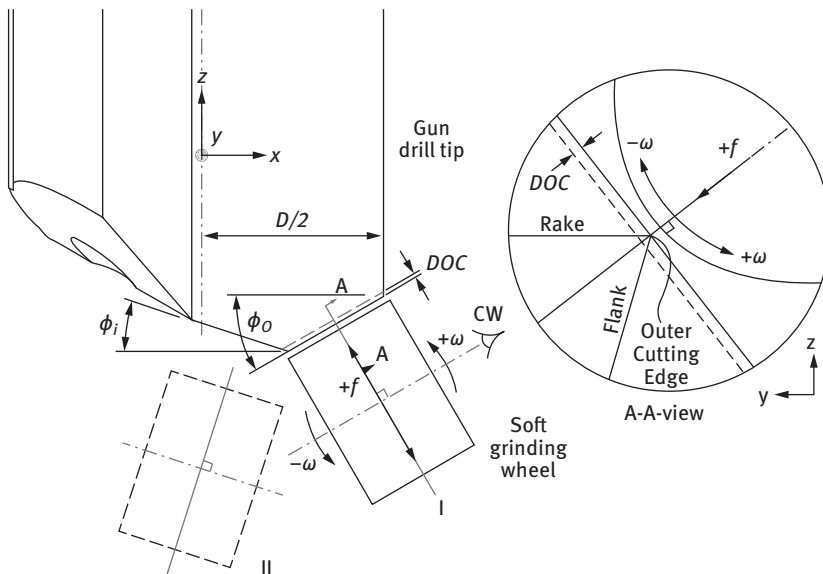


**Figure 2.46:** Illustration of cutting edge preparation using soft grinding wheel. (I) Outer cutting edge preparation and (II) inner cutting edge preparation.

### 2.8.4 Results and improvement

There are three critical parameters that indicate the integrity of cutting edges as well as efficiency of cutting edge preparation methods namely (a) average roughness $R_a$; (b) maximum depth of damage $R_z$ and (c) cutting edge radius $r$. Refer to Figure 2.47.



(a)   (b)   (c)
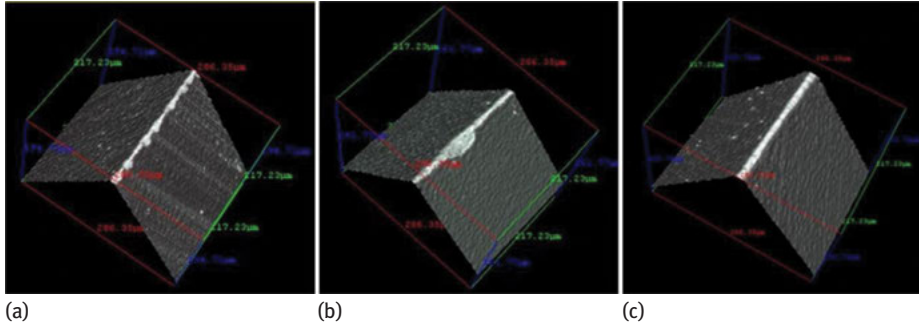
**Figure 2.47:** Quantifiable parameters of cutting edges. (a) Average roughness $R_a$, (b) maximum depth of damage $R_z$ and (c) cutting edge radius $r$.

For gun drills subjected only to re-sharpening, the resultant $R_a$, $R_z$ and $r$ based on approximately 48 drills are as follows:

| | Ra (µm) | Rz (µm) | r (µm) |
|---|---|---|---|
| **Average** | 0.13 | 0.59 | 5.21 |
| **Std. Deviation** | 0.03 | 0.11 | 0.83 |
| **Maximum** | 0.21 | 0.82 | 7.81 |
| **Minimum** | 0.09 | 0.41 | 3.36 |
| **Max-Min** | 0.12 | 0.41 | 4.45 |

With the use of soft grinding wheels to prepare the cutting edges in accordance to the procedure described in Section 6.3, the edge conditions become

| | $R_a$ (µm) | $R_z$ (µm) | r (µm) |
|---|---|---|---|
| **Average** | 0.07 | 0.33 | 10.47 |
| **Std. Deviation** | 0.01 | 0.05 | 0.40 |
| **Maximum** | 0.09 | 0.40 | 11.15 |
| **Minimum** | 0.05 | 0.23 | 9.84 |
| **Max-Min** | 0.04 | 0.17 | 1.31 |

From the results above, it can be immediately noticed that cutting edges of the 48 drills have become much more uniform after edge preparation. This aspect is

| | Std. Deviation | | Imp. (%) | Max-Min | | Imp. (%) |
|---|---|---|---|---|---|---|
| | Before | After | | Before | After | |
| $R_a$ (µm) | 0.03 | 0.01 | 33 | 0.12 | 0.04 | 33 |
| $R_z$ (µm) | 0.11 | 0.05 | 45 | 0.41 | 0.17 | 41 |
| $r$ (µm) | 0.83 | 0.40 | 48 | 4.45 | 1.31 | 29 |

indicated by the standard deviation and difference between maximum and minimum of $R_a$, $R_z$ and $r$. The quantum of improvements is summarized as follows:

### 2.8.5 Case study

To evaluate productivity performance gained with the capability to control edge uniformity of gun drills using soft grinding wheels, a 2.0-m drilling case study on Inconel 718 was conducted. Refer to Figure 2.48. Traditionally, when the cutting edges are not specially prepared, a feed rate of 5 mm/min and a drill depth of 40 mm are conservatively used. Adhering to these, 50 drilling passes were required to complete 2,000 mm of drilling and the drilling time involved was 400 min. Moreover, 49 cycles of drill re-sharpening was needed to restore the drill geometries after each pass of drilling. This took up 1,715 min where each re-sharpening cycle was approximately 35 min. The total process lead time was thus 2,115 min.



| 20% Feed rate increment | | 50% tool life improvement | |
|---|---|---|---|
| 5mm/min → | 6mm/min | 40mm → | 60mm |

| | Unprepared edges | Prepared edges |
|---|---|---|
| Drilling pass | 50 x | 33 x |
| Re-sharpening pass | 49 x | 32 x |
| Edge preparation pass | - | 33 x |
| Drilling time | 400 mins | 330 mins |
| Re-sharpening time | 1715 mins | 1120 mins |
| Edge preparation time | - | 264 mins |
| Total time | 2115 mins | 1714 mins |

Case study: 2.0-m drilling
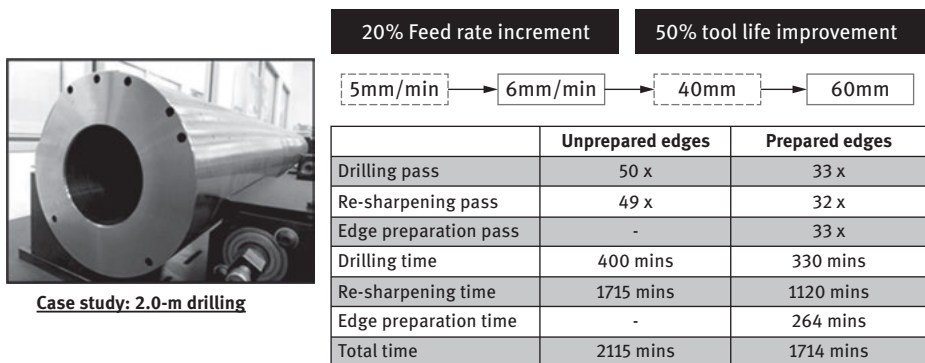
**Figure 2.48:** Productivity gained through the preparation of gun drill edges.

With the high levels of uniformity achieved as described in Section 2.8.4, the feed rate was increased by 20% to 6 mm/min and the drill depth was extended for 50% to 60 mm. The improvements brought down the number of drilling passes to 33 times, which saved 70 min of drilling time. So only 32 cycles of drill re-sharpening were needed and it helped to save close to 600 min of process lead time. To achieve this, three cycles of

cutting edge preparation using the soft grinding wheels and associated methodology were performed and occupied 264 min (approx. 8 min per cycle). The total lead time then added up to be 1,714 min, a productivity improvement close to 20% with comparable drilling outcome, when cutting edges of the gun drills are not properly prepared.

## 2.9 Summary and outlook

Drilling deep holes on nickel-based superalloys such as Inconel 718 is indeed challenging. This chapter provides the necessary fundamentals of the process, including cutting force generation, drill deflection, wall deformation and the overall process mechanics to realize the enormous challenges involved – from rapid tool degradation, catastrophic tool failure to undesirable hole misalignment. Complexity of these issues is further intensified by the tool edge radius effects due to conservative operating parameters. Thus, four effective methods to overcome the challenges namely coolant application, pilot hole drilling, drill re-sharpening and cutting edge preparation presented in this chapter are practically useful. To ensure the yield and productivity in producing deep holes, the following should be established:
–  Computational intelligent techniques to detect abnormality, drill degradation and straightness deviation using acoustic emission signals
–  Customizable adaptive damping system for the prevention of gun drill whipping beyond drilling aspect ratios of 100
–  Automated drill re-sharpening with integrated cutting edge preparation and inspection capabilities
–  High precision and rapid hole straightness and hole finishing assessment instrumentation and evaluation techniques
–  New category of tool materials with special emphasis on high temperature stability and brittle fracture resistance
–  Hole misalignment correction tooling, equipment and methodology for deep holes beyond aspect ratios of 100

## References

[1]  Woon KS, Chadhari A, Rahman M, Wan S, Kumar AS (2014) The effects of tool edge radius on drill deflection and hole misalignment in deep hole gundrilling of inconel-718. CIRP Annals, 63(1): 125–128.
[2]  Peeler H (1849) US Patent 6,088.
[3]  Ains NL (1915) US Patent 1,144,088.
[4]  Oakley J (1916) US Patent 1,189,727.
[5]  Stolle JW (1924) US Patent 1,513,350.

[6] Dixon JC (1941) US Patent 2,251,701.

[7] Ketter LC (2004) The Gun Drilling Handbook. Cambell Viking Press, Connecticut.

[8] Haldon JS (1967) Gundrilling, Trepanning and Deep Hole Machining. American Society of Tool and Manufacturing Engineers, Michigan.

[9] Astakhov Viktor P (2010) Geometry of Single-point Turning Tools and Drills. Springer-Verlag, London.

[10] Arunachalam R, Mannan MA (2000) Machinability of nickel-based high temperature alloys. Machining Science and Technology, 4(1): 127–168.

[11] Dudzinski D, Devillez A, Moufki A, Larrouquère D, Zerrouki V, Vigneau J (2004) A review of developments towards dry and high speed machining of Inconel 718 alloy. International Journal of Machine Tools & Manufacture, 44(4): 439–456.

[12] Astakhov VP, Frazao J, Osman MOM (1994) On the experimental optimization of tool geometry for uniform pressure distribution in single edge gundrilling. Journal of Engineering for Industry, 116(4): 449–456.

[13] Sterling Inc. (2013) Sterling Gun Drills Literature, www.sterlinggundrills.com. (last accessed 13 July 2018)

[14] Guhring Inc., 2013, Deep Hole Drills Catalogue, www.guhring.com.

[15] Star Cutter Company, 2013, Gundrill Product Flyers, www.starcutter.com.

[16] Johnson KL (1985) Contact Mechanics. Cambridge University Press, Cambridge.

[17] Marshall EA (1968) Rolling contact with plastic deformation. Journal of the Mechanics and Physics of Solids, 16: 243–254.

[18] Stoker JJ (1989) Differential Geometry. John Wiley & Sons, Inc, New York.

[19] Arunachalam R, Mannan MA (2000) Machinability of nickel-based high temperature alloys. Machining Science and Technology, 4(1): 127–168.

[20] Dudzinski D, Devillez A, Moufki A, Larrouquère D, Zerrouki V, Vigneau J (2004) A review of developments towards dry and high speed machining of Inconel 718 alloy. International Journal of Machine Tools and Manufacture, 44(4): 439–456.

[21] Woon KS, Chaudhari A, Kumar AS, Rahman M (2014) The effects of tool degradation on hole straightness in deep hole gundrilling of inconel-718. Proceedings of the 6th CIRP Conference on High Performance Cutting, Berkeley-USA, June 23 –25, 2014.

[22] Woon KS, Wan S, Kanno S, Tnay GL (2013) An experimental and simulation study on the thermal damage and failure of gun drills in high aspect ratio drilling of nickel-chromium-based superalloys. Proceedings of the Processing and Fabrication of Advanced Materials XXII, Singapore, December 18–20, 2013, pp. 202–219

[23] Huang Y and Liang SY (2004) Modeling of CBN tool flank wear progression in finish hard turning. Transactions of the ASME, 126: 98–106.

[24] Astakhov VP, Subramanya PS, Osman MOM (1995) An investigation of the cutting fluid in self-piloting drills. International Journal of Machine Tools and Manufacture, 35: 547–563.

[25] Latinovic V, Osman MOM (1986) Friction losses in coolant flow through kidney shaped gundrill shank. International Journal of Production Research, 24: 1319–1329.

[26] Astakhov VP, Galitsky VV, Osman MOM (1995) A novel approach to the design of self-piloting drills with external chip removal Part 2. Journal of Engineering for Industry, 177: 464–474.

[27] Woon KS, Tnay GL, Rahman M, Wan S, Yeo SH (2017) A computational fluid dynamics (CFD) model for effective coolant application in deep hole gundrilling. International Journal of Machine Tools & Manufacture, 113: 10–18.

[28] Michel Rieutord (2015) Fluid Dynamics: An Introduction, Springer International Publishing, Switzerland.

[29] Idelchik IE (2005) Handbook of Hydraulic Resistance. Jaico Publishing House, Mumbai.

[30] Rahman M, Seah KHW, Venkatesh VC (1988) Performance evaluation of endrills. International Journal of Machine Tools & Manufacture, 28(4): 341–349.

[31] Astakhov VP (2002) The mechanisms of bell mouth formation in gundrilling when the drill rotates and the workpiece is stationary. Part I: The first stage of drill entrance. International Journal of Machine Tools & Manufacture, 42: 1135–1144.

[32] Sakuma KH (1981) Self-guiding action of deep-hole-drilling tools. CIRP Annals-Manufacturing Technology, 30(1): 311–315.

[33] Chaudhari A, Woon KS, Rahman M, Kumar AS (2015) The effects of pilot hole geometry on tool-work engagement efficacy in deep hole drilling. Journal of Manufacturing Processes, 19: 135–141.

[34] Katsuki A, Sakuma K, Tabuchi K, Onikura H, Akitoshi H and Nakamuta Y (1987) The influence of tool geometry on axial hole deviation in deep drilling. JSME International Journal, 30(265): 1167–1174.

[35] Katsuki A, Onikura H, Sakuma K, Chen T, Murakami Y (1992) The influence of workpiece geometry on axial hole deviation in deep hole drilling. JSME International Journal, 35(1): 160–167.

[36] Deng C-S, Huang J-C, Chin J-H (2001) Effects of support misalignments in deep-hole drill shafts on hole straightness. International Journal of Machine Tools & Manufacture, 41(8): 1165–1188.

Krishnaraj Vijayan, Simin Nasseri, Vitale Kyle Castellano,
Herve Sobtaguim, Joshua Hilderbrand and Hari Chealvan

# 3 A new model pertaining to highspeed drilling of titanium alloy (Ti-6Al-4V)

**Abstract:** Many parameters affect the quality of drilling and the energy spent in high-speed drilling of titanium alloy (Ti-6Al-4V).In this chapter, experiments are conducted following the L16 Taguchi experimental design in a high-speed vertical machining center. The important drilling parameters such as torque, thrust force and uncut chip thickness (UCT) were measured at various spindle speed and feed rates. Nonlinear behavior of these parameters was analyzed using various regression methods. The nonlinear regression of model parameters followed an exponential trend in terms of independent parameters: spindle speed and feed rate in a unique new way. Energy of the cut was then estimated using these models and evaluated against the UCT. The new model can be used to optimize the best drilling parameters to obtain a longer tool life.

## 3.1 Introduction

Titanium is the fourth most abundant structural metals and is the ninth most abundant element on the Earth. Titanium alloy is typically employed in the area where metallic structure and high temperature strength is required. These lightweight materials are now being constituted in modern aircraft structure, especially in jet engine components that are subjected to temperatures up to 1,000°C. Ti-6Al-4V (an alpha + beta alloy) is the most used titanium alloy and so-called workhorse of the titanium industry. The increasing popularity of Ti-6Al-4V is due to its superior properties such as high strength-to-weight ratio, low density, high compressive and tensile strength, good formability and good corrosion resistance [1].Titanium alloy is a hard-to-machine material. Drilling is the most difficult process in comparison to milling and turning [2]. The drilling operation, which is involved in nearly all titanium applications, is one of the important machining processes used for making holes needed specially for the assembling of parts. The reason for poor machinability is due to its poor thermal conductivity; thermal conductivity of Ti alloy is one-sixth of that of steels [2]. About 90% of the work of plastic deformation during drilling is converted into heat, producing high temperatures in the deformation zones and the surrounding regions [2].This results in shorter tool life. High-speed machining (HSM) means using cutting speeds that are significantly higher than those used in conventional machining operations. HSM is preferred because of its potential for faster production rates, shorter lead times, cost reduction and improved quality. The definition of "high speed" in the term high-speed machining is material dependent.

Thrust forces and torque are necessarily needed to be controlled while drilling Ti alloy. The difficulty in machining is indicated by thrust force. Besides, smaller cutting force is preferred. The increased cutting force can cause vibration in the spindle axis and poor quality of machined surfaces. It can result in premature failure of drills. The larger the torque, the more friction exists between the drills and workpiece. This produces a large quantity of heat resulting in higher temperature at the tool-workpiece interface. Specific cutting energy or unit cutting energy is the power required to machine a unit volume of the work material. Specific energy requirement should be reduced as far as possible that depends not only on the work material but also on the process of the machining.

Chatterjee et al. [3] performed an experiment by utilizing the performance characteristics obtained through simulation. The results were compared to the experimental results. In their results, the percentage relative error of 4.93, 9.01, 6.04 and 3.0 for thrust, torque and circularity at entry and at exit was observed. Rodrigues et al. [4] presented specific cutting energy measurements as a function of the cutting speed and also tool's cutting edge geometry. An increase of 1° in tool chip breaker chamfer angle resulted in a reduction of specific cutting energy of about 13.7% when machining at high speeds and 28.6% when machining at conventional cutting speeds. Specific cutting energy demonstrated to be almost insensitive to cutting edge geometry at high-speed cutting. The tests carried out at high-speed cutting provided cutting forces significantly lower than those obtained at conventional cutting speed condition.

Abouridouane et al. [5] investigated the size effects in micro drilling of ferritic-pearlitic carbon steels. Various parameters such as chisel edge length, plowing, microstructure and built-up edge were discussed and finite element modeling of size effects was performed. The relation of the effect of plowing size to the ratio between UCT and cutting edge radius was established. It was concluded that plowing leads to a high increase of the related feed force and torque in micro drilling. Yifrach et al. [6] performed the grinding operation on the ceramic plate. The experiment was carried out by single slot cutting, without cooling. The specific cutting energy ($U$) was calculated by measuring the cutting power from the experiment and dividing by the calculated material removal rate from the cutting parameters (depth, width of cut and feed rate).

Sushinder et al. investigated the thrust force, torque and chip morphology in the drilling of Ti-6Al-4V using tungsten carbide tipped drill at a constant feed rate and at varying cutting speeds. They concluded that at higher cutting speeds, thermal softening effects dominate, which changes the thrust force and torque. They also noted that the discontinuous chip formation at high cutting speeds helps improve the machinability [7]. Huang et al. studied the identification of Johnson-Cook constitutive model parameters for high strain rate deformation [8]. It was concluded that the adiabatic heating phenomenon is present, and the temperature will rise due to plastic deformation.

Zhang et al. worked on the selection of Johnson-cook constitutive model parameters for Ti-6A1-4V using three types of numerical models of orthogonal cutting. They concluded that the best set of Johnson-Cook model parameters was not unique for the three numerical models of metal cutting [9]. Muhammad and his colleagues derived an experiment with a 3D finite element analysis (FEA) model to determine if heating the drilling specimen before drilling reduced the thrust force and torque of the drill bit. It was estimated that the reduction in torque at elevated temperature is larger when compared to the thrust force in "hot drilling" for selected temperature values [10]. Waqar and his colleagues studied the correlations between drilling parameters such as feed rate and spindle speed, and quality of machined surface. A conclusion was made that there was a nonlinear relationship between the feed rate and hole diameter deviation, which suggests that there are other factors influencing the hole diameter deviation. They also found a direct relationship between the spindle speed and surface roughness as well as an indirect relationship with the feed rate [11]. Yadav and his coworkers reviewed the drilling of Ti-6Al-4V and found that drilling with high-pressure coolant is the most desirable. Specifically, a titanium aluminum nitride (TiAlN)-coated carbide tool was considered the most appropriate tool for drilling Ti-6Al-4V alloy. It was concluded that a high-pressure water jet is also effective. Usually, lower drilling speeds were found to achieve better tool life, but this comes at the cost of a loss in productivity [12].

Bâdan and his coworkers experimented with a mathematical model based on power regression method that was dependent on cutting depth, cutting speed and feed rate. The project resulted in a software module capable of calculating the cutting parameters, power of drilling and verifying the thrust force [13]. Das and Das investigated the measurement and modeling for medium-scale manufacturing firms for their drilling operations, mainly focusing on axial thrust and also the torque through a back propagation neural network [14]. They concluded it is possible to give an initial loading to a trained neural network model and it will estimate the corresponding axial thrust and torque values.

In this work, experimental results of high-speed drilling of Ti-6Al-4V have been modeled using the exponential regressions in terms of spindle speed (RPM) and feed rate (mm/min). These types of equations have not been addressed by the research communities in the past. Measured torque, thrust force and UCT were modeled using MS Excel© and MATLAB (Mathworks©) and total energy for cutting is computed to select optimal independent parameters of spindle speed and feed rate.

## 3.2 Experimental conditions

The microscopic image of Ti-6Al-4V used for the experiments is shown in Figure 3.1. To find the composition, spark test was performed using the spectrometer Ametek
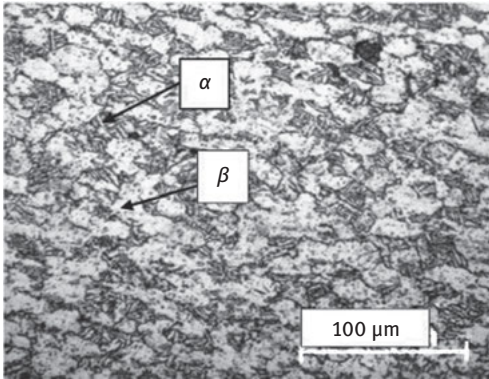
**Figure 3.1:** Microscopic image of Ti-6Al-4V.

**Table 3.1:** Composition of elements.

| Elements | Ti | Al | V | C | Fe | Ni | Cr | Si |
|---|---|---|---|---|---|---|---|---|
| Actual Value (%) | 89.20 | 6.32 | 4.18 | 0.071 | 0.065 | 0.028 | 0.024 | 0.015 |

SPECTROMAXx. The actual amount of alloying elements present in the workpiece is tabulated in Table 3.1.

Drilling of Ti-6Al-4V was performed using the CNC vertical machining center. Details on the experimental condition is shown in Table 3.2.

**Table 3.2:** Experimental conditions.

| Machine used | CNC vertical machining center (MAKINO S33) |
|---|---|
| Tool (Material) | Solid Carbide (uncoated) |
| Diameter of drill | 6 mm |
| Workpiece | Titanium alloy (Ti- 6Al- 4V) |
| Spindle Speed | 2,652, 3,183, 3,713, 4,244 rpm |
| Feed rate | 26.52, 63.66, 111.39, 169.76 mm/min |

The hardness of the workpiece material was found to be 335 brinell hardness number (BHN). The drill bit was made of solid carbide with flute length of 28 mm. The tool edge radius was calculated using an optical microscope equipped with DinoCapture software and the measurement was done at various locations. The average was taken and the edge radius was found to be 18 μm. To conduct the experiment for high-speed drilling on titanium alloy (Ti-6Al-4V), an L16 orthogonal array was chosen using Taguchi method with four levels of feed and speed. The drilling setup is shown in Figure 3.2.
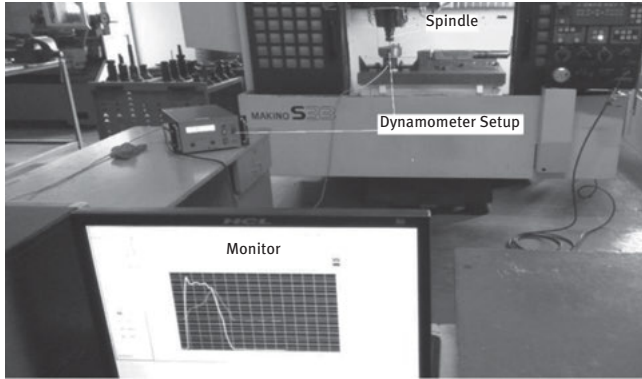
**Figure 3.2:** Experimental set-up.

The thrust force and torque during machining the workpiece was measured using the SYSCON drilling tool dynamometer. The workpiece was clamped on the dynamometer using a special fixture.

## 3.3 Governing equations

The governing equations behind the modeling work are related to each other algebraically [1]. The first equation that was used is the formula for the thrust speed ($V_t$), which is perpendicular to the workpiece and is given in mm/min and by the following equation:

$$v_t = SS(f) \tag{3.1}$$

where the spindle speed (*SS*) is given in revolutions per minute and feed or *f* is given in millimeters per revolutions. Cutting speed, $V_c$, in mm/min is also written in terms of the spindle speed and the drill diameter (*D*) in mm:

$$V_c = \pi D(SS) \tag{3.2}$$

The feed rate ($F_r$), in mm/min can be written in terms of the spindle speed and feed:

$$F_r = SS(f) \tag{3.3}$$

The material removal in drilling (mm$^3$/min) can be described by the following equations:

$$R_{mr} = \left(\frac{D(V_c)}{4SS}\right)F_r \text{ or } R_{mr} = \left(\frac{\pi D^2}{4}\right)F_r \tag{3.4}$$

Specific cutting energy, or $U$, in J/mm$^3$ is defined as the ratio of the cutting power ($P_c$) over the material removed.

$$U = \frac{P_C}{R_{mr}} \tag{3.5}$$

Cutting power, which is usually expressed in kW, can be written in terms of the torque and the spindle speed [15]:

$$P_c = \frac{T(SS)}{9550} = \frac{2\,\pi T(SS)}{60} \tag{3.6}$$

Notice that since we are keeping spindle speed in terms of mm/min, we no longer need to divide by 60 so the equation turns into the following:

$$U = \frac{8\,\pi T\,(SS)^2}{D\,F_r V_c} \tag{3.7}$$

The final equation for the energy can be derived as follows by using eqs. 3.2 and 3.7:

$$U = \frac{8\,T(SS)}{D^2 F_r} \tag{3.8}$$

## 3.4 Experimental results and modeling

### 3.4.1 Uncut chip thickness analysis

The first point of discussion in this chapter is about the relationship between UCT, spindle speed, and feed rate. Regression modeling was used to relate dependent values of UCT to independent values of the spindle speed and feed rate. This was achieved through plotting the experimental UCT versus spindle speed grouped by feed rate in MS Excel$^{©}$ and studying the relationships that occurred as shown in Figure 3.3. Curves were fitted and the trend lines were used to find equations that best reflected the data provided.

The plot showed an exponential relationship between these parameters, with $a$ and $b$ constants shown in the following equation:

$$UCT = ae^{b(SS)} \tag{3.9}$$

In this case, $b$ was found to have a reoccurring value of −0.0003 for all of the four curves. The constant $a$ was then plotted against feed rate and it was found that a
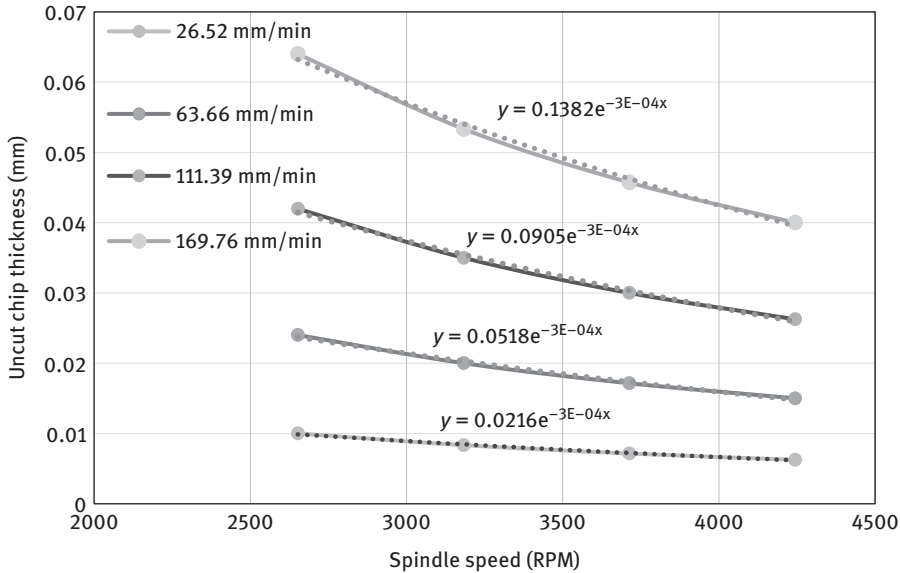
**Figure 3.3:** Exponential functions describing the behavior of UCT versus the spindle speed.

linear relationship exist between these quantities. This relationship was best expressed by the following equation:

$$a = 0.0008F_r - 0.00002 \tag{3.10}$$

After considering these coefficients, the following equation was found that best matches the experimental data that is measured in millimeters:

$$UCT = (0.0008F_r - 0.00002)e^{-0.0003SS} \tag{3.11}$$

However, the equation can be expressed in microns and the exponential term can be simplified into a new formula as the following:

$$UCT = (0.8F_r - 0.02)0.9997^{SS} \tag{3.12}$$

The comparison between the experimental data and the proposed equation, hereafter referred to as math model, is expressed in Figure 3.4. The linear fit proved the relation of UCT to spindle speed was directly proportional.

After eq. 3.12 was compared, it was put to test to make sure the values the equation would come up with would equate to the experimental values given. The average error between the experimental values and the model values had only about 4% percent difference. This percent difference is very small when considering the tolerances being used by many machinists today. When put into perspective, this average is essentially
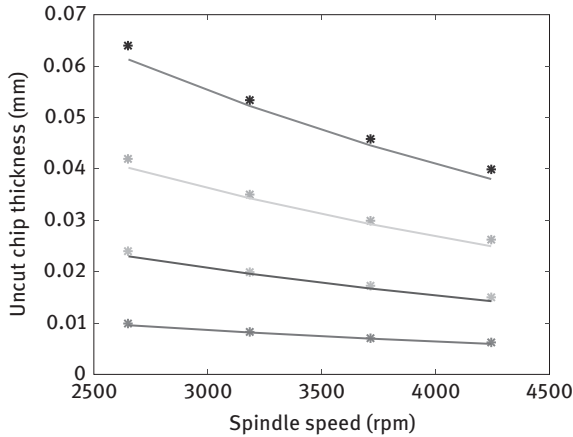
**Figure 3.4:** Uncut Chip Thickness (UCT) experimental values compared to the values obtained by the math model (using MATLAB curve fitting toolbox). The top curve is for the highest feed rate and the others for lower ones respectively.
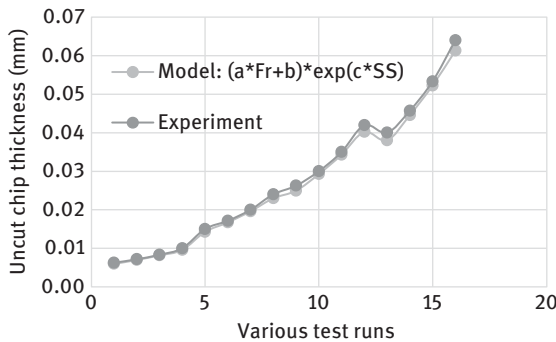


**Figure 3.5:** UCT Proximity.

only a difference of 0.0027 mm or about 3 μm. Figure 3.5 shows the overall proximity between the experimental UCT and the math model approximation.

## 3.4.2 Torque analysis

The relationships between torque, spindle speed and feed rate are also of importance to both the manufacturing and research community. It was found that the lowest torque value was recorded at spindle speed of 3,183 rpm and feed rate of 26.52 mm/min. The torque values increased constantly with increasing the feed rate in almost all the trails. This result may be caused by the high chip load. The experimental data showed that
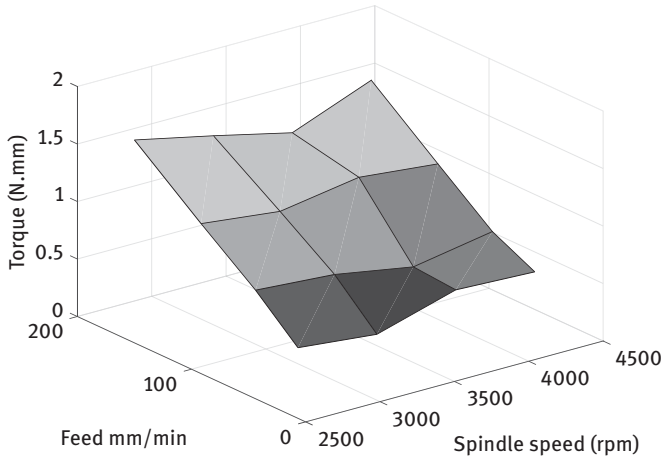
**Figure 3.6:** Experimental torque surface as a function of spindle speed and feed rate.

the torque was almost insensitive to the spindle speed at high-speed cutting condition. This association between these parameters can be viewed in Figure 3.6, where the 3D surface plot shows how the spindle speed and feed rate both influence the torque.

A similar process used for the torque equation was found in the same way the UCT equation was obtained. For the torque, the exponent happened to change with the spindle speed. It was more challenging to find the appropriate coefficients using the normal regression methods. Therefore, because of the complexity of these relationships, the curve fitting toolbox was used in MATLAB to process the data and find specific equations to define the coefficients.

This exponential equation based on the curve fitting results is as follows:

$$T = c \ e^{d(F_r)} \tag{3.13}$$

where $c$ and $d$ are coefficients in terms of spindle speed and feed rate. The $c$ and $d$ coefficients were determined as follow by MATLAB:

$$c = 0.6223 - (9.875E - 05)SS + (0.001709)F_r \tag{3.14}$$

$$d = 0.01969 - (4.522E - 06)SS + (3.768E - 05)F_r \tag{3.15}$$

Finally, this theoretical equation can then be compared to the experimental data that is presented in Figure 3.7. The top subplot represents the torque at the lowest spindle speed and the bottom one is for the highest spindle speed.

In addition, torque versus spindle speed graphs are provided in Figure 3.8 for various feed rates (lowest feed rate at the top subplot).
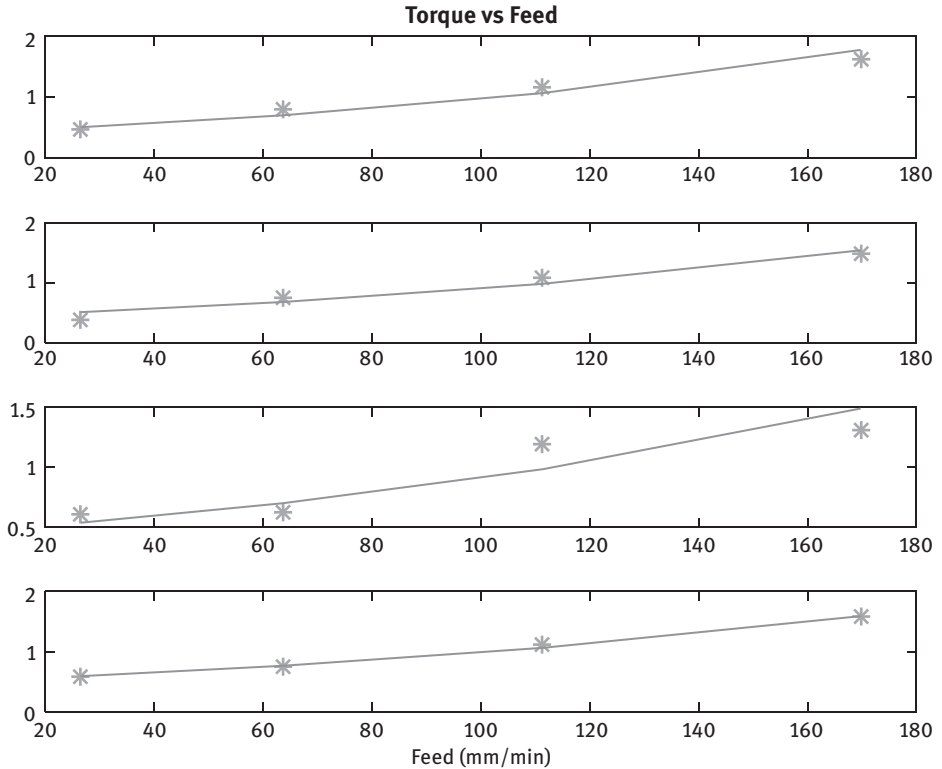
**Figure 3.7:** Experimental torque compared to the values obtained by the new model at varying feed rate. The top subplot is for the highest spindle speed and the bottom one for the lowest spindle speed.

To better predict the behavior of the torque, an alternative function was also found, which uses factors based on certain quantities. Some of these parameters include the diameter of the drill, the material of workpiece and the drill, the feed (mm/rev) and the ratio between the edge of the tool and the drill diameter. The following equation was found via [15] to theoretically predict the torque in N m:

$$M = \frac{K_d \ (F_f)(F_M)AW}{40000} \tag{3.16}$$

where $K_d$ is the work material factor based on the actual material; however, for titanium Ti-6Al-4V this number is based on a limited amount of experiments. The value for this quantity was given to be 18,000 [15]. $W$ is a tool wear factor and was assumed for drilling operations on a hard-to-machine material with a somewhat dull drill bit, which equated to a value of 1.50. $A$ is a chisel edge factor for torque, which utilizes the ratio between length of the chisel edge versus the drill diameter [15].

**Torque vs SS**
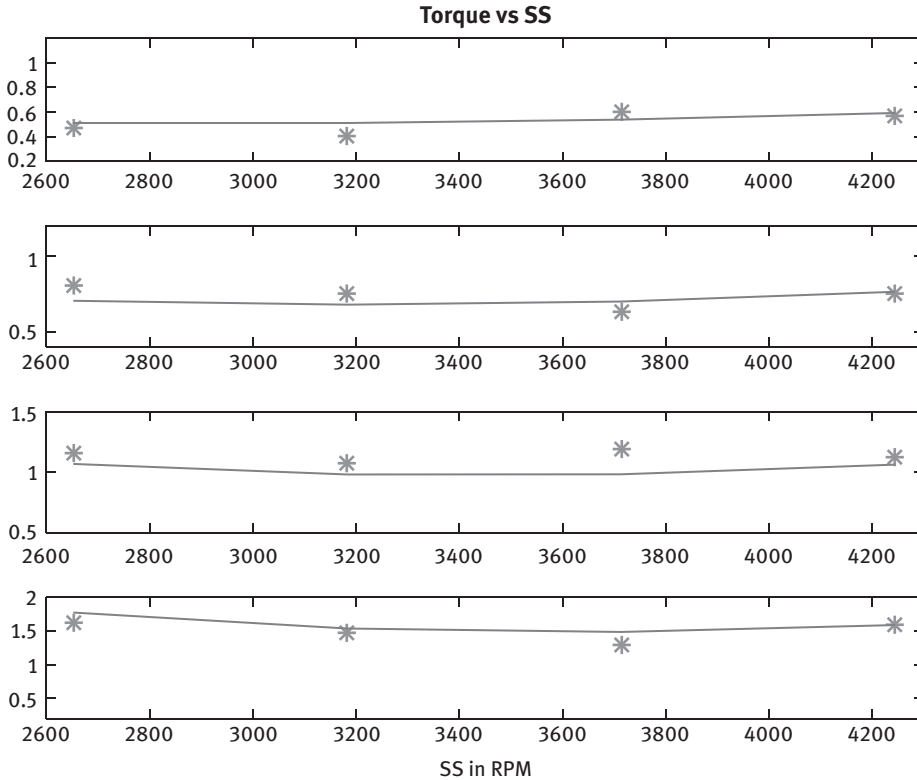


**Figure 3.8:** Experimental torque values compared to math model values in terms of spindle speed. The top subplot shows the torque at the lowest feed rate.

However, the drill used in this research work had a value less than the smallest value available; hence, the interpolation could have not been performed. Because of this, the smallest value of 1.000 was used. Furthermore, $F_f$ is a feed factor based on the feed (mm/rev). MS Excel was used to interpolate the data to get accurate values, with the exception of three feed values that were below the smallest values possible. Whenever the values were not available from the tables, the lowest values provided in the tables were used. The final factor was a drill diameter factor for torque, $F_M$, which after interpolation was found to be 25.24 [15]. The equation was used to find corresponding torque values; however, for better results Excel data solver was used to modify the $K_d$, A, W and 40,000 to reduce the norm of residuals (the square of the difference between the experimental torque and the torque calculated with the original equation above). After using the excel data solver, with a relative growth rate (RGR) nonlinear method, the values were found to be 17,921.67, 0.9956, 1.49 and 40,180.54, respectively for $K_d$, A, W and the initial constant. The validation of this method can be seen in the sum of the square differences, which became 0.3893, and
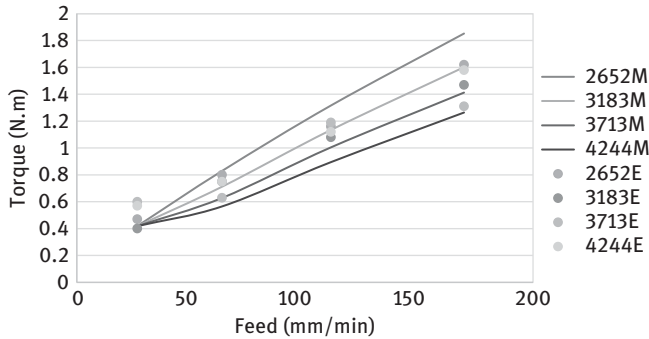
**Figure 3.9:** Experimental torque values compared to the values obtained by eq. 3.16.

is supposed to approach zero. Figure 3.9 shows the experimental data versus the modified theoretical equation, furthermore adding to the validity of the new values of the constants.

### 3.4.3 Thrust force analysis

Thrust force ($F_t$) was also studied using Excel and MATLAB curve fitting using spindle speed and feed rate. First, a surface plot was generated to show the complex relationship between the spindle speed, feed rate and thrust force, which can be seen in Figure 3.10.
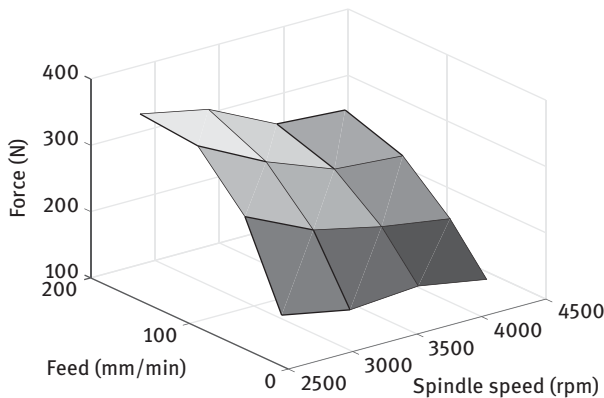


**Figure 3.10:** Experimental thrust force surface as a function of spindle speed and feed rate.

Comparable to the process of finding the torque equation, the first step to find the thrust force relationship was to plot the experimental data in Excel and find an
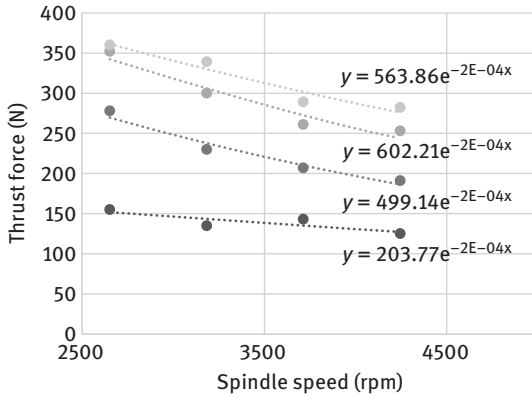
**Figure 3.11:** Thrust force vs spindle speed exponential fits. The bottom curve is for the lowest feed rate.

equation that best fit the data. A regression curve for thrust force was produced by plotting the thrust force versus the spindle speed. After this was done, again a series of equations were formulated as shown in Figure 3.11.

Ultimately an exponential was selected that follows the other equations for drilling parameters:

$$F_t = ge^{h(SS)} \tag{3.17}$$

The coefficients $g$ and $h$ are again in terms of spindle speed and feed rate and were found using MATLAB curve fitting toolbox:

$$g = -3720 + 1.638(SS) - 15.72(F_r) \tag{3.18}$$

$$h = 0.001045 - (4.809E - 07)SS + (4.716E - 6)F_r \tag{3.19}$$

The coefficients obtained from Excel were then presented against the abovementioned equations to show the effectiveness of this method. The experimental results were close to the ones predicted by math model.

This equation versus the experimental data obtained through testing is shown in Figures 3.12 and 3.13. The top subplots are related to the lowest spindle speed and lowest feed rate, respectively.

From Figure 3.12, it can be seen that the thrust force increases with the increase in feed rate. It was noted that the lowest thrust force was recorded at the lowest feed rate of 26.52 mm/min accompanied by the highest spindle speed of 4,244 rpm. When the UCT was below cutting edge radius, spindle speed has almost nil effect on the thrust force.
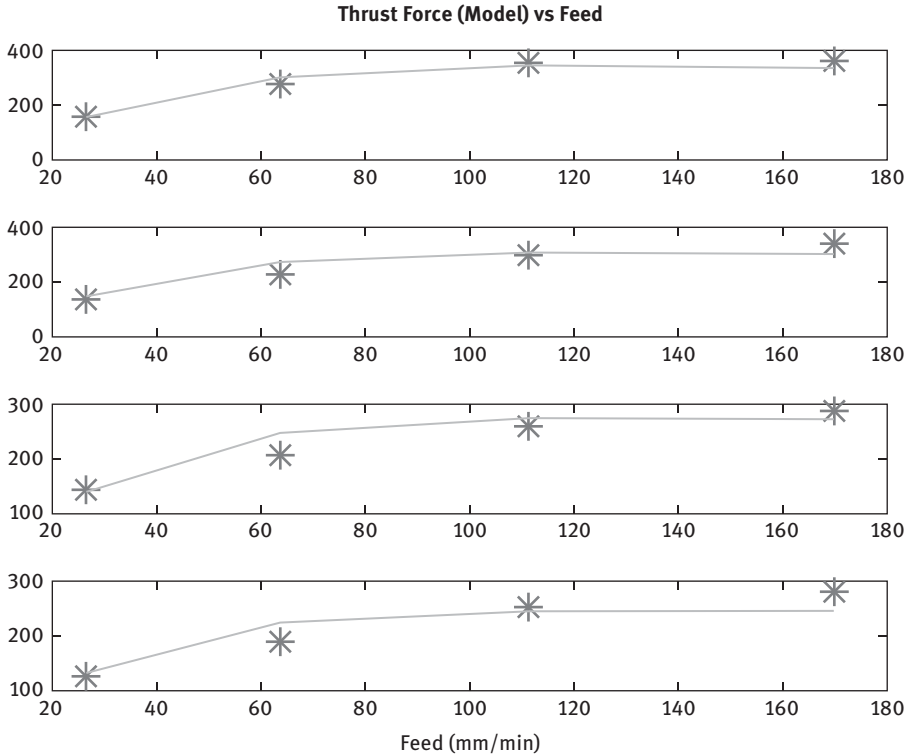
**Figure 3.12:** The experimental thrust force values versus feed rate, compared to the values obtained by the model. The top subplot is related to the lowest spindle speed and the bottom one for the highest.

It is evident that the increase in spindle speed decreases the thrust force. Even though the highest spindle speed is preferred, it is necessary to be cautious in selecting the feed rate. At 4,244 rpm, it was seen that the thrust force was 2.25 times higher at 169.76 mm/min than at 26.52 mm/min. At higher feed rates, the thrust force decreases with the increase in spindle speed. At the highest feed rate, there was about 22% reduction in thrust force value between 2,652 rpm and 4,244 rpm. The deviation of these percentages from the ones obtained by the exponential model depends on the number of experimental data. The more the data points, the closer the two values would be.

### 3.4.4 Specific cutting energy analysis

This analysis is based on the equation found for the specific cutting energy or eq. (3.8). The torque used in the calculation was theoretical torque produced from the math model. Figures 3.14 and 3.15 show the energy of cutting versus the feed rate and spindle speeds, respectively. The behavior of the specific cutting energy is shown against the UCT in Figure 3.16.

**Thrust Force (Model) vs SS**
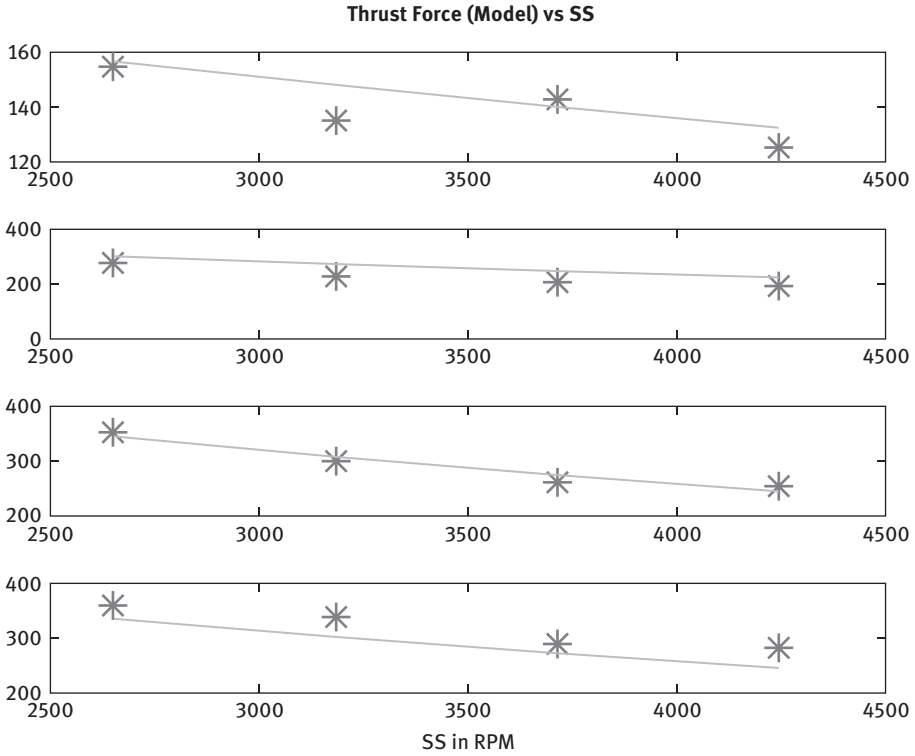


**Figure 3.13:** The experimental thrust force values versus spindle speed, compared to the values obtained by the model. The top subplot is related to the lowest feed rate and the bottom one for the highest.
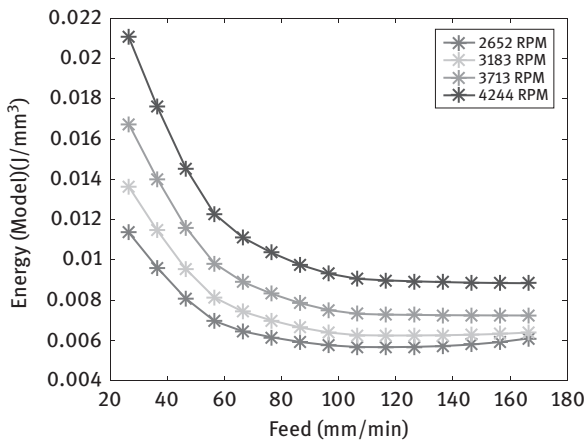


**Figure 3.14:** The Specific cutting energy against the feed rate at various spindle speeds.
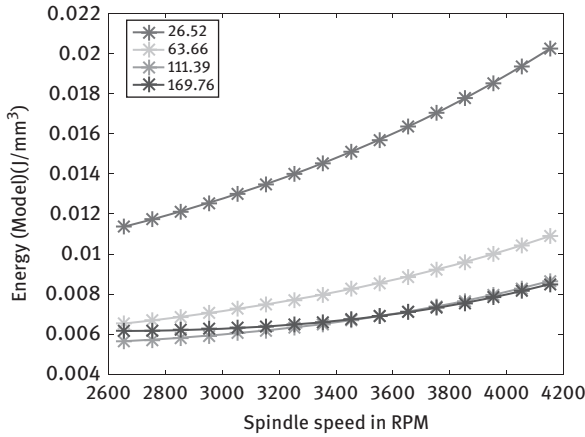
**Figure 3.15:** The Specific cutting energy against the spindle speed at various feed rates.
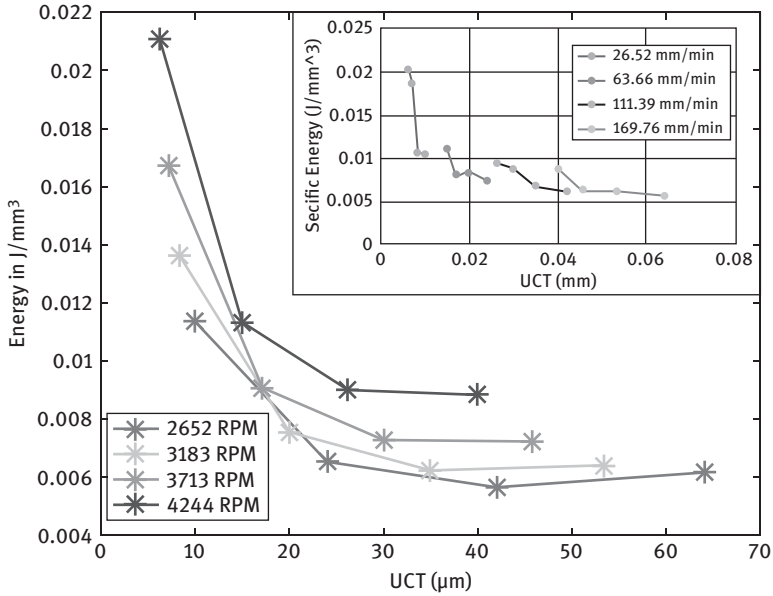


**Figure 3.16:** The Specific cutting energy obtained by math model against the measured uncut chip thickness at various spindle speeds. Inset shows the effect of the feed rate more clearly.

## 3.5 Conclusions and discussions

Thrust force and torque record the lowest value at the lowest feed rate (26.52 mm/min). Thrust force and torque values decrease with increase in the speed of cutting. This shows the significance of the high-speed cutting.

The feed rate shows the maximum percentage contribution toward the thrust force and torque. Torque value shows a significant rise with increase in feed rate. However, spindle speed does not have much effect on the torque. The thrust force was 2.25 times higher at 169.76 mm/min than at 26.52 mm/min.

The nonlinear trend was observed while analyzing the torque, thrust force and specific energy with respect to the feed rate or spindle speed (also the specific cutting energy with respect to UCT). This was assisted by plowing action and material hardening. The trend symbolizes the size effect. The exponential model, suggested for the first time, predicted the behavior of all the parameters very well. Increasing the data points adds accuracy to the constant values obtained in each exponential model.

Analysis of Variance (ANOVA) is a statistical technique for determining the degree of difference or similarity between two or more groups of data. From Tables 3.3 and 3.4, feed rate possesses the maximum percentage contribution to the thrust force and torque. The spindle speed shares a moderate contribution to the thrust force (13.97%). From Figure 3.8 and Table 3.4, it is clearly found that the spindle speed has almost null effect toward torque. In both the cases, it can be noticed that the percentage contribution due to error was less than 15%. This indicates that none of the more influencing factors are missed out by the experimenters.

**Table 3.3:** Analysis of variance for thrust force.

| Source | Degree of Freedom | Sum of Squares | % Contribution |
|---|---|---|---|
| Spindle Speed | 3 | 12,686 | 13.97 |
| Feed Rate | 3 | 75,539 | 83.18 |
| Error | 7 | 2,588 | 2.84 |
| Total | 15 | 90,813 | 100 (approx.) |

**Table 3.4:** Analysis of variance for torque.

| Source | DF | SS | % Contribution |
|---|---|---|---|
| Spindle Speed | 3 | 0.02,582 | 1.07 |
| Feed Rate | 3 | 2.28,673 | 95.58 |
| Error | 7 | 0.07,983 | 3.33 |
| Total | 15 | 2.39,238 | 100 (approx.) |

$R^2$ (coefficient of determination) = 96.66% (Torque).

The coefficient of determination, $R^2$, describes the amount of variation in the observed response values that is explained by the predictor(s) is 97.15% for thrust force.

CT-Uncut chip thickness       TR-Tool edge radius       α-Rake angle

(a) CT > TR                                              (b) CT < TR
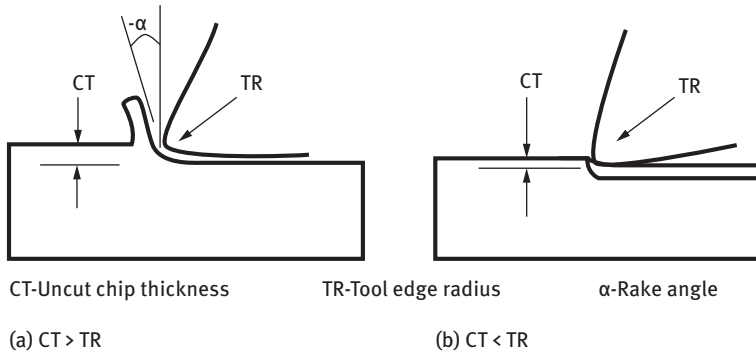
**Figure 3.17:** (a) Negative rake angle effect (b) Plowing.

When the depth of cut is greater than the tool cutting edge radius, then the cutting action occurs. When the depth of cut is lower than the cutting edge radius, the plowing action occurs as depicted in Figure 3.17 [16]. In plowing, the drill bit projects into the work, but not far enough to cause cutting. Instead, the work surface is deformed and energy is consumed without any material removal. In plowing, negative rake angle effect arises. When the ratio of UCT to cutting radius becomes one or less than one, rake angle becomes negative.

The specific cutting energy decreases with the increase in UCT (the size effect), which is clearly observed from Figure 3.16. The primary cause can be considered to be plowing. The material strengthening and the temperature generated at tool-chip interface are also considered as factors for the size effect. It is stated that the decrease in UCT increases the material shear strength. Dinesh et al. also suggested that the strain gradient can be a reason for the size effect [17]. The nonlinear trend that can be seen matches with the work conducted by various authors.

It was found that the specific cutting energy does not vary much after about 0.02 mm (20 μm) UCT. There was also high-specific cutting energy recorded when the UCT was below 18 μm (cutting edge radius). This was evident for the plowing action. The contribution of cutting edge–to-size effect was supported by material flow pattern and the increased contact length at the smaller UCT value [10]. When the UCT was too low, it was seen that the specific cutting energy at 2,652 rpm (lowest speed) was low compared to other speeds chosen. Rodrigues et al. produced similar results [4].

During high-speed drilling of Ti alloys, low feed rate is generally preferred and in case the feed rate is lower than the cutting edge radius, there will be ineffective material removal. At low feed rate, specific cutting energy increases when the UCT is less than 20 μm. This increase in specific cutting energy could be because of plowing and rubbing action; moreover, this increase in specific cutting energy can further reduce tool life.

# References

[1]   Groover MP, Fundamentals of modern manufacturing materials, processes, and systems. Hoboken, New Jersey, 2010.

[2]   Zhang PF, Churi NJ, Pei ZJ, Treadwell C. Mechanical drilling processes for titanium alloys. A literature review. Machining Science and Technology 2008, 12(4): 417–444.

[3]   Chatterjee S, Mahapatra SS, Abhishek K, Simulation and optimization of machining parameters in drilling of titanium alloys. Simulation Modelling Practice and Theory 2016, 62: 31–48.

[4]   Rodrigues RA, Coelho RT Influence of the tool edge geometry on specific cutting energy at high-speed cutting. The Journal of the Brazilian Society of Mechanical Sciences and Engineering 2007, 279–283.

[5]   Abouridouane M, Klocke F, Lung D, Adams O, Procedia CIRP 2012, 3: 91–96.

[6]   Yifrach Y, Ben-Hanan U (2013) Cutting zone temperature and specific cutting energy measurement and evaluation in machining metals. 13th International Conference on Fracture. 2013, 16–21.

[7]   Sushinder K, Shivaram PR, NivedhKannaa SB, Gupta N, Vijay Sekar KS. Investigation of thrust forces, torque and chip microstructure during drilling of ti-6Al-4V titanium alloy. Applied Mechanics and Materials 2015, 787: 431–436.

[8]   Huang X, Zhu J, Hu W. Identification of Johnson-Cook constitutive model parameters for high strain rate deformation. 15th International Conference on Experimental Mechanics 2012, 1–7.

[9]   Zhang Y, Outeiro JC, Mabrouki T. On the selection of Johnson-Cook constitutive model parameters for ti-6A1-4V using three types of numerical models of orthogonal cutting. Procedia CIRP 312015, 112–117.

[10]  Muhammad R, Ahmed N, Shariff YM, Siberschmidt VV. Finite-element analysis of forces in drilling of ti-alloys at elevated temperatures. Trans Tech Publications 2012, 188: 250–255.

[11]  Waqar S, Asad S, Ahmad S, Abbas CA, Elahi H. Effect of drilling parameters on hole quality of ti-6Al-4V titanium alloy in dry drilling. Materials Science Forum 2016, 880: 33–36.

[12]  Yadav M, Rathod PR, Dhameliya KM. Drilling of ti6Al4V a review. International Journal of Engineering Development and Research 2016, 4(4): 112–115.

[13]  Bâdan I, Oacnea GH, Vasiloni M. Mathematical model for drilling forces of 40CrMnMos8-6 steel. Bulletin of the Transilvania University of Brasov 2012, 5(54): 31–38.

[14]  Das G, Das P. Cutting forces in drilling operation: measurement and modeling for medium-scale manufacturing firms. International Journal of Computer Applications 2015, 121(8): 11–17.

[15]  Oberg E, Jones FD, Hortons HL, Ryffel HH. Machinery's handbook 29th edition. New York, New York, 2012.

[16]  Stephenson DA, Agapiou JS. Metal cutting-theory and practice, 2nd edn. Taylor and Francis Group, New York, 2016.

[17]  Dinesh S, Swaminathan S, Chandrasekar S, Farris TN. An intrinsic size-effect in machining due to the strain gradient. Proceedings of ASME Manufacturing Engineering Division-MED-vol. 12, ASME International Mechanical Engineering Congress and Exposition, 2001, NY, 197–204.

J. Babu, Lijo Paul and J. Paulo Davim

# 4 Drilling of composite materials: methods and tools

**Abstract:** Drilling is the most common machining process in the manufacture of components and structures from composite materials. Conventional drilling with a twist drill is widely adopted for this. However, it is difficult to ensure proper hole quality on composites due to their special characteristics. Special drill bits, in terms of their geometry and material and nonconventional hole-making processes have been developed to improve the quality of drilled holes in composites. Delamination is the major drilling defect that causes failure of composite structures. The severity of delamination damage is assessed by various measures or delamination factors. There are delamination suppression techniques that have been developed for different drilling applications.

## NOTATION

| | |
|---|---|
| $A_d$ | $= D_{MAR} =$ Delamination area in the vicinity of the drilled hole |
| $A_e$ | = Area of the envelope of damage zone that includes area of the hole |
| $A_H$ | = Heavily damaged area |
| $A_L$ | = Lightly damaged area |
| $A_{max}$ | = Area corresponding to $D_{max}$ |
| $A_M$ | = Medium damage area |
| $A_o$ | $= A_{nom} = A_{AVG} =$ Nominal hole area with diameter $D$ |
| AWJ | = Abrasive water jet |
| GFRC | = *Glass fiber-reinforced polymer composites* |
| GFRP | = Glass fiber reinforced plastics |
| CC | = Ceramic composite |
| CFRC | = *Carbon fiber-reinforced polymer composites* |
| CFRP | = Carbon fiber reinforced plastics |
| D | $= D_O =$ Nominal diameter of drilled hole |
| $D_e$ | = Equivalent diameter |
| $D_{ea}$ | $= D_{re}$ Equivalent diameter of a circle whose area is the same as $A_e$ |
| $D_{ea}$ | = Equivalent diameter of a circle whose perimeter is the same as $P_e$ |
| DF | $=$ D$i$ = Damage factor |
| $D_{eed}$ | = Effective equivalent diameter (average value of $D_{ea}$ and $D_{ep}$) |
| $D_{min}$ | = Diameter of the minimum enclosing area |
| $D_{max}$ | = Maximum diameter of delamination |
| $D_{RAT}$ | = Damage ratio |
| EDM | = Electric discharge machining |
| f | = Shape's circularity |
| F | = Feed rate |

*(continued)*

(continued)

| | |
|---|---|
| $F_a$ | = Two-dimensional delamination factor |
| $F_d$ | = Conventional delamination factor |
| $F_{da}$ | = Adjusted delamination factor |
| $F_{d_{min}}$ | = Minimum delamination factor |
| $F_{ed}$ | = Equivalent delamination factor |
| $F_{red}$ | = Refined equivalent delamination factor |
| FEED | = Effective equivalent delamination factor |
| FML | = Fiber metal-reinforced composite laminates |
| FRPC | = Fiber-reinforced polymer composites |
| HSS | = High-speed steel |
| MMC | = Metal matrix composite |
| PCD | = Polycrystalline diamond |
| $P_e$ | = Perimeter of the envelope of damage zone |
| PCBN | = polycrystalline boran nitride |
| NCM | = Nonconventional machining processes |
| NFRCs | = Natural fiber-reinforced composites |
| VATD | = Vibration-assisted twist drilling |
| USM | = Ultrasonic machining |

## 4.1 Introduction

Low density, excellent corrosion and chemical resistance and relatively high stiffness and strength properties extend the use of composites in industries such as defense, aerospace, power generation, automobile and transport [1–2]. Even though products with composites are generally made to near net shape, they may need machining to meet dimensional and/or assembly requirements. The secondary operations usually carried out on these products are: milling, turning and drilling. Drilling is the most common and essential machining operation necessary for fastening composite structures. Composites materials are considered difficult to machine materials when compared with conventional homogeneous materials, due to their nonhomogeneous, anisotropic nature, being reinforced with abrasive constituents [3].

Structural joint performance mainly depends on the quality of these drilled holes. Various drilling processes have been used in bolted and riveted joints for the assembly of composite structures. These joints demand defect-free and precise holes for joint strength and performance. Most common defects during drilling of composites are peel-up delamination, push-out delamination, geometric defects and thermal damages. Among these defects of drilling, delamination is considered the major defect. Literature shows about 60% rejection in the final assembly of aircraft manufacturing, because of delamination defects [4]. Drilling is usually the final machining operation before assembly; hence, delamination measurement and prevention are necessary ingredients of economic manufacturing. It is necessary to understand behavior of composite materials during drilling process to improve the performance. This chapter

presents a discussion on drilling of composites. The following sections discuss the drilling process and special drills developed by researchers, major defects in drilling especially on delamination damages and strategies for reducing the same.

## 4.2 Drilling processes

Hole making by conventional drilling is one of the most common processes in secondary machining of composites due to the need for fastening in mechanical parts and structures. Many nonconventional machining processes are developed as an alternative to conventional machining process, which includes laser beam drilling [5–6], water-jet drilling (with or without abrasives) [7], ultrasonic drilling [8–9] and electrical discharge machining [10–13]. Among the conventional drilling processes, twist drill performs better in terms of economy for machining composites. Currently 40% of machining in composites concentrates on hole making [14]. Because of lack of optimization in processes, chances of rejection in finished products is up to 60% due to poor quality of holes resulting in wastage of money [4]. The twist drill has complicated tool geometry in comparison to a straight edge tool. The efficiency of its cutting action with twist drill depends on the rate of efficiency of cutting at the outer diameter of the drill. The chisel edge and the lips near the center of the twist drill have a negative rake angle. The effect of a large negative rake angle is to fortify the action and make chip formation difficult. Following sections discuss conventional drilling with special drill bits and nonconventional machining processes, which includes laser machining [15–16], water-jet machining [17–18] and electrical discharge machining [19] in composites.

### 4.2.1 Conventional drilling

Conventional drilling of composite laminates with twist drill bits and with special intricate drills has shown greater attention in the industries. The major objectives of this research on conventional drilling in composite laminates can be subdivided into four major categories as follows:

1. Comprehensive experiments: A wide range of experiments are conducted by researchers to study the effect of parameters (such as feed rate, drill bit geometry, spindle speed and materials) and on output responses (such as thrust force and delamination) [20, 21].
2. Delamination studies: The major objectives of these studies are to reduce the delamination induced by drilling in composite laminates [22].
3. Tool materials: Effects of tool materials and drill bit geometry on quality and thrust forces exerted during drilling of holes [23].
4. Tool wear: Effect of tool wear on quality of holes due to thrust forces [4].

### 4.2.2 Grinding drilling

Park et al. [24] introduced grinding drilling process for composite laminate machining to improve the drilling performance with reduction in delamination. Metal-bonded PCD particles are introduced in drill bit, thereby increasing the strength and wear resistance of drill bit for machining of composites. The core of the drill bit is hollow and material removal takes place by grinding, and drill bit does not have any chisel edge in this case. As a result of this, the thrust force is much lower compared with twist drill bit in conventional machining processes [25].

Among the advanced types of twist drilling, vibration-assisted twist drilling (VATD) has shown tremendous scope in composite machining. In VATD, a low (<1,000 Hz) or high (>1,000 Hz) frequency and low amplitude vibration is superimposed on a twist drill bit along the feed direction during drilling. In VATD process, drilling is carried out intermittently with pulsed machining compared to continuous machining in conventional drilling process. The delamination effect is reduced in VATD during composite laminate machining. The experimental study has shown that drilling efficiency [26] and tool life [27] are much better with respect to conventional composite drilling process.

### 4.2.3 High-speed drilling

The demand for higher productivity has increased the need for high-speed drilling in machining of composites. High-speed drilling also reduces delamination effect in composite machining. The entire machining setup requires the high-speed drilling machine system, which makes it more expensive [28, 29]. The delamination effect is reduced in this process mainly due to lower thrust forces.

### 4.2.4 Nonconventional drilling processes

For the past 40 years, more than 25 nonconventional machining processes have been introduced and implemented in production. Each of these processes has its own benefits and limitations and cannot substitute for another. These processes are used to produce intricate profiles on various engineering materials with high accuracy without any subsequent processing steps. So these processes eliminate further processes such as finishing steps as seen in conventional machining processes, thereby reducing the time duration in production. High aspect ratios of 100:1 that are not met easily in conventional processes are attained in nonconventional machining processes. All these have resulted in the steady growth of nonconventional machining processes with promising results.

The nonconventional machining processes have better capabilities over conventional processes in terms of machining harder materials, compactness, reducing cost of machining and so on. Most of these processes are controlled automatically, thereby providing ease of operation, reliability and repeatability, resulting in wide acceptance of the processes. Many of these processes are automated with vision systems, laser gauges and other inspections systems. In addition, they have the capability to adjust with various process parameters to get better output results. These advantages are leading to wider acceptance among manufacturing engineers, product designers and metallurgical engineers [30]. The nonconventional machining processes can machine metals and alloys irrespective of their material properties. The workpiece shape and size to be produced influence the selection of the machining process. Though nonconventional machining processes are not replacing conventional machining processes, their relevance lies in the reliability of the process and the quality achieved.

Miniaturization of the products and processes is the latest trend, since one can derive the following benefits from such products and processes:
–   Simplicity
–   Occupy less space
–   Low power consumption
–   Flexibility

Composite machining in conventional process is found to be difficult especially while machining heterogeneous and anisotropic fiber-reinforced composite material due to its low thermal conductivity, heat sensitivity and the abrasive nature. In conventional methods, tool materials, tool geometry and operating conditions must be properly optimized to lower heat generation rates and avoid thermal or mechanical damage. In most of the conventional processes, the surface quality obtained is poor due to high tool wear and low cutting rates. The major objective in composite machining with nonconventional process includes either improving surface quality or increasing cutting rates that are difficult in conventional processes.

### 4.2.4.1 Ultrasonic machining

In ultrasonic machining (USM), the interface between the tool and the workpiece is filled with abrasive slurry. The tool is moved toward the workpiece under a certain static load. Either the tool or the workpiece vibrates at an ultrasonic frequency. The abrasive slurry is mainly a mixture of abrasive material suspended in water or oil. The material removal is caused by the impact of the abrasive particles in the slurry between the tool and the workpiece resulting in micro chipping due to vibration in the ultrasonic range. Soft steel and stainless steel are commonly used as tool materials. Important process variables include tool material, abrasive type, abrasive concentration, abrasive grain size, static load and vibration amplitude [31].

### 4.2.4.2 Ultrasonic Vibration-assisted machining

Ultrasonic vibration-assisted (UV-A) machining is the category of machining processes during which ultrasonic vibration is applied on either the workpiece or the cutting tool. UV-A machining processes that have been reported to machine three types of composite materials: (1) metal-matrix composites, (2) plastic matrix composites and (3) ceramic matrix composites. These processes include UV-A drilling, UV-A turning, UV-A grinding, rotary USM, UV-A electrical discharge machining and UV-A laser-beam machining.

The UV-A drilling uses a drill to cut or enlarge a hole in a workpiece with ultrasonic vibration applied on either the drill or the workpiece in the feed direction, as illustrated in Figure 4.1. The ultrasonic vibration is usually provided on the workpiece because it is more difficult to provide it on a rotating drill. However, when the workpiece is much large or much heavy, a vibrating tool will be preferred. Major process variables in UV-A drilling include drill type, rotation speed, feed rate and vibration amplitude [31].
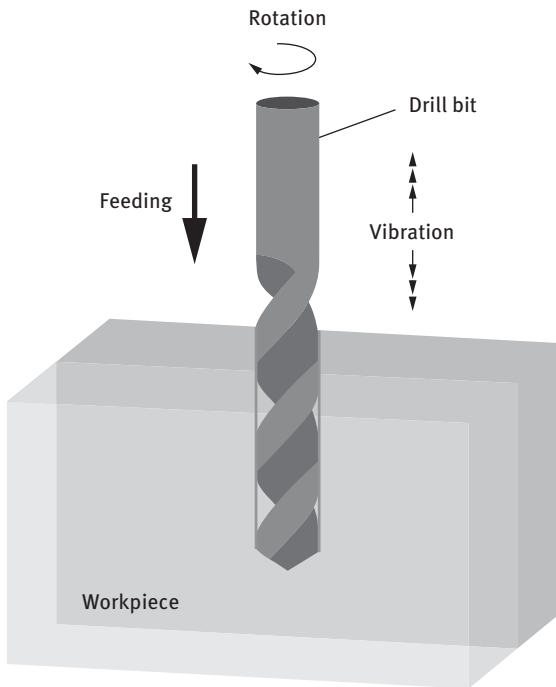


**Figure 4.1:** Schematic representation of ultrasonic vibration-assisted drilling process [31]

### 4.2.4.3 Laser machining

In laser drilling, a stationary laser beam with its high power density melt or vaporize material from the workpiece. In principle, laser drilling is governed by an energy balance (Figure 4.2) between the conduction heat into the workpiece and irradiating energy from the laser beam, the energy required for a phase change in the workpiece
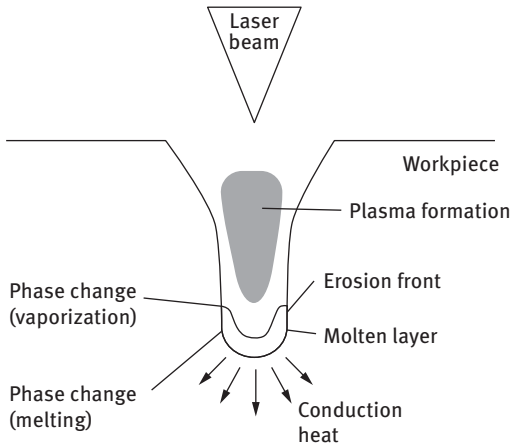
Laser
beam

Workpiece

Plasma formation

Erosion front

Phase change
(vaporization)

Molten layer

Phase change
(melting)

Conduction
heat

**Figure 4.2:** Schematic representation of laser drilling process [31]

and the energy losses to the environment. Energy losses occur for a number of different reasons, some of which are as follows: (1) when the material is being heated above the required temperature for melting, (2) plasma formation, (4) the low absorptivity of the material, (5) the convection of heat due to the use of gas jet and so on. However, the advantages ensuing from the use of laser drilling instead of mechanical drilling have to do with (1) its thermal nature (which does not depend on the mechanical properties of the workpiece), (2) the higher accuracies achieved and (3) the higher machining rates [31].

#### 4.2.4.4 Electric discharge machining

Electric discharge machining (EDM) can machine hard materials, provided that the ceramics have a sufficiently small electrical resistivity (<100 Ω cm). However, in practice, for some EDM process such as sinking EDM, the process is very difficult due to the difficult cooling conditions and flushing. EDM is preferred as a precision tool in machining conductive composites and ceramic composites with electroconductive phases [31].

#### 4.2.4.5 Electrochemical discharge machining

It is envisaged that hybrid processes such as electrochemical discharge machining (ECDM), which combine the actions of electrochemical machining (ECM) and EDM can increase the material removal rate to above that of either of the individual process in the machining of MMCs. Hybrid processes like electrochemical arc machining (ECAM), have shown tremendous scope in machining electrically conductive materials. The principles of metal removal by electrochemical process and electric discharge process are incorporated in the process.

ECAM has proved to improve the material removal rate from 5 to 50 times of those using individual processes of ECM and EDM

Electrochemical spark machining (ECSM) is another hybrid machining process, which is primarily used for shaping electrically nonconductive materials, such as glass, composites and ceramics. In ECSM, material from the workpiece is removed by the heat produced by sparking in the vicinity of the workpiece. With regard to the application of ECDM for shaping MMCs, very little information can be found in the open literature. Nonetheless, some results have shown that it is an ideal method for shaping particulate MMCs. The main advantage of ECDM over EDM, in addition to its higher material removal rate, is that it is a more stable machining process in nature than EDM, because ECDM uses a conducting electrolyte as the working medium, rather than dielectric as is the case with EDM. This gives rise to a relatively wide machining gap for electrical discharging and such a condition facilitates the removal of machined debris. When compared to ECM, ECDM again provides a higher material removal rate, but more importantly, due to the effect of the electrical discharge, a better surface finish can be obtained [31].

### 4.2.4.6 Water-jet machining

Water-jet cutting was introduced in 1971 as an economic process for making intricate shapes. Water-jet cutting is used on composites with organic, metal and ceramic matrices for operations such as cutting, milling, turning and drilling. The material is removed basically by localized shearing when a thin waterjet with very high pressures and high velocities impact on the workpieces. Pressures up to 400 MPa are used, and water jet diameters are in the 0.08–0.5 mm range. With pure water, aramid-epoxy or glass-epoxy laminates up to 6.35 mm thick can be cut, whereas for graphite-epoxy the upper limit is about 0.15 mm. The machining performance can be improved by mixing abrasive particles with water with higher speed of four times than conventional machining process [32, 33].

## 4.3 Drill bit classification

Drill bits of different geometries are used for drilling composite materials depending on their suitability to achieve efficient hole making. They can be generally classified into conventional type drill, special type drill and compound type drill. Based on the shape and application of the drills further subdivision may be done as shown in Fig. 4.3.

Drill bit geometry can also be classified into six categories, which include (1) twist drill bit, (2) step drill bit, (3) Brad-point drill bit, (4) slot drill bit, (5) straight-flute drill bit and (6) core drill bit. A few typical types of twist drill bits are shown in Fig. 4.4.
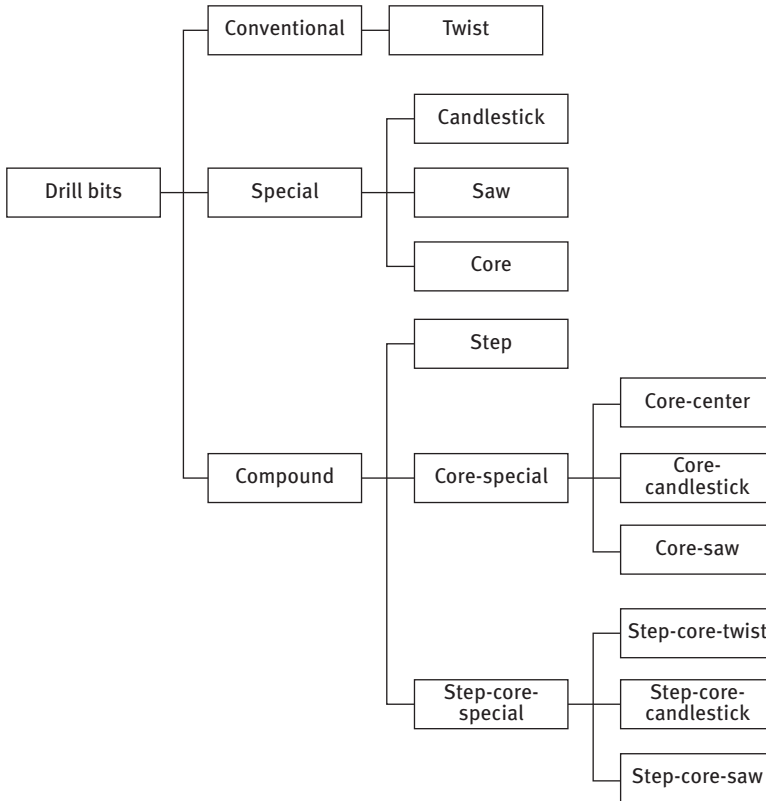
**Figure 4.3:** Classification of drill bits [31].

The quality of drilled holes depends mainly on the drill bit geometry [34, 35]. Tool properties such as longer tool life [21, 36] and reduction in delamination depend on the tool materials[37, 38, 39]. The benefits and advantages of using drill bits with different geometry and materials in drilling of composite laminates are discussed in detail in the following sections.

### 4.3.1 Twist drill

Twist drill bits made of carbides or high-speed steel (HSS) are the primary attraction in drilling of composite laminates. The twist drill wears severely when the SiC particle content in the composite is high. The main wear form was grinding abrasion, since the hardness of the matrix is lower than that of the SiC particles. The main edges and the chisel edge suffer more severe abrasion in conventional drilling [31]. The thrust force and torque increase with the rise in feed rate and drilling depth. In fact, the twist drill has quite complicated tool geometry in comparison to a straight edge tool. The
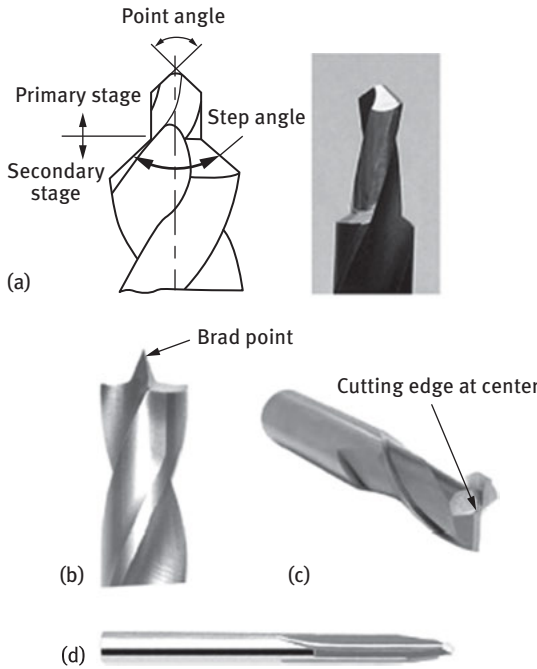
**Figure 4.4:** Typical drill bits: (a) step drill, (b) brad-point drill, (c) slot and (d) straight flute drill [39].

efficiency of the cutting action varies, being most efficient at the outer diameter of the drill and least efficient at the center. The chisel edge and the lips near the center of the twist drill have a negative rake angle. The effect of a large negative rake angle is to fortify this action and make chip formation more difficult. The relative velocity decreases linearly toward the center of the drill, approaching zero, which limits its performance in generating the hole. As a result, the materials under the chisel edge of the drill point that penetrates into the hole are more likely to be extruded than cut. The thrust force for pushing the twist drill through work is therefore high and this thrust force and the heat generated make the chisel edge of the drill point wear. Owing to the uncut thickness (last lamina) withstanding the drilling thrust force as the chisel edge approaches as the exit plane, delamination can occur.

### 4.3.2 Candlestick drill

Candlestick drills are composed of mainly a twist drill and a saw drill. They are extensively used for drilling composite materials. The thrust force of the candlestick drill can be considered as a concentrated center load with distributed circular load [31]. As in this drill the total thrust force is distributed to the periphery it allows a higher critical thrust force.

### 4.3.3 Saw drill

Saw drills are more complicated in drill geometry and manufacture compared with twist drills. The saw drill has in fact an equally spaced discrete loading during drilling. Therefore, the thrust of the saw drill can be regarded as a uniform circular load by proposing an analytical model for its discrete cutting edges. Saw drills can provide better machining quality in drilling composite laminates. One reason is that the saw drill utilizes the peripheral distribution of thrust for drilling. However, the cutting edges of the saw drill are prone to rapid wear in drilling composites because the cutting edges are very sharp. For graphite-epoxy or glass-epoxy, suitable tool materials are suggested as polycrystalline diamond (PCD) or solid tungsten carbide [33].

### 4.3.4 Core- drill

A core drill is a hollow grinding drill with bonded diamonds and a limited thickness. This tool results in a much smaller thrust and much better hole quality when compared with a twist drill in the drilling process. In general, the core drill is used for drilling hard, brittle materials, as in civil engineering structures, jewels and glass. However, the saw drill is a special type of core drill in drilling applications, where the thickness of the core drill approaches zero [31].

### 4.3.5 Step drill

The step drill can be considered to be composed of a primary stage and a secondary stage. HSS step drills allow for drilling multiple hole sizes with one bit. It is specially designed to automatically deburr holes as it drills. A balanced double flute design minimizes chattering [33].

### 4.3.6 Core-centered drill

The core-centered drill is physically an intermediate between the twist drill and the core drill [31]. The center of the circular core is provided with a twist drill. During machining the core-centered drill exerts a thrust force on the laminate that is composed of concentrated central force and the annular area force and it offers larger critical thrust force before the onset of delamination [31].

### 4.3.7 Core-candlestick drill

The thrust force of the core-candlestick drill can be considered as a sum of concentrated central load, periphery circular load and the annular area load. The core-

candlestick drill exerts a thrust force on the laminate that is composed of the concentrated force, the periphery circular force and the circular area force [31].

### 4.3.8 Core-saw drill

The thrust force of the core-saw drill can be considered as a periphery circular load plus the annular area load. The core-saw drill exerts a thrust force on the laminate that is composed of the periphery circular force and the circular area force [31].

### 4.3.9 Brad drill

Brad-point drill bits are designed to drill smooth, clean cuts in wood. The brand-point tip provides easy positioning and accurate starts. Extra-wide flutes yield fast chip removal.

### 4.3.10 Reamer drill

The built-up reamer drill consists of cutting edges made on the arc of a circle with the inclination of the plane of the main cutting edge relative to the plane perpendicular to the sweep axis [40, 41]. This reduces the thermal stress and power on the cutting edge, which leads to increased durability, reduced wear and better surface quality. Hole machining can be carried out on universal vertical drilling machine. Teeth cutters are attached to the reamer by means of special clamps and screws [42]. High heat steel is used as teeth cutter materials.

### 4.3.11 Special step core drill

Several studies have proved that delamination is related to the thrust force in drilling composite materials. The diameter ratio and the feed rate have reported to have more influence in thrust force in the case of step-core drills and step-core saw drills. The thrust force is distributed toward drill periphery in the case of step-core drill design. The step-core-special drill is composed of a core drill and special drill (twist drill, saw drill and candlestick drill). Different step-core-special drills are shown in Fig. 4.5. The diameter ratio may be a viable alternative for the step-core drill in terms of drilling thrust. Step-core-saw drill offers the highest drilling thrust force compared with other drills. The diameter ratio of step-core drill influences the thrust force when drilling composite materials. HSS twist geometry is the most
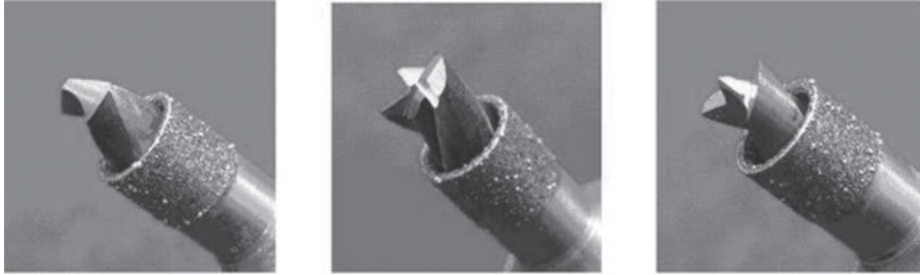
**Figure 4.5:** Different step-core drills: (a) step-core-twist drill, (b) step-core-saw drill and (c) step-core-candlestick drill [43].

commonly used type of drilling tool due to its outstanding performance with regard to better chip removal, availability, mass production and cost-effectiveness. The chisel edge, point and helical angles are the most important parts of twist drill design geometry. The quality of drilled hole depends greatly on the drill geometry, design, materials and selected drilling parameters [43]. Different drill bit materials used for drilling of composite materials is presented in the following section.

## 4.4 Drill bit materials

Drill bit materials in composite machining include HSS, coated cemented carbides, uncoated cemented carbides (ISO grades K10, K20, etc.) and PCD.

### 4.4.1 Carbide tools

Carbide drills perform better in terms of wear resistance, delamination effect and surface finish when compared with HSS under comparative low speed and feed at high temperatures when drilling the same composite materials. When the radius apart from the corner was measured, almost null wear land was shown in the flank surface of carbide drills, whereas HSS drill had considerable wear [44].

### 4.4.2 Diamond-coated drill

The biggest obstacle to the widespread use of diamond coatings in machining is poor adhesion of the diamond film to the substrate. The performance of diamond-coated tools is critically dependent on the workpiece material, feed rate, substrate type, cutting edge geometry and preparation and coating thickness [45].

### 4.4.3 Polycrystalline diamond (PCD)

PCD provides an impressive combination of mechanical and thermal properties, which makes it one of the most advanced cutting tool materials. Its hardness, toughness and strength are greater than those of PCBN and ceramics. It is also chemically stable, has low coefficient of friction and is an excellent heat conductor. The sintered PCD tools are costlier compared to normal twist drills. The technology for high-temperature, high-pressure sintering in PCD is expensive. The cutting and grinding the cutting edge are also very difficult. This in turn increases the production cost of PCD tools. For bulk production, PCD tools are economical due to their superior tool life and higher productivity. In addition, PCD tools have a limitation of higher affinity for ferrous metals at high temperatures [33]. The helical PCD drill geometry has the best overall performance when compared with other CC drills, but more reactive to feed rate changes, when delamination is considered [44].

The abovementioned sections present different drilling processes and drill bit geometries and materials that have been used for drilling of composite materials. The following sections deal with the drilling defects on composite materials.

## 4.5 Drilling defects

Drilling is the final operation prior to assembly, since generally reaming is not carried out in these materials. Therefore defect-free drilling is an essential requirement [46]. There are several methods to make holes in composite materials, of which conventional drilling is the most widely used method [3]. Drilling defects on composite materials can be listed as follows: peel-up delamination, push-out delamination, geometric defects and thermal damages [47]. Figure 4.6 represents the factors that influence hole quality in drilling of composite materials. The important factors among them are listed below.

1. Type and form of fibers
2. Fiber orientation
3. Primary manufacturing methods
4. Machining conditions
5. Fiber processing and arrangement
6. Type of drilling operation

### 4.5.1 Delamination and its mechanisms

Delamination is one of the important defects that cause the failure of composite structures. It is the separation of layers from each other in a laminate composite material
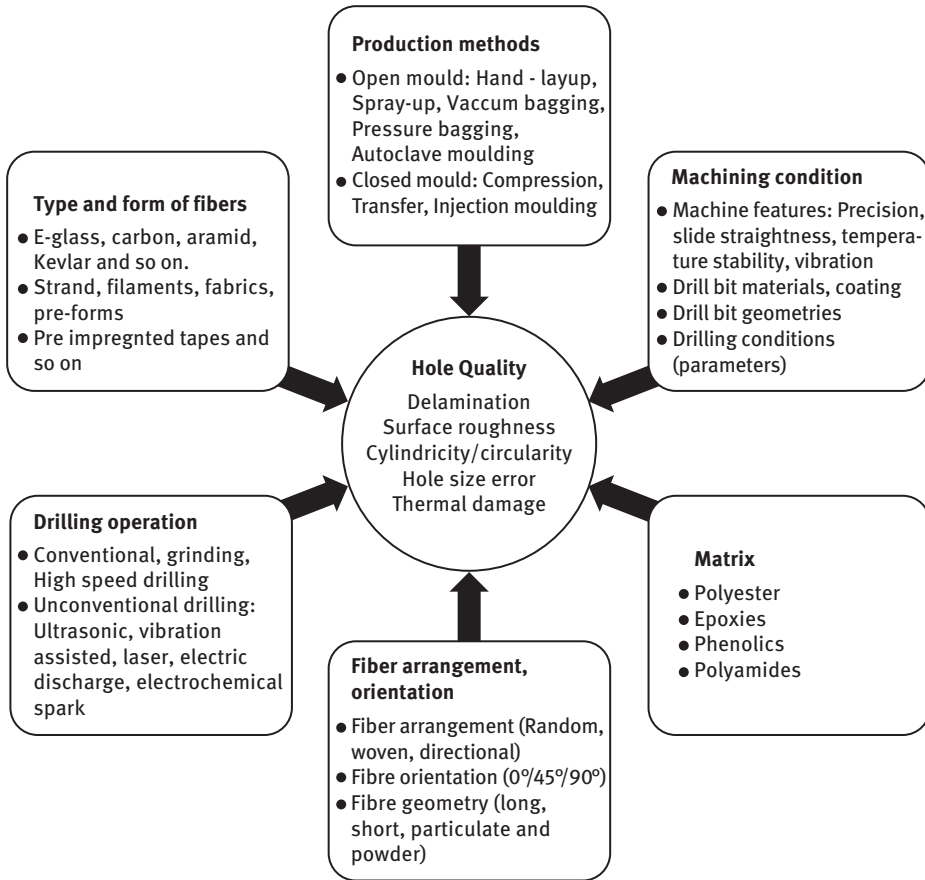
**Figure 4.6:** Factors effecting the hole quality in machining of composite materials.

and causes reduction in its mechanical strength. Delamination occurs during drilling of composite at different layers; however, it is more severe at exit when compared to entry. At intermediate layers this damage is less. During drilling at the hole entrance the cutting tool contacts the workpiece and due to the shearing action the first layers separate from those immediately below. It is called peel-up delamination. During drilling at the hole exit, the force exerted by the drill bit on the remaining few layers causes them to separate from each other. This is called push-out delamination. Figure 4.7 shows a schematic representation of peel-up and push-out delamination.

### 4.5.1.1 Measurement of delamination

The severity of delamination can be assessed by measuring the dimensions and nature of the delamination damage. These measurement methods are used to
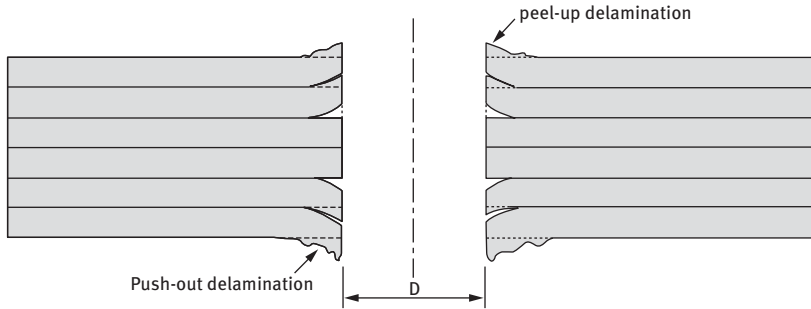
**Figure 4.7:** Schematic representation of peel-up and push-out delamination

evaluate delamination assessment factors to facilitate the analysis of the influence of the machining factors on the delamination of different composite materials. Major methods used in measuring delamination are as follows: profile projector, X-ray computerized tomography, ultrasonic C-scan, visual methods, image processing, scanning acoustic microscopy, acoustic emission, radiography and shadow moire laser interferometry. Researchers are also using machine vision systems to capture images of high quality for further processing and measurement of the damaged zone. The detailed description of these methods is presented in literature [48–50] may be refer to

- Profile projector
- X-ray computerized tomography
- Ultrasonic C-scan
- Visual methods
- Image processing
- Scanning acoustic microscopy
- Acoustic emission
- Radiography
- Shadow moire laser interferometry
- Machine vision system

#### 4.5.1.2 Assessment of Delamination

There are different techniques used by researchers to assess the delamination. Abrao et al. [51] showed the principal parameters that were used by the researchers to quantify delamination. Two different approaches used by researchers are as follows: (1) dimensional parameters such as delamination area or length and (2) dimensionless parameters such as ratio of damaged area to the hole area, ratio of maximum diameter of the delamination zone to the hole diameter and so on. This ratio allows comparisons of the results obtained by different machining conditions. Babu et al. [48] presented the overview of various delamination factors and their relative merits and demerits. Recent works of author and his colleagues altered equivalent delamination factor to
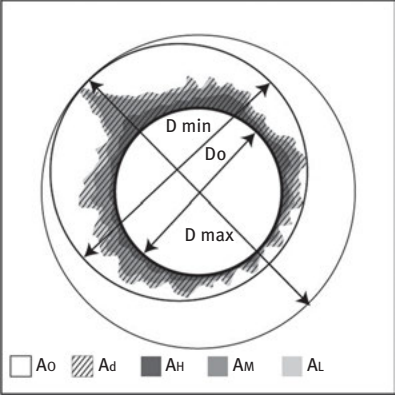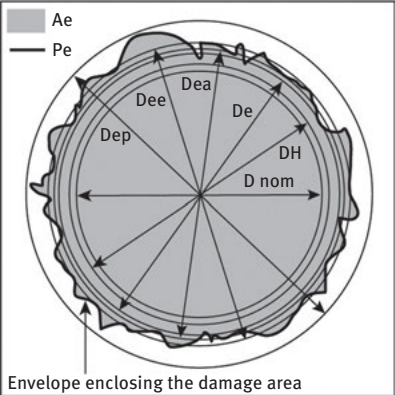
refined equivalent delamination factor in which the envelope enclosing the damaged area is used to calculate equivalent diameter [52]. Even this factor does not consider the crack length in the delamination damage assessment, hence, they proposed a comprehensive delamination assessment factor called effective equivalent delamination factor (FEED), which could be used for both conventional and high-speed drilling [53]. Complete parameters used for assessment of delamination are shown in Figure 4.3. Different methods used for the assessment of delamination are tabulated in Table 4.1 [54]. Lissek et al. [55] used adjusted delamination factor and conventional delamination factor with additional characteristic values considering shape and orientation of drilling-induced delamination for damage quantification. The details are shown in Table 4.1 and Figure 4.8.

The delamination factors describe the extent of delamination in absolute values or in ratios. These do not take into account the shape and orientation of the delamination around the drilled hole. Additional characteristics can be introduced to rectify this [55]. Through statistical analysis, analogical to surface roughness measurement, two factors for skewness and kurtosis are developed, which evaluate how concentric or skewed the damaged area is with respect to the drilled hole. The shape of the delamination profile is evaluated by two form factors. The conventional delamination factor, $F_d$ or $F_a$, is integrated with these factors to get a more complete evaluation of the extent, shape and orientation of the devaluation damage as shown in Figure 4.9.

### 4.5.1.3 Thrust force and its influence on delamination

The thrust force is one of important aspects in machining of composite materials as it affects the hole quality, mainly by delamination. It is proven that there is a critical thrust force below which no delamination exists [56]. The extent of delamination damage has positive correlation with the thrust force. First, analytical model for this critical thrust force for a twist drill was developed using linear elastic fracture mechanics by considering the thrust force as a concentrated single-point load and composite material with quasi-isotropic properties with uncut thickness of the layers below the drill bit for push-out delamination [7]. It was then followed by the development of special drills that give higher critical thrust force. Drill bits developed for this purpose are core drill, slot drill bit, brad-point drill bit and step drill bit. It was proven by analytical model and also experimentally that core drill allows higher critical thrust force when compared with other drill. Later, combination drill bits have been developed such as step drill, candlestick drill, core saw drill and so on. The total thrust force in drilling does not come through the center of twist drill bit as a concentrated force but spread over the chisel edge on the first phase crack opening. Hence, later studies used this thrust force as uniformly distributed load over the diameter [57]. A direct correlation exists between thrust force and the delamination. This demands to reduce reduction of the thrust force by controlling

**Table 4.1:** Different methods for evaluation of delamination factor delamination [Table from book chapter green composites].

| Sl. No | Evaluation of delamination factor | Formula used | Scheme |
|---|---|---|---|
| 1 | Conventional delamination factor($F_d$) | $F_d = \frac{D_{max}}{D_O}$ | |
| 2 | Delamination size | Delamination size $= R_{max} - R$ | |
| 3 | Two-dimensional delamination factor($F_a$) | $F_a = \left(\frac{A_d}{A_{nom}}\right)\%$ | |
| 4 | Damage ratio | $D_{RAT} = \frac{D_{MAR}}{A_{AVG}}$ | |
| 5 | Delamination factor | $F_d = \frac{A_d}{A}$ | |
| 6 | Adjusted delamination factor($F_{da}$) | $F_{da} = F_d + \frac{A_d\left(F_d^2 - F_d\right)}{A_{max} - A_O}$ | |
| 7 | Minimum delamination factor | $F_{d_{min}} = \frac{D_{min}}{D_0}$ | |
| 8 | Refined delamination factor($F_{Rd}$) | $F_{DR} = \frac{D_{max}}{D_O} + 1.783\left(\frac{A_H}{A_O}\right)$ $+0.7156\left(\frac{A_M}{A_O}\right)^2$ $+0.03692\left(\frac{A_L}{A_O}\right)^3$ | |



Scheme (top): D min, Do, D max. Legend: □ Aₒ ▨ A_d ■ A_H ■ A_M ■ A_L

| Sl. No | Evaluation of delamination factor | Formula used | Scheme |
|---|---|---|---|
| 9 | Shape's circularity | $f = 4\pi\frac{A_e}{P_e^2}$ | |
| 10 | Equivalent delamination factor($F_{ed}$) | $F_{ed} = \frac{D_e}{D_0}D_e = \left[\frac{4\left(A_d + A_0\right)}{\pi}\right]^{0.5}$ | |
| 11 | Refined equivalent delamination factor | $F_{ed} = \frac{D_{re}}{D_0}D_{re} = \sqrt{\frac{4\,A_e}{\Pi}}$ | |
| 12 | Effective equivalent delamination factor | $FEED = \frac{D_{ea} + D_{ep}}{2D_0}D_{ea} = \sqrt{\frac{4\,A_e}{\Pi}}-$ $D_{ep} = \frac{P_e}{\Pi}$ | |



Scheme (bottom): Ae, Pe, Dea, Dee, De, Dep, DH, D nom. Envelope enclosing the damage area
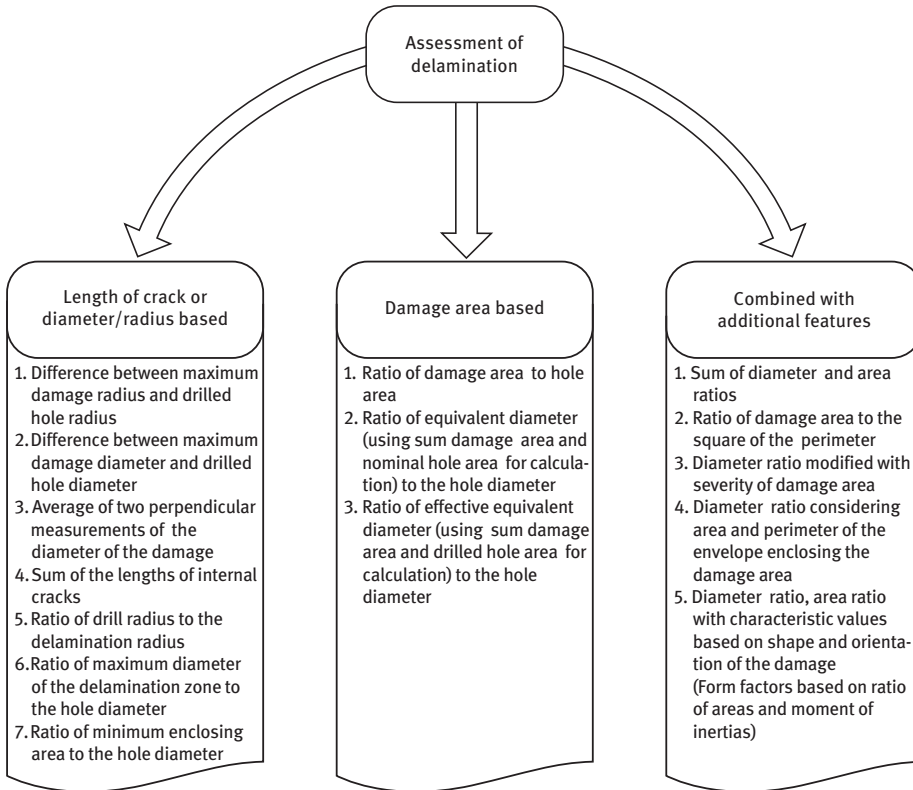
**Figure 4.8:** Parameters used by researchers for assessment of delamination.

the input variables. The following section explains the influence of cutting conditions on the thrust force.

#### 4.5.1.4 Effect of cutting conditions on thrust force

The important factors that influence the thrust force during drilling the composite materials are as follows:

1. Cutting speed or spindle speed
2. Size of the drill bit
3. Feed rate
4. Tool geometry
5. Tool wear or number of holes drilled
6. Drilling operation

#### Cutting speed or spindle speed

As the cutting speed increases, due to the high abrasiveness of reinforcement fibers, drill bit faces high frictional contact and cutting temperatures rise. This tends to
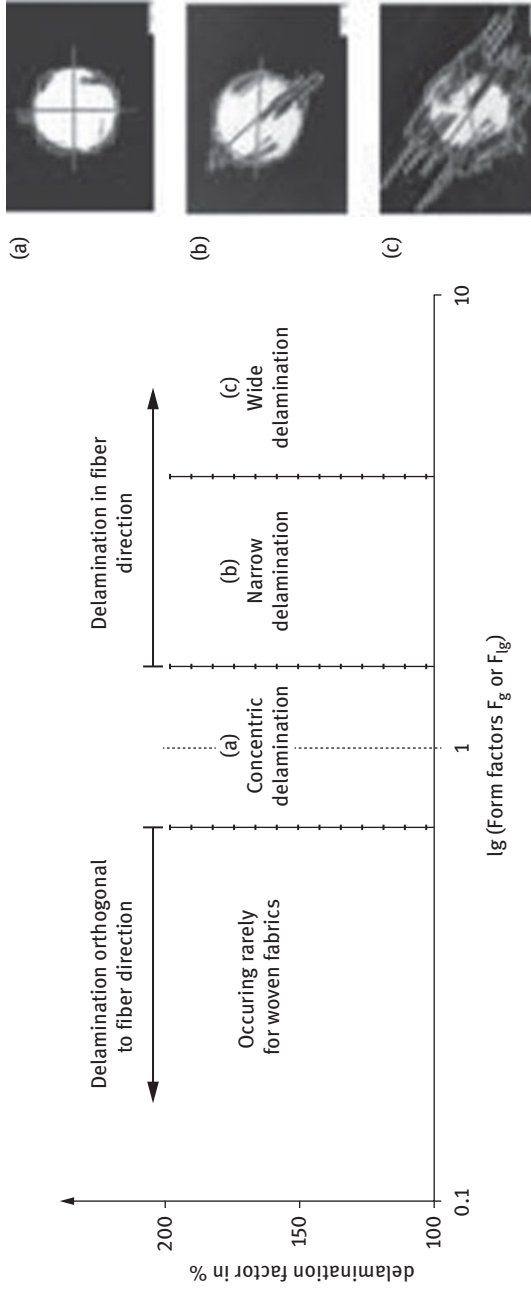
**Figure 4.9:** Quantification of delamination using form factors [55].

soften the materials and makes it easy for machining and reduces the thrust force. However, research shows that the effect of the cutting speed on feed rate is insignificant at usual speeds, but it becomes significant at higher cutting speeds [52].

### Drill bit diameter

As there is a direct relation between drill bit diameters with cutting speed, larger drill bit produces higher thrust force causing the delamination. It is advisable to drill the holes of smaller diameter to minimize the delamination damage.

### Feed rate

Feed rate is the important factor in drilling of composites. Higher feed rate implies higher productivity. Thrust forces have positive correlation with the feed rate and the influence is more significant when compared with the spindle speed [53–55].

### Drill bit geometry

Thrust force increases with point angle of a twist drill. Lower values of point angle are preferable to reduce the thrust force and hence delamination. It was proven that step drill bits, and brad-point drill bits produce less thrust force when compared with that of using slot drill bits and standard twist drill bits [61].

### Number of holes drilled/tool wear

It is difficult to drill the holes with tools with pre-wear, causing higher thrust force. It was proven that the effect of cutting speed on thrust force is higher using drills of pre-wear when compared with the fresh tools, where increase in cutting speed shows little influence on thrust force as represented in Fig. 4.10(b). It also shows that the rate of increase is gradually decreasing with the tool life [62]. However, the effect of feed rate on thrust force is notable for both fresh tool and tool with pre-wear. However, pre-wear tools show higher thrust force compared to fresh tools as shown in Figure 4.10(a). It is a known fact that there is direct correlation between delamination damage with the thrust force. Figure 4.11 shows delamination damages (push-out and peel-up) for a fresh tool and a tool with pre-wear. Hence, it is important to use proper tools of minimum tool wear to minimize this serious defect of delamination.

### Drilling operation

Researchers have been using vibration-assisted drilling for drilling of composites. It is proven that thrust force can be reduced to 20%–30% with low frequency vibration-assisted drilling when compared with conventional drilling at the same machining conditions [63–66]. It is also observed that drilling with high cutting speed generates less thrust force when compared to conventional drilling, especially at high feed rates. However, low feed rates in high-speed drilling can increase the delamination. Suitable high cutting speeds and appropriate feed rates can be used for improving the productivity.
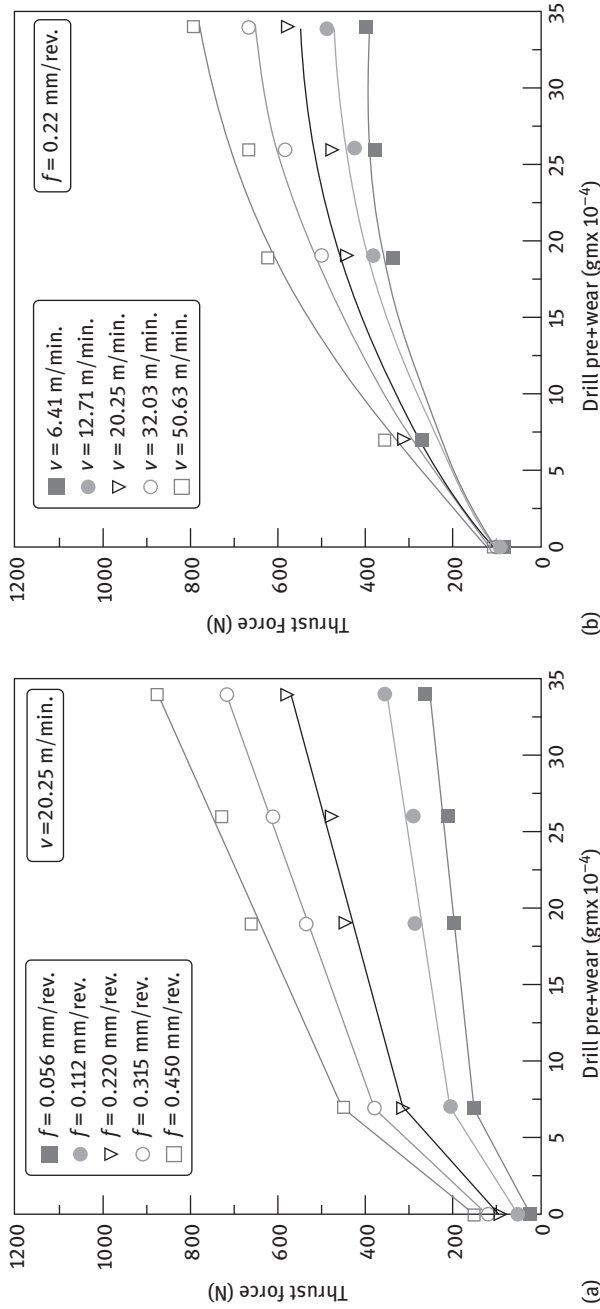
**Figure 4.10:** Effect of drill pre-wear on thrust force (a) at different feeds (b) at different speeds [62].
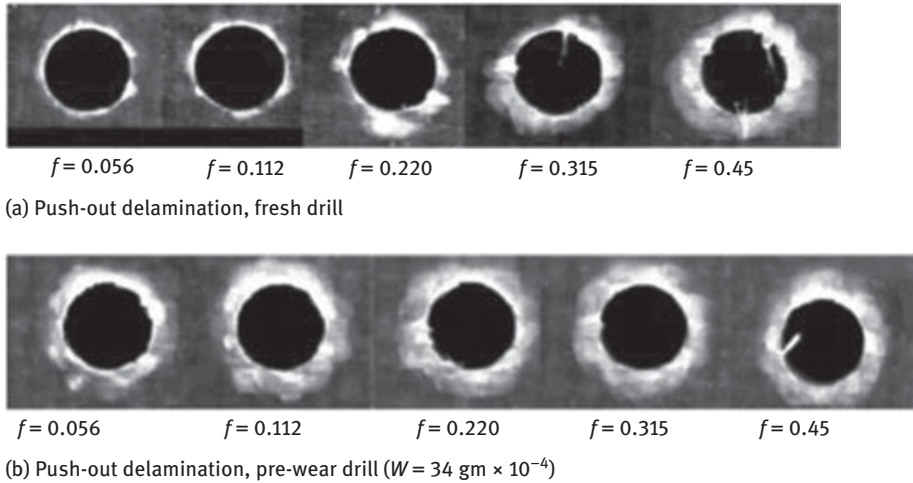
| $f = 0.056$ | $f = 0.112$ | $f = 0.220$ | $f = 0.315$ | $f = 0.45$ |

(a) Push-out delamination, fresh drill



| $f = 0.056$ | $f = 0.112$ | $f = 0.220$ | $f = 0.315$ | $f = 0.45$ |

(b) Push-out delamination, pre-wear drill ($W = 34$ gm $\times 10^{-4}$)

**Figure 4.11:** Influence of drill pre-wear and feed on delamination [62].

### 4.5.1.5 Methods to suppress delamination

Delamination is a critical defect in drilling of the composites causing rejection of parts. As explained earlier there is a critical thrust force below which no delamination exists. Its value depends on geometry of drill, properties of material of the work piece and its uncut thickness. Tsao et al. [31] presented the numerical relations for this critical thrust for different drill geometries. Researchers have tried to reduce the delamination by two approaches, that is, (1) either decreasing the thrust force during drilling (using back-up plates or back-up pressure, pilot or pre-drilled holes) or (2) increasing the critical thrust force (using special drills) The different methods and techniques to suppress or minimize this defect are briefly narrated below.

**Drilling with back-up plates**

It is a usual practice in the industry to use a back-up or support plate to reduce mainly push-out delamination while drilling of composites. It is proven experimentally that thrust force was reduced significantly with back-up while drilling composite laminate using twist drills [67]. Back-up plate provides additional support and minimizes the deflection and limits the dynamics of the workpiece. This causes reduction in push-out delamination. Later, research carried out using with and without back-up plates using core drill and slot drill showed that delamination reduces with back-up plate, because of the increase in critical thrust force. However, the mechanism of reduction of delamination with this method is not known [68]. Hence researchers mainly focus on the development of special drills to increase the critical thrust force and curtail both peel-up and push-out delamination.

**Drilling with active back-up force**

Previous method does not reduce the delamination completely. To overcome this, an efficient method to reduce push-out delamination is developed [69]. The main principle of this method is applying an adjustable back-up force applied with magnetic-driven mechanism, instead of simply applying a passive supporting back-up plate. This mechanism provides active back-up force more precisely neutralizing the push-out action of drilling thrust force that causes delamination. Figure 4.12 shows the experimental setup for providing active back-up force and Figure 4.13 shows ultrasonic C-scan images of delamination damages without and with an active back-up force. Higher reaction force (R)/active back-up force can be controlled by changing the applied voltage. Figure 4.14 shows reduction of delamination by active back-up force with varying magnitude of reaction force.
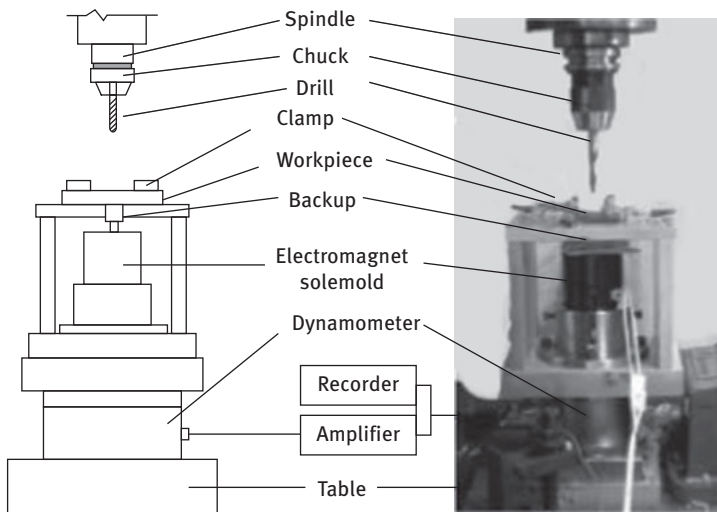


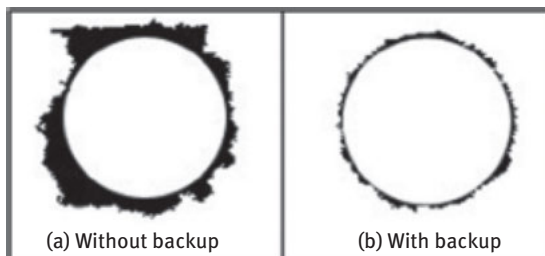**Figure 4.12:** Schematic experimental setup for applying back-up force [69].



**Figure 4.13:** Extent of delamination without and with active back-up force [69].
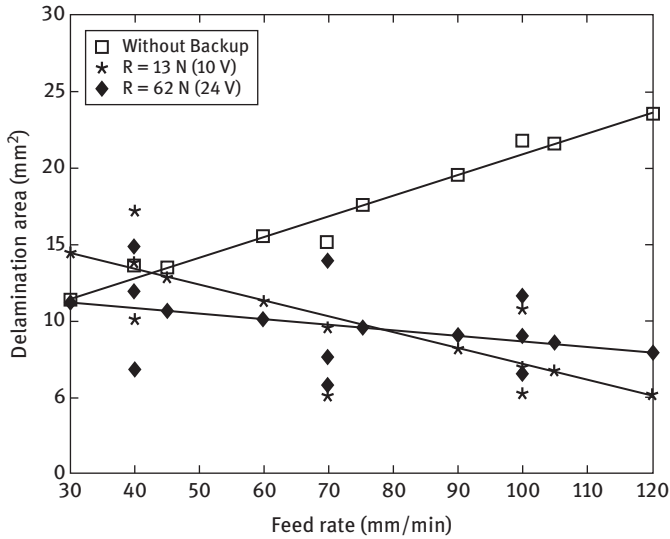
**Figure 4.14:** Delamination reduction with back-up force [69].

### Pilot or pre-drilled holes

For twist drill chisel edge and core drill removal of the chip are the major contributors to the thrust force. This contribution can be effectively avoided by drilling a pilot hole. It is proven analytically and experimentally that pre-drilled holes reduce the thrust force thus reducing the delamination damage [70, 71]. Experimental evidence provides that chisel edge contribution on the whole thrust force is 40% at lower feed rate and is as high as 60% at higher feed rates. This is the main reason for higher delamination damages at higher feed rates [72]. Thus a pre-drilled hole eliminates the thrust force due to removal of the chip [71] or due to chisel edge [72]. Pre-drilled diameter is generally same as the chisel edge length of twist drill bit to eliminate the chisel edge contribution on thrust force. In the case of core drill, this will become the inner diameter to facilitate ease of removal of the chip. With the use of these methods higher feed can be provided during drilling of composites to improve the efficiency of drilling at reduced delamination damage.

### Underwater drilling

Another method to provide back-up is underwater drilling. It is a known fact that brittle materials can be machined without shattering under water. Underwater drilling is similar to back-up drilling with supporting plates and applying back-up force by magnetically driven mechanism. In underwater drilling water provides the damping energy and reduces the delamination [73]. Figure 4.15 shows a setup that uses underwater drilling for damping to minimize the damage propagation during AWJ drilling of CFRP plate. Figure 4.16. shows the extent of delamination under different delamination
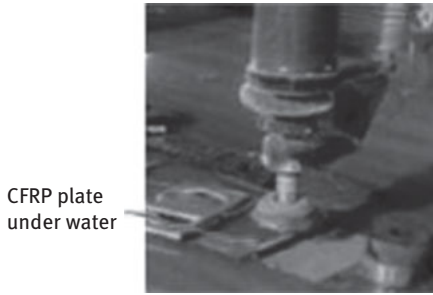
CFRP plate
under water

**Figure 4.15:** Underwater drilling of CFRP plate [73].



(a) Water pressure (bar)

(b) Stand off distance (mm)



(c) Abrasive flow rate (g/s)
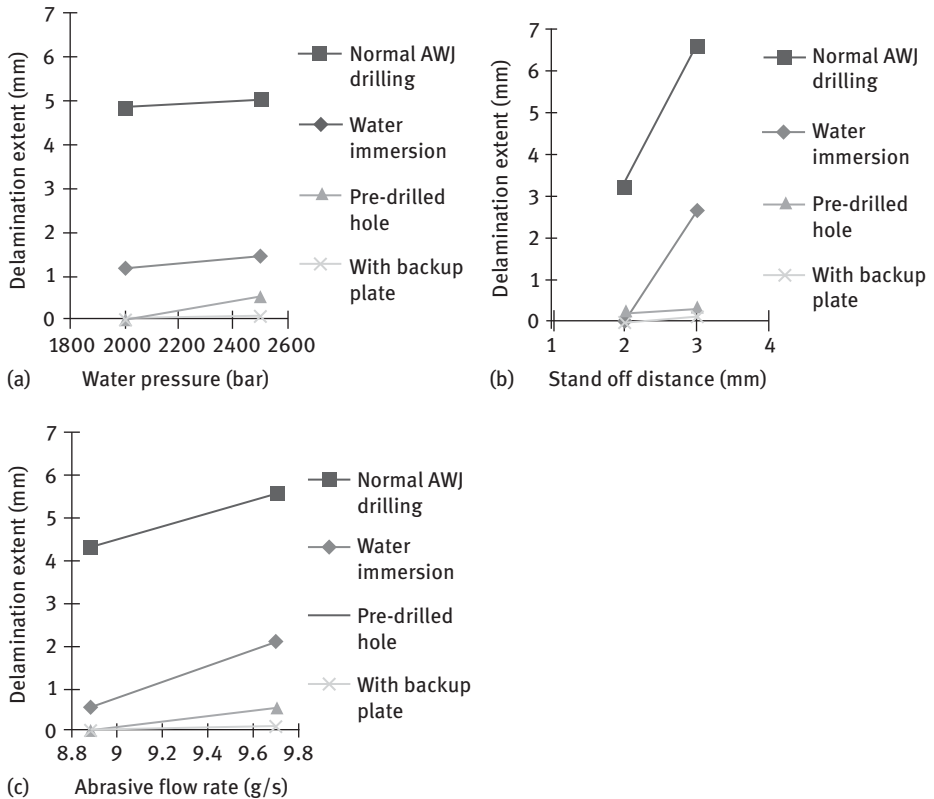
**Figure 4.16:** Comparison of delamination extent with different delamination suppression methods [73].

control techniques such as pre-drilled hole with back-up plate and underwater drilling. It is clear that back-up plate method is more efficient than the other two methods for controlling the delamination damage during drilling of CFRP composite plate using AWJ machining. However, there is need for more research to compare these methods with the delamination controlling technique using the active back-up force.

**Special drills**

As explained earlier twist drill without back-up plates provide lower critical thrust force, and higher thrust force makes conventional drilling fail in producing delamination free holes. This is the motivation behind the development of special drill with higher critical thrust force. These special tools include step drill, straight flute drill bit, core drill (hollow grinding drill) and step-core drill. Benefits of these special drill bits compared to twist drill bit are their higher critical thrust forces and higher feed rates without delamination [31]. Hence, these special tools aid to improve efficiency of drilling.

**Vibration-assisted drilling**

In this method rotation and vibration are provided to the drill simultaneously during drilling operation. The main purpose of using ultrasonic vibration is for chip breakage and reduction of friction. These mechanisms aid in reduction of thrust force and hence reduce delamination [74]. While drilling tangential cutting speeds vary along the cutting edges and increases with radius. At the chisel edge of the drill, when back rake angle is negative, cutting speed will be less. This results in increase in the thrust force in the zone. An ultrasonic vibration of suitable amplitude creates cracks in reinforcement fibers and makes this area as an impact regime, thus reducing the thrust force.

Comparison of the thrust force between conventional and ultrasonic-assisted drilling experiments is shown in Figure 4.17. This figure shows a considerable reduction in thrust force that results in the reduction of delamination damage as shown in Figure 4.18.
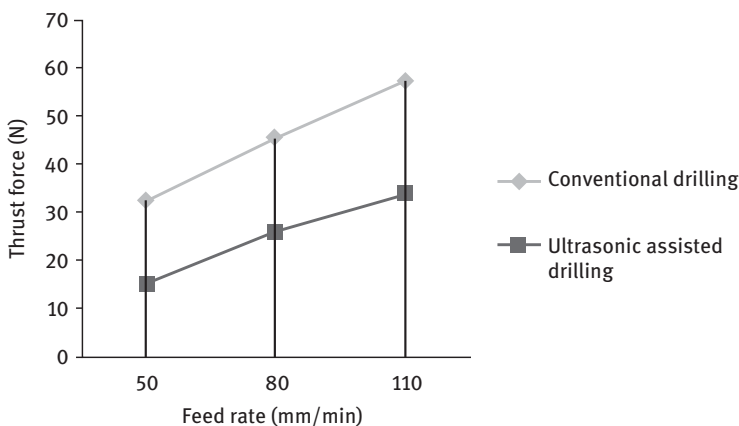


**Figure 4.17:** Comparison of thrust force of conventional and ultrasonic-assisted drilling at different feed rates [74].
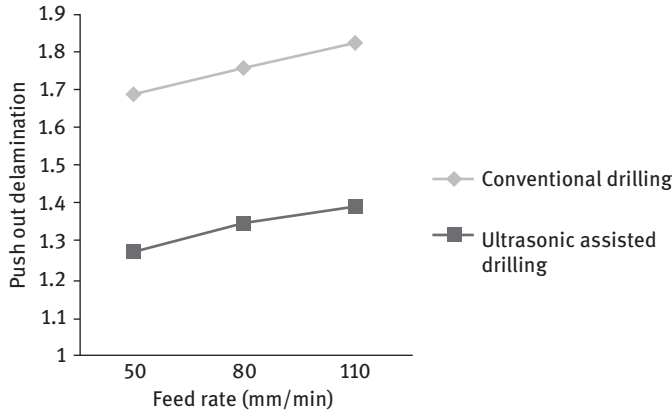
**Figure 4.18:** Comparison of push-out delamination of conventional and ultrasonic-assisted drilling at different feed rates [74].

## 4.5.2 Geometrical damages in drilling

### 4.5.2.1 Surface finish

The performance of machined hole is significantly influenced by surface finish obtained in drilling. This facilitates better integrity with the fasteners in assembly. Researchers have worked to optimize the drilling parameters to obtain a better surface finish. It was found that feed rate has greater effect on surface finish [75]. Low feed rates aid in minimizing the delamination damage at the entry as well as the exit side of hole. This results in better surface finish [76]. However, cutting speed shows lesser effect than feed rate on surface finish. Higher cutting speeds favor better finish [77]. It is shown that arithmetic average roughness values have positive correlation coefficient with feed rate and negative correlation coefficient with spindle speed [78]. Some times higher cutting speed may deteriorate machined texture. This is due the generation of higher temperatures causing the softening of the matrix of the composite [79]. Doping of multi-walled carbon nanotube (MWCNT) to carbon/epoxy polymeric composite material shows improvement in surface finish during drilling. It is shown that higher percentages of MWCNT in polymer matrix improve the surface finish because of proper severing of fibers, and less cracking of matrix. Hence there is less chance for the formation of built-up edge on hole wall [80].

Tool wear plays an important role on surface finish during drilling of composites. It is proven that drilling with drill bit of pre-wear shows higher surface roughness values when compared with fresh drills as shown in Figure 4.19 [62]. Coated tools minimize the tool wear when compared with uncoated tools and improve the surface finish. It is proven experimentally that drilling of CFRP composite plates with aluminum chromium nitride-coated tools gives better surface finish when compared with HSS [81]. Research with delamination control techniques such as pre-drilled hole,
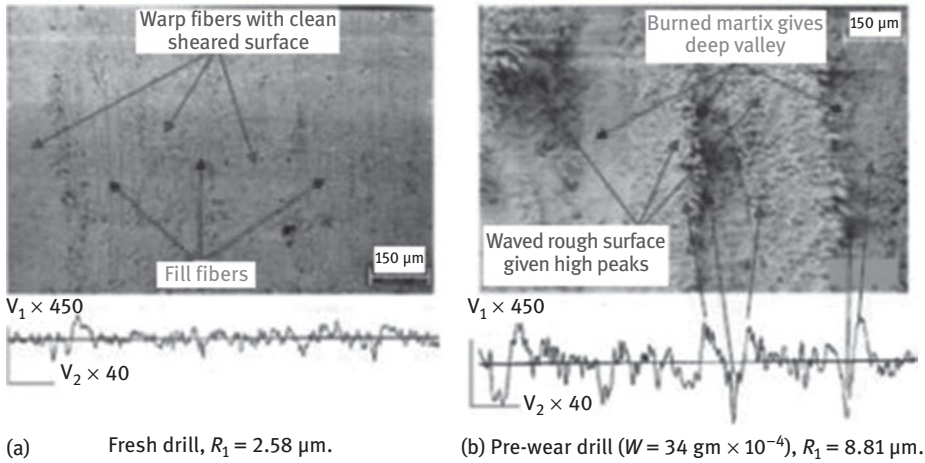
(a)  Fresh drill, $R_1 = 2.58$ μm.  (b) Pre-wear drill ($W = 34$ gm $\times 10^{-4}$), $R_1 = 8.81$ μm.

**Figure 4.19:** Surface roughness comparison, holes drilled with fresh drill and pre-wear drill [62].

back-up plate and underwater drilling show that these techniques can also be used for improvement of surface finish as shown in Figure 4.18. [73]

### 4.5.2.2 Hole size error

The accuracy of the drilled hole has a significant effect on joint performance and facilitates better assembly. The hole diameter decreases with increasing feed rate, whereas hole diameter increases with cutting speed, especially at low feed rates. The cutting temperature increases with lower feed rates because of the low thermal conductivity of composite materials [82]. Higher cutting speeds also cause vibration [83]. These cause increase in hole diameters with increasing cutting speed. Drill bit point angle also influences the hole diameter. Holes of nominal size can be obtained by drilling with higher point angled drill bits. Increasing the point angle decreases the cutting lip length and height causing decrease in tool-chip contact area. This reduces the friction at the contact area and aids in obtaining the holes of nominal size [84]. Figure 4.21 shows machinability maps for composite materials [29]. This figure shows that high spindle speeds and low feed rates cause greater hole size error. Hole size error can be negative (undersized holes) at higher feed rates.

High-speed drilling of CFRP composites in the range of 16,000–40,000 rpm shows that high spindle speeds can reduce the thrust force and thereby reduce the delamination damage [34]. However, high spindle speeds with low feed rates are not preferable; these combination increases both temperature and vibration as mentioned earlier. Figure 4.22 [85] shows a hole size error at a typical spindle speed of 1,200 rpm and low feed rate of 0.01 mm/rev as 0.95 mm, whereas at high feed rate of 0.1 mm/rev this error is only 0.02 mm during drilling of CFRP composite laminates. Investigations on
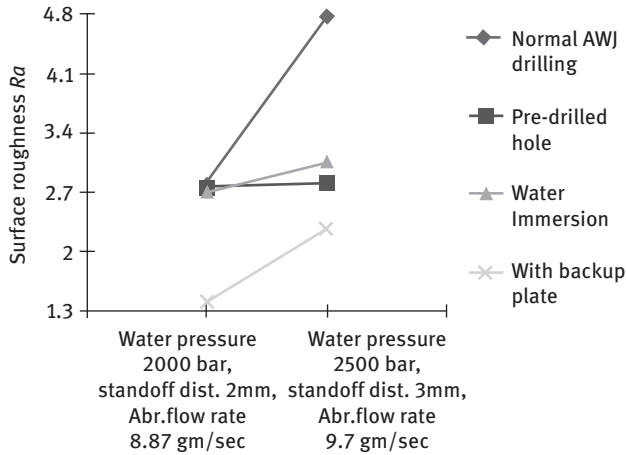
**Figure 4.20:** Surface roughness comparison of the holes drilled with different delamination suppression methods [73].

delamination damage in high-speed drilling of GFRP composites in the range of 12,000–20,000 rpm also confirm that the proper selection of process parameters would be necessary to prevent hole size errors, as shown in Table 4.2. and Figure 4.23 [53].

### 4.5.2.3 Cylindricity/circularity error

This is also called roundness error. It is the radial difference of maximum inscribing circle and minimum circumscribing circle schematically shown in Figure 4.24. This error can be measured using roundness testing machine or coordinate measuring machine (CMM).

Generally, delamination and surface finish have direct correlation with circularity error. For minimum circularity error, high spindle speed and low feed rates are recommended [86, 87]. Higher feed rates increase the fiber pull-out and the roundness error [86]. Feed rate has greater influence on roundness error compared with other drilling parameters. Drill bit geometry also affects the roundness error. Higher point angle and lower chisel edge width reduce the frictional area leading to minimum roundness error [87]. Coated drills produce holes of less roundness error when compared with uncoated drills [81]. For coated drills, as wear of cutting edges is less, these hold the cutting edge and corner integrity for longer periods of time resulting in less fiber pull-out and consequently minimum roundness error.

### 4.5.3 Thermal damages in drilling

Any machining process including drilling involves an interaction of workpiece with the cutting tool causing a frictional force. This mechanism generates heat in
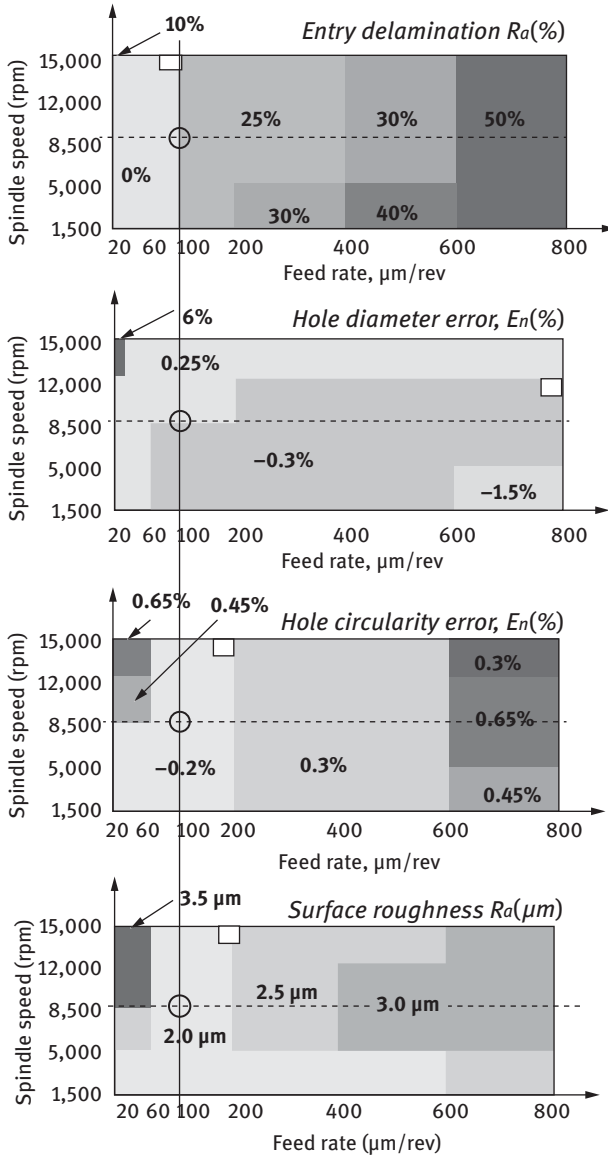
**Figure 4.21:** Machinability maps representing effect of cutting parameters on hole quality [29].

the conventional machining process. Even machining with unconventional methods such as laser drilling also causes the heating of the composite materials and damages the workpiece. Thermal defects are those defects that are generated in high temperature during drilling. Moderate temperatures generated during drilling of composites may be beneficial in softening the matrix and thereby reducing thrust force. This results in decrease in delamination. However, higher tempertures nearer or above the

Ø 5.02 mm
0.10 mm/rev

Ø 5.95 mm
0.01 mm/rev

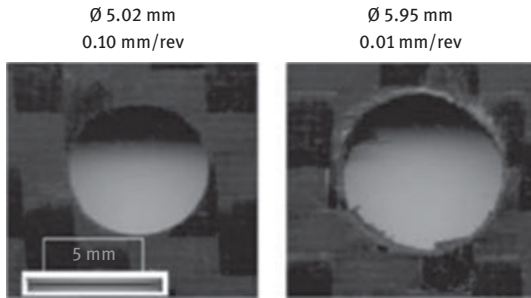5 mm

**Figure 4.22:** Hole size errors at different feed rates at 12,000 rpm [85] (Figure 4.7).

**Table 4.2:** Experimental results of diameter of hole at selected cutting conditions [53]

| Experiment No. | Spindle speed (rpm) | Feed rate (m/min) | Hole diameter (mm) for | |
|---|---|---|---|---|
| | | | 4 mm drill | 5 mm drill |
| 1 | 12,000 | 0.1 | 4.14 | 5.80 |
| 2 | 12,000 | 1 | 4.30 | 5.03 |
| 3 | 12,000 | 3 | 4.40 | 5.02 |
| 4 | 16,000 | 0.1 | 4.42 | 5.70 |
| 5 | 16,000 | 1 | 4.26 | 5.60 |
| 6 | 16,000 | 3 | 4.19 | 5.04 |
| 7 | 20,000 | 0.1 | 4.67 | 6.28 |
| 8 | 20,000 | 1 | 4.48 | 6.25 |
| 9 | 20,000 | 3 | 4.10 | 5.01 |

glass transitition temperature reduce the strength of the composite material and may cause increase in delamination [88]. Glass transition temperature for epoxy-based matrix is in between 120 °C and 270 °C. Accurate monitoring of this temperature calls for a good understanding of heat transfer models that determine the temperature distribution on the workpiece. Another aspect is the measurement of the temperature accurately by using sensors that are placed at cutting edge and at the workpiece. Prediction of the temperature distribution in the workpiece is useful for optimizing the cutting process [89, 90]. For measuring the temperature, most commonly used sensor is K type thermocouple, which is more reliable than other sensors such as infrared cameras [91].

It is a known fact that the increase of temperature at cutting edges during drilling of composite materials is much lower when compared with metallic materials. This is due to the smaller amount of heat that is generated during plastic deformation because composite laminates are brittle and chip is pulverized in the process. The temperature generated during drilling of CFRP and GFRP composites shows differing
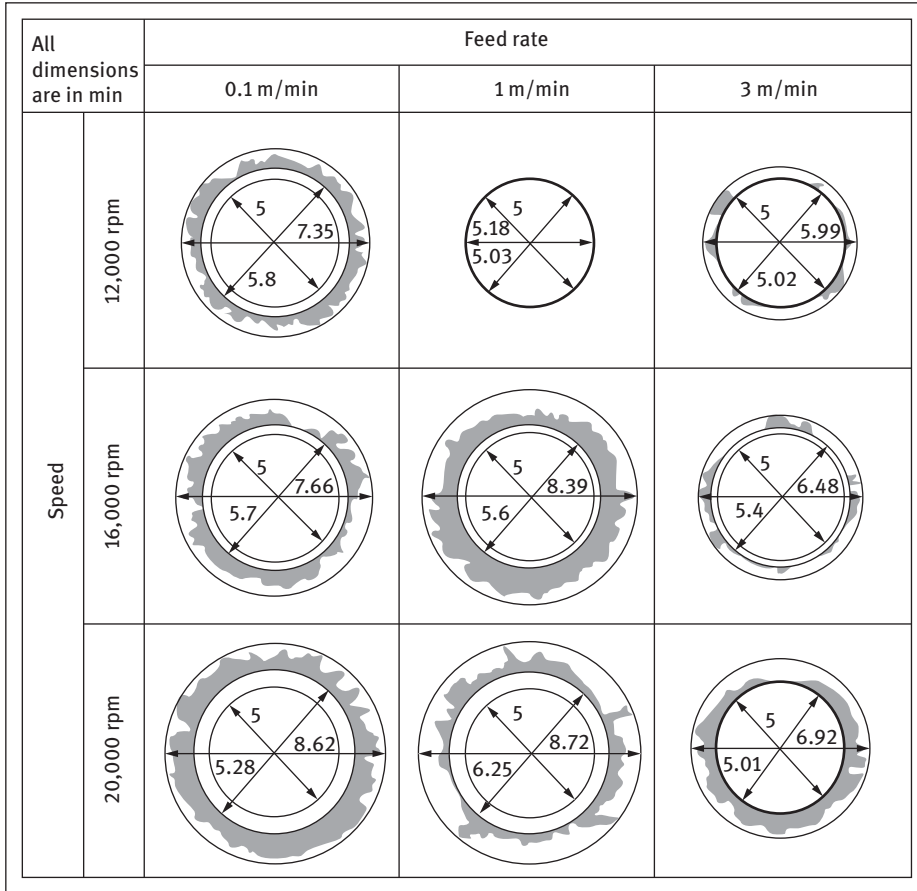
**Figure 4.23:** Processed images of drilled holes showing nominal diameter, diameter of drilled hole and maximum diameter [53].

trends. This is because of the higher thermal conductivity of CFRP compared to GFRP. Therefore, heat transfer models and temperature distribution between tool and workpiece will be different. It demands a comprehensive analysis of the heat generation and its distribution at the tool-workpiece interaction zone to understand the drilling-induced damage in the thermoplastic composite laminates, both qualitatively and quantitatively. Similar opinion is expressed by Khasaba that the correlations between thermal and mechanical damages are not fully understood [92].

## 4.6  Tool wear

The aforementioned sections present the damages occurring during drilling of composites. During the drilling process, damages also occur on the tool (tool wear) because of
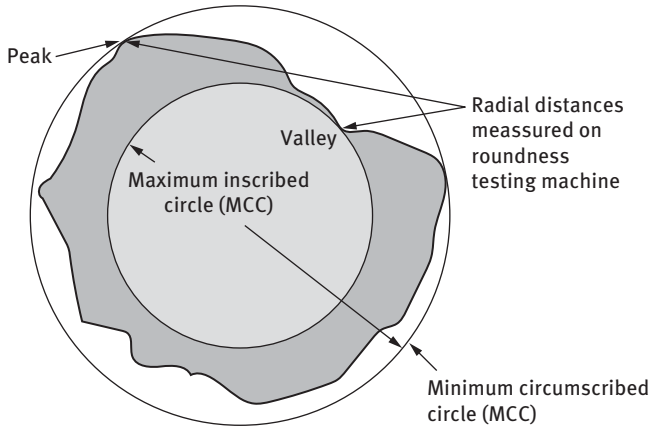
**Figure 4.24:** Roundness error measurement.

the friction and temperature at the cutting zone. The tool wear increases the thrust force and the delamination, and hence understanding of tool wear mechanisms and the cutting parameters that influence the tool wear is necessary to control the delamination.

Tool wear during drilling happens in several ways such as flank wear, wear at rake face, corner edge and chisel edge. The extents of these damages depend on a number factors such as combination of tool/work materials and cutting conditions. Different tool materials include the most commonly used HSS [38], cemented carbide [93], diamond-coated carbides [36] and aluminum chromium nitride coating on cobalt steel substrate (HSS-E) [81].

Tool wear mechanisms of drilling composites vary from that of metallic material drilling because of

1. Varying loads at the cutting edge due to anisotropic nature of composite materials.
2. Thermomechanical forces between drill bit and workpiece as composite materials are poor conductors of heat. Heat transfer from cutting zone to drill bit, but not to the workpiece.
3. Hard and abrasive fibers that cause more frictional heat leading to excessive tool wear.
4. Sticky and soft nature of matrix that makes the tool edge dull by clogging [21].

Major tool wear mechanisms during drilling of composites include the following:

1. Abrasive wear
2. Chipping
3. Adhesion

**Abrasive wear**

This type of wear occurs because of scratching of the reinforced fibers (carbon fibers in CFRP, glass fibers in GFRP) embedded in a soft matrix. This wear mechanism is

the same for both CFRP and GFRP because of abrasive nature of carbon/glass fibers. This wear occurs for both conventional as well as high-speed drilling [21, 36, 93, 94].

**Chipping and adhesion**

Chipping occurs when drill bit is unable to withstand the high stresses developed due to cutting of hard fibers. Adhesion is the carbon sticking on the flank face because of the high temperature at the cutting zone and cause wear.

In high-speed drilling of CFRP, tool wear can be divided into three distinct regions. [93]

1.  Primary wear region: At the beginning of drilling, cutting edges are sharp (when drilling with fresh tools) that are unable to withstand high stresses developed due to cutting of hard fibers resulting in chipping of drill bit. This type of wear can be observed at secondary cutting edge, at rake face, at chisel edge and at the drill bit corner.
2.  Secondary wear region: This is also called steady wear or abrasion wear and can be observed on flank faces.
3.  Tertiary wear region: This wear is because of carbon adhesion and can be observed on flank face because of high temperature

Abrasive wear on flank surfaces is the most commonly observed wear while drilling of composites [21, 36, 38, 93–96]

Tool wear while drilling of composites depends on cutting conditions such as spindle speed; feed rate and geometry and materials and coatings of the drill bits. Tool wear increases with increase in cutting speeds and feed rates. The coated drill bits give better cutting performance and less tool wear than uncoated drill bits during conventional drilling of CFRP composites [97, 98, 81].

## 4.7 Conclusions

Composite materials are emerging as advanced materials for high strength and low specific weight applications. Even though composite materials are made to near net shape, machining is necessary for assembly and dimensional requirements. Drilling is the most common machining operation in composite materials. Though conventional drilling of composites with twist drills is widely adopted, it is prone to develop many drilling defects on the workpiece. Such defects can be considerably reduced by using special drills or through nonconventional hole-making processes such as laser beam drilling, water-jet drilling (with or without abrasives), ultrasonic drilling and electrical discharge machining.

Proper selection of drilling process and parameters is important to obtain high quality holes. Drilling defects of composites depend on several factors: machining parameters and mode, and the type, nature and geometry of the tools. Delamination is a major drilling defect. Several tools are developed to increase the critical thrust

force and to reduce the delamination. Similarly, special methods such as drilling with back-up plate, back-up force, underwater drilling and ultrasonic-assisted drilling are developed to suppress the delamination. There are several techniques or methods developed to measure the delamination, and the delamination factor obtained by different techniques may differ from one another. Till now, there is no common standard in assessing the delamination factor.

Hole size error, cylindricity error and thermal damages are other drilling defects. Temperature generated during machining plays a vital role in hole quality. Moderate temperatures may be beneficial in softening the matrix, thereby reducing thrust force and, in turn, reducing delamination. However, higher temperatures near or above the glass transitition temperature reduce the strength of the composite material and may cause increase in delamination and other defects such as matrix burning and hole size error.

# References

[1]    Soutis C. Fibre reinforced composite in aircraft construction. Progr Aerosp Sci 2005; 41: 143–51.
[2]    Nagarajan VA, Selwin Rajadurai J, Annil Kumar T. A digital image analysis to evaluate delamination factor for wind turbine composite laminate blade. Compos Part B 2012; 43: 3153–59.
[3]    Liu DF, Tang YJ, Cong WL. A review of mechanical drilling for composite laminates. Compos Struct 2012; 94: 1265–1279.
[4]    Wong TL, Wu SM, Croy GM. An analysis of delamination in drilling composite materials. In: 14th National SAMPE technology conference. Atlanta, GA, USA; 1982. pp. 471–383.
[5]    Yung KC, Mei SM Yue TM. A study of the heat-affected zone in the UV YAG laser drilling of GFRP materials. J Mater Process Technol 2002; 122: 278–285.
[6]    Dubey AK Yadava V. Experimental study of Nd: YAG laser beam machining – An overview. J Mater Process Technol 2008; 195: 15–26.
[7]    Hocheng H Dharan CKH. Delamination during drilling in composite laminates. Trans ASME J Eng Ind 1990; 112: 236–239.
[8]    Hocheng H, Tai NH Liu CS. Assessment of ultrasonic drilling of C/SiC composite material. Compos Part A Appl Sci Manuf 2000; 31(2): 133–142.
[9]    Zhang LB, Wang LJ Wang X. Study on vibration drilling of fiber reinforced plastics with hybrid variation parameters method. Compos Part A Appl Sci Manuf 2003; 34(3): 237–244.
[10]   Azarhoushang B Akbari J. Ultrasonic-assisted drilling of Inconel 738- LC. Int J Mach Tools Manuf 2007; 47: 1027–1033.
[11]   Hocheng H, Lei WT Hsu HH. Preliminary study of material removalin electrical-discharge machining of SiC/Al', J Mater Process Technol 1997; 63: 813–818.
[12]   Singh NP, Raghukandan K, Rathinasabapathi M Pai BC. Electric discharge machining of Al 10% SiCP as-cast metal matrix composites J Mater Process Technol 2004; 155–156:1653–1657.
[13]   Singh NP, Raghukandan K Pai BC. Optimization by Grey relational analysis of EDM parameters on machining Al-10% SiCP composites. J Mater Process Technol 2004; 155–156:1658–1661.
[14]   Widia, Hole-making with carbides', *Technical Information Publication No. WI-T-129-00-85*, The Widia Company, Latrobe. (1985) PA, USA.

[15] Lau WS, Lee WB, Pang SQ. Pulsed Nd: YAG laser cutting of carbon fibre composite materials. CIRP Annals Manuf Technol 1990; 39:1 79–820.

[16] Lau WS, Yue TM, Lee TC, Lee WB. Un-conventional machining of composite materials. J Mater Process Technol 1995; 48: 199–205.

[17] Lemma E, Chen L, Siores E, Wang J. Study cutting fiber-reinforced composites by using abrasive water-jet with cutting head oscillation. Compos Struct 2002; 57: 297–303

[18] Shanmugam DK, Nguyen T, Wang J. A study of delamination on graphite/epoxy composites in abrasive water jet machining. Compos Part A 2008; 39: 923–9.

[19] Lau WS, Wang M, Lee WB. Electrical discharge machining of carbon fibre composite materials. Int J Mach Tools Manuf 1990; 30: 297–308.

[20] Lee SC, Jeong ST, Park JN, Kim SJ, Chao GJ. Study on drilling characteristic and mechanical properties of CFRP composites. Acta Mechanica Solida Sinica 2008; 21: 364–8.

[21] Chen WC. Some experimental investigation in the drilling of carbon fiberreinforced plastic (CFRP) composite laminates. Int J Mach Tools Manuf 1997; 37:1097–108.

[22] Stone R, Krishnamurthy K. A neural network thrust force controller to minimize delamination during drilling of graphite-epoxy laminates. Int J Mach Tools Manuf 1996; 36: 985–1003.

[23] Davim JP, Reis P, Antonio CC. Experimental study of drilling glass fiber reinforced plastics (GFRP) manufactured by hand lay-up. Compos Sci Technol 2004; 64: 289–97

[24] Park KY, Choi JH, Lee DG. Delamination-free and high efficiency drilling of carbon fiber reinforced plastics. J Compos Mater 1995; 29:1988–2002.

[25] Tsao CC, Hocheng H. Parametric study on thrust force of core drill. J Mater Process Technol 2007; 192–193:37–40.

[26] Zhang LB, Wang LJ, Wang X. Study on vibration drilling of fiber reinforced plastics with hybrid variation parameters method. Compos Part A 2003; 34: 237–44.

[27] Ramkumar J, Aravindan S, Malhotra SK, Krishamurthy R. An enhancement of machining performance of GFRP by oscillatory assisted drilling. Int J Adv Manuf Technol 2004; 23: 240–4.

[28] Lin SC, Chen I K. Drilling carbon fiber-reinforced composite material at high speed. Wear 1996; 194:156–62.

[29] Rawat S, Attia H. Characterization of the dry high speed drilling process of woven composites using machinability maps approach. CIRP Annals Manuf Technol 2009; 58: 105–8.

[30] Gary, F.B. Non Traditional Manufacturing Processes, New York: CRC Press, 1987.

[31] Hocheng H. Machining Technology for Composite Materials, Woodhead Publishing Limited, 2012.

[32] Aams RB. "Waterjet machining of composites" Composites in Manufacturing, Los Angeles, CA, USA, Jan 13–16, 1986, SME Paper EM86-113.

[33] Hashish M. Trimming of CFRP aircraft components. In: WJTA-IMCA, ed. American WJTA-IMCA Conference & Expo; 2013.

[34] Lin SC, Chen IK. Drilling carbon fiber-reinforced composite material at highspeed. Wear 1996; 194: 156–62.

[35] Zitoune R, Collombet F. Numerical prediction of the thrust force responsible of delamination during the drilling of the long-fibre composite structures. Compos Part A 2007; 38: 858–66.

[36] Iliescu D, Gehin D, Gutierrez ME, Girot F. Modeling and tool wear in drilling of CFRP. Int J Mach Tools Manuf 2010; 50: 204–13.

[37] Abrao AM, Campos Rubio J, Faria PE, Davim JP. The Effect of cutting tool geometry on thrust force and delamination when drilling glass fibre reinforced plastic composite. Mater Des 2008; 29: 508–13

[38] Kim D, Ramulu MR. Drilling process optimization for graphite/bismaleimidetitanium alloy stacks. Compos Struct 2004; 63: 101–14.

[39] DeFu Liu, YongJun Tang, W.L. Cong. A review of mechanical drilling for composite laminates. Compos Struct 2012; 94: 1265–1279.

[40] Dudak NS, Taskarina AZ, Kasenov AZ, Itybaeva GT, Mussina Z, Abishev K, Mukanov R. Hole Machining based on using an incisive built-up reamer, Int J Precis Enf Manuf 2017;18(10): 1425–1432.

[41] Dudak NS. Kasenov AZ, Musina Z, Itybaeva GT Taskarina AZ. Processing of holes with a Reamer-Broach. Life Sci J 2014; 11 (10s): 282–288.

[42] Taskarina A Z, Mendebaev T M, Dudak N S, Itybaeva G T, Musina, Z K Kasenov A Z. Improving the design of the sweep tool with peakless teeth. Sci J Shakarim Semipalatinsk State Univ 2012; 32–35.

[43] Tsao CC. Experimental study of drilling composite materials with step-core drill. Mate Des 2008; 29: 1740–1744.

[44] Ismail SO, Dhakal1 HN, Dimla E, Popov I. Recent advances in twist drill design for composite machining: A critical review. Proc. IMech E Part B: J Eng Manuf 2016; 1–16. doi:10.1177/0954405416635034.

[45] Köpf, A., Feistritzer, S., Udier, K. Diamond coated cutting tools for machining of non-ferrous metals and fibre reinforced polymers. Int J Refractory Metals Hard Mater 2006; 24: 354–359.

[46] Abrao AM, Faria PE, Campos Rubio JC, Reis P, Davim JP. Drilling of fiber reinforced plastics: A review. J Mater Process Technol 2007; 186: 1–7.

[47] Lachaud F, Piquet R, Collembet F et al. Drilling of composite structures. J Compos Struct 2001; 52(3–4): 511–516.

[48] Babu J, Philip J, Zacharia T, Davim JP. Delamination in composite materials: Measurement, assessment and prediction. In: Davim JP. Machinability of fibre-reinforced plastics Berlin: De Gruyter, 2015, 139–162.

[49] Ramesh M, Palanikumar K Reddy KH. Mechanical property evaluation of sisal-jute-glass fiber reinforced polyester composites. Compos B 2013; 48: 1–9.

[50] Babu J, Sunny T, Paul NA, Mohan KP, Philip J, Davim JP. Assessment of delamination in composite materials: a review. Proc Inst Mech Eng B J Eng Manuf. 2016; 230(11): 1990–2003.

[51] Abrao AM, Faria PE, Campos Rubio JC, Reis P, Davim JP. Drilling of fiber reinforced plastics: A review. J Mater Process Technol 2007; 186: 1–7.

[52] Babu J, Paul NA, Mohan KP, Philip J, Davim JP. Examination and modification of equivalent delamination factor for assessment of high speed drilling. J Mech Sci Technol 2016; 30 (11): 5159–5165.

[53] Babu J, Paul NA, Sonu P. Abraham, Anoop BN Philip J, Davim JP. Development of comprehensive delamination factor and it's assessment of high speed drilling. Proc Inst Mech Eng B J Eng Manuf (in press) doi:10.1177/0954405417690552

[54] Babu J, Philip J, Davim JP. Machining defects in green composites. In: Davim JP. Green Composites Berlin: De Gruyter, 2017, 115–131.

[55] Lissek F, Tegas J, Kaufeld M, Damage quantification for the machining of CFRP: An introduction about characteristic values considering shape and orientation of drilling-induced delamination, Procedia Engineering 2016; 149: 2–16.

[56] Khashaba UA, El-Sobaty IA, Selmy AI, Megahed AA. Machinability analysis in drilling woven GFR/epoxy composites: Part I – Effect of machining parameters. Compos Part A 2010; 41: 391–400.

[57] Upadhyay PC, Lyons JS. On the evaluation of critical thrust for delamination free drilling of composite laminates. J Reinf Plast Compos 1999; 18: 1287–303.

[58] Davim JP, Reis P. Drilling carbon fiber reinforced plastics manufactured by autoclave – Experimental and statistical study. Mater Des 2003; 24: 315–24.

[59] Davim JP, Reis Pedro. Study of delamination in drilling carbon fiber reinforced plastic (CFRP) using design experiments. Compos Struct 2003; 59: 481–7.

[60] Singh I, Bhatnagar N, Viswanath P. Drilling of uni-directional glass fiber reinforced plastics: Experimental and finite element study. Mater Des 2008; 29: 546–53.

[61] Abrao AM, Campos Rubio J, Faria PE, Davim JP. The Effect of cutting tool geometry on thrust force and delamination when drilling glass fibre reinforced plastic composite. Mater Des 2008; 29: 508–13.

[62] Khashaba UA, EI-Sobaty IA, Selmy AI, Megahed AA. Machinability analysis in drilling woven GFR/epoxy composites: Part II – Effect of drill wear. Compos Part A 2010; 41:1130–7.

[63] Wang X, Wang LJ, Tao JP. Investigation on thrust in vibration drilling of drilling of fiber-reinforced plastics. J Mater Process Technol 2004; 148: 239–44.

[64] Ramkumar J, Malhotra SK, Krishamurthy R. Effect of workpiece vibration ondrilling of GFRP laminates. J Mater Process Technol 2004; 152: 329–32.

[65] Arul S, Vijayaraghavan L, Malhotra SK, Krishnamurthy R. The effect of vibratory drilling on hole quality in polymeric composites. Int J Mach Tools Manuf 2006; 46: 252–9.

[66] Zhang LB, Wang LJ, Liu XY, Zhao HW, Wang X, Luo HY. Mechanical model for predicting thrust and torque in vibration drilling fibre-reinforced composite materials. Int J Mach Tools Manuf 2001; 41: 641–57.

[67] Tsao CC, Hocheng H. Effects of exit back-up on delamination in drilling composite materials using a saw drill and a core drill. Int J Mach Tools Manuf 2005; 45: 1261–70.

[68] Liu D, Tang YJ, Cong WL. A review of mechanical drilling for composite laminates. Compos Struct 2012; 94: 1265–1279.

[69] Tsao CC, Hocheng H, Chen YC, Delamination reduction in drilling composite materials by active backup force. CIRP Ann Manuf Technol 2012; 61: 91–94.

[70] Tsao CC, Hocheng H. The effect of chisel length and associated pilot hole on delamination when drilling composite materials. Int J Mach Tools Manuf 2003; 43: 1087–92.

[71] Tsao CC. The effect of pilot hole on delamination when core drill drilling composite materials. Int J Mach Tools Manuf 2006; 46: 1653–61.

[72] Won MS, Dharan CKH. Chisel edge and pilot hole effects in drilling composite laminates. J Manuf Sci Eng 2002; 124(2): 242–7.

[73] Phapale K, SinghR, Patil S Sing RKP, Delamination characterization and comparative assessment of delamination control techniques in abrasive water jet drilling of CFRP. Proc Manuf 2016; 5: 521–535.

[74] Mehbudi P, Baghlani V, Akbari J, Bushroa AR, Mardi NA, Applying ultrasonic vibration to decrease drilling-induced delamination in GFRP laminates. Procedia CIRP 2013; 6: 577–82.

[75] Davim JP, Reis P, Lapa V, Conceiçao C A, Machinability study on polyetheretherketone (PEEK) unreinforced and reinforced (GF30) for applications in structural components. Compos Struct 2003; 62: 67–73.

[76] Mohan NS, Kulkarni SM, Ramachandra A. Delamination analysis in drilling process of glass fiber reinforced plastic (GFRP) composite materials. J Mater Process Technol 2007; 186: 265–271.

[77] Ramulu M, Arola D, Colligan K, Preliminary investigation of machining effects on the surface integrity of fiber reinforced plastics. Eng Syst Des Anal, ASME PD, 1994; 64: 93–101.

[78] Kumar D, Singh KK, Zitoune R. Experimental investigation of delamination and surface roughness in the drilling of GFRP composite material with different drills. Advanced Manufacturing: Polymer & Composites Science 2016; 2(2): 47–56, DOI:10.1080/20550340.2016.1187434

[79] Takeyama H, Lijima N. Machinability of glass fibre reinforced plastics and application of ultrasonic machining. CIRP Ann 1988; 37(1): 93–96.

[80] Kumar D Singh K K, An experimental investigation of surface roughness in the drilling of MWCNT doped carbon/epoxy polymeric composite material. IOP Conf Ser Mater Sci Eng 2016; 149: 1–10.

[81] Muhammad Harris, Muhammad Asif Mahmood Qureshi, Muhammad Qaiser Saleem, Sarmad Ali Khan and Muhammad Mahmood Aslam Bhutta, Carbon fiber-reinforced polymer composite

drilling via aluminum chromium nitride-coated tools: Hole quality and tool wear assessment. J Reinf Plast Compos 2017; 36(19): 1403–1420.

[82] Ashrafi SA, Miller PW, Wandro KM, Kim D, Characterization and effects of fiber pull-outs in hole quality of carbon fiber. Reinf Plastics Composite. Materials (Basel) 2016; 9(10): 828.

[83] Rusinek R, Cutting process of composite materials: An experimental study. Int J Nonlinear Mech, 2010; 45: 458–462.

[84] Yaşar N, Korkmaz ME Günay M. Investigation on hole quality of cutting conditions in drilling of CFRP composite, MATEC Web of Conferences 112, 01013 (2017) doi:10.1051/matecconf/20171120101IManE&E 20173

[85] Krishnaraj V, Prabukarthi T, Ramanathan A et.al. Optimization of machining parameters at high speed drilling of carbon fiber reinforced plastic (CFRP) laminates. Compos Part B Eng 2013; 43 (4): 1791–1799.

[86] Sina Alizadeh Ashrafi, Peter W. Miller, Kevin M. Wandro Dave Kim. Characterization and effects of fiber pull-outs in hole quality of carbon fiber reinforced plastics composite. Materials 2016, 9: 828. doi:10.3390/ma9100828

[87] Vinod Kumar V, Venkateswarlu G. Optimization of process parameters in drilling of GFRP composite using Taguchi method. J Mater Res Technol 2014; 3(1): 35–41.

[88] Kennametal (2011) Composite machining. https//www.kennametal.com Composite machining guide for Aerospace pdf A34-55N.

[89] Koboević N. Jurjević M. Koboević Z. Influence of cutting parameters on thrust force, drilling torque and delamination during drilling of carbon fibre reinforced composites. Technical Gazette 2012; 19: 391–398.

[90] José Díaz-Álvarez, Alvaro Olmedo, Carlos Santiuste, María Henar Miguélez. Theoretical estimation of thermal effects in drilling of woven carbon fiber composite. Materials 2014; 7: 4442–4454 doi:10.3390/ma7064442

[91] Liu J, Chen G, Ji C, Qin X, Li H, Ren C, An investigation of workpiece temperature variation of helical milling for carbon fiber reinforced plastics. Int. J. Mach. Tools Manuf. 2014; 86: 89–103.

[92] Khashaba UA, Drilling of polymer matrix composites: A review. J Compos Maters 2012; 47(15): 1817–1832.

[92] Abrao AM, Campos Rubio J, Faria PE, Davim JP. The Effect of cutting tool geometry on thrust force and delamination when drilling glass fibre reinforced plastic composite. Mater Des 2008; 29: 508–13.

[93] Rawat S, Attia H. Wear mechanisms and tool life management of WC-Co drill during dry high speed drilling of woven carbon fibre composites. Wear 2009; 267: 1022–30.

[94] Velayudham A, Krishnamurthy R, Soundarapandian T. Evaluation of drilling characteristics of high volume fraction fibre glass reinforced polymeric composite. Int J Mach Tools Manuf 2005; 45: 399–406.

[95] Faraz A, Biermann D, Weinert K. Cutting edge rounding: An innovative tool wear criterion in drilling CFRP composite laminates. Int J Mach Tools Manuf 2009; 49: 1185–96.

[96] Ramulu M, Branson T, Kim D. A study on the drilling of composite and titanium stacks. Compos Struct 2001; 54: 67–77.

[97] Murphy C, Byrne G, Gilchrist MD. The performance of coated tungsten carbide drills when machining carbon fibre-reinforced epoxy composite materials. Proceedings of the institution of mechanical engineers. Part B: J Eng Manuf, 2002; 216: 143–52.

[98] Shyha IS, Aspinwall DK, Soo SL, Bradley S. Drill geometry and operating effects when cutting small diameter holes in CFRP. Int J Mach Tools Manuf 2009; 49: 1008–14.

Akshay Hejjaji, Redouane Zitoune, Ameur Mohamed Fayçal,
Bougherara Habiba

# 5 Challenges of machining natural fiber-reinforced composites: A review

**Abstract:** This chapter was aimed to enlighten readers on topics concerning machining natural fiber composites, mainly drilling. This study summarizes the challenges faced during machining natural fiber composites and defects observed. Delamination (both entry and exit), burrs, uncut fibers, fiber matrix debonding and uncut fibers are the predominant damage types seen during drilling all kinds of natural fiber composites.

## 5.1 Introduction

It has been fairly more than a decade since the composite materials have taken over the aerospace industry. The popularity of composite materials is due to its high specific strength-to-weight ratio. In spite of inheriting demerits such as difficulty in manufacturing and machining, brittle nature, high costs, health hazards and disastrous environmental after effects, the composite materials have been the most desired choice of structural material in the aerospace industry and now it has also made its way to the automobile sector. The exponential rise in popularity and use of these composites has raised issues concerning environmental impact, high costs, long-term sustainability, recyclability and disposal. As always, researchers have effectively attempted to address these issues by replacing synthetic fiber reinforcements by natural fibers that are available in abundance across all regions of the world.

Natural fiber-reinforced composite materials are in their nascent stages of development and have a great potential to be used in engineering applications and also nonengineering applications such as furniture, household panels and so on. The advantages of natural fiber composites include attributes such as economical, renewable, abundant availability, lightweight, less abrasiveness and also composites that are suitable to be used in nonstructural engineering applications. Natural fibers can be classified into animal and plant fibers. Animal fibers are generally body hair of mammals such as sheep, rabbit, alpaca and so on or fibers derived from dried saliva of bugs like silk. Depending on the region, the natural plant fibers can be derived from main agricultural crops such as sisal, hemp, jute, kenaf and so on, or a by-product of main agricultural crops such as flax, oil palm, sugar palm, bagasse, date palm, coir, banana stem, roselle, rice husk, betel nut husk, cocoa pod and so on. However, due to availability and consideration of humane practices, plant fibers are more prominent and also will be cost-effective due to large production. The typical production process of a plant based natural fiber-reinforced composite comprises of agricultural production of plants that

yeild the fibers, biological and chemical treatment of the plants to obtain the fibers and finally manufacturing of the composite part using an appropriate resin and curing method (Figure 5.1).
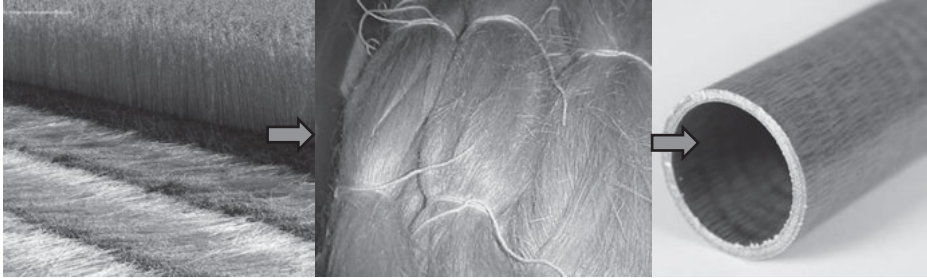


**Figure 5.1:** From plantation crop to fibers and finally to structural composite materials. https://www.coyuchi.com/the-naturalista/flax/ https://www.rockwestcomposites.com/round-tubing

The advantages of natural fibers are quite obvious and it is sure that they will fill-up for all shortcomings of synthetic fibers and prove to a more sustainable alternative. However, detailed studies on mechanical properties and behavior of natural fibers have to be carried out to ascertain their credibility. Research on various aspects of natural fiber composites such as manufacturing, characterization, determination of properties, machining and design has been extensively carried out. It is seen that the mechanical properties of natural fiber composites are inferior to that of typical synthetic fiber composites, but it is still within comparable range. This difference in properties is mainly due to the variation in properties of synthetic and natural fibers (Table 5.1). Other aspects that downgrade the mechanical behavior are the heterogeneous nature of natural fibers, presence of defects, manufacturing and machining defects and environmental degradation. The lack of knowledge in these aspects hinders the usage of natural fiber composites effectively.

**Table 5.1:** Comparison of physical properties of typical synthetic and natural fibers.

| Fiber type | Density (g/cm$^3$) | Tensile Strength (GPa) | Young's Modulus (GPa) | Specific Strength (GPa/gcm$^{-3}$) | Specific Stiffness (GPa/gcm$^{-3}$) |
|---|---|---|---|---|---|
| Carbon Fiber | 1.8 | 4 | 230 | 2.2 | 128 |
| Glass Fiber | 2.54 | 2.4 | 70 | 0.9 | 28 |
| Flax Fiber | 1.54 | 0.4–1.5 | 30–60 | 0.3–1 | 20–39 |
| Softwood Fiber | 1.5 | 0.2–1 | 15–30 | 0.1–0.7 | 10–20 |

As discussed previously, it is necessary to have assimilated knowledge on characterization, environmental effects, manufacturing and machining of natural fiber composites. Keeping our discussion confined to plant fibers, we can estimate that the sources of variation in the mechanical properties are as listed as follows:

Heterogeneous properties – The overall physical and mechanical properties of natural fiber composites depend on the chemical composition of single fiber and its water content, which is largely governed by growing conditions, harvesting period and processing techniques. These conditions are naturally derived and we have no much control over them. The repeatability in mechanical properties of natural fibers is difficult to achieve, which is easily attainable for synthetic fibers as the process is in our control.

Manufacturing – A single natural fiber has a complex structure, which includes cellulose in the center covered with various layers of organic matter such as lumen and lignin and is different for different plants. This indicates that different fibers will behave differently with the same hosting matrices and vice versa. Varying mechanical performances have been observed through the application of the same fiber in different hosting matrices. Hence, selecting an appropriate matrix material is essential for good performance of the composite. Apart from this, the product strength can be affected by a number of issues such as wettability of the natural fiber, presence of degradation at the fiber/matrix interface (following the fiber's attractive or repulsive response to water) and fiber destruction during the processing stage.

Machining – After fabrication of the composite structural part, it is necessary to perform secondary manufacturing operations that involves machining. Operations such as trimming, drilling, milling and so on can induce a lot of defects into the composite part, which becomes stress concentration zones that diminish the strength of the component.

The research community's effort to achieve mechanical strength to natural fiber composites on par with synthetic fiber composites has led to significant improvement in fiber processing techniques and robust manufacturing processes. However, the field of machining and its effect on the performance of natural fiber composites is relatively been ignored and barely any information is available on this. In fact, the lack of machining experience and inadequate availability of machining database and parameter setting has become a barrier for effective usage of these composites. In this chapter, we try to throw some light on the machining of natural fiber composites and its effect on the quality of composite. Abundant research data available for conventional and nonconventional machining of synthetic fiber composites reveal that the machining alters the surface characteristics and induces damage in fiber-reinforced plastics that leads to inferior mechanical behavior [1–6]. We also try to discuss certain cases of machining effects on natural fiber composites by making comparisons with synthetic fiber composites.

## 5.2 Machining of natural fiber composites

Manufacturing of the natural fiber-reinforced composite can be classified into two steps as primary and secondary manufacturing. The primary manufacturing results in a near net shape of the final product. The secondary manufacturing is to meet the geometric and tolerance conditions so that the component can be used in an assembly of the final product. Machining is the major secondary manufacturing operation that is carried out for all composites. Machining is a process of material removal from a component to get a specific shape and geometrical tolerance; in this course of action, a new surface is created and generally in the case of fiber-reinforced composites the integrity of new surface created commonly is inferior to that of the original one, which is also the case of natural fiber composites. The new surface will have two types of alterations, physical/geometrical modification due to creation of micro geometry and chemical alterations due to plastic deformation, frictional heating and phase changes. Both kinds of alterations are due to the virtue of type of machining process and its principle of material removal [6, 7]. In this section, we try to assimilate various researches on drilling natural fiber composites. In addition, ample information about surface formation and its characteristics is discussed along with different types of machining damage induced in the component. Concise information is provided on the topic of effect of machining parameters on surface characteristics and induced damage.

### 5.2.1 Drilling

Hole making is one of the important machining operations executed that is required for fastening of various components in the final assembly of the product. Although there are a number of approaches to make holes in composite laminates, the conventional drilling is still the most widely accepted and frequently practiced machining operation for hole making due to its versatility. This conventional technique of machining process has been lasting for years in the industry and plenty of research has been done to optimize the process to obtain best quality damage-free holes. Even though lots of new tool materials and tool designs are available for drilling fiber reinforced plastics (FRPs) complete damage free operation is inevitable. FRPs are highly abrasive in nature that advances the phenomenon of tool wear and hence induces numerous defects. For example, work conducted by Hejjaji et al. on drilling of carbon fiber reinforced plastic (CFRP) and glass fiber refinforced plastic (GFRP) composites by polycrystalline diamond (PCD) drill bit reveals damages in the form of fiber peel-up at the entry side of the drill, fiber pull-outs in $40^\circ$ and $90^\circ$ plies, delamination at the drill bit exit side along with thermal effects such as matrix degradation and smearing [7]. Delamination and surface quality were experimentally found to be influenced by the cutting parameters, drill bit geometry and cutting force. The surface roughness was also measured for varying drilling parameters and it was found that roughness

subsequently increased with increase in feed rate (mm/rev), which means that better hole surface quality was obtained with a combination of higher cutting speed and lower feed, which is also acknowledged by other researchers such as Eneyew et al. [8]. Though machining of natural fiber composites can be assumed similar to machining synthetic fiber composites, they differ in one major aspect. It is the lack of a good adhesion of natural fibers to most polymeric matrices. The hydrophilic nature of natural fibers negatively affects adhesion to a hydrophobic matrix and, as a result, it may cause a lack of interlocking between the fiber and the matrix [9, 10]. This has limited the machinability of natural fibers. However, to prevent this, the fiber surface must be modified to promote adhesion and, hence, improve the machinability of the composites [11, 12]. Mylsamy and Rajendran investigated the influence of alkali treatment of short agave fiber-reinforced composites on machinability during milling for untreated and alkali-treated fibers in terms of fiber matrix interaction [13]. Rough surfaces were observed on treated fibers, which led to better adhesion of fiber and matrix, showcasing better machinability. In contrast, voids were noticed in composites manufactured using untreated fibers, which would lead to inferior mechanical behavior and poor machinability.

Jayabal et al. investigated the effect of drilling parameters, such as drill bit diameter and spindle speed and feed rate, on machinability in terms of tool wear for hybrid composites, E-glass and natural coir fiber [14]. It was reported that the feed rate played an important role in the tool wear mechanism compared with other factors because of the size of the hole made and the counter force of fibers in composites. However, the spindle speed and drill bit diameter had mere influence on machinability that was attributed to softness of the composite. Nevertheless, this could be a complete contrasting outcome for synthetic fiber composites owing to their hard and abrasive nature. The most effective interaction on machinability was found to be between drill bit diameter and feed rate. Further, optimum levels to attain a minimum value of tool wear were determined.

Babu et al. investigated the drilling parameters to maximize the tensile strength of hemp fiber-reinforced composites with Taguchi and ANOVA analysis method [15]. They performed an experiment with different setting of feed rate and spindle speed, analyzed the result and performed another experiment to conform. The investigation has concluded that the feed rate and spindle speed are seen to make the major contribution to the delamination effect.

Sridharan et al. studied the effect of drilling parameters on machinability of jute fabric composites by studying the delamination factor [16]. Untreated and alkali-treated jute fabric was fabricated, machined and analyzed. The quality of hole was determined in terms of delamination factor at both entry and exit sides. Optimal cutting conditions were found using grey relational analysis and ANOVA was performed to find the highest influential parameter on delamination. It was concluded from the study that delamination increases with feed rate, which is same in the case of synthetic fiber composites. However, in case of jute fiber composite dominant peel up delamination is seen along
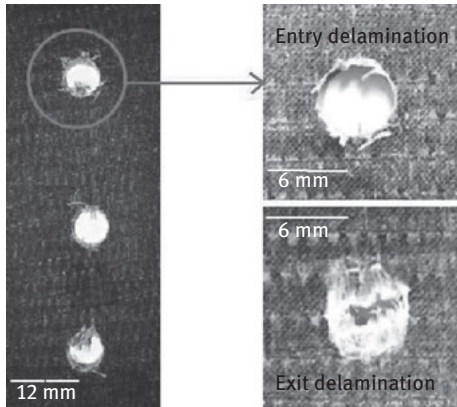
**Figure 5.2:** Entry and exit delamination (Push-up and push-out) in flax fiber reinforced composite.

with exit/pushout delamination. Similar findings have been reported for flax fiber composites in the work of Lou et al., where pronounced entry and exit delamination is present (Cf. Figure 5.2). For both just and flax fiber composites, it was reported that for maximum delamination both entry and exit occurs at highest feed rate.

Ismail et al. have studied machinability of hemp fiber-reinforced polymer (HFRP) during drilling with high-speed steel (HSS) drills under dry machining conditions and also they provide a comprehensive comparison by drilling carbon fiber-reinforced polymer (MTM 44-1/CFRP) composite laminates [17]. The drilling-induced damage analysis, mainly on delamination and surface integrity are presented. Surprisingly, the drilling-induced damage is more prominent and severe in the CFRP than the HFRP samples when machined with the same conditions (Cf. Figure 5.3). There are more fractured carbon fibers than the hemp fibers, most importantly at an increased feed rate of 90.15 and 0.20 mm/rev.



**Figure 5.3:** SEM micrographs showing fractured carbon fibers and hemp fibers in samples with 10.0 mm diameter hole drilled at f = 0.05 mm/rev and v = 20 m/min [17].

They also discuss the effect of machining parameters on the delamination factor and surfaces roughness. It was reported that the increase in feed rate caused an increase

in delamination and surface roughness of both hemp and carbon fiber composites. Also the delamination and surface roughness of both samples increased with a decrease in cutting speed. However, an increase in cutting speed caused a nonlinear decrease in the surface roughness of the two samples, which was inconsistent in the case of CFRP samples. It is also observed that the surface roughness of carbon fiber samples are less than that of hemp fiber samples for all drilling conditions and, on the contrary, delamination factor of hemp fiber composites was 10%–15% lesser in hemp fiber samples than that of carbon fiber samples for all cutting conditions. The work also reports that damages observed in the CFRP composite samples are point concentrated defects, while that of HFRP are uniform damage, mainly caused by the melted and sintered matrix. Apart from delamination, burrs and uncut fibers on both entry and exit sides are evident in hemp fiber samples that are more prominent in samples drilled at low feed rate and cutting speed. However, burrs and uncut fibers were absent in carbon fiber samples (cf. Figure 5.4).
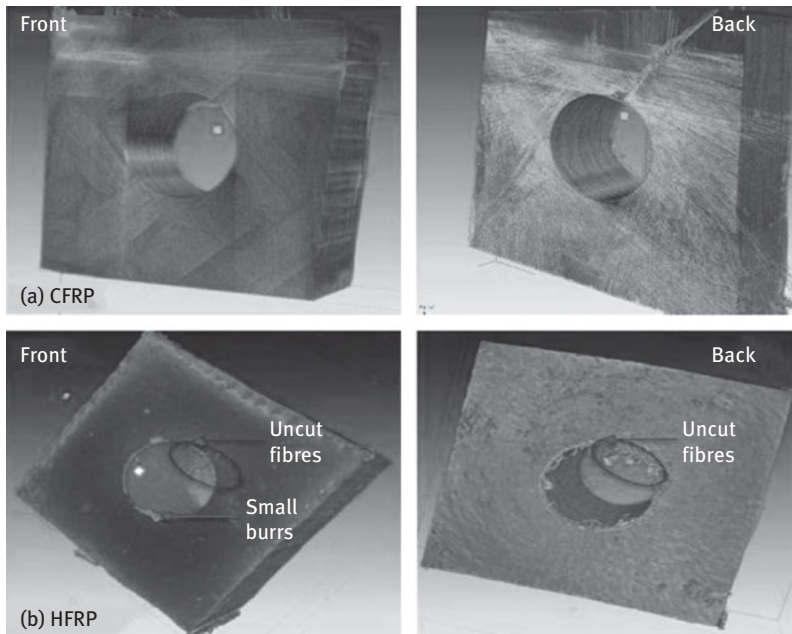


**Figure 5.4:** X-ray CT scanning micrographs, showing (a) CFRP without uncut fibers and burrs and (b) HFRP with uncut fibers and burrs damage [17].

Another area where extensive research is performed is tool coating. Many studies on machining synthetic fiber composites have shown that machinability improves with lower frictional coefficient between the tool and the composite. However, completely contradictory results are observed in the case of flax fiber composites.

Short natural fiber composites are becoming a viable alternative to synthetic fiber in many industrial applications that do not require extreme structural performances. When it comes to machining of these composites it becomes much more complicated. Chegdani et al. have investigated machinability of three types of short natural fibers (bamboo, sisal and miscanthus)-reinforced polypropylene(PP)composites [18]. The quality of natural fiber reinforced plastic (NFRP) machined surface was quantified to identifiy the impact of natural fibers (fiber stifness and interface quqlity) on the machined surface quality and cutting mechanisms. It was found that the quality of machined surface is significantly dependent on the stiffness of the fiber and interface quality. Also it was established that machined surface roughness decreases linearly with fiber stiffness at fiber bundle cross-section scales. A viscoelastic behavior of natural fiber aggravates an important fiber deformation, which leads to an interface break during the contact with the machining tool that generates fiber extremities and debonding leading to increase in surface roughness. As a result of this, bamboo fiber-reinforced plastics that exhibit high contact stiffness had the least surface roughness post-machining.

Till now, we have discussed many aspects describing various factors affecting the machining quality and the corresponding damage caused by machining. As it was discussed earlier, machining affects the bulk mechanical properties of the composite that leads to inferior mechanical behavior. The effect of machining on mechanical behavior of composites was considerably neglected until recent times. Not just this, it was always considered that the post-machining surface quality was the strength deciding factor. In plain terms, it was thought that lower surface roughness values led to better material integrity, same as in metals. Recent substantial research works on synthetic fiber composites have proven otherwise that the surface roughness does not preferably point out the machining quality and material integrity/mechanical behavior dependency [6, 21]. Hence, it is of high priority that the link between machining quality and mechanical behavior is well established for ascertaining the worthiness of composites in structural applications. One of the very few works that throws some light on link between machining quality and mechanical behavior is by El Sawi et al. [19]. The impact of the process of machining on the machining quality of flax/epoxy with different stacking sequences (unidirectional, quasi-isotropic and cross ply) was investigated. For comparison of two machining techniques was examined, viz. conventional drilling and abrasive waterjet machining (AWJM). Delamination was the major damage during drilling these flax/epoxy composites and micro cracks was most prevalent damage when AWJM was done. Typical micrographs of the machined hole surfaces are displayed on Figure 5.5. These cracks are highlighted by circles on Fig5.5 (a, b and c). On the other hand, machining hole using conventional machining (CM) technique (dry drilling with twist drill made of tungsten carbide) creates a surface quality that has a fish scale like structure. This surface type has not been observed when drilling conventional fiber-reinforced polymer materials such as carbon or glass fibers. The authors report that the inherent viscoelastic properties of the cellulose-based fiber as the main reason behind this surface formation. The surface roughness of specimens machined with abrasive
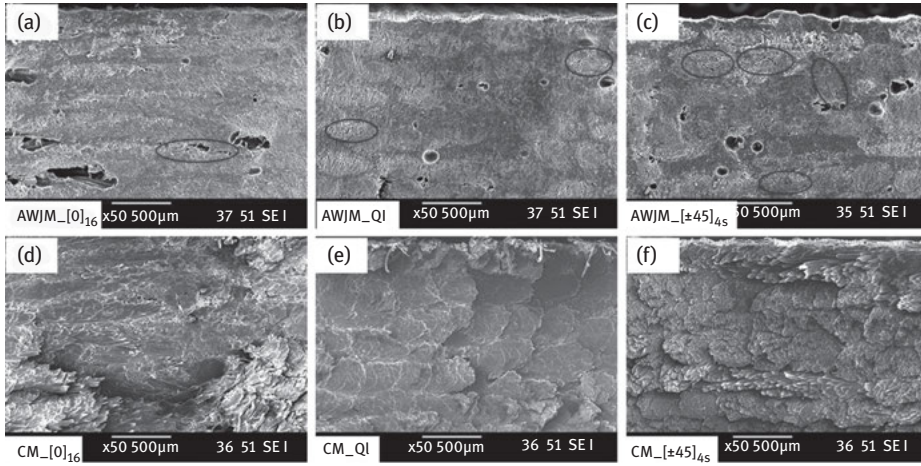
**Figure 5.5:** Scanning electron microscopy images of the drilled hole surface machined with AWJM (a, b and c) and conventional machining (d, e and f) [19].

water jet is around 1.9 μm ±0.3, whereas CM yields surface with higher surface roughness of around 3.1 μm ±0.3.The higher roughness of conventionally machined surface is attributed to the scaly surface.

The machined flax/epoxy composite was subjected to static tensile and fatigue tests to investigate the effect of machining on the mechanical behavior. It was reported that both abrasive waterjet and conventional machined specimens did not indicate any difference in ultimate tensile strength. When comparing the influence of the machining fatigue behavior on these composites with respect to stacking sequence, it was observed that the elevation of temperature during the cyclic tests was similar for both machining techniques and also for respective stacking sequence viz. unidirectional and quasi-isotropic laminates (Figure 5.6 a–1, b-1). However, a noticeable difference between specimens machined with CM and AWJM can be observed on the profile of the temperature elevation of cross ply $[\pm45]_{4S}$ laminates as shown in Figure 5.6 (c-1).

Figure 5.6. (a-1, b-1, c-1) Thermal variation versus number of cycles (percentages represent the percentage of maximum applied stress). (a-2, b-2 and c-2) Average temperature increase versus the maximum applied stress.

This means that composites with $[\pm45]_{4S}$ stacking sequence machined with AWJ fail earlier than the same laminate machined with CM technique as seen from Figure 5.6 (c-2). Since the mechanical properties of laminates with $[\pm45]_{S}$ plies are sensitive to delamination and matrix and fiber/matrix interface, this difference of the mechanical behavior must be due to the initial damage (micro-cracks) caused by the AWJM that resulted in further increase of temperature as the number of loading increases and lead to an early failure of the laminate.

The high cycle fatigue strength (HCFS) determined by the IR thermography method was around 58% of the UTS for the unidirectional $[0]_{16}$ composite laminates and 53.5%
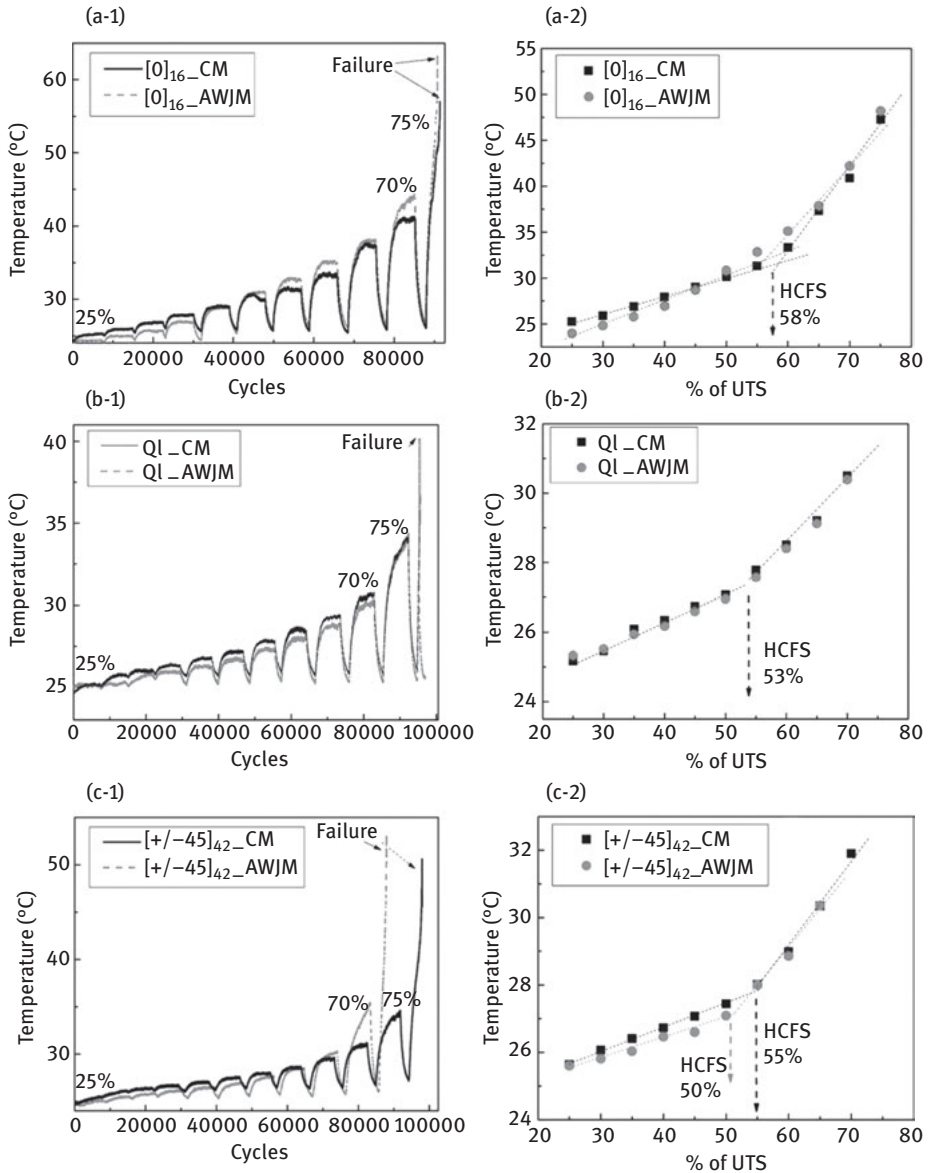
**Figure 5.6:** (a-1, b-1, c-1) Thermal variation versus number of cycles (percentages represent the percentage of maximum applied stress). (a-2, b-2, c-2) Average temperature increase versus the maximum applied stress [19].

of the UTS of the quasi-isotropic laminates. For the cross ply [±45]₄ₛ laminates the determined HCFS was around 55% of ultimate tensile strength (UTS) and 50% of UTS for the specimen machined with CM and AWJM, respectively. A decrease by 9% is observed when the AWJM is used. The decrease of the mechanical fatigue performance

can be explained by the initial damage caused by AWJM. In fact, in the work conducted by Toubal et al. [20], which focuses on the impact of the water absorption on the mechanical properties of jute/epoxy laminate, it was reported that the Young's modulus and shear modulus decrease at least by 20% before and after exposure to moisture (water) till saturation. It was explained that this reduction is attributed to the creation of intra-fiber bundle micro cracks network due to water absorption [20]. However, it is important to notice that, in case of composite specimens made of synthetic fibers machined by AWJM process present a better quality in terms of mechanical behavior compared to the same specimens machined with conventional process, which is opposite to the behavior seen in natural fibers [21]. Hence, it is important to study the natural fiber composites under a separate purview and not include them under the same category of synthetic fiber composites to avoid confusion and misleading results.

So, it is very much evident from this work that the study of machining techniques used and the corresponding machining damage is very critical in determining the mechanical behavior of the natural fiber composites.

## 5.3 Remarks

This chapter was aimed to enlighten readers on topics concerning machining natural fiber composites, mainly drilling. This study summarizes the challenges faced during machining natural fiber composites and defects observed. Delamination (both entry and exit), burrs, uncut fibers, fiber matrix debonding and uncut fibers are the predominant damage types seen during drilling of all kinds of natural fiber composites. It is seen that formation of defects can be reduced by selecting appropriate machining technique, cutting parameters, machining conditions and tool geometry and tool material. Feed rate is the most influential drilling parameter deciding the extent of delamination; lower the feed rate lesser the delamination damage. Apart from machining parameters, fiber treatment, fiber stiffness, tool material and tool coating all play an important part in deciding the machinability of natural fiber composites. Overall it can be concluded that by utilizing scrutinized machining practices available from the research databases, it is possible to effectively machine natural fiber composites.

## References

[1]    Haddad, M., Zitoune, R., Eyma, F. & Castanie, B. Study of the surface defects and dust generated during trimming of CFRP: Influence of tool geometry, machining parameters and cutting speed range. Compos. Part A Appl. Sci. Manuf. 66, 142–154 (2014).

[2]    Zitoune, R. & Bougherara, H. Advances in composites manufacturing and process design 177–195 (2015). doi:10.1016/B978-1-78242-307-2.00009-9

[3]    Saleem, M., Zitoune, R., El Sawi, I. & Bougherara, H. Role of the surface quality on the mechanical behavior of CFRP bolted composite joints. Int. J. Fatigue 80, 246–256 (2015).

[4] El Sawi, I., Fawaz, Z., Zitoune, R. & Bougherara, H. An investigation of the effect of the machining processes of circular holes on the mechanical behaviour of flax fiber reinforced polymer. 16th Eur. Conf. Compos. Mater. ECCM 2014 22–26 (2014).

[5] Saleem, M., Toubal, L., Zitoune, R. & Bougherara, H. Investigating the effect of machining processes on the mechanical behavior of composite plates with circular holes. Compos. Part A, Appl. Sci. Manuf. 55, 169–177 (2013).

[6] Hejjaji, A., Zitoune, R., Crouzeix, L., Roux, S. Le & Collombet, F. Surface and machining induced damage characterization of abrasive water jet milled carbon/epoxy composite specimens and their impact on tensile behavior. Wear 376–377, 1356–1364 (2017).

[7] Hejjaji, A., Singh, D., Kubher, S., Kalyanasundaram, D. & Gururaja, S. Machining damage in FRPs: Laser versus conventional drilling. Compos. Part A Appl. Sci. Manuf. 82, 42–52 (2016).

[8] Eneyew, E. D. & Ramulu, M. Experimental study of surface quality and damage when drilling unidirectional CFRP composites. J. Mater. Res. Technol. 3, 354–362 (2014).

[9] Herrera-Franco, P. J. & Valadez-González, A. Mechanical properties of continuous natural fibre-reinforced polymer composites. Compos. Part A Appl. Sci. Manuf. 35, 339–345 (2004).

[10] Nam, T. H., Ogihara, S., Tung, N. H. & Kobayashi, S. Effect of alkali treatment on interfacial and mechanical properties of coir fiber reinforced poly(butylene succinate) biodegradable composites. Compos. Part B Eng. 42, 1648–1656 (2011).

[11] Valadez-Gonzalez, a., Cervantes-Uc, J. M., Olayo, R. & Herrera-Franco, P. J. Effect of fiber surface treatment on the fiber–matrix bond strength of natural fiber reinforced composites. Compos. Part B Eng. 30, 309–320 (1999).

[12] Van de Weyenberg, I., Chi Truong, T., Vangrimde, B. &Verpoest, I. Improving the properties of UD flax fibre reinforced composites by applying an alkaline fibre treatment. Compos. Part A Appl. Sci. Manuf. 37, 1368–1376 (2006).

[13] Mylsamy, K. & Rajendran, I. Influence of alkali treatment and fibre length on mechanical properties of short Agave fibre reinforced epoxy composites. Mater. Des. 32, 4629–4640 (2011).

[14] Jayabal, S., Natarajan, U. &Sathiyamurthy, S. Effect of glass hybridization and staking sequence on mechanical behaviour of interply coir-glass hybrid laminate. Bull. Mater. Sci. 34, 293–298 (2011).

[15] DilliBabu, G., SivajiBabu, K. & Uma MaheswarGowd, B. Optimization of machining parameters in drilling hemp fiber reinforced composites to maximize the tensile strength using design experiments. Indian J. Eng. Mater. Sci. 20, 385–390 (2013).

[16] Sridharan, V. & Muthukrishnan, N. Optimization of machinability of polyester/modified jute fabric composite using Grey Relational Analysis (GRA). Procedia Eng. 64, 1003–1012 (2013).

[17] Ismail, S. O., Dhakal, H. N., Popov, I. & Beaugrand, J. Comprehensive study on machinability of sustainable and conventional fibre reinforced polymer composites. Eng. Sci. Technol. Int. J. 19, 2043–2052 (2016).

[18] Chegdani, F., Mezghani, S., El Mansori, M. & Mkaddem, A. Fiber type effect on tribological behavior when cutting natural fiber reinforced plastics. Wear 332–333, 772–779 (2015).

[19] El Sawi, B. Papini, I., Fawaz, Z., Zitoune, R. &Bougherara, H.A comparative experimental study of machining flax fiber reinforced polymer composite laminates using abrasive waterjet and drilling tool. CANCOM2015 – Canadian International Conference on Composite materials. Edmonton, Alberta (2015).

[20] Toubal, L., Zitoune, R., Collombet F. and N. Rocher Gleizes. Moisture Effects on the Material Properties of a Jute/Epoxy Laminate: Impulse Excitation Technique Contribution. J. Nat. Fibers 1–14 (2017).

[21] Haddad, M., Zitoune, R., Bougherara, H., Eyma, F. & Castanie, B. Study of trimming damages of CFRP structures in function of the machining processes and their impact on the mechanical behavior. Compos. Part B Eng. 57, 136–143. (2014).

V. N. Gaitonde, Shashikant, Anand Lakkundi, S. R. Karnik,
A. S. Deshpande, J. Paulo Davim

# 6 Analysis and optimization of hole quality parameters in cenosphere-multiwall carbon nanotube hybrid composites drilling using artificial neural network and gravitational search technique

**Abstract:** Analysis and optimization of hole quality parameters in drilling of cenosphere-multiwall carbon nanotubes (MWCNTs) – epoxy composite materials have been presented in this chapter. The hybrid composite material is being prepared with 40% by weight of cenosphere with varying 0.2%, 0.3% and 0.4% of MWCNT as a filler and epoxy as matrix. The full factorial design (FFD) was planned to reduce the drilling experiments. The influence of four factors: explicit cutting speed, feed, % weight of MWCNT and drill diameter of hole quality parameters such as circularity error, drilled hole surface roughness and delamination factor have been studied. The artificial neural network (ANN)-based modeling analysis indicates that an addition of MWCNT reinforced with cenosphere-epoxy resin decreases the circularity error and surface roughness, whereas delamination is found to be minimal for 0.2% of MWCNT reinforcement drilling. To reduce the circularity error, 0.3% MWCNT reinforcement is desirable for drill diameters in the range 8–16 mm. For a particular drill size and MWCNT combination, the concurrent increase in cutting speed with feed has visible consequence for reducing the surface roughness. With 0.4% MWCNT reinforcement drilling, more delamination is observed for all the specified speed-feed combinations. ANN models were later used for gravitational search (GS) technique to decide the best combinations of cutting conditions for a particular drill diameter and % MWCNT for minimal circularity error, surface roughness and delamination factor.

## 6.1 Introduction

Syntactic foams are lightweight and low cost materials; they find broader applications in structural components and transport vehicles such as marine, aircraft and automobiles; while the structural weight reduction straightaway converts into fuel reduction and improved payload proficiency [1, 2]. The syntactic foams are preferred because they demonstrate superior properties in compression over the foams having gas porosity in matrix. In thermal power plant, the industrial waste known as the fly ash contains the cenospheres, which are nothing but the hollow microspheres. The

cenosphere contains silica and alumina; filled with inert gas or air that makes the cenosphere hollow, inert and lightweight.

The experimental research on cenosphere/vinyl ester composites by Labella et al. [3] exposed that cenosphere accumulation could diminish the flexural strength, while flexural modulus increases. Studies on phenolic-filled cenosphere-reinforced composites by Balaji et al. [4] highlighted a visible decline in the thermal degradation due to the occurrence of cenospheres. Das et al. [5] developed the cenosphere/polypropylene composites with 30% cenosphere reinforcement for improved tensile and flexural properties and morphological properties were also studied. The research carried out by Uju and Oguocha [6] on Al–Mg alloy A535 with silicon carbide fly ash composites revealed that an addition of fly ash as well as the silicon carbide decreases the coefficient of thermal expansion. Chand et al. [7] improved mechanical as well as tribological properties by adding cenosphere to high-density polyethylene composites. Morimoto et al. [8] prepared the porous particles-filled phenolic composites and decrease in fracture toughness as well as the wear rate was evidenced as a result of increased volume fraction of hollow particles. Gupta et al. [9] stated that the mechanical properties and density of syntactic foams could be changed by using different inner radius; however, cenospheres of outer radius in the matrix remains same. The studies by Balaji and Sasikumar [10] on cenosphere-loaded ceramic/phenolic composites revealed that the thermal degradation augment with the addition of cenosphere for cenosphere-filled composites.

Nowadays, the manufacturers are using carbon nanotubes (CNTs) into composites to make the materials still lighter. The CNTs have better stiffness, superior strength, exceptional thermal conductivity and chemical resistance, excellent mechanical and numerous other prospective functional properties [11–16]. Divya et al. [17] conducted several experiments on high-density polyethylene reinforced with cenosphere-MWCNT composites and observed enhanced mechanical properties and increased flammability properties compared to the composites without cenosphere and MWCNTs. Dimchev et al. [18] studied the control of carbon nanofiber on hollow particle-filled composites. 0.25 wt % carbon nanofibers were found to be effective for better tensile and modulus properties compared to particulate composites without nanofibers.

Even if the syntactic foams are shaped to near net, machining is vital in final stage of production for crucial surface quality and dimensional stability. Drilling is the key operation to fit the fasteners for composite laminates assembly. In the manufacturing industries of aircrafts, drilling is carried out on laminates of composites for joining by using nuts, bolts and rivets. The excellence of drilled hole is significantly affected by cutting parameters, drill geometry and the work material. Therefore, for improved hole quality, the variables affecting the drilling process are vital. In recent past, the machinability assessment has been done with glass and carbon fibers in plastic composites [19–22]. At entry and exit of composite drilling, delamination has been observed [23–28]. The drilled hole quality was also analyzed

by Palanikumar et al. [29] and Krishnaraj et al. [30] in GFRP and CFRP composite drilling.

From the past works on drilling of composites, the information on low cost as well as lighter weight material, as a prospective structural constituent having better hole quality is barely obtainable. In view of a profile with an exceptional property and wider applications of syntactic foams with CNTs, understanding the drilling characteristics of these composites is essential. Thus, the present investigation makes an effort to plug the gap through investigative research cenosphere-CNT-epoxy hybrid composites on hole quality parameters such as circularity error, drilled hole surface roughness and delamination factor. The hybrid composites were developed with 40% by weight of cenosphere with varying 0.2%, 0.3% and 0.4% of MWCNT as a filler and epoxy resin as the matrix. The artificial neural network (ANN)-based models of circularity error, drilled hole surface roughness and delamination factor were developed with small number of experiments using full factorial design (FFD) [31]. The supremacy of cutting speed, feed, % weight of MWCNT and drill diameter on proposed hole quality parameters have been analyzed through ANN modeling. Further, the gravitational search (GS) technique has been employed for obtaining the best possible cutting conditions for a specified combination of drill diameter and % MWCNT.

## 6.2 Artificial neural network modeling

ANN contains neurons interrelated throughout the unidirectional signal guides that emulate the human brain [32]. Every constituent has a distinct output association that twigs into preferred guarantee connections. The ANNs can attain, accumulate and make use of the investigational data.

ANN model with error back propagation training algorithm (EBPTA) [32] is used to model and analyze the consequences of factors on proposed hole quality parameters. The EBPTA consists of training patterns that involves inputs and essential outputs. The information gathered through interrelated weight is attuned in the learning phase all the way through EBPTA to decrease the mean square error (MSE) among real and requisite output pattern. ANN model has input layer, hidden layer (s) and output layer.

For $b^{th}$ neuron, the net activation input is as follows[32]

$$net_b = \sum_{a=1}^{n} w_{ba} x_a \qquad (6.1)$$

where $w_{ba}$ is the weight of connection from neuron $b$ to $a$; $x_a$ is the $a^{th}$ input.

The $b^{th}$ neuron output for unipolar sigmoid activation is as follows

$$o_b = \frac{1}{1 + e^{-\lambda\, net_b}} \tag{6.2}$$

where $\lambda$ is the scaling factor.

The sum of squared error for $S$ output neuron is as follows

$$E = \frac{1}{2} \sum_{s=1}^{S} (d_{s,p} - o_{s,p})^2 \tag{6.3}$$

where $d_{s,p}$ is the $p^{\text{th}}$ pattern preferred output.

The weights of connections restructured at the $n^{\text{th}}$ learning step are as follows

$$w_{ba(n+1)} = w_{ba(n)} + \alpha\, \Delta_{pa} o_{pa} + \beta\, \Delta w_{ba(n)} \tag{6.4}$$

where $\alpha$ is the learning rate and $\beta$ is the momentum constant.

Error signal term $(\Delta_{pb})$ is specified by

For output layer, $\Delta_{kp} = (d_{s,p} - o_{s,p})(1 - o_{s,p}); \quad s = 1, \cdots S$     (6.5)

For hidden layer, $\Delta_{pb} = o_{pb}(1 - o_{pb}) \sum \Delta_{ps} w_{sb}; \quad b = 1, \cdots B$     (6.6)

where $B$ is the total number of hidden layer neurons.

ANN training involves the following stages:

1. Synaptic weights to the random values are to be initialized.
2. Input – output pattern one at a time is to be presented; the weights for each time to be updated.
3. *MSE* at the end of every epoch is to be computed using the following equation:

$$MSE = \frac{1}{n_p} \sum_{p=1}^{n_p} \sum_{s=1}^{S} (d_{s,p} - o_{s,p})^2 \tag{6.7}$$

where $n_p$ is the number of patterns.

4. Training ends, if (MSE< specified tolerance) or (epochs > [epochs]$_{\max}$)

Then stop.
Else, go to stage 2.

## 6.3 Gravitational search optimization

GS optimization is fundamentally based on gravity law and notion of mass interactions [33]. GS exercises the Newtonian physics theory and searcher objects. Gravitational force (GF) translates information among the different masses and hence each mass in the system can perceive conditions of other masses. GF causes

collective association of every agent toward objects through strong masses. The strong masses for finer results progress further gradually.

The position, inertial mass, active gravitational mass and passive gravitational mass are the main terms involved in every object of GS. Mass position refers to a problem result, whereas inertial and gravitational masses are derived through fitness function. Hence, every mass offers an answer and GS technique is appropriately guided by fine-tuning gravitational as well as inertial masses. After specified duration, the masses will be fascinated by the strongest mass for better results in search space. In GS optimization, the masses comply with the following laws

– **Gravity Law**: Every unit attracts the other unit and GF among the two is straight-away related to multiplication of masses and conversely related to distance between them ($r$).
– **Motion Law**: Recent velocity of every mass is computation of portion of preceding velocity and velocity acceleration. The velocity acceleration of every mass is the force acting on the system divided by inertia mass.

For $Z$ objects in a system, location of $i^{th}$ object is $X_i = (x_i^1, \cdots, x_i^l, \cdots, x_i^z)$ for $i = 1, 2, \dots \dots, Z$ where $x_i^l$ is location of $i^{th}$ object in $l^{th}$ dimension.

For particular duration "$t$", the force on mass "$i$" to "$j$" is as follows

$$f_{ij}^l(t) = g(t) \frac{m_{pi}(t) \times m_{aj}(t)}{r_{ij}(t) + \omega} [x_j^l(t) - x_i^l(t)] \tag{6.8}$$

where $m_{aj}$ is the active gravitational mass for $j^{th}$ object, $m_{pi}$ is the passive gravitational mass for $i^{th}$ object, $g(t)$ is the gravitational constant at $t$, $\omega$ is the constant and $r_{ij}(t)$ is the Euclidian distance between $i$ and $j$; given by

$$r_{ij}(t) = \left\| X_i(t), X_j(t) \right\|_2 \tag{6.9}$$

In GS, the total force acting on object $i$ in a dimension $l$ be a randomly weighted sum of $l^{th}$ components of forces exerted from other objects and is given by

$$f_i^l(t) = \sum_{j=1, j \neq i} (rand)_j F_{ij}^l(t) \tag{6.10}$$

where $(rand)_j$ is a random number in the range [0,1].

By motion law, for any object $i$ with inertial mass $m_{ii}(t)$, its acceleration at $t$ in $l^{th}$ direction is as follows

$$a_i^l(t) = \frac{f_i^l(t)}{m_{ii}(t)} \tag{6.11}$$

The subsequent object velocity is a portion of present velocity, which is supplementary to its acceleration. Hence, location and velocity are calculated as follows:

$$v_i^l(t+1) = (rand)_i \times v_i^l(t) + a_i^l(t) \tag{6.12}$$

$$x_i^l(t+1) = x_i^l(t) + v_i^l(t+1) \tag{6.13}$$

The $g$ constant is initialized and then will be condensed with duration to manage search accuracy. Hence, $g$ is a function of initial value $(g_o)$ and $g(t) = g(g_0, t)$.

The gravitational and inertia masses are computed through fitness evaluation. Stronger mass is the competent object, that is, superior objects have superior attractions and they stroll gradually. The gravitational and inertial masses are updated as follows

$$m_{ai}(t) = m_{pi}(t) = m_{ii} = m_i; \quad i = 1, \ldots, Z \tag{6.14}$$

$$k_i(t) = \frac{fit_i(t) - worst(t)}{best(t) - worst(t)} \tag{6.15}$$

$$m_i(t) = \frac{k_i(t)}{\sum_{j=1}^{Z} k_j(t)} \tag{6.16}$$

where $fit_i(t)$ is fitness value of object $i$ for duration $t$.

For minimization problem, the *worst (t)* and *best (t)* are as follows

$$worst(t) = \max[fit_j(t)]; \; for \; j = \{1, \ldots, Z\} \tag{6.17}$$

$$best(t) = \min[fit_j(t)]; \; for \; j = \{1, \ldots, Z\} \tag{6.18}$$

GS optimization involves the following:
- (a) Identifying search space
- (b) Initializing randomness
- (c) Evaluating fitness for objects (masses)
- (d) Updating $g(t)$, $best(t)$, $worst(t)$ and $m_i(t)$ for $i = 1, 2, \ldots, Z$.
- (e) Determining total force in diverse paths
- (f) Computing acceleration and velocity
- (g) Updating location of objects
- (h) Repeat (c) to (g) till the stop criterion is arrived

## 6.4 Experimental details

### 6.4.1 Preparation of cenosphere-MWCNT-epoxy specimens

In the current investigation, a light gray color hollow inert silicate spherical-shaped cenosphere (75 microns size; hardness of 5–6.5 MOH; density of 0.75) filler is used. The chemical composition of the cenosphere is silicon oxide–55%, aluminum oxide–34%, ferric oxide–1.5%, titanium oxide–1.2%, calcium oxide – 0.3%, magnesium oxide–1.8% and sodium oxide–0.5%. In the current study, LAPOX L-12 epoxy resin with K-6 hardener is employed. Multiwalled nanotube (MWNT) utilized in the existing study comprises of various moved layers of graphene. The specifications with the dimensions are given in Table 6.1.

**Table 6.1:** Specifications with dimensions of MWCNT.

| | |
|---|---|
| Diameter | 10–30 nm |
| Length | 1–2 mm |
| Purity | 95% |
| Surface area | 350 m$^2$/g |
| Bulk density | 0.05–0.17 g/cm$^3$ |
| Density | 1.8 g/cm$^3$ |
| Tensile strength | 3,500 MPa |
| Fiber length | 5 mm |
| Fiber thickness | 0.3 mm |

The cenosphere-MWCNT-epoxy hybrid composites were prepared using hand lay-up procedure with 40% cenosphere with varying concentrations of MWCNTs from 0.2 to 0.4 wt% in 0.1% increment in the epoxy. The aluminum mold of size 100 mm × 100 mm × 16 mm was used for the specimen preparation and completely enclosed with teflon sheet on either side. The silicone was used as releasing agent for easy exclusion of cast sample. Planned cenosphere – MWCNT mixture with intended amount of epoxy (heated at 60°C temperature) with reasonable magnetic stirring was employed for least air entrapment. For proper dispersion of the cenosphere-MWCNT, the hardener was measured in 10% of epoxy weight and then stirred with the mixture of cenosphere-MWCNT-epoxy for 10 min in a slow and distinct pattern. The mixture was gradually poured into the mold using center pouring methodology and cured for 24 h at ambient temperature. The suitable dimensional workpieces are used for dry drilling experiments.

## 6.4.2 Drilling experimentation and hole quality measurement

Design of experiments (DOE) is vital for reducing the experiments to develop ANN models. The hole quality analysis for the current investigation of drilling of ceno-sphere-MWCNT-epoxy hybrid composites involves the cutting speed ($v$), feed ($f$), % MWCNT($c$) and drill diameter ($D$) as factors. The intended hole quality parameters identified are circularity error ($C_e$), drilled hole surface roughness ($R_a$) and delamination factor ($F_d$). The limits for identified factors were chosen through preliminary trials and three levels for every factor were considered. The selected factors and the corresponding limits are given in Table 6.2. The FFD was employed and 81 trials were planned; the design plan is given in Table 6.3.

**Table 6.2:** Input parameters and their limits.

| Parameter | Limit | | |
|---|---|---|---|
| | 1 | 2 | 3 |
| Cutting speed ($v$), m/min | 25 | 75 | 125 |
| Feed ($f$), mm/rev | 0.04 | 0.08 | 0.12 |
| MWCNT ($c$), % | 0.2 | 0.3 | 0.4 |
| Drill diameter ($D$), mm | 8 | 12 | 16 |

**Table 6.3:** Experimental layout plan with experimental values of hole quality parameters.

| Trial No. | Parameter settings | | | | Hole quality parameters | | |
|---|---|---|---|---|---|---|---|
| | $v$ (m/min) | $f$ (mm/rev) | $c$ (%) | $D$ (mm) | $C_e$ (mm) | $R_a$ (microns) | $F_d$ |
| 1 | 25 | 0.04 | 0.2 | 8 | 0.037 | 3.347 | 1.0045 |
| 2 | 25 | 0.04 | 0.3 | 8 | 0.035 | 3.320 | 1.004625 |
| 3 | 25 | 0.04 | 0.4 | 8 | 0.028 | 3.362 | 1.007 |
| 4 | 25 | 0.08 | 0.2 | 8 | 0.037 | 3.517 | 1.004625 |
| 5 | 25 | 0.08 | 0.3 | 8 | 0.027 | 3.518 | 1.006125 |
| 6 | 25 | 0.08 | 0.4 | 8 | 0.018 | 3.535 | 1.00725 |
| 7 | 25 | 0.12 | 0.2 | 8 | 0.061 | 3.422 | 1.004625 |
| 8 | 25 | 0.12 | 0.3 | 8 | 0.059 | 3.370 | 1.00625 |
| 9 | 25 | 0.12 | 0.4 | 8 | 0.042 | 3.437 | 1.00925 |
| 10 | 75 | 0.04 | 0.2 | 8 | 0.011 | 2.757 | 1.005875 |
| 11 | 75 | 0.04 | 0.3 | 8 | 0.007 | 2.587 | 1.00775 |
| 12 | 75 | 0.04 | 0.4 | 8 | 0.006 | 2.772 | 1.007875 |
| 13 | 75 | 0.08 | 0.2 | 8 | 0.029 | 3.237 | 1.007375 |
| 14 | 75 | 0.08 | 0.3 | 8 | 0.014 | 3.162 | 1.009125 |

**Table 6.3:** (*continued*)

| Trial No. | Parameter settings | | | | Hole quality parameters | | |
|---|---|---|---|---|---|---|---|
| | $v$ (m/min) | $f$ (mm/rev) | $c$ (%) | $D$ (mm) | $C_e$ (mm) | $R_a$ (microns) | $F_d$ |
| 15 | 75 | 0.08 | 0.4 | 8 | 0.013 | 3.340 | 1.011875 |
| 16 | 75 | 0.12 | 0.2 | 8 | 0.045 | 2.972 | 1.007625 |
| 17 | 75 | 0.12 | 0.3 | 8 | 0.029 | 2.740 | 1.009125 |
| 18 | 75 | 0.12 | 0.4 | 8 | 0.022 | 2.862 | 1.012375 |
| 19 | 125 | 0.04 | 0.2 | 8 | 0.01 | 2.342 | 1.005875 |
| 20 | 125 | 0.04 | 0.3 | 8 | 0.009 | 2.257 | 1.007875 |
| 21 | 125 | 0.04 | 0.4 | 8 | 0.001 | 2.410 | 1.0085 |
| 22 | 125 | 0.08 | 0.2 | 8 | 0.022 | 2.867 | 1.01175 |
| 23 | 125 | 0.08 | 0.3 | 8 | 0.019 | 2.757 | 1.011875 |
| 24 | 125 | 0.08 | 0.4 | 8 | 0.013 | 2.920 | 1.012125 |
| 25 | 125 | 0.12 | 0.2 | 8 | 0.022 | 2.477 | 1.01175 |
| 26 | 125 | 0.12 | 0.3 | 8 | 0.021 | 2.257 | 1.01225 |
| 27 | 125 | 0.12 | 0.4 | 8 | 0.021 | 2.477 | 1.012375 |
| 28 | 25 | 0.04 | 0.2 | 12 | 0.061 | 4.545 | 1.004917 |
| 29 | 25 | 0.04 | 0.3 | 12 | 0.02 | 4.545 | 1.006583 |
| 30 | 25 | 0.04 | 0.4 | 12 | 0.013 | 4.555 | 1.006583 |
| 31 | 25 | 0.08 | 0.2 | 12 | 0.085 | 4.962 | 1.0055 |
| 32 | 25 | 0.08 | 0.3 | 12 | 0.023 | 4.730 | 1.0065 |
| 33 | 25 | 0.08 | 0.4 | 12 | 0.059 | 4.987 | 1.00675 |
| 34 | 25 | 0.12 | 0.2 | 12 | 0.098 | 4.602 | 1.005583 |
| 35 | 25 | 0.12 | 0.3 | 12 | 0.021 | 4.455 | 1.006333 |
| 36 | 25 | 0.12 | 0.4 | 12 | 0.043 | 4.590 | 1.006917 |
| 37 | 75 | 0.04 | 0.2 | 12 | 0.056 | 3.657 | 1.007083 |
| 38 | 75 | 0.04 | 0.3 | 12 | 0.013 | 3.660 | 1.009833 |
| 39 | 75 | 0.04 | 0.4 | 12 | 0.047 | 3.667 | 1.009833 |
| 40 | 75 | 0.08 | 0.2 | 12 | 0.084 | 4.240 | 1.007417 |
| 41 | 75 | 0.08 | 0.3 | 12 | 0.043 | 4.247 | 1.008083 |
| 42 | 75 | 0.08 | 0.4 | 12 | 0.032 | 4.472 | 1.01 |
| 43 | 75 | 0.12 | 0.2 | 12 | 0.086 | 3.940 | 1.00825 |
| 44 | 75 | 0.12 | 0.3 | 12 | 0.016 | 3.885 | 1.009167 |
| 45 | 75 | 0.12 | 0.4 | 12 | 0.026 | 3.955 | 1.015833 |
| 46 | 125 | 0.04 | 0.2 | 12 | 0.04 | 3.457 | 1.010917 |
| 47 | 125 | 0.04 | 0.3 | 12 | 0.014 | 3.345 | 1.011833 |
| 48 | 125 | 0.04 | 0.4 | 12 | 0.028 | 3.500 | 1.012 |
| 49 | 125 | 0.08 | 0.2 | 12 | 0.073 | 4.035 | 1.009417 |
| 50 | 125 | 0.08 | 0.3 | 12 | 0.034 | 3.947 | 1.011083 |
| 51 | 125 | 0.08 | 0.4 | 12 | 0.01 | 3.945 | 1.012667 |
| 52 | 125 | 0.12 | 0.2 | 12 | 0.079 | 3.450 | 1.01125 |
| 53 | 125 | 0.12 | 0.3 | 12 | 0.009 | 3.457 | 1.012083 |
| 54 | 125 | 0.12 | 0.4 | 12 | 0.002 | 3.540 | 1.01325 |
| 55 | 25 | 0.04 | 0.2 | 16 | 0.035 | 6.025 | 1.001875 |

(*continued*)

**Table 6.3:** (*continued*)

| Trial No. | Parameter settings | | | | Hole quality parameters | | |
|---|---|---|---|---|---|---|---|
| | $v$ (m/min) | $f$ (mm/rev) | $c$ (%) | $D$ (mm) | $C_e$ (mm) | $R_a$ (microns) | $F_d$ |
| 56 | 25 | 0.04 | 0.3 | 16 | 0.025 | 5.950 | 1.002125 |
| 57 | 25 | 0.04 | 0.4 | 16 | 0.028 | 6.072 | 1.003875 |
| 58 | 25 | 0.08 | 0.2 | 16 | 0.046 | 6.525 | 1.001688 |
| 59 | 25 | 0.08 | 0.3 | 16 | 0.031 | 6.447 | 1.002188 |
| 60 | 25 | 0.08 | 0.4 | 16 | 0.039 | 6.625 | 1.002188 |
| 61 | 25 | 0.12 | 0.2 | 16 | 0.061 | 6.255 | 1.002375 |
| 62 | 25 | 0.12 | 0.3 | 16 | 0.02 | 6.087 | 1.002375 |
| 63 | 25 | 0.12 | 0.4 | 16 | 0.04 | 6.265 | 1.002563 |
| 64 | 75 | 0.04 | 0.2 | 16 | 0.035 | 5.232 | 1.002438 |
| 65 | 75 | 0.04 | 0.3 | 16 | 0.029 | 5.160 | 1.00275 |
| 66 | 75 | 0.04 | 0.4 | 16 | 0.029 | 5.237 | 1.003 |
| 67 | 75 | 0.08 | 0.2 | 16 | 0.041 | 5.072 | 1.002125 |
| 68 | 75 | 0.08 | 0.3 | 16 | 0.035 | 5.872 | 1.002813 |
| 69 | 75 | 0.08 | 0.4 | 16 | 0.039 | 6.035 | 1.004625 |
| 70 | 75 | 0.12 | 0.2 | 16 | 0.053 | 5.350 | 1.003375 |
| 71 | 75 | 0.12 | 0.3 | 16 | 0.036 | 5.157 | 1.003625 |
| 72 | 75 | 0.12 | 0.4 | 16 | 0.036 | 5.462 | 1.003813 |
| 73 | 125 | 0.04 | 0.2 | 16 | 0.026 | 4.227 | 1.003625 |
| 74 | 125 | 0.04 | 0.3 | 16 | 0.022 | 3.960 | 1.003063 |
| 75 | 125 | 0.04 | 0.4 | 16 | 0.028 | 4.257 | 1.003 |
| 76 | 125 | 0.08 | 0.2 | 16 | 0.038 | 4.860 | 1.004188 |
| 77 | 125 | 0.08 | 0.3 | 16 | 0.029 | 4.637 | 1.004188 |
| 78 | 125 | 0.08 | 0.4 | 16 | 0.037 | 4.857 | 1.005188 |
| 79 | 125 | 0.12 | 0.2 | 16 | 0.049 | 4.270 | 1.006813 |
| 80 | 125 | 0.12 | 0.3 | 16 | 0.037 | 4.145 | 1.006813 |
| 81 | 125 | 0.12 | 0.4 | 16 | 0.041 | 4.277 | 1.006688 |

The "Maxmill plus vertical machining center" (CNC machine with 7.5 kW power and 9,000 rpm speed) was used to conduct dry drilling experiments. The machining center employed for the present experimental study is illustrated in Figure 6.1. K20 grade tungsten carbide twist drills of 8, 12 and 16 mm diameter were used during experimentation. An aspect of drilling the cenosphere-MWCNT-epoxy hybrid composite is illustrated in Figure 6.1.

The "Mitutoyo SJ-201" (Figure 6.3) was utilized to evaluate centerline mean surface roughness ($R_a$) of the drilled hole. Measurements were performed with 0.8 mm cutoff length and average of four measurements for each trial was recorded.

The circularity error ($C_e$) was measured by "Faro gauge" (Figure 6.4) and maximum diameter ($D_{max}$) of drilled hole at the entrance. The delamination factor ($F_d$) is given by [26]

**Figure 6.1:** Maxmill plus vertical machining center.
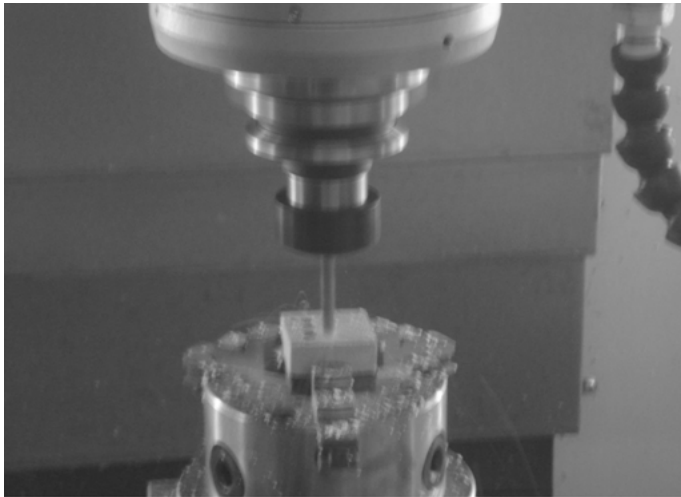


**Figure 6.2:** An aspect of drilling the cenosphere-MWCNT-epoxy hybrid composite.

$$F_d = \frac{D_{max}}{D} \tag{19}$$

where $D$ is the drill diameter. CAM Smart Inspect is a software package exclusively designed for the accurate measurements and inspection of intricate features merely by inputting the 3D measurements. Faro gauge is having a calibrated measuring ball.
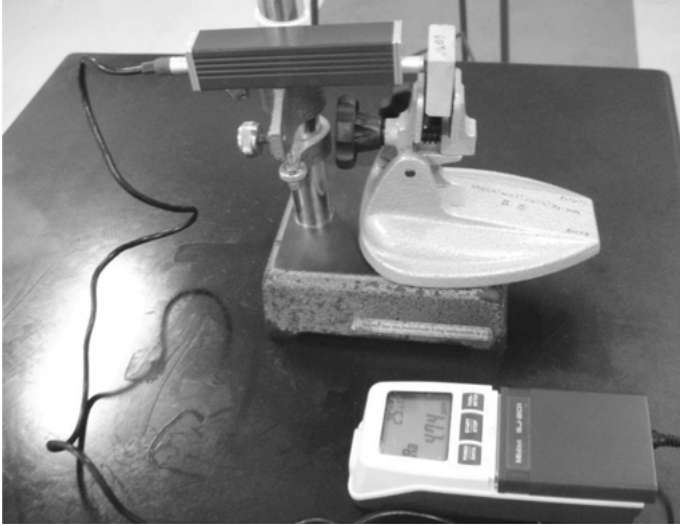
**Figure 6.3:** Experimental setup for measuring the surface roughness.
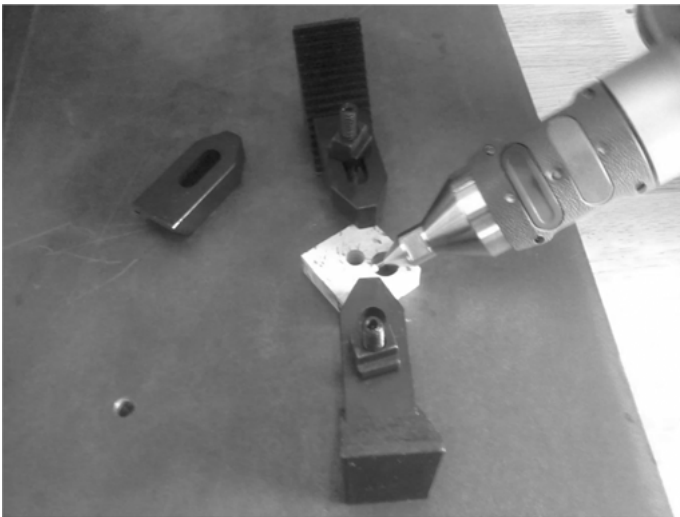


**Figure 6.4:** Faro gauge used for the measurement of circularity error.

The ball is checked for the flatness of measuring specimen by clamping it on the surface plate. Faro gauge is connected to the computer system with the installed package of CAM, which records the measured hole quality parameters.

Measured values of centerline average surface roughness ($R_a$) as well as the circularity error ($C_e$) and computed delamination factor ($F_d$) for 81 trials are presented in Table 6.3.

## 6.5  Results and discussion

### 6.5.1  ANN models for hole quality parameters

ANN for existing study involves four neurons in input layer (related to four input variables), three neurons in output layer (associated to three hole quality parameters), two hidden layers, that is, the first hidden layer with 10 neurons and second hidden layer with 6 neurons. In the current investigation, 65 patterns of the experimental design plan were randomly selected for the ANN training and trained with "traingdx" of MATLAB neural network toolbox [34] using variable learning rate method. The left over 16 input parameter combinations of the experimental design plan were utilized for the validation purpose. The patterns (inputs and outputs) are normalized earlier to training to lie in the range −1 to +1. After several trial runs, learning rate ($\alpha$) with 0.1 and momentum constant ($\beta$) with 0.9 were chosen for successful training for the selected ANN architecture. For every epoch, 65 training input-output patterns were consecutively employed and for each training pattern, the error is determined, which is back-propagated to adjust the synaptic weights. Toward the end of every epoch, the MSE due to 65 training patterns is computed. Further, remaining 16 patterns were presented for validation purposes and the MSE due to validation patterns is also computed. At the end of 1000 epochs, the MSE for training and validating patterns are 0.0075 and 0.033, respectively. Figure 6.5 gives the performances of ANN training and validation of the present study.
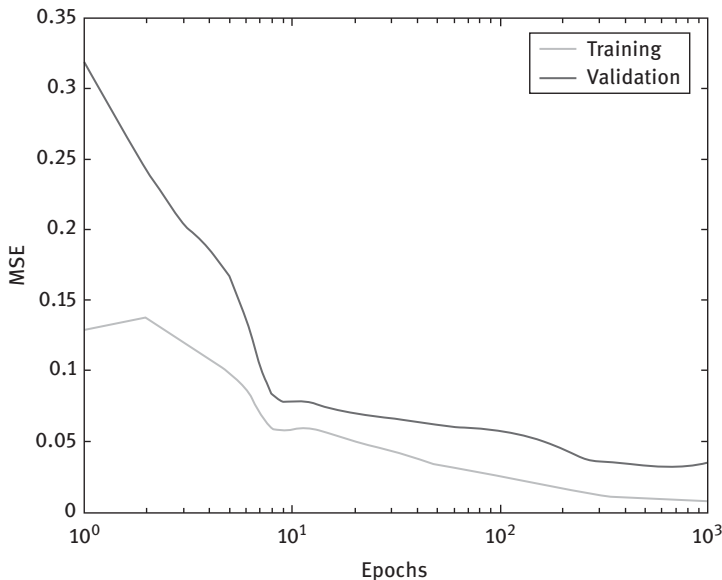


**Figure 6.5:** ANN training and validation performance.

The proposed ANN models were used to predict the circularity error ($C_e$), drilled hole surface roughness ($R_a$) and delamination factor ($F_d$) by altering cutting speed ($v$), feed ($f$), % weight of MWCNT ($c$) and the drill diameter ($D$) within the limits of the factors. The influence of factors on intended hole quality parameters are demonstrated in Figures. 6.6–6.8. Every hole quality parameter is plotted with drill diameter ($D$) for three combinations of cutting speed ($v$) – feed ($f$) and for 0.2%, 0.3% and 0.4% MWCNT ($c$) values. It is fairly apparent from Figures. 6.6–6.8 that there exist considerable interaction effects between the parameters on circularity error ($C_e$), drilled hole surface roughness ($R_a$) and delamination factor ($F_d$) for developed cenosphere-MWCNT-epoxy hybrid composites.

### 6.5.1.1 Circularity error analysis

Figure 6.6 depicts the interaction effects of input factors on circularity error for the drilled hole of cenosphere-MWCNT-epoxy hybrid composites. Greater circularity error is noticed for 0.2% MWCNT reinforcement for all the specified cutting condition combinations when compared to 0.3% and 0.4% MWCNT drilling. With 0.2% MWCNT reinforcement and for all the mentioned specified cutting condition combinations, the circularity error nonlinearly augments with increased drill diameter (8–12 mm); reaches the highest value and after that the circularity error decreases beyond 12 mm. It is evidently revealed from Figure 6.6 that, for all the specified cutting condition combinations, the circularity error is found to be minimal for 8 mm drill diameter.

With 0.3% MWCNT reinforcement, if both the cutting conditions are at low levels, the circularity error at the beginning augments with smaller range drill diameter (8 and 9 mm) and then decreases with 9–12 mm and finally circularity increases beyond 12 mm drill diameter. Moreover, the circularity error is highly nonlinear for medium levels of cutting conditions. For this combination of cutting conditions, the circularity more or less remains same for 8–10 mm drill diameter, drastically increases for 10 to 12 mm drill diameter and then the circularity error almost remains constant for12 to16 mm drill diameter. However, the circularity error reduces with increased drill diameter in low to medium range (8–11 mm) and after that the error augments beyond 11 mm drill diameter for higher level of cutting conditions with 0.3% MWCNT reinforcement. Hence, the drilling of cenosphere-MWCNT- epoxy hybrid composite with 11 mm diameter, operating at higher cutting speed and feed combination is found to be advantageous for minimal circularity error for 0.3% MWCNT reinforcement.

For the drilling operating at lower levels of cutting speed – feed combination, the circularity error increases with the drill diameter (8–12 mm) and then decreases up to14 mm drill diameter and the error almost remains constant from 14 to 16 mm drill diameter with 0.4% MWCNT reinforcement. On the other hand, the circularity behavior for the drilling cenosphere-MWCNT-epoxy hybrid composite operating at
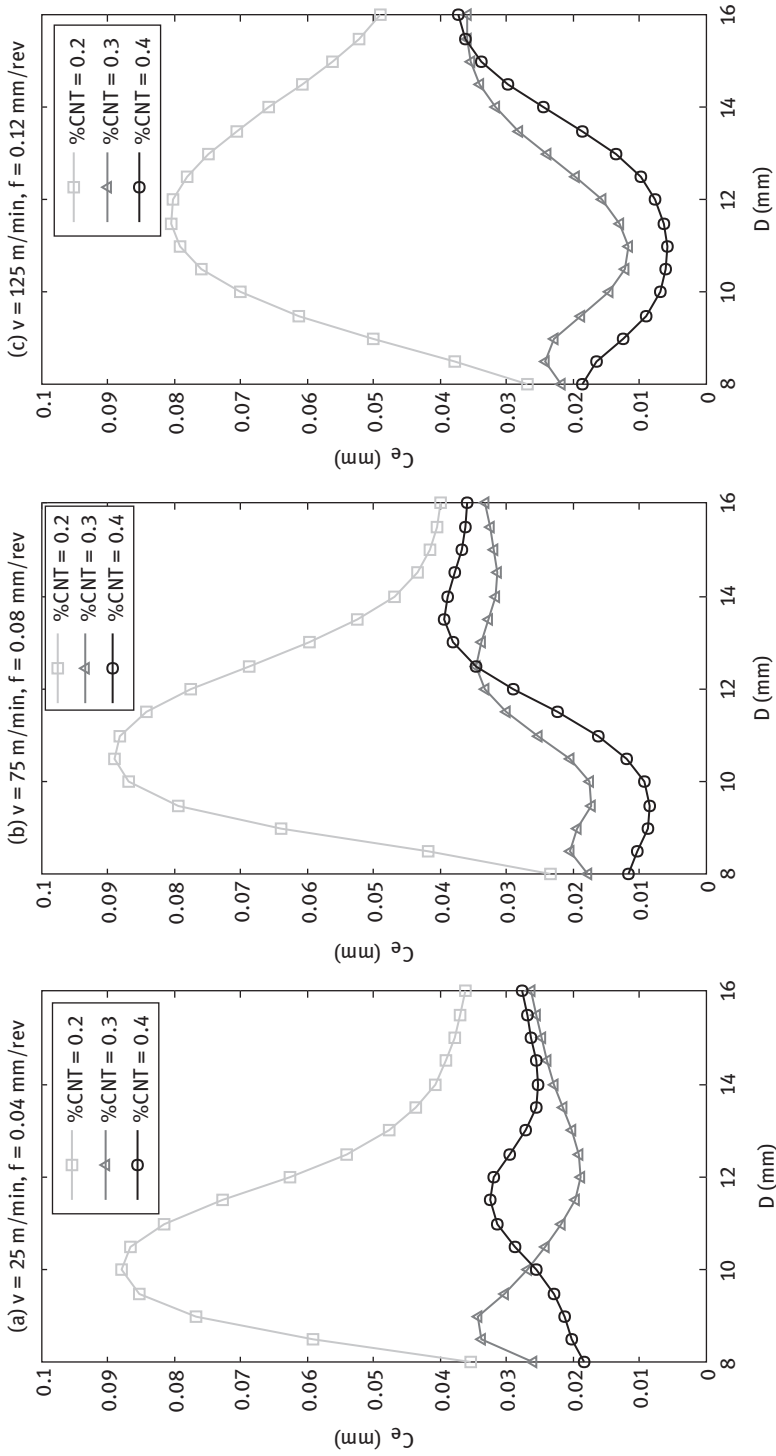
**Figure 6.6:** Effects of process parameters on circularity error.
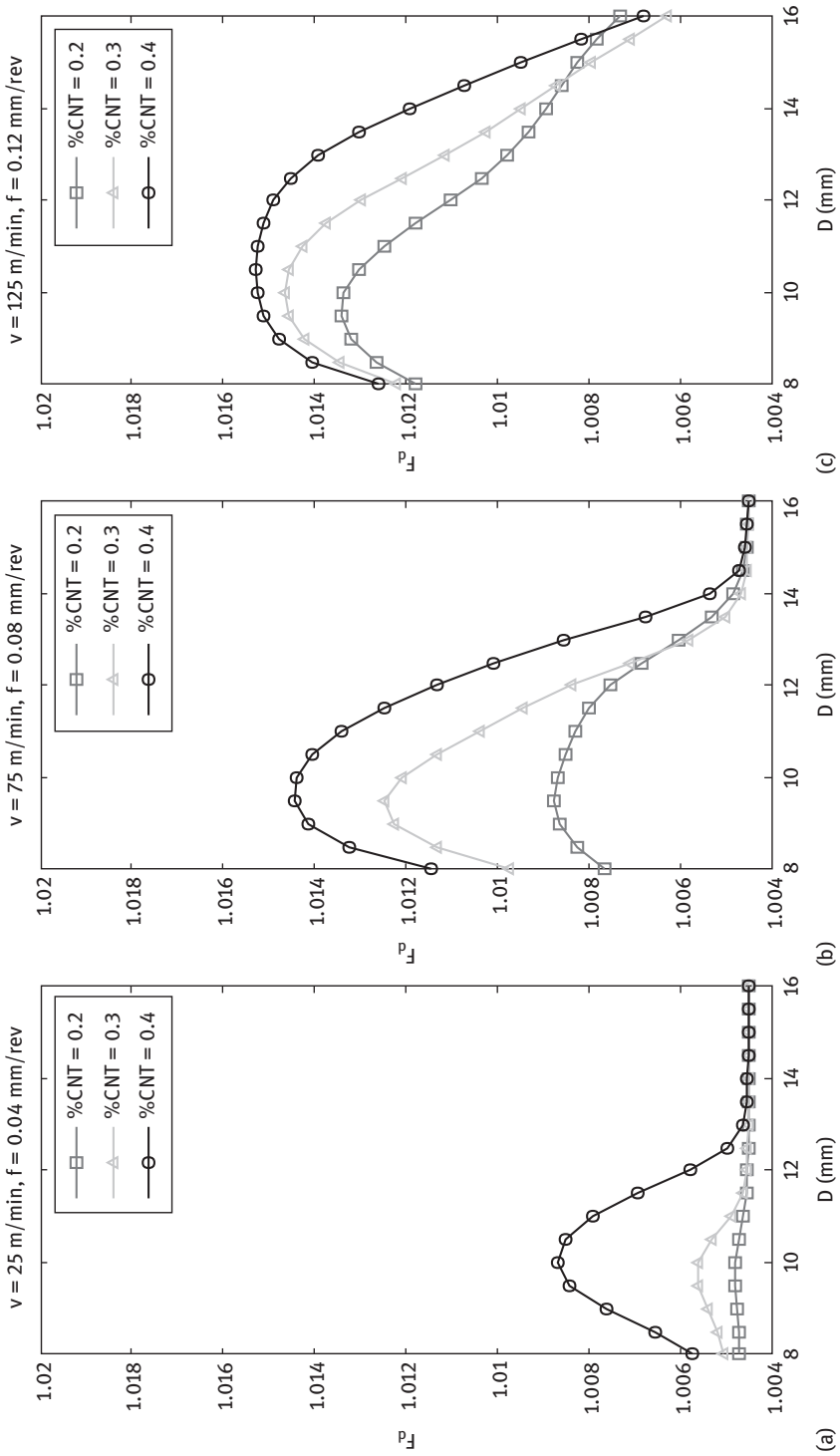
**Figure 6.7:** Effects of process parameters on surface roughness.
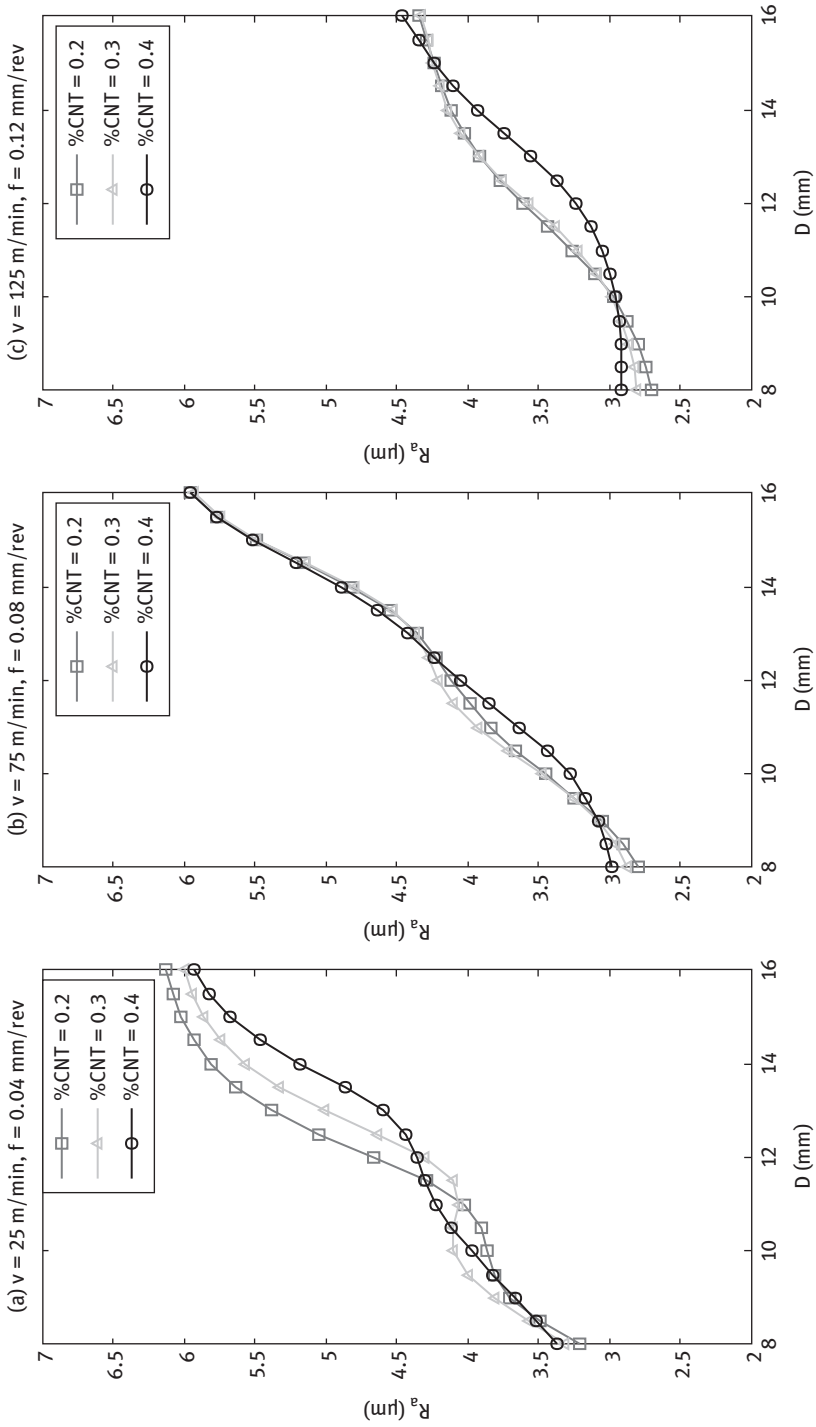
**Figure 6.8:** Effects of process parameters on delamination factor.

medium levels of cutting speed and feed is completely unusual. It is evidenced that the circularity error decreases initially with smaller drill diameter values (8–10 mm); the error drastically increases with drill diameter (10–14 mm range) and then decreases beyond 14 mm drill diameter. However, the circularity behavior for drilling with 0.4% MWCNT reinforcement is more or less similar to the behavior observed in drilling with 0.3% MWCNT. Consequently, the circularity error is minimal for drilling of cenosphere-MWCNT-epoxy hybrid composite operating at higher cutting speed and feed combination with 11 mm drill diameter for 0.4% MWCNT reinforcement.

From Figure 6.6, it is observed that the circularity error is minimal for higher cutting speed-feed combination. Krishnaraj et al. [30] also observed similar findings on high-speed drilling of CFRP composites. They indicated that the rotational stability is superior at higher speeds compared to lower speeds and hence circularity error is less. Alternatively, lower feed creates greater circularity mainly due to ploughing and frictional heating.

### 6.5.1.2 Surface roughness analysis

The variation of hole surface roughness with drill diameter for different MWCNT reinforcement, operating at different combinations of cutting conditions is depicted in Figure 6.7. It is seen that for all specified combinations of cutting speed and feed, increased drill diameter augments surface roughness. Additionally, it is found that with the increase in MWCNT from 0.2% to 0.4%, surface roughness drastically decreases with drill diameter in the range 8–16 mm. Reduced roughness is observed at higher levels of cutting conditions when compared to medium and lower level cutting conditions. Hence, 0.4% MWCNT is found to be beneficial in reducing the surface roughness irrespective of the cutting conditions and drill diameter.

It is noticed from Figure 6.7 that an elevated speed-feed combination along with lesser drill diameter and enhanced %MWCNT reinforcement results in reduced surface roughness. At the commencement, epoxy, cenosphere and MWCNT are uneven and thus robust interlocking takes place, leading to poor surface quality. With enhanced speed, the uneven profiles of epoxy and both the fillers are smoothened owing to abrasiveness and hence an improved surface quality. As reported by Angadi et al. [34], an addition of filler had a considerable influence in minimizing the surface roughness in drilling of syntactic foams. Our current investigation on cenosphere-multiwall carbon nanotubes (MWCNTs)-reinforced epoxy composite also supports this finding.

### 6.5.1.3 Delamination analysis

The estimation of delamination tendency with drill diameter is presented in Figure 6.8, which clearly exhibits extremely nonlinear behavior. In general, the delamination is found to be more for 0.4% MWCNT reinforcement for all specified combinations of

cutting conditions. For lower levels of cutting conditions, delamination almost remains constant for 0.2% MWCNT reinforcement. However, for 0.3% MWCNT reinforcement, initially, the delamination enhances with drill diameter operating at lower range (8–10 mm) and then decreases beyond 10 mm drill diameter after attaining the peak value and later the delamination virtually remains constant from 12 to 16 mm drill diameter. More or less similar pattern is observed for 0.4% MWCNT reinforcement, but at increased delamination damage. However, the delamination more or less remains stable from 13 to 16 mm drill diameter after reaching the maximum value at 13 mm drill diameter. It is worth mentioning here that the delamination tendency almost remains unaffected for any specified MWCNT reinforcement with the drilling operating at low levels of cutting conditions and higher drill diameter in the range 13–16 mm.

For medium and high level cutting condition combinations, the delamination formerly amplifies with drill diameter, reaches the highest value and subsequently the delamination continuously decreases beyond 10 mm for all specified combinations of cutting conditions and any specified MWCNT reinforcement. Hence, it is visibly noticed from Figure 6.8 that the minimal delamination is observed at lower cutting speed-feed combination with 0.2% MWCNT reinforcement. The highest delamination damage was observed at higher level cutting speed-feed combination with 10 mm drill diameter with 0.2% MWCNT reinforcement drilling.

As seen from Figure 6.8, delamination increases with the increased speed-feed combination. It is obvious that thrust increases with feed. The drilling investigations on polymeric composites by Velayudham and Krishnamurthy [35] revealed that delamination enhances with increased thrust. At higher cutting speed values, delamination might originate at lesser forces due to matrix heating of those results in minor stiffness [30].

Figures 6.6–6.8 obviously indicate the nonlinear behavior between the proposed hole quality parameters and the chosen process parameters. The behavior of individual hole quality parameter with input parameters is completely dissimilar from other hole quality parameter. Further, it is also noticed that, dissimilar combination of cutting conditions and % MWCNT is crucial for concurrently minimizing the circularity error, hole surface roughness and delamination factor. This necessitates a competent multi-response optimization method for the selection of optimal combination of cutting conditions, which concurrently minimize the circularity error, hole surface roughness and the delamination factor. Hence, GS technique, a multi-objective optimization tool has been employed for concurrently minimizing circularity error, hole surface roughness and the delamination factor.

## 6.5.2 GS optimization for hole quality parameters

The constructed ANN models were used with GS optimization to decide the optimal combinations of cutting conditions for a specific drill diameter ($D$) and % MWCNT (c)

for minimal of circularity error ($C_e$), drilled hole surface roughness ($R_a$) and delamination factor ($F_d$). All three hole quality parameters are normalized and combined to form a fitness value "Fit", that is to be minimized. In existing study, optimization statement is as follows:

For a given drill diameter ($D$) and % MWCNT ($c$),

Determine optimal cutting speed ($v$) and feed ($f$),

So as to minimize,$Fit = [(\frac{C_e}{0.1}) + (\frac{R_a}{7}) + (\frac{F_d}{1.02})]$

Subject to: $25 \leq v \leq 125$ m/min and $0.04 \leq f \leq 0.12$ mm/rev.

GS optimization utilizing ANN models is performed using MATLAB software [36] with a population size ($Z$) = 50 and 300 iterations (max). The convergence of GS for 16 mm drill diameter ($D$) and 0.2% MWCNT is depicted in Figure 6.9.
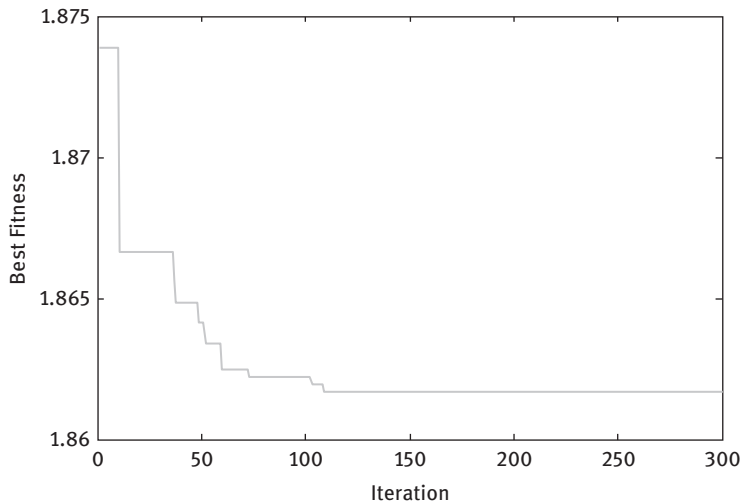


**Figure 6.9:** Convergence of GS (D = 16 mm, %MWCNT=0.2).

For every "$D$" in 8–16 mm range, the best grouping of cutting speed ($v$) and feed ($f$) for 0.2%, 0.3% and 0.4% of MWCNTs were recorded for minimal circularity error ($C_e$), drilled hole surface roughness ($R_a$) and delamination factor ($F_d$). Figures 6.10 and 6.11 depict optimal values of cutting conditions. The optimal values of circularity error ($C_e$), delamination factor ($F_d$) and drilled hole surface roughness ($R_a$) for 0.2%, 0.3% and 0.4% MWCNT reinforcement for each $D$ specified in the range 8–16 mm were also recorded. Figures 6.12–6.13 illustrate the optimal values of hole quality parameters for different drill diameter values.

As observed from Figure 6.10, the optimal cutting speed is at the higher level that is, in the range 123–125 m/min irrespective of the MWCNT reinforcement and for any specified drill diameter for better hole quality. Figure 6.11 indicates that the optimal
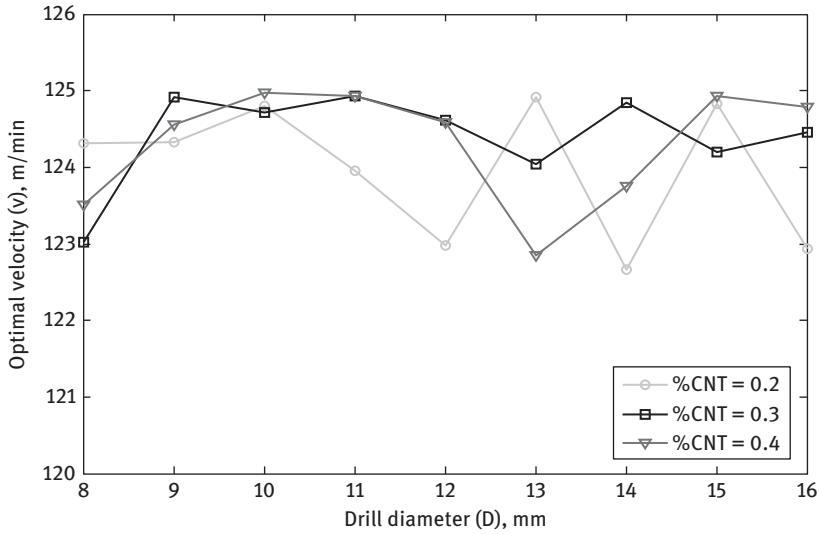
**Figure 6.10:** Relationship between optimal cutting speed and drill diameter.
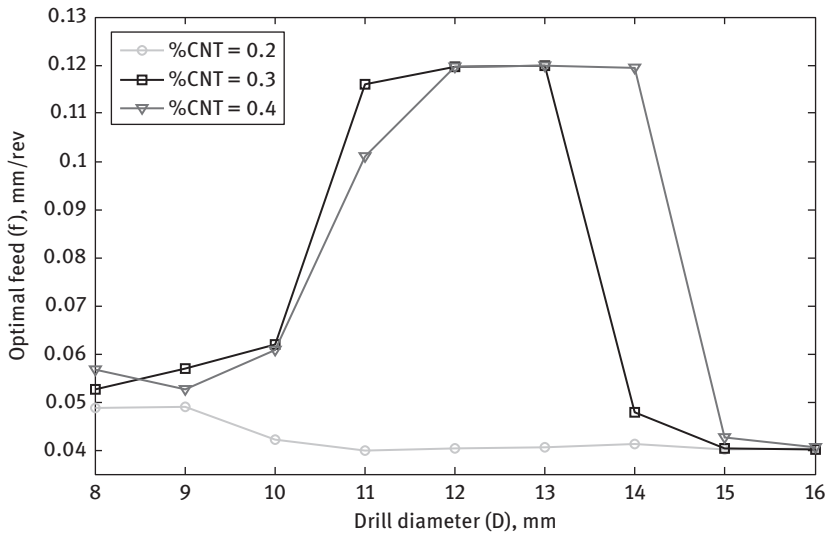


**Figure 6.11:** Relationship between optimal feed and drill diameter.

feed almost remains constant at lower level, that is, 0.04–0.05 mm/rev for any specified drill diameter with 0.2% MWCNT reinforcement in order to have better quality. On the other hand, with 0.3% MWCNT reinforcement, the optimal feed is 0.05–0.12 mm/rev, which is in straight proportion to drill diameter in 8–11 mm range; the optimal feed remains constant (0.12 mm/rev) for drill diameter (11–13 mm); whereas the optimal feed

diminishes with drill diameter beyond 13 mm. Similar behavior was also observed for 0.4% MWCNT reinforcement drilling, where the optimal feed requirement is 0.12 mm/rev for 12–14 mm drill diameters.

From Figure 6.12, it is noticed that, through 0.2%MWCNT reinforcement, the optimal circularity error is in straight proportion to drill diameter in low to medium range (8–12mm); remains constant from 12 to 13 mm drill diameter and the optimal circularity error decreases beyond 13 mm drill diameter. However, with 0.3 and 0.4% MWCNT reinforcement, the optimal circularity error is in direct proportion with the drill diameter up to 14 mm and then suddenly decreases beyond 14 mm. However, an increase in MWCNT decreases the circularity error for 8–16 mm drill diameters. However, this reduction is much more significant for all the drill diameters, when the MWCNT is increased from 0.2 to 0.3%MWCNT; there is no much remarkable reduction in the circularity error when the MWCNT is increased from 0.3% to 0.4% MWCNT. As can be seen from Figure 6.12, 0.3%MWCNT is found to be beneficial to reduce the circularity error for the whole drill diameters in the range 8–16 mm.
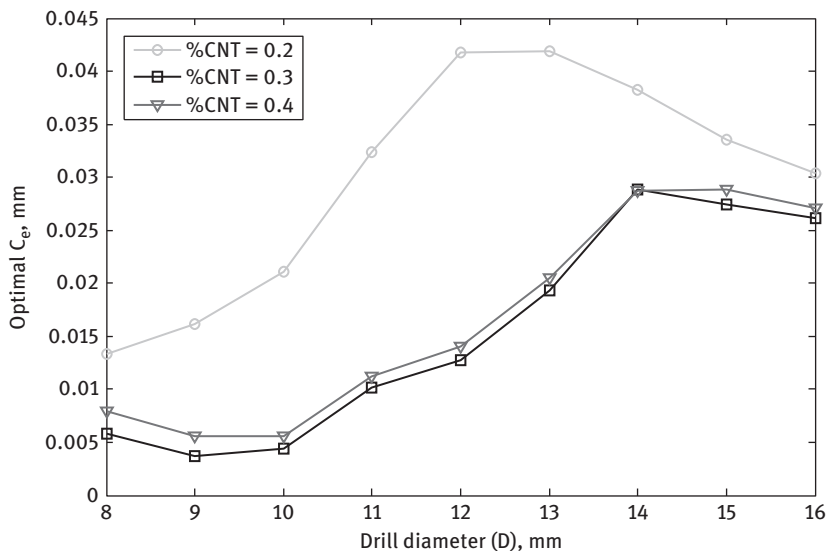


**Figure 6.12:** Optimal circularity error obtained by GS optimization for different values of drill diameter.

From Figure 6.13, it is observed that the optimal surface roughness is in proportion to drill diameter in the range 8–16 mm for all the specified MWCNT reinforcement drilling. However, a higher value of 0.4%MWCNT is required to reduce the surface roughness for drill diameter in the range 8–13 mm, whereas a lower value of 0.2%MWCNT is beneficial for the reduction of surface roughness with further increased drill diameter beyond 13 mm. On the other hand, as shown in Figure 6.14, the optimal delamination increases
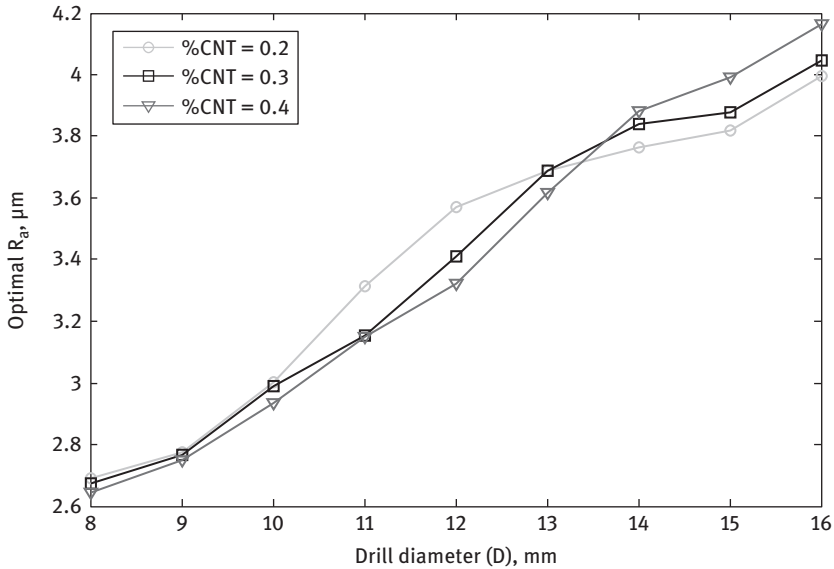
**Figure 6.13:** Optimal surface roughness obtained by GS optimization for different values of drill diameter.
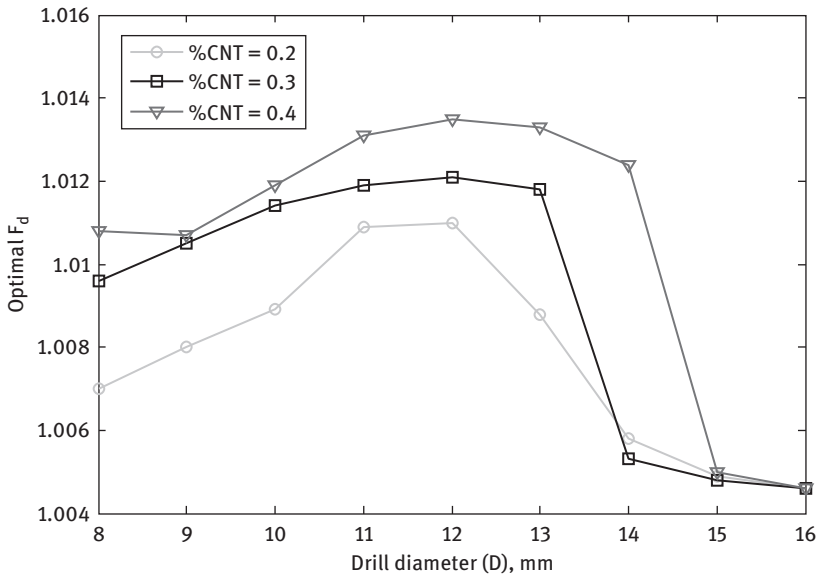


**Figure 6.14:** Optimal delamination factor obtained by GS optimization for different values of drill diameter.

with drill diameter up to 12 mm and after that decreases beyond 12 mm drill diameter for all the specified MWCNT reinforcement drilling and relatively similar behavior was

observed for all the MWCNT reinforcement drilling. Moreover, 0.2%MWCNT is found to be useful for minimizing the delamination for all drill diameters.

From the present experimental results and subsequent analysis of cenosphere-MWCNTs composites drilling, it is observed that the ANN has the competence to acquire every amount of nonlinearity with excellent generalization potential and high degree of precision. The topology of developed ANN modeling for the present research and the parameters chosen for training and the validation performances are obtained through several simulations and found to be apt for ANN modeling of the planned hole quality parameters. Conversely, the GS optimization results revealed that for every drill diameter, the optimal situation of MWCNT is different for different hole quality parameter. GS optimization presented here is one such best probable result and hence exists in numerous optimal solutions, as the association among planned hole quality and selected variables is nonlinear.

## 6.6 Conclusions

ANN modeling for circularity error, surface roughness and delamination factor and the GS optimization for concurrent minimization of proposed hole quality parameters in drilling of MWCNTs-reinforced epoxy composite materials has been presented. The minimum trials were conducted using FFD and ANN models for intended hole quality parameters were developed considering the cutting speed, feed, drill diameter and % MWCNT as input factors. Fitness function was evaluated through linear mapping. For each value of drill diameter and %MWCNT combination, the optimal cutting speed and feed values have been obtained through GS simulation. The following are concluded:

– An increase in MWCNT seems to reduce the circularity error for any given drill diameter and cutting condition combinations. However, this reduction is more significant for the 10–14 mm drill diameter range.
– The surface roughness increases with drill diameter for all MWCNT and specified cutting condition combinations. For a given drill diameter and MWCNT, simultaneous increase in cutting conditions has noticeable effect on surface roughness reduction. MWCNT has less cause in reducing the surface roughness, though higher MWCNT is preferred.
– For a known drill diameter and cutting condition, more % MWCNT has noteworthy effect in increasing the delamination. For a specified drill diameter and MWCNT, concurrent increased cutting conditions have larger effect in increasing the delamination.
– The optimal cutting speed requirement is at higher level, that is, in the range 123–125 m/min for better hole quality, irrespective of the drill diameter and MWCNT reinforcement drilling.

- The optimal feed is more or less remains steady at lower level, that is, 0.04–0.05 mm/rev with 0.2% MWCNT reinforcement drilling; this is in direct proportion to drill diameter (8–12 mm range) and decreases with drill diameter beyond 12 mm with 0.3% and 0.4% MWCNT reinforcement drilling.
- For minimizing the circularity error, 0.3% MWCNT reinforcement is desirable for all drill diameters.
- Optimal surface roughness is in straight proportion to drill diameter for all MWCNT reinforcement drilling.
- 0.2%MWCNT is helpful for minimizing the delamination for every drill diameter.

## References

[1]    W. D. Scott, Vinyl Ester/Cenosphere composite materials for civil and structural engineering, Fiber Reinforced Polymer International. 2(3) (2005) 2–5.

[2]    R. J. Cardoso, A. Shukla, A. Bose, Effect of particle size and surface treatment on constitutive properties of polyester cenosphere composites, Journal of Materials Science. 37(3) (2002) 603–613.

[3]    M. Labella, S. E. Zeltmann, y V. C. Shunmugasam, N. Gupta, K. P. RohatgiMechanical and thermal properties of fly ash/vinylester syntactic foams, Fuel. 121 (2014) 240–249.

[4]    R. Balaji, M. Sasikumar, A. Elayaperumal, Thermal, thermo oxidative and ablative behavior of cenosphere filled ceramic/phenolic composites Polymer Degradation and Stability. 114 (2015) 125–132.

[5]    A. Das, B. K. Satapathy, Structural, thermal, mechanical and dynamic mechanical properties of cenosphere filled polypropylene composites, Materials and Design. 32 (2011) 1477–1484.

[6]    W. A. Uju, I. N. A. Oguocha, A study of thermal expansion of Al–Mg alloy composites containing fly ash, Materials and Design. 33 (2012) 503–509.

[7]    N. Chand, P. Sharma, M. Fahim, Correlation of mechanical and tribological properties of organosilane modified cenosphere filled high density polyethylene, Materials Science and Engineering A. 527 (2010) 5873–5878.

[8]    T. Morimoto, T. Suzuki, H. Iizuka, Wear rate and fracture toughness of porous particle-filled phenol composites, Composites Part B. 77 (2015) 19–26.

[9]    N. Gupta, E. Woldesenbet, P. Mensah, Compression properties of syntactic foams: Effect of cenosphere radius ratio and specimen aspect ratio, Composites: Part A. 35 (2004) 103–111.

[10]   R. Balaji, M. Sasikumar, A study on the effect of cenosphere on thermal and ablative behavior of cenosphere loaded ceramic/phenolic composites, Polymer. 55 (2014) 6634–6639.

[11]   J. B. Bai, A. Allaoui, Effect of the length and the aggregate size of MWNTs on the improvement efficiency of the mechanical and electrical properties of nanocomposites-experimental investigation, Composite Part A: Applied Science and Manufacturing. 34 (2003) 689–694.

[12]   F. H. Gojny, M. H. G. Wichman, B. Fiedler, K. Schulte, Influence of different carbon nanotubes on the mechanical properties of epoxy matrix composites – A comparative study, Composites Science and Technology. 65 (2005) 2300–2313.

[13]   P. Guo, X. Chen, X. Gao, H. Song, H. Shen, Fabrication and mechanical properties of well-dispersed multiwalled carbon nanotubes/epoxy composites, Composites Science and Technology. 67 (2007) 3331–3337.

[14] L. Liu, K. C. Etika, K. S. Liao, L. A. Hess, D. E. Bergbreiter, J. C. Grunlan, Comparison of covalently and non covalently functionalized carbon nanotubes in epoxy, Macromolecular Rapid Communications. 30 (2009) 627–632.

[15] Z. Spitalsky, C. A. Krontiras, S. N. Georga, C. Galiotis, Effect of oxidation treatment of multi-walled carbon nanotubes on the mechanical and electrical properties of their epoxy composites, Composites Part A: Applied Science and Manufacturing. 40 (2009) 778–783.

[16] M. Yang, Y. Gao, H. Li, A. Adronov, Functionalization of multiwalled carbon nanotubes with polyamide 6 by anionic ringopening polymerization, Carbon. 45 (2007) 2327–2333.

[17] V. C. Divya, K. M. Ameen, B. Nageshwar Rao, R. R. N. Sailaja, High density polyethylene/cenosphere composites reinforced with multi-walled carbon nanotubes: Mechanical, thermal and fire retardancy studies, Materials and Design. 65 (2015) 377–386.

[18] M. Dimchev, R. Caeti, N. Gupta, Effect of carbon nanofibers on tensile and compressive characteristics of hollow particle filled composites, Materials and Design. 31 (2010) 1332–1337.

[19] N. S. Mohan, A. Ramachandra, S. M. Kulkarni, Influence of process parameters on cutting force and torque during drilling of glass–fiber polyester reinforced composites, Composite Structures. 71 (2005) 407–413.

[20] J. C. Rubio, T. H. Panzera, A. M. Abrão, P. E. Faria, J. P. Davim, Effects of high speed in the drilling of glass whisker-reinforced polyamide composites (PA66 GF30): statistical analysis of the roughness parameters, Journal of Composite Materials. 45 (2011) 1395–1402.

[21] C. C. Tsao, H. Hocheng, Evaluation of thrust force and surface roughness in drilling composite material using Taguchi analysis and neural network, Journal of Materials Processing Technology. 203 (2008) 342–348.

[22] R. Zitoune, V. Krishnaraj, F. Collombet, Study of drilling of composite material and aluminium stack, Composite Structures. 92 (5) (2010) 1246–1255.

[23] U. A. Khashaba, Delamination in drilling GFR thermoset composites, Composite Structures. 63 (2004) 313–327.

[24] C. C. Tsao, H. Hocheng, Effects of special drill bits on drilling-induced delamination of composite materials, International Journal of Machine Tools and Manufacture. 46 (2006) 1403–1416.

[25] J. P. Davim JP, P. Reis, V. Lapa, C. C. Antonio, Machinability study on polyetheretherketone (PEEK) unreinforced and reinforced (GF30) for application in structural components, Composite Structures. 62 (2003) 67–73.

[26] J. P. Davim, J. C. Rubio, A. M. Abrão, A novel approach based on digital image analysis to evaluate the delamination factor after drilling composite laminates, Composites Science and Technology. 67 (2007) 1939–1945.

[27] V. N. Gaitonde, S. R. Karnik, J. C. Rubio, A. E. Correia, A. M. Abrão, J. P. Davim, Analysis of parametric influence on delamination in high-speed drilling of carbon fiber reinforced plastic composites, Journal of Materials Processing Technology. 203 (2008) 431–438.

[28] S. R. Karnik, V. N. Gaitonde, J. C. Rubio, A. E. Correia, A. M. Abrão, J. P. Davim, Delamination analysis in high-speed drilling of carbon fiber reinforced plastics (CFRP) using artificial neural network model, Materials and Design. 29 (2008) 1768–1776.

[29] K. Palanikumar, L. Karunamoorthy, L. Manoharan, Mathematical model to predict the surface roughness on the machining of glass fiber reinforced polymer composites, Journal of Reinforced Plastics and Composites. 25 (2006) 407–417.

[30] V. Krishnaraj, A. Prabhukarthi, A. Ramanathan, N. Elanghovan, M. Senthil Kumar, R. Zitoune, J. P. Davim, Optimisation of machining parameters at high speed drilling of Carbon Fiber Reinforced Plastic (CFRP) laminates, Composites Part B. 43 (2012) 1791–1799.

[31] D. C. Montgomery, Design and Analysis of Experiments, New York: John Wiley and Sons, 2003.

[32] L. Fausett L, Fundamentals of Neural Networks: Architectures, Algorithms and Applications. New York: Prentice–Hall, 1994.

[33]  R. Esmat, N. Hossein, S. Saeid, GSA: A Gravitational Search Algorithm, Information Sciences. 179 (2009) 2232–2248.

[34]  S. B. Angadi, R. Melinamani, V. N. Gaitonde, M. Doddamani, S. R. Karnik, Experimental investigations on drilling characteristics of cenosphere reinforced epoxy composites, Advanced Mechanics and Materials. 766–767 (2015) 801–811.

[35]  A. Velayudham A, R. Krishnamurthy, Effect of point geometry and their influence on thrust and delamination in drilling of polymeric composites Journal of Materials Process Technology. 185 (2007) 204–209.

[36]  Math Works Incorporation. MATLAB User Manual, Version 7.1, R 14, Natick, MA, 2005.

# Index

# De Gruyter Series in Advanced Mechanical Engineering

www.degruyter.com